MONITORING MORPHOLOGY IN ORGANIC PHOTOVOLTAIC BLEND SYSTEMS

A Dissertation
Presented to
The Academic Faculty

by

Ian Pelse

In Partial Fulfillment
of the Requirements for the Degree
Doctor of Philosophy in the
School of Chemistry and Biochemistry

Georgia Institute of Technology
August 2020

MONITORING MORPHOLOGY IN ORGANIC PHOTOVOLTAIC BLEND SYSTEMS

Approved by:

Dr. John R. Reynolds, Advisor
School of Chemistry & Biochemistry
School of Materials Science & Engineering
Georgia Institute of Technology

Dr. Shannon K. Yee
School of Mechanical Engineering
Georgia Institute of Technology

Dr. Elsa Reichmanis
School of Chemical & Biomolecular Engineering
Georgia Institute of Technology

Dr. Natalie Stingelin
School of Materials Science & Engineering
School of Chemical & Biomolecular Engineering
Georgia Institute of Technology

Dr. Mostafa El-Sayed
School of Chemistry & Biochemistry
Georgia Institute of Technology

Date Approved: April 29, 2020

For my family

ACKNOWLEDGEMENTS

As I approach the end of my graduate career, I am constantly reminded of the importance of friends and family. I would not be completing my thesis without their unwavering support of my academic development. I would like to start by thanking my father, Igor Pelse, for instilling in me the kind of skepticism that makes me a good scientist. You were the only one to ask me if college is right for me, and the only one to stop and ask me if pursuing a Ph.D. was something that I truly wanted to do. I think about those conversations often and they really help to place all aspects of my life into perspective. I think about you every day and I miss you.

I would like to thank my mother, Caren Donahue, for her love and support. Knowing that you are always trying to do what's best for me is a constant source of comfort and encouragement. Your support through the ups and downs of life in graduate school is the only reason that I was able to stay and finish. I would like to thank my sister, Elena Pelse, for the jokes and the diversions that are always welcome. I would like to thank my second parents, my aunt and uncle, Marina Pelse and Richard Burns. I would like to thank Randolph Huff for joining my family.

I would like to thank my partner, Marta Garibaldi. You moved down with me to Atlanta so I could attend Georgia Tech, and I will always be grateful for that. You have been a constant source of love, encouragement, and support. Thank you for putting up with the late nights and the hot summers. I can't wait to see where we end up next.

I would like to thank my undergraduate advisor, Dr. Christopher Lafratta, for setting me on the course to graduate school. Your enthusiasm of science and teaching pulled me toward a major in chemistry, and onto the path of scientific research. I would also like to thank Dr. Swapan Jain, who was my second college advisor whether he knew it or not.

I would like to thank my graduate advisor, Dr. John Reynolds, for welcoming me into his research group with open arms. You have been a fantastic advisor and mentor and I am constantly thankful that I was able to find such an excellent research group to join. For your technical expertise, your careful reading, your willingness to help with life's many challenges, I am grateful. Thank you for nurturing both my academic and professional development in the many ways that you have done.

I would like to thank the members of my thesis committee: Dr. Elsa Reichmanis, Dr. Mostafa El-Sayed, Dr. Shannon Yee, and Dr. Natalie Stingelin, and Dr. Joseph Perry. Your input at the various milestones of my graduate career has been immensely helpful and reassuring. Thank you for the time that you have dedicated to my scientific development.

I would like to thank my collaborators at NIST: Dr. Lee Richter, Dr. Sebastian Engmann, and Dr. Andrew Herzing. Thank you for providing the resources and expertise to take my research to the next level. I am constantly humbled by your expertise.

As a builder of devices, I am of no use without materials to study. Fortunately, I have had the privilege to work with talented synthetic chemists who have made materials well worth investigating. Thank you to Dr. Bing Xu, Dr. Austin Jones, and Dr. Rylan Wolfe

for making polymers that the work presented this dissertation relied on. For the other projects not presented herein: thank you to Dr. Hayden Black, Dr. Graham Collier, Dr. Brian Schmatz, and Dr. Jungho Lee for bringing me onto your projects and trusting me to make good use of the materials that you have made.

On the device side, I would like to first thank my mentor Dr. Jeff Hernandez, who taught me how to make organic photovoltaic devices and how to work efficiently. I would also like to thank my other device colleagues outside of the Reynolds group: Dr. Shruti Agarkar, Felipe Larrain, and Victor Rodriguez-Toro. Sometimes it gets lonely making solar cells and troubleshooting the glovebox or the solar simulator or the EQE by yourself, and I have appreciated working with you all over the years.

To Dr. Anna Österholm and Dr. Eric Shen, thank you both for your leadership, guidance, and friendship. Thank you to the rest of my friends in the Reynolds group, both past and present: Dr. Sandra Pittelli, Dr. Brian Schmatz, Dr. Dylan Christiansen, Dr. Kin Lo, Dr. James Ponder, Dr. Erdal Uzunlar, Dr. Jeff Hernandez, Dr. Bing Xu, Dr. Michel De Keersmaecker, Dr. Austin Jones, Dr. Graham Collier, Gus Lang, Brandon DiTullio, Austin Bassett, Linda Nhon, Lisa Savagian, Abigail Advincula, and Josh Rinehart. Thank you especially to Dr. Austin Jones and Abigail Advincula for taking over the solid state device laboratory after my departure.

The information in the introduction has been pulled in large part from a variety of journal articles, including review articles and many of the original publications that they cite, but much of my inspiration has come from my peers in the Reynolds Research Group. Thus, I find it appropriate to acknowledge here my fellow group members who have come

before me and written their own dissertations, from which I have taken both inspiration and references. In essence, this paragraph serves to acknowledge those former students whose quality work has helped me and to advertise their dissertations for further reading. Caroline Grand, Brian Schmatz, and Chi Kin Lo were hybrid graduate students, working both in the synthesis lab and in the characterization and device laboratories to design their own polymers and bring their projects to completion. Caroline's dissertation is especially thorough on the fundamentals of organic electronic materials from a structural perspective, Brian's synthetic perspective led him to strong discussions regarding processability and environmental impact, and Kin's work emphasized the importance of thorough material synthesis and characterization when attempting to draw conclusions from the complexities of the solid-state world. The concise introduction in James Ponder's dissertation offers an excellent history of the field and reflects his passion for redox active polymers, and was adapted from his book chapter in The WSPC Reference on Organic Electronics.[1] The dissertation of Sandra Pittelli explains color and electrochromism from her strong background in redox chemistry and chemical doping. Finally, Jeff Hernandez, my mentor in organic photovoltaics, did a wonderful job explaining the field of organic photovoltaics from a processing perspective.

TABLE OF CONTENTS

LIST OF TABLES

LIST OF FIGURES

LIST OF SYMBOLS AND ABBREVIATIONS

AFM	atomic force microscopy
BHJ	bulk-heterojunction
CB	chlorobenzene
CN	1-chloronaphthalene
CT	charge transfer
$Đ$	dispersity
DCB	*o*-dichlorobenzene / 1,2-dichlorobenzene
DIO	1,8-diiodooctane
DMN	dimethylnaphthalene
DPE	diphenyl ether
DSC	differential scanning calorimetry
ECD	electrochromic device
EMCCD	electron multiplying charge coupled device
EQE	external quantum efficiency
$f_{\perp}$	molecular orientation parameter
FF	fill factor
FREA	fused ring electron acceptor
FWHM	full width at half maximum
ΔG_m	Gibbs free-energy of mixing
GISAXS	grazing incidence small angle X-ray scattering
GIWAXS	grazing incidence wide angle X-ray scattering
GPC	gel permeation chromatography

ΔH_m	enthalpy of mixing
HOMO	highest occupied molecular orbital
HSP	Hansen solubility parameters
ICBA	indene-C_{60} bisaccudct
IPA	isopropyl alcohol
IPCE	incident photon to charge carrier efficiency
IQE	internal quantum efficiency
ISI	integrated scattering intensity
ITO	indium tin oxide
J-V	current density – voltage
J_{SC}	short circuit current density
k_B	Boltzmann constant
LAADF	low-angle annular dark-field
L_C	crystal correlation length / coherence length
LUMO	lowest unoccupied molecular orbital
M_n	number average molecular weight
M_w	weight agerage molecular weight
NDI	naphthalene diimide
NFA	non-fullerene acceptor
NIR	near infrared
NMR	nuclear magnetic resonance
ODT	1,8-octanedithiol
OECT	organic electrochemical transistor
OFET	organic field effect transistor
OPV	organic photovoltaics

P3HT	poly(3-hexylthiophene)
$PC_{61}BM$	phenyl-C_{61}-butyric acid methyl ester
$PC_{71}BM$	phenyl-C_{71}-butyric acid methyl ester
PCE	power conversion efficiency
PDI	perylene diimide
PEDOT:PSS	poly(3,4-ethylenedioxythiophene):poly(styrene sulfonate)
PS	polystyrene
q	momentum transfer / scattering vector
R2R	roll-to-roll
Ra	distance in solubility space
rDoC	relative degree of crystallinity
RSoXS	resonant soft X-ray scattering
ΔS_m	entropy of mixing
S	Herman orientation parameter
S_0	singlet ground state
S_1	singlet excited state
SCLC	space-charge-limited current
STEM	scanning transmission electron microscopy
SVA	solvent vapor annealing
TEM	transmission electron microscopy
TMB	1,2,4-trimethylbenzene
VBG	volume Bragg grating
V_m	molar volume
V_{OC}	open circuit voltage
δ	Hildebrand solubility parameter

μ charge mobility

χ Florry-Huggins interaction parameter or polar angle

SUMMARY

Solution processed organic solar cells based on a bulk-heterojunction morphology have attracted attention as a promising source of energy, featuring materials that can be integrated into devices with the potential for scalable production at low cost. This dissertation discusses the processing of blends of conjugated polymers and discrete molecules, which are typically electron donating and accepting materials, respectively, for thin-film photovoltaic applications. Critical to the performance of the blend film is the nano- and micro-scale morphology, which is dictated by inter- and intra-molecular interactions among the blend components. This morphology can be controlled during the solution processing step, which is the focus of this dissertation. Traditionally, spin-coating has been used to process the active layer, but due to the dynamic nature of the coating process, this technique is not considered to be industrially scalable. Thus, the work featured herein makes use of blade coating to deposit the active layer and explores techniques to understand the dynamics of the blade coating process. Dynamic measurement techniques and detailed X-ray scattering analysis are used to monitor the solidification process and the developing morphology of pristine materials and their blends.

Chapter 1 introduces the basic concepts of organic photovoltaics: materials design, solution processing, device construction, and characterization. Special attention is paid to understanding solid state morphology and understanding its development in real time, which leads into chapter 2, on experimental methods and characterization techniques. All aspects of device fabrication and characterization need to be addressed carefully to ensure reproducible measurements. Special care is taken to address calibration of necessary

equipment as well as proper workflows for processing rich data sets such as 2-D X-ray scattering patterns. Chapters 3, 4, and 5 are the main project chapters of this dissertation; each focuses on a different polymer to understand the structure and morphology development during solution processing, and the subsequent effect on photovoltaic performance. Each polymer is blended with $PC_{71}BM$, a commonly used electron acceptor phase material, to make a device. Chapter 3 discusses DT-PDPP2T-TT, a polymer that is naturally highly aggregated and minimally soluble. Multiple different solvent additives are able to prevent polymer aggregation and develop a finely phase separated network for improved performance in relatively thick film active layers. Both chapters 3 and 4 use real time optical and X-ray scattering measurements to monitor solidification and crystallization during the coating process and identify the factors that affect the final dry film morphology.

Chapter 4 makes use of a new polymer, PffBT4T_{80}-co-3T_{20}-2OD, which was designed to be more soluble but just as high performing as the well-studied PffBT4T-2OD. This polymer has a thermally accessible aggregation transition, and it's the aggregation state during coating strongly effects the resultant thin film morphology. Morphology development was monitored as a function of molecular acceptor, where $PC_{71}BM$ and IDTBR were compared; it was shown that the crystalline acceptor IDTBR disrupts the crystallization of the polymer and limits the performance of devices relative to those with $PC_{71}BM$. Chapter 5 investigated the non-halogenated solvent processing of P(DTG-TPD), and subtle morphological changes that result from transferring solvent systems. Both DT-PDPP2T-TT and P(DTG-TPD) were easily transferred from spin coating to blade coating

with minimal optimization, which is attributed to the avoidance of aggregate transitions during processing as well as low crystalline order in the solid state.

Finally, chapter 6 concludes the work with perspective on the field of organic photovoltaics within the context of what was learned from the three projects described above.

CHAPTER 1. INTRODUCTION

1.1 General background on organic electronics

1.1.1 Organic electronics and conjugated polymers

Organic electronics is a broad term that covers a wide variety of devices built with π-conjugated carbon-based materials that are designed to be conducting or semiconducting. While these materials have similar properties to widely used inorganic semiconductors based primarily on silicon, they possess inherent advantages that make them attractive for research and industrial application. They have inspired a new generation of devices that can be made lightweight, flexible, and inexpensive to produce, such as organic photovoltaics (OPVs), photodetectors, organic field-effect transistors (OFETs), organic electrochemical transistors (OECTs), and electrochromic devices (ECDs). Essential to the realization of these advantages is the dual component nature of solution processable organic electronic polymers or materials, where the conjugated polymer backbone or material core comprises the core of the molecule from which electronic and chemical properties are derived from, and the peripheral side chains allow for solution processing. While stacking of discrete molecules and subsequent strong intermolecular interactions are sufficient for transporting charges, extending the delocalized electron system along a covalent network via conjugation offers additional avenues for making use of charge transport within polymer systems.

1.1.2 Electronic states in conjugated materials

The electronic properties of organic π-conjugated polymers are derived from an alternating single and double bond network. The properties of this alternating bond structure is a result of a network of p_z orbitals that are perpendicular to the covalent, fixed sigma bonds that define the steric component of the molecular structure. These p_z orbitals overlap, forming a conjugated network of π-bonds through which electrons can move. As the number of conjugated bonds in a molecule are increased, the energy gap between the frontier molecular orbitals decreases with discrete energetic states that are added to the molecule's energetic landscape. Through light absorption, an electron can be promoted to a higher energy level, and the color of light absorbed is dependent on the molecule's energy levels. The lower energy band, populated with valence electrons, is called the highest occupied molecular orbital (HOMO) and is also referred to as the valence band. The higher energy band, the lowest unoccupied molecular orbital (LUMO), is vacant in the molecule's ground state and also referred to as the conduction band. Most of the building blocks of simple semiconducting polymers, like 3-hexylthiophene, are colorless in the visible spectrum, absorbing high energy light. However, upon polymerization and extension of the conjugated network, additional energetic states develop and decrease the optical gap between the occupied and unoccupied molecular orbitals. Furthermore, as more energy levels are added to the system, they become closer together and approach an electronic band structure without discrete energy levels within the occupied and unoccupied orbitals.[2] Light absorbed by increasingly longer conjugated chains of monomer units moves toward longer wavelengths and lower energies that eventually cover visible light with broad absorptions.

1.2 Material design principles

1.2.1 Overview of the types of materials used in organic photovoltaics

A critical part of an OPV device is the photoactive layer, which consists of π-conjugated materials responsible for absorbing light, generating charges, and transporting charges out of the device. Polymer:molecule blends are the most commonly used combination of active layer materials in OPV, and they are the basis for the three main projects featured in this dissertation. Semiconducting polymers that encompass the current state-of-the-art for OPV are comprised of two main components: solubilizing components and an (electron) donor-acceptor structure. These two aspects of material design will be discussed in the following sections 1.2.2 and 1.2.3, respectively.

The first organic solar cells were reported in the 1970s, but they primarily consisted of a single absorber and had power conversion efficiencies less than 0.5%.[3] The first donor-acceptor bilayer device was reported by C. W. Tang 1984, and with an active layer of copper phthalocyanine as the electron donor and a perylene tetracarboxylic derivative as the electron acceptor, a record PCE of 0.95% (under AM2 illumination, 75 mW cm^{-2}) was achieved.[4] The donor, acceptor, and top silver electrode were sequentially deposited under vacuum onto indium tin oxide (ITO) on glass, which acted as the bottom transparent conductor and substrate.

The first detailed report of the nature of the photovoltaic process within polymer semiconductors was in 1992 from Heeger and coworkers, where the polymer 2-methoxy-5-(2-ethylhexyloxy) - 1,4-phenylenevinylene (MEH-PPV), either as a pristine film or in a blend film with Buckminsterfullerene (C_{60}), was photoexcited.[5] Excitation in the pristine film led to characteristic fluorescence at longer wavelengths compared to the light

absorbed. However, in the blend, fluorescence was strongly suppressed, which was attributed to photoinduced electron transfer from the polymer to the fullerene. Due to the efficiency at which this electron transfer occurred, the authors hypothesized the existence of heterostructures intermixed on the nanoscale to generate a network of phase interfaces. Following this study was the report of a polythiophene derivative that showed enhanced electron transfer rates.[6] In both cases, the nature of the morphology within the solid state was not well understood, especially given the minimal solubility of C_{60}.

To further explore these donor-acceptor phase heterostructures, Yu and Heeger solution processed a blend of MEH-PPV and a cyano-PPV polymer. This was in an attempt to directly address low photovoltaic efficiency when considering electron transfer from a single donor phase to single acceptor phase versus a bulk film with a complex phase separated microstructure.[7] This work established two requirements for efficient active layers: (1) large interfaces for charge separation, and (2) pure domains for charge transport and extraction. This describes the newly defined "bulk-heterojunction", which is a bicontinuous network of intermixed phases with high surface area. This morphology is critical for the photovoltaic process in disordered, low dielectric constant materials, and it is the basis for almost all reported organic photovoltaic devices going forward.

As hinted to in the previous section, this dissertation will focus on donor-acceptor phase material blends, where the active layer that is responsible for light absorption and charge generation consists of a donor phase and acceptor phase that are (ideally) intermixed on the nanoscale into a morphology called the bulk-heterojunction (BHJ). The BHJ is an interpenetrating, phase-separated network of the donor and acceptor materials which can feature pure domains, mixed domains, and anything in between. Understanding the nature

of this network, how it forms, and how to control it is the essential focus of this dissertation, and this topic will be more thoroughly introduced in section 1.4.

1.2.2 Electronic vs. solubilizing components

One of the most widely studied active layer systems for organic photovoltaics is a blend of the electron donor poly(3-hexylthiophene) (P3HT) and electron acceptor phenyl-C_{61}-butyric acid methyl ester ($PC_{61}BM$) (Figure 1-1). Compared to early semiconducting polymers like polyacetylene, the donor phase material P3HT has an n-hexyl alkyl chain off each repeat unit in the backbone, which is used to impart solubility that polyacetylene lacks. Solution processability is a key trait that has massively increased the accessibility and potential industrial applicability of organic photovoltaics and is a topic central to this thesis. The alkyl side chain is also a structural director in the solid state, the effects of which will be discussed in the forthcoming solid-state morphology section (Chapter 1.7). Fullerene-based materials were the champion electron accepting phase materials in the field for about two decades. Despite limited light absorption primarily in the ultraviolet due to a large optical band gap, the strong electron affinity and spherical buckyball structure afforded efficient charge transfer after photoexcitation and isotropic charge transport through the film, making it an excellent acceptor phase material. Akin to the n-hexyl chain attached to the thiophene repeat unit on P3HT, the phenyl butyric acid methyl ester functionality was added to the C_{60} moiety as a solubilizing component to complement the electronic component.[8]

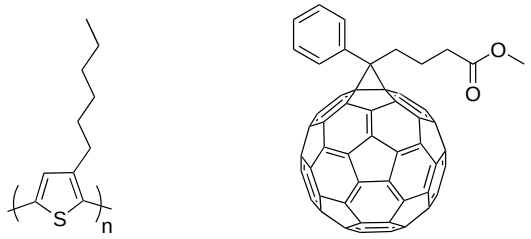

poly(3-hexylthiophene)
P3HT

phenyl-C_{61}-butyric acid methyl ester
$PC_{61}BM$

Figure 1-1 – poly(3-hexylthiophene) (P3HT) and phenyl-C_{61}-butyric acid methyl ester ($PC_{61}BM$), the most well studied organic photovoltaic blend system

1.2.3 Donor-acceptor polymers

A significant drawback of the P3HT:PCBM system is the limited light absorption of both blend components, especially in comparison to the broad range of wavelengths incident on the Earth's surface from the sun. PCBM absorbs primarily in the ultraviolet, and the onset of absorption of P3HT is around 650 nm. Almost all state-of-the-art highly performing donor polymers have a copolymer structure with a combination of electron-rich and electron-poor units in order to lower the absorption onset energy, as shown in Figure 1-2. The optical band gap energies of both the donor (E_D) and the acceptor (E_A) are both larger than the gap of the alternating copolymer (E_{DA}). The first demonstration of this electron-rich and electron-poor approach, also referred to as a donor-acceptor approach, was reported by Havinga et al. for polysquarines and polycroconaines.[9] Due to the mixing of the energy bands, a new, lower energy absorbing state is formed, which is beneficial for light absorption and subsequent photocurrent generation in a device. Additionally, the dipole created from a covalently attached donor and acceptor group can help stabilize the excited state generated after light absorption. However, the maximum voltage that can be generated from a device is limited by the difference in energy between the ionization

potential of the donor phase material and the electron affinity of the acceptor phase material. When the field was once limited by fullerene acceptors with fixed energy levels, there was often a tradeoff between active layer systems with high current vs. high voltage.

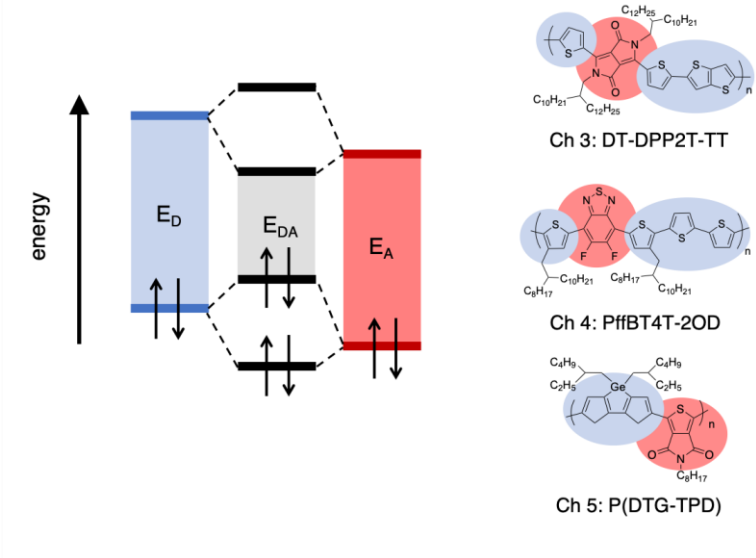

Figure 1-2 – Energy level diagram of the frontier molecular orbitals of a donor-acceptor alternating copolymer (adapted from Havinga et al.[9]) Repeat unit structures of the three polymers featured in this dissertation, with the electron-donating and electron-accepting groups highlighted in blue and red, respectively.

The repeat unit structures of the three polymers featured in this dissertation are shown in Figure 1-2, with the electron-donating and electron-accepting groups highlighted. Chapter 3 describes DT-DPP2T-TT, with a diketopyrrolopyrrole as the acceptor unit, and flanking thiophenes and a thienothiophene as the donor units. Chapter 4 describes a family of random copolymers based on the well-studied PffBT4T-2OD (aka PCE11), which has difluoro-benzothiadiazole as the acceptor unit and quaterthiophene as the donor group. The resulting randomly alternating copolymers switch out some quaterthiophene units for terthiophene, which is used to increase solubility and improve processability. Lastly,

Chapter 5 describes P(DTG-TPD), with a dithienogermole electron-donating group and a thienopyrrolodione accepting unit. Comparing polymers with dithienogermole (DTG) to those with dithioenosilole (DTS) and cyclopentadithiophene (DTC), the structure of the fused electron donating group was shown to change solid state molecular packing and subsequent photovoltaic performance.[10]

1.2.4 Random terpolymers

To further develop the complexity of these donor-acceptor copolymers, additional monomer species can be used during the polymerization process. This idea is the core concept behind the PCE11-based random terpolymers that are the subject of Chapter 4 of this dissertation.[11] In the case of the PCE11 random terpolymer synthesis, shown in Figure 1-3, the donor-acceptor-donor monomer, with thiophene and diflurobenzothiadiazole (monomer 1) was functionalized with bromines, while the bithiophene (monomer 2) and monothiophene (monomer 3) monomers were functionalized with trimethyl tin. Therefore, in the resulting polymer, there is a random assortment of 1-2 and 1-3 monomer couplings. While polymer composition is being tuned by the relative ratios of the two thiophene monomers, additional properties are imbued to the polymer by way of the random repeat unit composition. Our group has shown that solubility and device performance can be improved with this random polymerization technique.[11] Others have shown that various systems polymerized with a random terpolymer approach can exhibit broader light absorption due to a variety of chromophores being present, which often leads to improved device properties when properly tuned.[12–17] A recent review article has summarized the extensive efforts on developing random terpolymers for organic photovoltaics.[18] While optimizing terpolymer design can simultaneously improve a variety of photovoltaic

properties, the random nature of the polymerization requires careful handling of monomers and the polymerization to ensure minimal batch-to-batch variation and subsequent reproducibility.

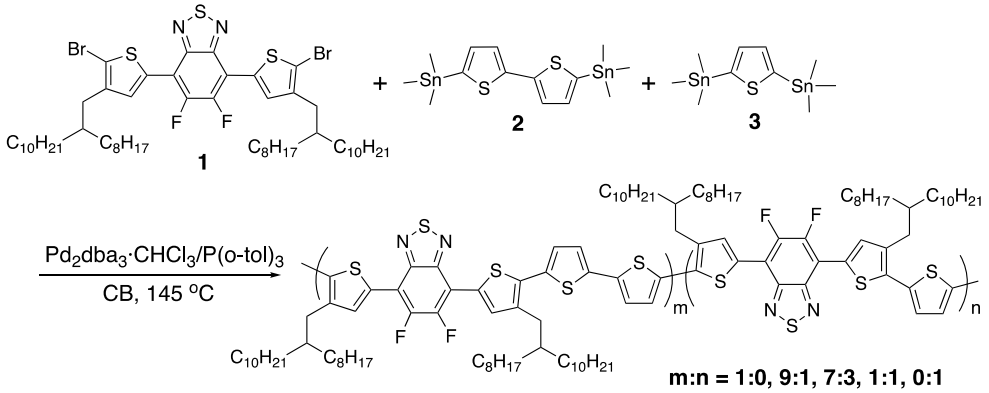

Figure 1-3 – Synthetic polymerization scheme of the PCE11-based copolymer, PffBT4T$_m$-co-3T$_n$-2OD, where the thiophene-diflurobenzothiadiazole monomer (1) is mixed with a blend of either bithiophene (2) or monothiophene (3). PCE11 is m:n = 1:0. Reproduced from Xu et al.[11]

1.2.5 Polymer molecular weight consequences on solid state properties

While the repeat unit structure and chemical purity are of critical importance to the nature of a particular polymer sample, molecular weight and dispersity (together known as the molecular weight distribution) also play a role in polymer and device properties. The effect of molecular weight on P3HT properties has been well studied, and it has been shown that crystallinity, film morphology, and charge transport properties are all related to molecular weight.[19,20] Increasing the number average molecular weight (M_n) of P3HT from ~ 2 kg mol^{-1} to ~ 19 kg mol^{-1} is correlated with a charge mobility increase from 10^{-7} cm^2 V^{-1} s^{-1} to 10^{-3} cm^2 V^{-1} s^{-1} and an increase in power conversion efficiency from ~ 0.1 % to 3 %.[21,22] On the other hand, molecular weight affects solubility; a polymer with too high a molecular weight may lead to low solubility and difficult processing. As one would expect,

connections among molecular weight and polymer properties are not limited to the all donor P3HT, but extend to donor-acceptor polymers as well.[23] The all-polymer solar cell community has paid particular interest to molecular weight effects, since the improved mechanical stability inherent to all-polymer solar cells compared to polymer:molecule solar cells is also strongly dependent on the molecular weights of both polymers in the active layer blend.[24] However, too high a molecular weight can lead to polymer blend systems that are highly crystalline but also coarsely phase separated, and as a result, electrical characteristics of those systems are poor.[25]

1.2.6 Fullerene-based acceptors

As mentioned in section 1.2.2, PCBM is the most well-studied electron acceptor for use in organic photovoltaics. A soluble derivative of the C_{60} fullerene (aka buckminsterfullerene), $PC_{61}BM$, was first reported in 1995 by Fred Wudl and coworkers.[8] It should be noted here that the terms $PC_{60}BM$, $PC_{61}BM$, and [60]PCBM (and subsequently $PC_{70}BM$, $PC_{71}BM$, [70]PCBM) are generally used interchangeably in the literature and arise from whether one considers the newly added connecting carbon atom as a part of the fullerene. There are a number of advantageous properties of fullerenes that have caused them to dominate the field of organic photovoltaics for roughly two decades.[26,27] Electronic structure calculations have shown that the LUMOs of fullerenes are delocalized across the entire 3D surface of the molecule, allowing for efficient isotropic charge transport. These delocalized molecular orbitals also promote weak π-π interactions that can lead to aggregation, which can form pure domains ideal for transporting free charges through a blend film. These interactions are sufficient for favorable fullerene aggregation while

accommodating a wide variety of donor polymers, independent of their crystallinity and phase behavior.

The origin of the low light absorption of C_{60} and its derivative can be attributed to its high degree of symmetry, due to it being spherical. The lowest energy transitions are formally dipole forbidden. However, C_{70} is an asymmetrical ellipsoid, and as a result these low energy transitions are allowed and, thus, it absorbs more light than C_{60}. In effort to improve the limited light absorption of $PC_{61}BM$, René A. J. Janssen and coworkers reported on the synthesis and characterization of a C_{70} fullerene with an analogous phenyl-butyric-acid methyl ester solubilizing group in 2003.[28] When blended with MDMO-PPV into a bulk-heterojunction OPV, the increased light absorption in the blend offers a 50% increase in current density of the $PC_{71}BM$ device compared to the $PC_{61}BM$ device. This photocurrent enhancement is offset by a slight decrease in voltage and fill factor, giving a drastic increase in power conversion efficiency when using $PC_{71}BM$. This acceptor was widely adopted and, for the most part, replaced $PC_{61}BM$ as the champion fullerene acceptor, with a record high PCE of almost 11 % with PffBT4T-2OD (aka PCE11) reported by He Yan and coworkers in 2014.[29] Further iteration on the PCE11 backbone found that by using slightly longer side chains and processing from a non-halogenated solvent system, average power conversion efficiencies of 11.3 % were achieved, which remains the highest reported efficiency from a single junction binary blend OPV using a fullerene acceptor.[30]

Another well studied fullerene acceptor is indene-C_{60} bisaccudct (ICBA), with two indene groups on the fullerene instead of a butyric acid methyl ester. This material was first reported by Jianhui Hou, Yongfang Li and coworkers, and with a higher LUMO level relative to P3HT, higher open circuit voltages (V_{OC}) were achieved.[31] Despite a slightly

lower current density in the initially reported solar cells, the P3HT:ICBA blend achieved a power conversion efficiency of 5.4 % compared to 3.9 % with $PC_{61}BM$ and otherwise identical processing. Further optimization brought the P3HT:ICBA system up to a PCE of 6.5 %, which is the highest reported efficiency using P3HT and a fullerene acceptor.[26] Our Georgia Tech colleagues in the Kippelen group have made use of P3HT:ICBA blends to test their solution doping method of OPV active layers to create vertical doping gradients for improved photovoltaic performance and facile device fabrication.[32–34]

The structure that provides all the beneficial properties of fullerene derivatives as acceptors also leads to their most significant drawbacks. Low levels of light absorption have been discussed in the previous section. Some chemical functionalization has been attempted in order to improve the light absorption through frontier energy level modification, but only small changes in structure have been demonstrated, leading to comparably small changes in electrochemical properties, such as with ICBA. In addition to limited light absorption, more facile energy level tuning could further improve the donor phase HOMO – acceptor phase LUMO offset, which is the origin of the V_{OC} and therefore maximum voltage achievable by the solar cell. On the morphology side, fullerene aggregation over time has been shown to occur in the solid state, which eventually will hinder charge separation and increase charge recombination rates.[35] Fullerene aggregation can also occur during the film coating and be present in freshly made films. During the solution processing step, this aggregation is often mediated with the use of high-boiling point solvent additives, which themselves can pose problems if they are not thoroughly removed from the system.[36] The use of additives is a key focus of this dissertation and will

be discussed in more detail in the solution processing section (1.5). Successful non-fullerene acceptors (NFAs) have avoided the drawbacks listed above.

1.2.7 Non-fullerene acceptors

The most widely studied types of non-fullerene molecular acceptor generally fall into one of two main structural motifs: perylene diimides (PDI) and acceptor-donor-acceptor fused ring electron acceptors (FREA). FREAs are the current state of the art and have shown power conversion efficiencies in single junction cells of over 17 %, and they are used in chapter 4 of this dissertation. Though they are relatively new to the field of organic photovoltaics, FREAs have overtaken PDI based acceptors with respect to ongoing research efforts and new publications.

1.2.7.1 Perylene diimide acceptors

The PDI unit features a core donor motif of fused benzene rings, flanked by diimide electron acceptor groups. The planar core has a high degree of order in the solid state, which results in high charge carrier mobilities that can exceed 1 $cm^2 V^{-1} s^{-1}$.[37] However, this same tendency to pack often causes micron-scale aggregates, which are detrimental for photovoltaic performance. The first notably high power conversion efficiency with the first and most simple PDI was 3.0 % with the discrete molecular donor p-DTS$(FBTTh_2)_2$, reported in 2013 from the groups of Thuc-Quyen Nguyen and Guillermo Bazan.[38] PDI has been iterated on over the years, most commonly by linking two PDI units together with an aromatic linker and subsequently tuning morphology through side chains. PCEs with the well-known polymer donor PTB7-Th, aka PCE10, blended with a large tetra-PDI molecule

have reached 8.5 %,[39] and a PCE11 derivative (P3TEA) blended with SF-PDI_2 achieved a PCE of 9.5 %.[40]

The abbreviated version of PDI, naphthalene diimide (NDI), has found much use in the field of polymer acceptor phase materials. The most common repeat unit structure consists of NDI and bithiophene (T2 or 2T), side chain engineering has been investigated to control the high degree of crystallinity inherent to the backbone; the initial problems with these polymers often arise from strong phase separation and aggregation. This strong phase separation is made more complicated in blends when the donor material is also a polymer, as the mixing of two polymer components is generally less favorable than a mixture of polymer and discrete molecule. Morphology development in all polymer solar cells will be discussed briefly later in this chapter.

The most commonly used NDI-T2 polymer has a pair of 2-octyldodecyl side chains on the NDI unit, is called P(NDI2OD-T2) (aka N2200), and is shown in Figure 1-4. It was first reported in 2009 in a transistor study where it was shown to have high stability due to a low LUMO, and a high field effect electron mobility of ~ 0.5 $cm^2\ V^{-1}\ s^{-1}$.[41] Early reports of blending this polymer with P3HT showed negligible power conversion efficiencies, below 0.5 %, most significantly due to large scale phase separation which gave a poor morphology.[42,43] Active engineering of P(NDI2OD-T2) systems involved using different paired donors, iterating on the side chains of both species, and manipulating the solvent system. A record high PCE of 9.9 % was achieved in 2017 with the polymer donor PTzBI-Si, with trimethylsiloxane side chains on the acceptor unit, and with the blend being processed from the green solvent 2-methyl-tetrahydrofuran.[44] The electron rich region of the donor polymer features a benzodithiophene group with pendant thiophenes as part of

the side chains, which is a structural moiety that is now commonly used in the current state of the art FREA systems. The siloxane groups on the ends of the side chains were sufficient to just solubilize the polymer while allowing crystallization during the drying and annealing processes, ensuring both high carrier mobilities and a morphology conducive to photovoltaic operation.

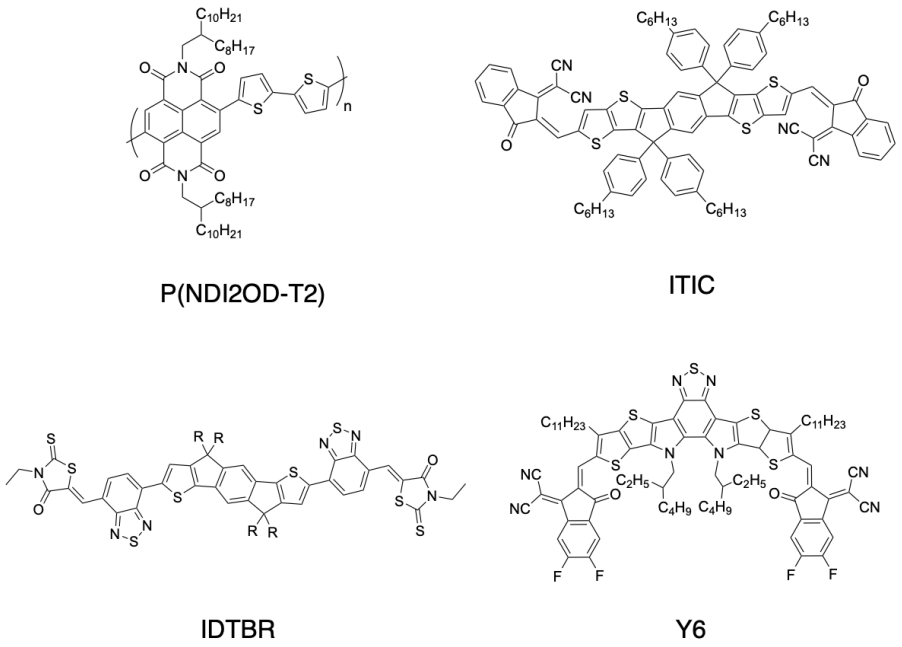

Figure 1-4 – Four selected non-fullerene acceptors: P(NDI2OD-T2), ITIC, IDTBR, and Y6. Common variants of IDTBR have R = n-octyl or 2-ethylhexyl.

1.2.7.2 Fused ring electron acceptors (FREAs)

Fused ring electron accepting (FREA) discrete molecules, generally found with an acceptor-donor-acceptor structure, are the current state-of-the-art materials for organic solar cells. Devices with these molecules as the acceptor phase material regularly surpass the 11 % limit found with binary PCBM devices, with the current state of the art binary

devices reaching 17 % using Y6 as the acceptor molecule (Figure 1-4). Use of a fused ring aromatic core with flanking acceptor units means that the structures of these FREAs are modular and synthetically tunable, so that frontier molecular orbitals and absorption spectra can be easily tuned. Early reports of this type of material emerged in 2014, where blends of carbazole-rhodanine and fluorene-rhodanine acceptor molecules were blended with P3HT and achieved high voltages compared to PCBM due to the readily tunable energy levels, but efficiencies of only up to ~ 3 %.[45] These types of materials were iterated on, with a maximum PCE from a thiophene-fused fluorene core FREA to be up to 10.0 % with the donor polymer PBDB-T, shown in Figure 1-5.[46] The rest of this section will discuss three molecules: (1) ITIC, the acceptor that revitalized the OPV community with an efficiency surpassing PCBM, (2) IDTBR, a slightly less high performing material that has worked well with derivatives of PffBT4T-2OD, and (3) Y6, one of the currently highest performing materials to date.

It is important to note that these non-fullerene acceptors essentially shifted the paradigm of materials design for organic photovoltaics. Previously, high performing electron accepting materials were limited to fullerenes, which have large optical band gaps and absorb primarily in the UV. Therefore, donor polymers were designed to be as narrow-banded as possible to absorb as long of wavelengths as possible and spread absorption of device across the region of maximum solar irradiance, which is essentially from 400 nm to the near-infrared (NIR). These new classes of acceptors can be widely tuned, and with a strong push-pull molecular design, can have substantially long wavelength absorptions. With this development, the light absorption properties of donor phase polymers began to

be tuned back toward the visible, with NFA absorption being pushed further out into the near IR.

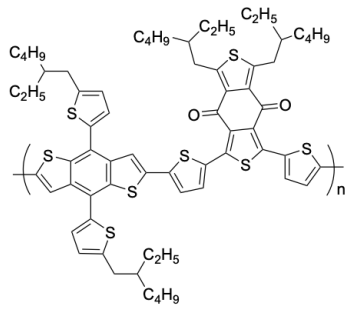

PBDB-T (PCE12)

Figure 1-5 – Repeat unit structure of PBDB-T (PCE12).

In 2016, Jianhui Hou and co-workers blended PBDB-T (aka PCE12) with a new non-fullerene acceptor, ITIC, to achieve a record maximum polymer solar cell PCE of 11.2 %, surpassing the performance of most reported PCBM solar cells.[47] This record high performance was attributed to a few factors: high voltage due to minimized energy losses between the donor and acceptor materials and high current due to improved light absorption compared to the PBDB-T:$PC_{71}BM$ blend. Optimized devices used thermal annealing to slightly enhance the performance, a technique used for a variety of polymer:NFA blends. The PBDB-T:ITIC blend also proved to be more stable than the PCBM blend counterpart, another trend that holds for many different NFA systems. An optimized variant to ITIC, ITIC-4F (aka IT-4F) features two fluorine atoms on each of the two dicyanovinylindanone end groups. This fluorination served to lower the energy levels and increase the planarity of the molecule, and with a complementary fluorinated version of PBDB-T, a new record PCE of 13.1 % was achieved.[48,49]

Compared to ITIC, IDTBR features a smaller donor core and extended electron accepting peripheral groups, with both benzothiadiazole and rhodanine units. With either n-octyl or 2-ethylhexyl solubilizing chains attached to the electron rich core, the molecule is strongly planar and crystallizes in the solid state. This acceptor achieved one of the highest power conversion efficiencies in a P3HT solar cell, 6.4 %, due to complementary light absorption and an ideal nanoscale morphology.[50] Using a PffBT4T-2OD analogue with longer side chains, devices with up to 11.1 % PCE were built from active layers cast from the non-halogenated solvent mesitylene.[51]

In 2019, using the fluorinated version of PBDB-T, PBDB-T-F (aka PM6), a new acceptor unit was unveiled with a record PCE of 15.7 %.[52] This acceptor, Y6 (aka BTP-4F), is a relatively massive molecule with an incredibly long and broad wavelength absorption, with a thin film absorption onset of 931 nm. For reference, ITIC and IT-4F onsets are around 800 nm and 820 nm, respectively, and EH-IDTBR and O-IDTBR have onsets around 750 nm and 780 nm, respectively. The structure of the molecule is an acceptor-donor-acceptor-donor-acceptor moiety, highlighting the development of increasingly complex molecules that are pushing the field of NFA solar cells forward. This blend system has been further iterated on through device engineering methods: adding 10 % of $PC_{71}BM$ to the PM6:Y6 blend to make a ternary cell increased PCE to a record 16.7 %,[53] and adding instead a small amount of chlorinated graphdiyne as a solid additive has increased the maximum PCE to a new record of 17.3 %.[54] Molecular optimization and device engineering continue to push the field well beyond the fullerene solar cell limit of 11 %, but scaling up these increasingly complex molecules for large-scale industrial production will be a great challenge.

1.3 Organic photovoltaic principles

At this point, the nature of the components that compose the light absorbing layer of the organic solar cell have been introduced. This section discusses the phenomena of light absorption and the processes that follow relating to the other components in a complete device, as well as the techniques used to characterize the device.

1.3.1 Device operating principles

The photovoltaic effect is the generation of electrical power (current and voltage) upon a material's exposure to light. In crystalline inorganic semiconductors, lattice order and rigidity ensure much larger charge carrier mobilities (typically 10^2 cm^{-2} V^{-1} s^{-1} or greater) than can be found in organic semiconductors. Related to this are the much lower dielectric constants of organic semiconductors relative to inorganic semiconductors; where organics such as P3HT have values of 3 – 4, the dielectric constant of silicon is ~ 11.[55] Upon exposure of a semiconductor to light, an excited state is formed in that material, whereby an electron is promoted to a higher energy state and leaves behind a vacancy that acts as an effective positive charge, called a hole. These opposing charges are electrostatically bound. The dielectric constant influences the ability for these charges to be screened by an external electric field. In inorganic semiconductors, such as silicon or lead halide perovskite, high dielectric constants lead to low exciton binding energies on the order of 10 – 15 meV. When an exciton is generated in that material, it can be immediately split into free charge carriers by thermal energy, k_BT, which is the Boltzmann constant ($8.617 \cdot 10^{-5}$ eV K^{-1}) times temperature in Kelvin and is ~ 25 meV at room temperature. Conversely, exciton binding energies in organics are on the order of 100 meV, meaning

that within the bulk of a single-phase organic material, a photogenerated exciton is likely to recombine and thus will not contribute photovoltaic power to a device. This is why both an electron donating and electron accepting phase material are required to generate free charge carriers in organics, and why tuning their intermixed morphology is critical for controlling device performance. Understanding the fundamentals of tuning and characterizing this morphology is a major focus of this dissertation.

The fundamental electronic states involved in photoexcitation for a donor-acceptor binary phase system are shown in the Jablonski diagram in Figure 1-6 (a), which is reproduced from a review of organic photovoltaic fundamentals by Kippelen and Brédas.[56] The ground state of a π-conjugated system is the singlet (S_0) state, and absorption of an incident photon into either chromophore with energy greater than or equal to the difference in energy between the first excited singlet state (S_1) and S_0 will promote an electron to the S_1 excited state. On the graphical diagram in Figure 1-6 (b), this excitation occurs on the red donor polymer and forms an exciton. The exciton must then diffuse to a donor-acceptor interface if it is to ultimately generate photocurrent, and this occurs through a hopping mechanism.

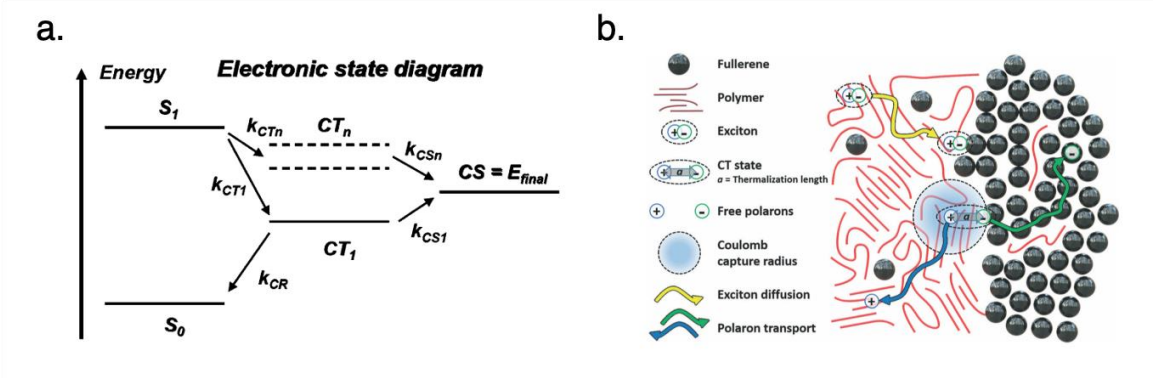

Figure 1-6 – (a) Electronic state diagram of photoexcitation leading to charge separation in a chromophore. Reproduced from Kippelen and Brédas.[56] (b) Diagram of the photoexcitation and charge separation process at a polymer-fullerene interface. Reproduced from Pelzer and Darling.[57]

The lifetime of a singlet exciton is on the order of nanoseconds, which corresponds to the timescale of fluorescence which is an S_1 to S_0 decay process. If the exciton encounters the donor-acceptor interface before decaying, it can enter the intermolecular charge transfer state (CT), where the hole will remain on the donor and the electron will transfer to the acceptor phase. Once the charges have been separated at the interface into a charge separated state, the free charges (i.e. polarons) will move through their respective phase material, at a rate governed by the material's charge mobility, to the electrodes for charge collection. There are a variety of theories and models that have been used to describe the dynamics of charge generation and separation, and their summary and analysis is beyond the scope of this dissertation.[57] Chapter 2 will describe space-charge-limited current mobility, commonly used for measuring charge mobilities in OPV materials.

Performance of an electronic semiconductor device depends on the efficiency with which charge carriers move. From an OPV perspective, charge mobility refers to the rate at which free charges move within a material in response to an applied electric field. These

charges are generated when a photogenerated exciton is able to diffuse to a donor-acceptor interface. Ideally, once a charge is separated, it will move through the material to its corresponding electrode at a rate described by the charge mobility.

1.3.2 Interlayer and electrode architectures

The sections above describe the processes occurring within the active layer of the solar cell, and the structure of that active layer is the focus of this dissertation. However, there is more to a photovoltaic device than just the light absorber, and the interfaces between the active layer and the external connections to the device are crucial for operation. Typical research-level organic photovoltaic devices, including those built for this dissertation, are comprised of the following layers: (1) Indium tin oxide (ITO), a transparent conductor, coated on a glass slide, (2) a charge-carrier selective interlayer, (3) the active layer, (4) the opposite charge-carrier selective interlayer, and (5) a reflective, opaque top electrode. Entire dissertations have been written on understanding the importance and optimizing each individual layer, and as every active layer system is different, so is the ideal architecture that pairs with it.

However, as device fabrication is somewhat of an art rather than a science, it is all too easy to lose the forest for all the trees and get stuck changing too many variables so that reproducible science becomes impossible. For that reason, the three projects featured in this dissertation are comprised of devices all having same composition aside from the active layer. Prepatterned ITO was used, onto which a zinc oxide (ZnO) precursor solution was spun coat and baked in ambient air, to form a transparent electron transporting layer. Onto this layer, the active layer was deposited, either via spin coating or blade coating.

Finally, this stack was brought into the thermal evaporator within an argon filled glove box, where molybdenum oxide (MoO_x) as the hole transporting layer and silver as the reflective back electrode were sequentially deposited under vacuum. This is an "inverted" device architecture and specific details on its construction will be discussed in chapter 2.

Early organic solar cells were built using poly(3,4-ethylenedioxythiophene): poly(styrenesulfonate) (PEDOT:PSS) as the solution processed layer spun coat onto ITO, and low work function cathode materials deposited as the top, evaporated layer, with common configurations being calcium/aluminum or lithium fluoride/aluminum, with aluminum as the reflective back electrode. PEDOT:PSS is a transparent hole conductor, and calcium and lithium fluoride (LiF) act as the electron transport layer. This early architecture, now known as a "conventional" architecture, features a number of significant drawbacks that have made it essentially obsolete in the organic photovoltaics community. PEDOT:PSS is acidic and hygroscopic, and over time in ambient air it can degrade both the underlying ITO layer and the active layer deposited on top. Calcium metal readily oxidizes in ambient air, LiF is actually insulating and needs to be deposited in a very thin layer to form a dipole at the active layer interface without introducing resistances, and aluminum oxidizes in air to form a thin layer of aluminum oxide at the metal-air interface, which could limit the quality of external electrical connections to the device.

The most widely known cathode interlayer material for inverted device architectures is ZnO, which is spin coated in air and annealed at moderate conditions. The ZnO precursor solution can either take the form of a colloidal suspension of nanoparticles, or a sol-gel solution made from Zn acetate, the latter of which is typically annealed with slightly harsher conditions compared to the prepared nanoparticle solution.[58] Compared to

their counterparts in the conventional architecture, these interlayers and electrodes are more stable in ambient condition. However, both ZnO and MoO_x have been shown to degrade in ambient condition under solar illumination. This is primarily a result of UV exposure, and use of a 400 nm long pass filter before the device was shown to be effective in delaying the degradation.[59]

1.3.3 Active layer structure – the bulk heterojunction

Identified in the 1990s and discussed in section 1.2.1, the bulk heterojunction describes an active layer morphology that is both realistically attainable and suitable for efficient photovoltaic operation in organic materials. A heterojunction is the interface between two dissimilar semiconductors with different properties, of which different energy levels is the most relevant property for photovoltaics. Three general forms of a phase separated donor-acceptor active layer blend are shown in Figure 1-7. The bulk heterojunction describes a bicontinuous network of donor and acceptor phase materials that are intermixed on nanoscale dimensions, realized in active layers processed from a blend solution. Before blend solution processing was possible, bilayer devices were made through sequential evaporation of one material followed by another. Because the photogenerated exciton, with a limited diffusion length of around 5-10 nm,[60,61] needs to diffuse to the donor-acceptor interface in order to separate into free charges, light absorbed far from that interface tends not to contribute to photocurrent. With a very thin film, most excitons could diffuse to the donor-acceptor interface, but such a film would have to be around 20 nm and as a result would be semitransparent with low photocurrent and overall low power conversion efficiency. This idea implies that morphology becomes more important with increasing film thickness.

An idealized donor-acceptor network, with features that to some extent the bulk heterojunction approximates, is shown in the middle of Figure 1-7. Between the hole and electron extracting interlayers and electrodes is an array of alternating high aspect ratio donor (green) and acceptor (grey) domains, with a pure polymer layer in contact with the anode for hole extraction, and a pure donor layer in contact with the cathode for electron extraction. This active layer morphology, with phases alternating with a horizontal period of about 20 nm corresponding to the exciton diffusion length, ensures that at any point within the film, a photogenerated exciton is able to readily diffuse to a donor-acceptor interface for separation, and free charges are able to transport through a single continuous phase to its corresponding charge transporting layer.

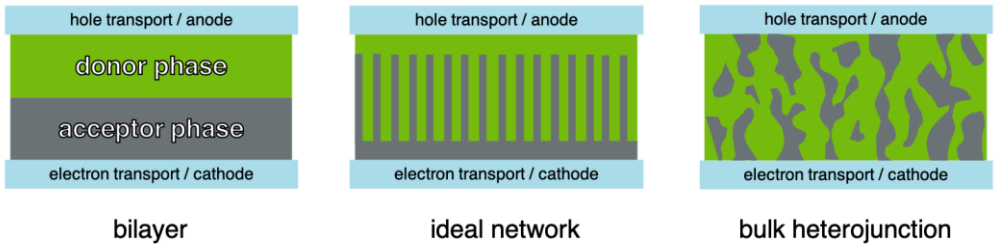

Figure 1-7 – Three active layer architectures: (1) bilayer, (2) an idealized interpenetrating donor-acceptor network, and (3) the bulk heterojunction. Structural elements are not drawn to scale.

The active layer morphology of the blend films fabricated for this dissertation is developed during the complex and dynamic process of solution processing and solvent evaporation, with phase separation being driven by many types of inter- and intramolecular interactions. As a result, a bulk heterojunction is formed that is structurally inhomogeneous and subsequently challenging to characterize and describe. The work in this dissertation attempts to understand the morphology development for a select few blends of polymer

donors and molecular acceptors, but it is accepted in the field that virtually every system is different. Furthermore, no tool is available to definitively characterize the complex three-dimensional morphology from the molecular sized angstrom/nanoscale to the domain sized nano-/microscale, all length scales of which affect electronic properties in a device.

All that being said, a simplified approximation of a single slice of the bulk heterojunction is shown on the right side of Figure 1-7. A randomly assembled, interpenetrating, bicontinuous network is shown, with both phase materials in contact with both charge transporting interlayers. If we compare the length scales to the ideal network, we find some features that are smaller than the exciton diffusion radius, and some that are larger. It is important to note that the domains are shown as a single layer of a three-dimensional network, so where there appears to be an isolated acceptor domain in a sea of donor, this domain could connect to another through the plane of the page. With that in mind, one could imagine that a photogenerated exciton in most of the regions of this slice could reach a donor-acceptor interface, and that free charges formed at that phase interface could make their way to the corresponding electrode. However, this schematic, which functions on the tens of nanometer length scale of phases, also captures some features of the bulk heterojunction that can be detrimental to photovoltaic efficiency. Unlike in our idealized network, here we have domains that are in contact with the wrong charge transport layer. This causes charge leakage that will limit the maximum amount of voltage that can be extracted, but its presence is inevitable when casting a blend solution.[62] There also may be isolated domains not a part of the bicontinuous network, where free charges will likely thermalize and not contribute to photocurrent.

This simple schematic shows two materials with a sharp interface, but in the reality of a bulk heterojunction, there is likely to be all kinds of mixed donor-acceptor phases in addition to the pure phases. As suggested by the donor-acceptor interface schematic in Figure 1-6, a mostly pure phase of acceptor can have a few polymer chains in it, or vice versa. Depending on the materials used, the drying process, and any post processing on the dried film, there can be any degree of mixed phases, with varying content of each material. The usefulness of the mixed phase in organic photovoltaics is system dependent (photovoltaic properties being system dependent is a common theme of the field). For P3HT:PCBM the amount of mixing among the two domains is a function of processing method and molecular weight, and it subsequently affects the charge separation efficiency.[63] The presence of a mixed phase has been experimentally verified in several polymer:PCBM systems aside from P3HT, such as PTB7[64] and PBDTTPD.[65] For the discrete molecular donor X2 blended with PCBM, it was shown that both molecules aggregate independently and efficient solar cells were fabricated with no mixed phase.[66] For these studies, X-ray diffraction techniques were used to measure PCBM aggregation, which is representative of pure PCBM domains rather than the existence of a mixed phase. If PCBM loading increases but the characteristic PCBM scattering signal does not, that is evidence of a polymer:fullerene mixed phase. With respect to non-fullerene acceptor blend systems, the field is sufficiently new and expanding rapidly that there are few detailed studies that have drawn many significant conclusions from morphological results. For that reason, the role of the mixed phase in these systems is not well understood.

1.3.4 Efficiency characterization

Once a device is built, two main metrics are used to benchmark its efficiency, the most important of which is its output power under simulated solar illumination. We also use quantum efficiency measurements to measure photocurrent response as a function of wavelength.

1.3.4.1 Illumination under the AM1.5G reference solar spectrum

Many variables affect the incident power from solar radiation, such as location on the earth, time of day, and atmosphere composition. A set of conditions have been chosen and defined as a reference spectra for photovoltaic analysis, called AM1.5G. "AM1.5" corresponds to the fact that due to the tilt of the earth relative to the sun, the light travels through ~ 1.5 "atmospheres" worth of air mass which provides a reasonable average for the contiguous 48 states of the United States of America over a period of one year, with atmospheric materials absorbing various wavelengths of light. The "G" stands for global and takes into account the diffuse scattered light from a blue sky and the surrounding ground. The total irradiance is 100 mW cm^{-2}. The AM1.5G spectra is shown in Figure 1-8, with maximum spectral irradiance in the visible region (400 nm – 700 nm) moving out into the infrared. It is in this region of maximum power that a solar cell should absorb for maximum efficiency. Solar simulators used in a laboratory environment approximate this AM1.5G spectrum with varying degrees of conformity. These will be discussed in Chapter 2, Experimental Methods and Characterization Techniques.

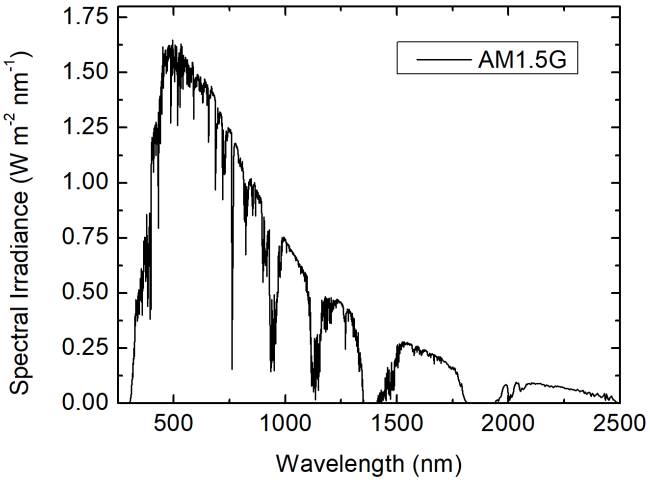

Figure 1-8 – Air Mass 1.5 Global solar spectrum (AM1.5G). Data taken from the National Renewable Energy Laboratory (http://rredc.nrel.gov/solar//spectra/am1.5/).

To characterize the solar cell under illumination, a source meter unit sweeps a voltage and measures the current response from the device, with representative data shown in Figure 1-9. In the dark, the solar cell operates as a diode with current flow in only one direction. Upon illumination, charge carriers are created, electrons flow to the cathode and holes flow to the anode, and a reverse bias current is generated. Parameters taken from the current density – voltage curve that are used to characterize the solar cell are: short circuit current density (J_{SC}), open circuit voltage (V_{OC}), fill factor (FF), and power conversion efficiency (PCE). J_{SC} is the current density measured at short circuit, when V = 0. V_{OC} is the voltage at open circuit, when J = 0. PCE is the ratio of output power to input power, the former of which is equivalent to the product of V and J at the maximum power point (i.e. max power = $V_{max} \bullet J_{max}$), and the latter being 100 mW cm^{-2} at AM1.5G. The ratio of $V_{max} \bullet J_{max}$ to $V_{OC} \bullet J_{SC}$ is called the fill factor. As has been previously discussed, voltage parameters are mainly derived from the electronic levels of the donor and acceptor phase

materials, but are also less significantly affected by the nature of the interfacial layers and can be reduced if too much of one of the phase materials is in contact with the wrong interfacial layer. Current density is largely controlled by light absorption, but it can also be affected by the morphology of the active layer. Of all the device metrics discussed here, fill factor is the most direct reflection of morphology, and can be visualized by how rectangular the J-V curve is in the fourth quadrant of the graph. Since the projects in this dissertation are exclusively about controlling and understanding the morphology of the active layer, the manipulation of power conversion efficiency will mainly be reflected in changes in J_{SC} and FF rather than voltage. However, changing acceptor phase materials, such as comparing $PC_{71}BM$ to non-fullerene acceptors in Chapters 5 and 6, will modify the V_{OC} of a device.

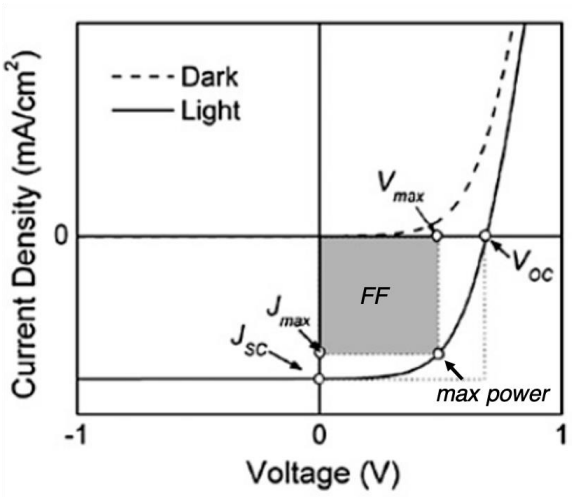

Figure 1-9 – Current density – voltage curve of a solar cell in the dark and under illumination. Included are the origins of the various parameters used to quantify the efficiency of a solar cell. Adapted from Kippelen and Bredas.[56]

1.3.4.2 Quantum Efficiency

In general, quantum efficiency is a measurement of a device's electrical sensitivity to light and is the ratio of charge carriers to incident photons. The idea can be divided into internal and external quantum efficiencies. External quantum efficiency (EQE), also known as incident photon to charge carrier efficiency / incident photon to current efficiency (IPCE, which appears to be used interchangeably in the field), is a measurement of the percentage of incident photons that are converted into measurable current. While this metric is a function of photovoltaic efficiency in a device, it is also a function of the fraction of light that is absorbed by the device rather than transmitted. This is the most well reported measurement of quantum efficiency, as it allows for direct comparison of photocurrent between systems, and when integrated across the AM1.5G solar spectrum it can be used to calculate J_{SC}. Internal quantum efficiency (IQE) measures the ratio of photocurrent generated from light that was absorbed and is therefore always the same or higher than the EQE at any one wavelength. In essence, IQE as a function of wavelength is the EQE divided by the light not reflected at that wavelength (transmission/absorption cannot be used here due to the back reflective electrode).

1.4 Solution processing

One of the main benefits of organic electronic materials is their ability to be dissolved in a solvent and solution processed. This section will focus on the nature of these solutions and the fundamental processes involved in coating and drying of the active layer. The next section will discuss specific methods of thin film deposition.

1.4.1 Solubility thermodynamics

Solubility is the property of a material to dissolve in a solvent, which for our purposes in this work describes a solid material being separated from the bulk and completely surrounded by liquid solvent. Material dissolution is a specific case of mixing, and is driven by both entropic and enthalpic terms, with an entropic benefit gained from moving a solid into a more dynamic state in solution. Thus, while heat may be required to dissolve a material and bring it into solution, that does not necessarily mean it will spontaneously precipitate. The general equations used to describe the mixing of two components arises from classical theory and has been well studied by Joel Hildebrand, a physical chemist who pioneered the fundamental understanding of the thermodynamics of solubility and was at one point shot and wounded by a disgruntled colleague.[67]

The free energy change for a physical process such as mixing (ΔG_m) is given by the following equations:

$$\Delta G_m = \Delta H_m - T\Delta S_m \quad (1)$$

$$\Delta S_m = -R \sum_{i=1}^{i} n_i \ln \phi_i \quad (2)$$

where ΔH_m is the enthalpic change of mixing, a function of the molecular interactions between components, T is temperature in Kelvin, ΔS_m is the entropic change in mixing, R is the gas constant, n_i is the number of moles of each component of the system, and ϕ_i is the volume fraction of each component. In an ideal system, with no intermolecular interactions, $\Delta H_m = 0$ and $\Delta S_m > 0$, so the free energy change is negative, and mixing is spontaneous. Phase separation is a result of intermolecular interactions, which we will

describe with χ, the Flory-Huggins interaction parameter. Flory and Huggins introduced this parameter to further refine Hildebrand theory in order to treat polymer-solvent and polymer-polymer interactions, to understand component mixing from a polymer perspective.[68,69] Molecular connectivity complicates the thermodynamic processes involved in mixing. For two components, A and B, the enthalpy of mixing is defined as:

$$\Delta H_m = \chi_{AB} \phi_A \phi_B k_B T \tag{3}$$

where k_B is the Boltzmann constant. Therefore, the magnitude of the interaction parameter determines the spontaneity of mixing. In the simplest case, of non-polar molecules A and B interacting exclusively through dispersion forces, the interaction parameter, χ_{AB}, is:

$$\chi_{AB} = \frac{\nu_0}{k_B T} (\delta_A - \delta_B)^2 \tag{4}$$

where υ_0 is a reference volume and δ_A and δ_B are the Hildebrand solubility parameters for A and B, respectively. The Hildebrand solubility parameter provides a numerical estimate for the degree of intermolecular interactions between materials.

$$\delta = \sqrt{\frac{\Delta H_v - RT}{V_m}} \tag{5}$$

ΔH_v is the heat of vaporization and V_m is the molar volume of the molecule in the condensed phase. The Hildebrand solubility parameter is the square root of the cohesive energy density, which represents the energy required to remove one molecule from the bulk of the same molecule.

With respect to the development of an ideal bulk heterojunction morphology, it is important to balance the intermolecular interactions so that there is just the right amount of material mixing. This can be controlled via materials design, solution formulation, and processing condition, the latter two of which are the main topics herein. A large dissimilarity in chemical composition will yield a low degree of interactions, and will preferentially have a molecule interacting with itself, thus forming large phase separated domains. A close similarity in composition will yield a high degree of interactions, which can be treated as the $\Delta H_m = 0$ case with perfectly even mixing. This will prevent continuous percolated pathways from forming, which are essential for charge transport. The above equations and the Flory-Huggins treatment of mixing have a few drawbacks that limit their ability to completely describe the system. These equations describe non-polar interactions, whereby adding polar units to the equation will additionally complicate things. These equations are also limited to amorphous materials, whereas many semiconducting polymers including the ones featured in this dissertation are semi-crystalline, which require additional energy to solvate.

To extend the Hildebrand solubility parameter and Flory-Huggins theory into more complicated systems, Charles Hansen in 1967 developed a set of solubility parameters to help predict if one material would dissolve in another.[70] Like the Hildebrand parameter, the fundamental principle behind Hansen solubility parameters (HSPs) is the idea that like dissolves like, so if two molecules have similar structures they are likely to be miscible. In addition to the dispersive term δ from the Hildebrand parameters, HSPs incorporate terms for polar and hydrogen bonding interactions. An individual molecule is assigned three parameters: δ_d, the energy from dispersion forces; δ_p, the energy from polar forces; and δ_h,

the energy from hydrogen bonds between molecules. These three values give a coordinate to the molecule in a three-dimensional solubility space. The closer two materials are in solubility space, the more likely they are to be miscible. This can be calculated from equation 6 below, where Ra is the distance in solubility space between two components, indicated in the subscripts by 1 and 2.

$$(Ra)^2 = 4(\delta_{d2} - \delta_{d1})^2 + (\delta_{p2} - \delta_{p1})^2 + (\delta_{h2} - \delta_{h1})^2 \quad (6)$$

It is important to note the coefficient of 4 in front of the dispersion calculation. There is some theoretical basis for its inclusion as a greater contributor for the solubility prediction, and ultimately it improves the empirical success of the equation.[71] However, three numbers are not sufficient to distill all the inter- and intramolecular interactions that determine solubility. These parameters also do not take into account the connectivity of a polymer chain and are designed for discrete molecular interactions only. However, there have been cases of reported empirical success with the use of Hansen solubility parameters in polymer systems; for example, Reichmanis and coworkers have used a poor solvent additive to induce P3HT aggregation during processing and enhance the field effect mobility in the solid state.[72] Ultimately, Hansen solubility parameters should be used to predict solvent systems and inform choices for designing experiments in conjunction with empirical data. Hansen Solubility Parameters in Practice is a tool, designed by Steven Abbott, that can use experimental data combined with literature data to determine the HSPs of new materials.

True molecular solubility is not a requirement for solution processability. However, having an incompletely dissolved solution can limit a complete understanding of the nature of the ink, which can complicate efforts to address reproducibility. Early solution processed

solar cells with C_{60}, discussed in section 1.2.1, likely featured aggregates of C_{60} rather than completely solvated molecules. Some of the polymers used in this dissertation also aggregate, despite long solubilizing side chains, due to the planarity of the backbone and tendency to π-π stack. The indirect evidence used to clarify the tendency of DT-PDPP2T-TT (chapter 3) and PffBT4T-2OD (chapter 4) to aggregate will be discussed in their respective chapters. The true nature of these aggregates is not well understood, nor are the best methods to characterize them. As with the P3HT system in the previous paragraph, but depending on the system, some aggregate formation in solution can improve solid state properties.

1.4.2 Phase separation

For a typical polymer blend solution use for organic electronics, solute-solvent interactions dominate the system, rather than solute-solute interactions due to the much higher volume percentage of solvent vs. solute. As solvent evaporation occurs, the likelihood of solute-solute interactions increases, which will drive the system to solidify into various phases, whether they be pure or mixed. There are two fundamental kinetic mechanisms of phase separation: nucleation and growth and spinodal decomposition. A nucleation and growth mechanism occurs when the blend system is in a metastable region and there is an energy barrier to solidification. Only once nucleation sites in the form of seeds form do domains begin to form as the film solidifies. This is in contrast to a spinodal decomposition mechanism, where the energy barrier toward phase separation is negligible and relatively small concentration fluctuations in a drying film are sufficient to initiate solidification.

Spinodal liquid-liquid demixing has been experimentally verified in an additive free blend of polymer and fullerene, by Janssen and coworkers.[73,74] In great detail, they studied the film formation process of a DPP based polymer, PDPP5T, which is similar to DT-PDPP2T-TT, which is another DPP based polymer that is the subject of chapter 3. In their work, they introduce the various aspects of solvent evaporation and phase separation during the solution processing of a binary mixture from a single solvent, as shown in Figure 1-10.

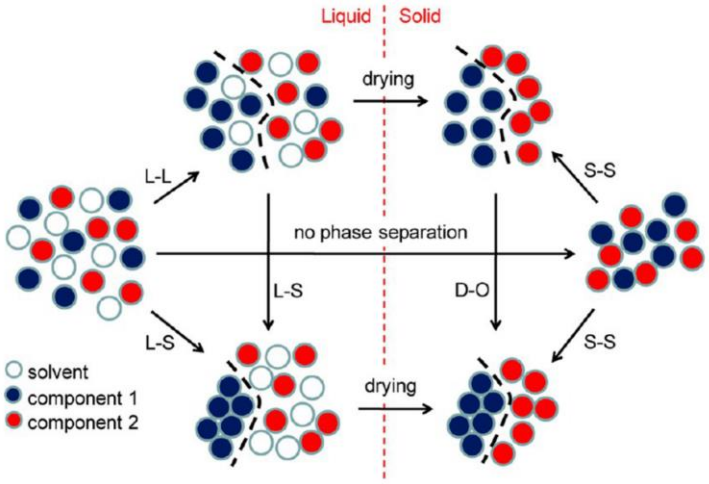

Figure 1-10 – Schematic overview of the phase separation processes that may occur during the drying of a two-component solution. Reproduced from Kouijzer et al.[73]

After coating but before the solvent has fully evaporated, either liquid-liquid (L-L) or liquid-solid (L-S) phase separation may occur. Otherwise, a finely intermixed film will likely form. Additional L-S de-mixing may occur from a L-L separated system, which will likely allow the solid phase to order more than if both components solidified simultaneously. Once the film is dried, it is possible to order one or both components in the mixture through a disorder-order (D-O) transition, which is typically achieved via thermal annealing (TA) or solvent vapor annealing (SVA). Optimum performance for

P3HT:PCBM is often achieved with thermal annealing, due to the blend being too finely mixed after processing.[75,76] Other polymers generally use high boiling point solvent additives, which are generally thought to increase fullerene solubility in order to inhibit aggregation of that component until polymer crystallization has begun,[77] but most studies do not provide a mechanism for solvent additive morphology adjustment during processing.

1.4.3 Side-chain design

As the field of solution processable organic electronics ramped up, so did the realization that solubilizing functionalities were required for facile solution processing. Those early solution processable materials all featured side chains mainly consisting of aliphatic groups: MEH-PPV and its derivatives, P3HT, and PCBM, which granted has a little more complexity on its solubilizing group. As the field progressed, it became clear that there needed to be a balance between a side chain that is sufficiently long to enable solubility, but not so long that solid state properties like microstructure are compromised. Relating back to earlier in this section, the enthalpy of mixing should be balanced between very strong and very weak mixing. P3HT features a simple hexyl side chain on each repeat unit, which imparts solubility for the polymer to be solution processed, but also allows and helps the polymer to order in the solid state. Rachael Segalman and coworkers have shown with differential scanning calorimetry (DSC) that decreasing temperature is required to melt poly(3-alkythiophenes) when comparing the linear hexyl alkyl chain on P3HT to a longer linear docecyl chain, and lastly to a branched 2-ethyl hexyl chain.[78] The reduced ordering due to the branch point is attributed to both the additional steric bulk close to the backbone as well as the introduction of a stereocenter at that branching position, which

further increases order-disrupting randomness. Side chain engineering via increasing the length or adding branch points is critical when developing donor-acceptor polymers with stronger intermolecular interactions than an all-donor P3HT. Instead of a small side chain on each ring on the backbone, as with P3HT, many donor-acceptor polymers have a repeat unit structure with longer side chains on only some of the rings in the repeat unit. This can be seen in DT-PDPP2T-TT and PffBT4T-2OD, the polymers studied in chapters 3 and 4, where the rings with long side chains attached are flanked by, respectively, bithiophene-thienothiophene or bithiophene without side chains.

In addition to exploring different lengths and configurations of alkyl side chains, other functional groups are commonly used to further enhance molecular interactions in polymers: alkoxy groups, ester groups, pendant conjugated rings like thiophene or benzene, siloxanes, oligoethers, fluoroalkyl chains, ionic groups, and even reactive units like vinyls or azides which can participate in crosslinking reactions and further direct morphology.[79] In addition to controlling the steric behavior of the molecule, if these functional groups are adjacent to the backbone their atomic orbitals can interact with the molecular orbitals along the polymer backbone and modulate the polymer's frontier molecular orbitals. For example, Jianhui Hou and coworkers synthesized a polythiophene derivative called PDCBT, with a repeat unit of 4 thiophene units: two with no side chains, and two with 2-butyloctyl carboxylate groups as the side chains.[80] The carboxylate/ester groups are electron withdrawing to the extent that this polymer has donor-acceptor character, and with drastically reduced frontier molecular orbital energies, the open circuit voltage of a device when blended with $PC_{71}BM$ is enhanced to 0.91 V in the optimized condition compared to 0.60 V for a P3HT device.

1.4.4 Solvent additives

As the major component of the blend solution, the composition of the solvent system used to deposit the active layer drastically effects the resultant active layer morphology. Commonly used solvents to dissolve donor-acceptor blends are halogenated organics which include chloroform, chlorobenzene, and 1,2-dichlorobenzene. While these solvents are generally sufficient to dissolve the mixture, casting from a single solvent usually results in a non-ideal morphology with either insufficient or excess phase separation between the bulk heterojunction blend components, as well as lack of order within the domains, all of which can contribute to poor device performance. Even among these non-optimized cases, solvent choice is still important. For example, initial reports of an MDMO-PPV:PCBM blend show enhanced photovoltaic performance when the blend is deposited from a chlorobenzene solution rather than toluene solution.[81]

The use of small amounts of high boiling point solvent additives is ubiquitous in the OPV literature as a technique to improve the solid state morphology in a blend film. Initial reports of solvent additive based morphology manipulation of a polymer:molecule donor:acceptor blend for improved electrical properties were of P3HT:PCBM films processed with *n*-octylthiol.[82] This work and subsequent studies on bulk-heterojunction solar cells was led by Guillermo Bazan and co-workers. The initial test, published in 2006, was a photoconductivity measurement tested via a thin film transistor (TFT). Their follow up study was on the low-bandgap polymer poly(cyclopentadithiophene-benzothiadiazole) (PCPDTBT),[83] whose blend with PCBM does not respond well to annealing as P3HT:PCBM does.[84] Compared to processing from a single solvent of chlorobenzene, adding a small amount (24 mg mL^{-1}) of 1,8-octanedithiol (ODT) to the coating solution

resulted in drastic increases in photocurrent and fill factor in the device, ultimately increasing power conversion efficiencies from 2.8 % to 5.5 %. This study explored varying the alkyl chain length of the thiol additive, and the thin film UV/vis measurements showed that a lower energy polymer peak emerged in the ODT additive processed film relative to the shorter alkanedithiols, indicating that the polymer backbone was more planar with a greater extent of conjugation. Concurrently with this work was the discovery that processing poly(9,9-di-n-octylfluorene) (PFO) with 1,8-diiodooctane (DIO) increased the presence of a specific polymorph in the polymer, the β-phase.[85] The β-phase of PFO corresponds to an alternating side chain configuration where the polymer is in its most planar form with the correspondingly lowest energy optical absorbance.

Following the initial studies and successes with ODT and DIO, a follow up study compared directly a series of 1,8-disubstituted octane additives, with end substitutions of either thiol (for ODT), chlorine, bromine, iodine (for DIO), cyano, or acetate.[86] This study attempted to clarify the mechanism for solvent additive activity on PCPDTBT:PCBM blends, where it was shown that a few additives improved current and fill factor via increased intensity of the low energy polymer absorption peak and improved domain connectivity as seen with AFM and TEM. DIO processing was shown to yield films with the best performance due to the highest degree of morphology enhancement with respect to the above criteria. The authors propose a mechanism for the morphology improving additives: once the solution is coated and the host solvent chlorobenzene evaporates, the remaining additive will selectively dissolve fullerene over the polymer due to differences in solubility. This prevents large fullerene aggregates from forming, which was identified to be a problem early in the introduction of fullerenes, even those functionalized with

solubilizing groups. With these results, the authors propose two criteria for processing additives that will improve BHJ morphology and photovoltaic performance: (1) selective solubility for PCBM over the polymer and (2) a higher boiling point than the host solvent, ensuring that it is the last to evaporate. Ultimately, as new, more complex donor polymers were constructed, polymer aggregation also plays a role in morphology development with respect to the use of solvent additives. To this day, DIO remains the champion solvent additive in most cases, especially for fullerene-based OPV.

1.4.5 Drying techniques

Once the film is coated from solution, via the coating methods that will be discussed in section 1.5, solvent evaporates and leaves behind a dry film. The method by which this film drying is accomplished has a large effect on the morphology and stability of the resultant blend film and device. For systems cast from a single solvent, this is likely not to be a concern, since relatively low boiling point solvents are used. A chloroform film typically evaporates in seconds under all conditions, with a boiling point of 61 °C and a vapor pressure of 21.1 kPa. At a room temperature solution and stage coating of DT-PDPP2T-TT:$PC_{71}BM$ from chloroform, demonstrated in Chapter 3, the solution dries in a few seconds. A chlorobenzene film generally evaporates within a few minutes, but this does depend on the temperature of the solution and the substrate, with a higher boiling point of 132 °C and a lower vapor pressure of 1.6 kPa. For a 50 °C solution of PffBT4T_{80}-co-3T_{20}-2OD blade coated on a 50 °C substrate, a wet film cast from chlorobenzene will dry in approximately 10 seconds – 20 seconds, as will be shown in Chapter 4. And when using *o*-dichlorobenzene as a cosolvent, at 7.5 $\%_v$, the DT-PDPP2T-TT:$PC_{71}BM$ film coated with a room temperature solution and stage is dry in approximately one minute.

Taking care to dry the films properly is more of a concern when high boiling point additives are used. For example, the boiling point and vapor pressure of DIO are 258 °C and 2.67×10^{-3} kPa, respectively. If a film with just 3 $\%_v$ of DIO is coated at room temperature, it will take several hours to dry in ambient conditions. Here, it is important to mention common practice in laboratory device fabrication, which is to bring a freshly coated active layer into the vacuum chamber of a thermal evaporator, in order to deposit the back electrodes to complete the device. We as device fabricators generally aim to bring the films into this vacuum chamber as soon as possible. Therefore, within minutes of coating, the DIO-wet film is forcibly dried under vacuum. Failure to do this has been shown to have negative consequences on morphology. I have observed that devices built from DIO additive films that have been allowed to dry in ambient conditions are more poorly performing than their actively dried counterparts. Tremolet de Villers et al. have examined in detail the effect of residual DIO on morphology of blends of PTB7 and PTB7-Th with $PC_{71}BM$.[36] This work was inspired in part by the work of others who have shown that washing films with a polar non-solvent can improve performance or delay degradation, the latter which has been observed with DIO additive solutions.[87,88] The PTB7-Th pristine and blend films were shown to be unstable to photooxidation, and DIO accelerates this degradation by acting as a radical initiator and likely abstracting a hydrogen atom from the 2-ethylhexyl side chain on the polymer. This DIO is removed during a high vacuum process, like that used for thermal evaporation of electrodes, but this need complicates transition to high throughput roll-to-roll processing techniques, where vacuum processing steps are not commonly used. Thermal annealing, while effective for removing DIO, can disrupt the morphology and reduce device performance.[65,89]

For the active layer films and devices built in this dissertation, and especially those cast with the high-boiling point solvent additives DIO and diphenyl ether (DPE), films were immediately brought into the vacuum chamber of a thermal evaporator after coating, in order to remove the additive quickly and reproducibly.

1.4.6 Solid additives

In attempt to evade the downsides of solvent additives for processing OPV, solid additives have been explored as a means to controlling morphology during processing. For example, McDowell et al. showed that the use of 2.5 wt% polystyrene (PS) in a blend of the molecular donor p-DTS(FBTTh$_2$)$_2$ and PC$_{71}$BM was shown to improve the morphology and photovoltaic performance.[90] This additive, similar to DIO, improved polymer crystallinity via extended CB drying time, since PS was able to retain solvent during the spin coating process. However, the DIO devices were higher performing due to the further extended drying time afforded by DIO compared to the CB with PS.

Recently, volatilizable sold additives have been explored with polymer:FREA blends, which are designed to be removed via post processing treatments like thermal annealing. Yu et al. have demonstrated a family of molecules, designed to improve the π-π stacking of ITIC-4F in a blend film, that have similar structures to the electron deficient end groups on ITIC-4F.[91] The proposed mechanism of the solid additives is as follows: the additive mixes with ITIC-4F during the coating process and may enhance the intermolecular ordering; upon thermal annealing, the additive sublimates and the resulting void in the film allows the already ordered additive domains to order even further. The resultant devices have higher fill factors and currents than their counterparts processed

without solid additives, likely due to improved charge mobilities. This technique has shown to work with a variety of different polymers and FREAs, suggesting universal applicability of the volatilizable solid additive technique toward improving device performance of FREA based organic solar cells.[92]

1.4.7 Post-processing treatments

Aside from solvent choice and/or the use of a solvent or solid additive, which affects the film morphology as the film is coated and drying, the morphology of a film can also be modified once the film dries. The two main methods through which this is achieved are thermal annealing and solvent vapor annealing.

1.4.7.1 Thermal annealing

As alluded to in the previous section, thermal annealing is a well-known technique in the OPV community though for polymer:fullerene blends it often worsens the morphology rather than improves it. The practice was popularized with the well-studied P3HT:PCBM blend, where annealing at a moderate temperature has been shown to drastically increase the voltage, fill factor, and current density.[93] With initial results of PCE enhancement of up to 3.5 % at an annealing temperature of 70 °C, further optimization of the annealing temperature led to reported PCEs approaching 5 % with an annealing temp of 150 °C.[94] In general, annealing is thought to require temperatures above the glass transition temperature of the polymer, in order to enable segmental chain motion and organization into more crystalline structures. There is a drop in PCE when increasing the temperature of P3HT:PCBM annealing to 170 °C or higher, indicating an over-coarsening of the system and an increase in domain size past the ideal regime.

While most high performing polymer:fullerene blends rely on solvent additives rather than thermal annealing to improve the morphology, the widespread use of fused-ring electron acceptors has led to the return of thermal annealing as a method to improve device performance. Thermal annealing generally does not lead to as drastic changes as seen with P3HT:PCBM described above, but there is still typically some improvement. For example, in the initial report of PBDB-T:ITIC, annealing the ideal 0.5 % DIO case at 160 °C (for an undisclosed duration) increased the average PCE from 9.8 % to 11.0 %, exclusively through the increase in fill factor.[47] This is likely a result of improved ordering of ITIC, and increasing annealing temperatures to 200 °C drops the performance back down to below 10 %, suggesting an over-coarsening of the system.

1.4.7.2 Solvent vapor annealing

Other reported non-fullerene acceptor systems have also seen success using solvent vapor annealing (SVA or SA) as a post-processing treatment. For typical SVA procedures, a dry active layer film is exposed to solvent vapor in an enclosed container, ensuring penetration of solvent into the film and likely morphological reorganization. The blend of PTQ10:IDIC, is one example, where PTQ10 is a simple regiorandom thiophene-difluoroquinoxaline polymer and IDIC has a similar structure to ITIC but with a shorter donor core and a lack of pendant benzene groups connecting the side chains to the backbone.[95] The as cast PCE of this system is 10.4 %, thermal annealing brings efficiency up to 11.7 %, and finally thermal annealing followed by solvent annealing with chloroform further increases the efficiency to 12.7 %. A slight drop in V_{OC} with these post processing treatments is more than offset by a small increase in J_{SC} and a drastic increase in fill factor,

from 65 % to 74 %. This performance enhancement was ascribed to charge carrier mobilities that became higher and more balanced.

Solvent vapor annealing has been shown to improve the morphology of P3HT:PCBM solar cells, with the use of DCB that increases polymer crystallinity and therefore improves the hole mobility.[96] Multi-step SVA processes have been used to more carefully tune domain size, by first using THF to form PCBM aggregates, followed by CS_2 to simultaneously reduce the size of those aggregates to an appropriate size of ~ 20 nm and increase P3HT crystallinity, as measured via TEM, AFM, and GIWAXS.[97] SVA has also been used with donor-acceptor polymer:fullerene blends and all polymer solar cells.[98]

1.4.8 Non halogenated solvent processing

As alluded to in the initial discussion of host solvents for P3HT:PCBM processing, using toluene compared to chlorobenzene generated a more drastically phase separated morphology, likely due to poorer solubility of the blend materials. However, there is great fundamental and practical interest in moving away from halogenated solvent systems, despite their efficacy and widespread use in OPV solution processing. Solvents which include chloroform and chlorobenzene present many health and environmental risks and hinder the transition of organic electronics from research lab to industrial printing operations. Most of the successful reports of non-halogenated solvent systems have involved solvents that are still aromatic and therefore somewhat toxic. Ideally, processing would occur from environmentally benign solvents that are non-aromatic such as ketones, esters, alcohols, 2-methyl-THF, and even water.[99] But rigid backbones that are beneficial for charge transport in the solid state limit solubility in those types of solvents. Adding

polar functionalities to side chains, like glycols and esters, improves processability at the expense of solid state morphology when compared to traditional alkyl sidechains.[100]

1.5 Thin film deposition techniques

One of the main benefits of organic electronics compared to their inorganic counterparts is their ability to be solution processed from liquid inks. This enables the use of low-cost printing techniques already used in industry, such as screen printing, blade coating, slot-die coating, inkjet printing, rotogravure printing, and spray coating. Importantly, these techniques are amenable to roll-to-roll (R2R) processing techniques, which reduces the cost of production compared to batch processing. This section will discuss the fundamentals of commonly used solution processing techniques used to deposit the active layer of an organic solar cell, shown below in Figure 1-11.

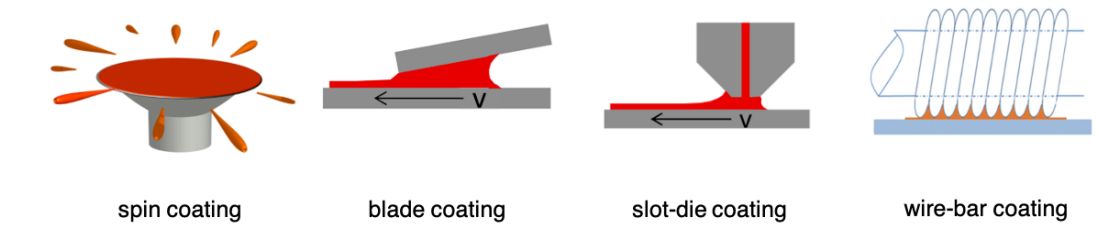

Figure 1-11 – Schematic illustration of four solution processing methods: spin coating, blade coating, slot-die coating, and wire-bar coating. Adapted from Richter et al.[101] and Khim et al.[102]

1.5.1 Spin coating

Spin coating is the most widely used solution processing technique used in the field of organic electronics, due to its ease of use. A substrate is attached to a vacuum chuck, a

solution is dispensed onto the surface, and the substrate is rotated at rates generally ranging from 400 rpm to 5000 rpm. As the substrate spins, the solution is drawn from the center to the edge of the substrate and flung off the edge, leaving behind a film that is generally quite uniform, but potentially possessing a radial thickness gradient. This means that a large portion of solution is typically lost, and that fact, combined with the dynamic movement of the substrate, means that spin coating is not amenable to continuous R2R processing methods. The final film thickness is a function of acceleration, spin speed, spin duration, and solution properties, with concentration being the easiest to modulate.[103] Due to the dynamic nature of the spin coating process, the film often dries more rapidly than in stationary techniques and the final film morphology is generally in a kinetically trapped state.[104]

1.5.2 Blade coating

Blade coating, also known as doctor blade and sometimes solution shearing, is the active layer deposition technique central to the work presented in this dissertation. In general, doctor blade refers to removing the excess solution from a gravure cylinder for coating a pattern on a R2R web, while blade coating refers to the one-dimensional patterning technique for depositing a uniform thin film.[105] A blade is fixed a certain distance above a substrate, a reservoir of solution is deposited at the blade-substrate gap, and one moves laterally relative to the other, leaving behind a film on the substrate. In continuous R2R processing methods, the blade is generally fixed while the substrate web is moved below it. For lab scale devices with rigid glass substrates, as used in the work featured in this dissertation, the substrate is affixed to a stage, and the blade is attached to an electric motor that is moved across the length of the substrate.

Compared to spin coating a comparably thick film on a substrate, a higher solution concentration is required along with drastically lower solution volume. This leads to blade coating requiring less solid material to coat, in large part due to negligible material waste compared to the solution ejected from the substrate with spin coating. The blade gap, which is the distance between the blade and the substrate, affects the film thickness, with a larger gap giving a thicker film. Similar to spin coating, final film thickness is also function of solution concentration and blade speed. However, there is not a simple linear relationship between blade speed and film thickness; for most systems there are two coating regimes depending on the drying dynamics. At relatively slow speeds, increased film thickness is achieved through slowing down the coating, in what is called the evaporative regime, while at faster speeds, increased film thickness is achieved through speeding up the coating, called the Landau-Levich regime.[106] A direct example of this phenomenon is shown by Zhenan Bao and coworkers, with the polymer PDPP3T (similar to DT-PDPP2T-TT, the subject of Chapter 3), shown in Figure 1-12.[107]

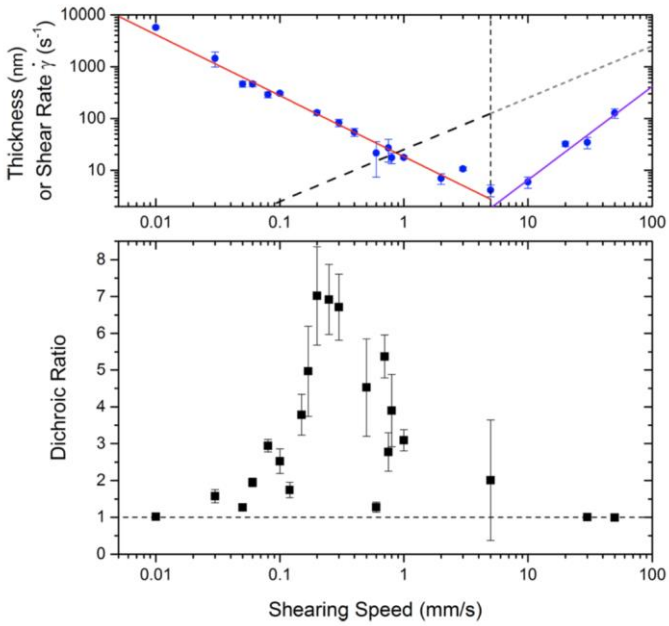

Figure 1-12 – Film thickness (blue points) and dichroic ratio (black points) as a function of coating speed for blade coated films of PDPP3T. The red curve represents a fit to the evaporative drying regime, and the purple curve represents a fit to the Landau-Levich drying regime. The dotted angled line represents the shear rate as a function of coating speed, and the vertical dotted line represents the transition from the evaporative to Landau-Levich drying regime. Reproduced from Shaw et al.[107]

The evaporative regime is marked by a red fitting line to the film thickness at low shearing speeds, and the Landau-Levich regime is marked by a purple fitting line at high shear speeds. In the evaporative regime, the time scales of solvent evaporation and solid film deposition are similar, so that the film is essentially dry after being coated. Thus, films are directly influenced by the lateral forces exerted by the coating technique, and polymer features can assemble and align with respect to the coating direction, as observed for PDPP3T. At faster speeds, in the Landau-Levich coating regime, there is a noticeable delay between when the wet film is formed and when solvent evaporates. In this regime, the drying process relates more to drop-casting methods, and polymer solidification is directed by the evaporation of a uniform thin layer of evaporating solvent from solution. Therefore,

despite a high shear rate (grey dotted lines) that aligns the polymer during coating, the polymer has ample time to relax to a more isotropic lateral orientation before the film is dry. As a result, at an optimum balance of shear rate and film thickness in the evaporative coating regime, around 0.2 mm s^{-1}, the dried polymer is in a strongly anisotropic morphology as seen with polarized UV/vis spectroscopy (black points) and variable angle GIWAXS.

For the practical blade coating of active layer blends for organic solar cells, we are generally operating in the Landau-Levich regimes, at speeds of 20 mm s^{-1} or greater. Therefore, the drying process is dominated by solvent (and solvent additive) evaporation rather than the coating apparatus. As a result, anisotropy in polymer alignment is neither expected nor observed. In general, efficiency for organic solar cells with active layers deposited via blade coating is on par or lower than those efficiencies observed for spin coated solar cells. This can be attributed to a few factors: (1) a greater volume of research efforts and greater understanding of the spin coating process make it a more appealing option for trialing new systems, (2) blade coating requires increased concentration of the active layer solution, which could push the system toward instabilities due to poor solubility of the blend components, and (3) change in drying dynamics to a more thermodynamically stable morphology rather than a kinetically trapped one.

Wire-bar coating is analogous to blade coating except, instead of a blade with a sharp and uniform interface, like the edge of a glass slide, a wire-wound bar is used. Similarly to blade coating, wire-bar coating allows for comparable control of coating and drying regimes as well as compatibility with roll-to-roll processing methods.[108] An additional variable being the geometry of the wire is added: both the gauge of the wound

wire as well as the pitch of the wrapping can be varied (whether there is a gap or not), further expanding the tunability of the technique and variables that need to be considered when optimizing processing conditions. Like blade coating, reports of wire-bar coating for organic electronic systems show that it is a reliable technique for generating highly performing films, such as in OFETs.[102] However, reports of OPV layers deposited via wire-bar coating are few and far between.[109]

1.5.3 Other solution processing methods

While spin coating and blade coating were the only two coating methods used in the body of the work featured in this dissertation, I will take a moment to address two additional well known solution processing techniques used in the field of organic electronics: slot-die coating and spray coating.

Slot-die coating is similar dynamically to blade coating, but instead of manually depositing the solution into the meniscus, the die, or physical coating apparatus (analogous to the blade) has solution continuously fed through a slot within it.[105] Therefore, it is amenable to continuous processing with even higher material use efficiency compared to blade coating. While at one point our research group had a slot-die coater, it was not widely used for OPV due to the prohibitively large volume of solution required to fill the lines of the instrument, which is challenging when dealing with batches of polymer synthesized at the 100s of mg scale. Recent research efforts have shown the promising potential of the slot-die coating method, with a record high power conversion efficiency of 10.0 % with PBDB-T:ITIC on a glass/ITO substrate, and 7.1 % on PET/ITO in a flexible substrate, roll-to-roll configuration.[110]

Spray coating is another roll-to-roll compatible technique used in the field of organic electronics, whereby a carrier gas carries droplets of a solution through air to the substrate. Ideally, these droplets will hit the surface and form a wet film that may then dry to generate a smooth uniform solid film. In practice, solvent evaporates concurrently with the possible generation of this smooth film, so the resulting surface texture resembles that of discrete droplets that have dried together. In order to modulate droplet size, ultrasonic spray deposition is often employed, which generates smaller and more uniform droplets compared to an analogue handheld airbrush, as is often used for less morphologically sensitive organic electronic applications such as electrochromics. Some recent work in OPV has shown promising results from ultrasonically spay cast active layers that are comparable, yet still lag in PCE compared to those processed via spin coating and blade coating, with average PCEs of about.[111] Zhang et al. have reported an ultrasonically sprayed blend of PTB7-Th:$PC_{71}BM$ with an average PCE of 7.5 %.[112] For comparison, the best reported PCE with this blend processed via spin coating is over 10 %.[113] It is likely that due to the drastic differences in coating dynamics between spray coating and other mentioned processing techniques, materials design may need to be revaluated and modulated in addition to simple solution formulation adjustment.

1.6 Film properties

Once films are formed, characterizing their morphology is critical in understanding relationships among the variety of tunable variables that controlled their formation. Molecular interactions and domain morphology all contribute to photovoltaic performance, and a wide span of techniques are used to characterize these features that span a wide range of length scales, from angstroms (10^{-10} m) to millimeters (10^{-3} m). The techniques used to

acquire this data will be discussed in Chapter 2, but their importance will be introduced here.

1.6.1 Optical properties

As discussed in the organic photovoltaic principles section, 1.4, active layer blends should be designed to absorb as much light as possible in the region of maximum spectral irradiance, which lies approximately in the visible region going into the NIR. The degree of optical absorption is itself dependent on the polymer structure, where high optical absorption has been connected to the persistence length of the polymer, and that quantity itself is affected by molecular weight.[114]

If relatively large phase separated domains with length scales on the order of those wavelengths exist (400 nm – 1000 nm), light is likely to be scattered rather than absorbed. Domains on that length scale are also detrimental to performance due to limited charge mobilities and exciton diffusion lengths as previously mentioned. Film thickness should be modulated so the film is thick enough to absorb as much light as possible, but not too thick as to decrease the likelihood that free charges will make their way to the electrodes. Most reported active layer thicknesses are in the 100 nm – 200 nm range, but some new NFA systems have been shown to maintain PCEs around 10% with active layer thicknesses up to 600 nm, which would benefit the transition to roll-to-roll processing.[115,116]

Aggregation is another polymer property that affects the optical absorption, and notable ways to monitor this in solution are with UV/vis absorption spectroscopy and visible light scattering. Both techniques have their downsides: UV/vis spectroscopy provides indirect evidence for aggregation via the planarization of the backbone related to

the solution to film transition discussed in the next paragraph. This concept is explored thoroughly in Chapter 4 with PffBT4T-2OD, where increasing the temperature of the solution from 25 °C to 95 °C causes a drastic blueshift of the absorption spectra and a reduction in distinct features evident of aggregate order.[117] We interpret this phenomenon literally as the polymer backbone transitioning from a planar geometry to a coiled configuration, which serves as indirect evidence that aggregates are breaking up.[118] Visible light scattering to monitor aggregates has been explored by Rene Janssen and co-workers, but interpretation is complex.[74] This will be discussed in section 1.8 on in situ measurements. Commercially available solutions for monitoring light scattering in opaque coating solutions for OPV applications are currently non-existent.

Optical properties of conjugated molecules and polymers generally change when transitioning from the solution state to the solid state. A well-known example is P3HT, which has a drastic color change when going from solution to thin film, whereby the optical absorption onset moves to a lower energy and its UV/vis spectrum is redshifted. This is indicative of planarization of the backbone, afforded by polymer inter- and intramolecular interactions that dominate once solvent evaporates. In addition to the P3HT absorbance spectra red shifting upon drying, there is often the emergence of sharper peaks or shoulders indicative of vibronic transitions due to increased homogeneity as this aggregation forms. This phenomenon can be modelled in terms of different types of aggregate order, but adapting those models to more complex donor-acceptor polymers has yet to be achieved, in large part to less dramatic optical transitions going from solution to solid.[101,119]

1.6.2 Topology

Surface measurements such as atomic force microscopy (AFM) can often provide some insight into properties that affect device performance, but care must be taken to understand the limitations of connecting device properties that depend on the bulk to measurements that are limited to the small fraction of the film that is the surface. When domain sizes are prohibitively large, on the order of hundreds of nanometers, this will almost always be visible on the surface and be a strong indicator of poor device performance. On the other hand, AFM can also be used to identify large aspect ratio structures like nanofibers, which can be helpful for charge transport.[120]

1.6.3 Texture: crystallinity and orientation

Most of the semiconducting polymers and small molecules used for organic photovoltaics can form semicrystalline phases, with some degree of order that develops in the solid state. This order is derived primarily from π-π interactions between backbones, and lamellar interactions between side chains, and involves length scales around 2 Å and 2 nm, respectively. This ordering is typically measured via grazing incidence wide angle scattering (GIWAXS), but crystallinity in general can also be measured via thermal methods such as differential scanning calorimetry (DSC). While charge transport through polymer semiconductors primarily occurs along the polymer backbone, charges can certainly hop between chains given sufficient geometric overlap of the backbones, which relates back to charge delocalization and mobilities. Lamellar ordering can further help facilitate backbone ordering and charge transport, despite its origins from the aliphatic insulating side chains.[121] The GIWAXS measurement involves the use of an area detector, where the orientation of these various crystallites can be probed and their distribution can be quantified. For example, improved isotropic crystal texture could help enhance charge

transport through a film with 3-dimensional variation in composition. While electrodes are stacked in a vertical configuration sandwiching the film, domains are likely not aligned with those electrodes.

1.6.4 Phase behavior: domain size and purity

As shown in the bulk heterojunction schematic, donor and acceptor phase materials separate and form a nanostructured network with length scales ranging from single nanometers to hundreds of nanometers. Ideally, domains are phase separated on the order of 10 nm – 20 nm, but depending on material properties and drying conditions, materials could phase separate into a finer or coarser morphology, or not phase separate at all. The interface between phases is also important, whether the phase is sharp and well defined or diffuse and mixed can affect the efficacy of charge separation at a donor-acceptor interface.

Two techniques are used for probing phase behavior in blend films: grazing incidence small angle scattering (GISAXS) and resonant soft x-ray scattering (RSoXS). These techniques are able to measure characteristic length scales derived from phases with different material composition. Like GIWAXS, GISAXS uses hard x-rays with energies in the 10 keV range,[122] while RSoXS uses soft x-rays with energies in the hundreds of eV range (i.e. 0.2 keV – 0.3 keV).[123] For hard x-rays, the contrast between two phases is determined by differences in electron density, while soft x-rays are sensitive to differences in chemical bonding environment.[124] As a result, GISAXS works very well for polymer:fullerene blends, since the electronic densities of these two materials are very different. On the other hand, GISAXS is generally unsuccessful for looking at polymer:NFA blends, since these materials typically have similar thiophene-based cores

with comparable electron densities. Therefore, RSoXS is generally used to characterize domain information for those systems.

1.7 In situ methods

So far, we have discussed the nature of the solution and of the resulting thin film morphology. That final film morphology is established during the dynamic coating process as a function of solution properties. Therefore, to better understand the factors that control the final film morphology, real time characterization methods are used as the film dries to get a complete picture of the coating process. UV/vis absorbance, white light interference, and x-ray scattering methods are the most commonly used and were implemented in the work featured in this dissertation, but visible light scattering measurements have also been employed by others. The goal here is to develop formulation-property-structure-function relationships that may be related back to all parts of the process. Although virtually all initial reports of OPV systems have been done via spin coating the active layer, the nature of the stationary substrate made blade coating the technique of choice for in situ measurements.[101]

Early reports of these experiments were with P3HT:PCBM from single solvent systems. In 2009, groups at Karlsruhe Institute of Technology measured optical interferometry to monitor wet film thickness as a function of time.[125] In 2010, groups at University of Sheffield used ellipsometry for wet film thickness along with GIWAXS to monitor the development of polymer crystallinity.[126] Together these results began to establish relationships between solvent choice and drying dynamics, as well as how crystals

developed during solvent evaporation and as both P3HT and PCBM approached their solubility limits.

In situ GISAXS measurements were first reported by Richter at al., where P3HT:PCBM morphology development was studied as a function of solvent additive.[76] Combined with the use of GIWAXS and UV/vis, the authors show that without additive, P3HT crystallization is inhibited by the high glass transition temperature (T_g) of the blend. Depending on the nature of the additive, further morphological development occurs after the host solvent chlorobenzene evaporates. When 1-chloronaphthalene (CN) is used as the additive, P3HT continues to crystallize in the CN wet film due to a lowered T_g and domains continue to form. When ODT is used, two liquid phases are formed, and crystallization is paused while domains form and solvent continues to evaporate, due to poor solubility of P3HT in ODT. The ODT additive mechanism supports previous work indicating that the solvent additive should be a selective solvent for fullerene, while the CN additive mechanism suggests that it has reasonable solubility for both components. Ultimately, this report was one of the first that was able to establish a relatively complete picture of phase behavior during coating and solidification and highlights the advantages of using comprehensive in situ techniques. A more complete discussion of in situ characterization of solvent additive processed films for non-P3HT systems is presented in Chapter 3.

1.8 Overview of dissertation

This thesis attempts to explain the morphological behavior of three polymers by way of thoroughly characterizing the polymer solution, the film processing method, and the morphology of the dried film. I will attempt to address these polymers' tendency to

aggregate, which affects the ease with which they are solution processed as well as their resulting microstructural properties. This chapter has focused on the fundamentals of materials design, device construction, solution phase behavior, solid state morphology, and the transition between the latter two topics in the form of in situ characterization. Many experimental techniques were introduced and placed in historical context. Chapter 2 will discuss the details of these experimental techniques from a fundamental physical understanding to practical application and use. Chapters 3, 4, and 5 are the three main projects that I have worked on in my graduate career, and they will each discuss a select few of these characterization techniques in more detail and in context. Chapter 3 is on the polymer DT-PDPP-2T-TT, a low solubility, highly aggregated polymer that was processed with a variety of cosolvents and the effects of these cosolvents on the drying process and morphology. Chapter 4 discusses the PCE11 derivative PffBT4T$_{80}$-co-3T$_{20}$-2OD, which was engineered to have improved processability but improved solid state properties relative to PCE11. Both moving from spin coating to blade coating, and moving from PCBM to a non-fullerene acceptor, reduce the overall power conversion efficiency, and this chapter addresses the fundamental morphological reasons for those changes. Chapter 5 discusses P(DTG-TPD), which has no accessible aggregation transitions and can be processed via spin coating or blade coating, from halogenated or non-halogenated solvent systems, to give virtually identical morphologies and device performance. This property is attributed to its high solubility and limited reliance on microstructural order for that optimally performing case. Chapter 6 will provide a brief outlook and perspective on the field of OPV relating to the work presented in this dissertation, focusing on aggregation and facile solution processing.

CHAPTER 2. EXPERIMENTAL METHODS AND CHARACTERIZATION TECHNIQUES

This chapter will discuss the experimental tools used in this dissertation as well as the theory behind them. The techniques used herein begin with polymer and solution characterization, end with thin film fabrication and device measurement, and include real time solution processing characterization along the way. Polymer syntheses and synthetic characterization were done by Dr. Bing Xu and Dr. Austin L. Jones for Chapter 4, and Dr. Rylan M. W. Wolfe for Chapter 5.

2.1 Polymer characterization

2.1.1 Basic synthetic characterization

Along the course of polymer synthesis, monomer units need to be thoroughly characterized with their purity confirmed, commonly via nuclear magnetic resonance spectroscopy (NMR) and elemental analysis. A number of techniques are commonly used in conjugated polymer synthesis, which affects the end groups attached to the monomer units. Two commonly used polymerization techniques are Migita-Stille-Kosuge (aka Stille) and direct heteroarylation polymerization (DHAP). While Stille coupling relies on toxic organotin coupling groups, it is a more versatile and facile polymerization technique compared to DHAP. The reader is directed to the dissertations of Brian Schmatz, Chi Kin Lo, and Caroline Grand for discussion on polymerization techniques used to prepare polymers for organic photovoltaics.

After initial polymer purification steps, the polymer is fractionated into various distributions of molecular weight via Soxhlet extraction. Sufficiently high polymer molecular weight is important for solar cell performance and understanding material properties is important for reproducibility. A common Soxhlet extraction solvent schedule is as follows: methanol (removal of salt and catalyst materials), acetone, hexanes (the first solvent likely to dissolve polymer material, low molecular weight oligomers), dichloromethane (DCM) and chloroform ($CHCl_3$). Polymers with ideal molecular weights for organic photovoltaics generally emerge from the last two solvent extractions. More powerful solvents like chlorobenzene can be used after DCM and $CHCl_3$, but the resulting polymer fractions are likely too high weight and of too low solubility to be much use for the processing methods that are commonly used.

2.1.2 Gel permeation chromatography

In order to characterize a polymer's molecular weight distribution, gel permeation chromatography (GPC) is commonly used. Also known as size exclusion chromatography (SEC), GPC is a technique where a polymer sample is characterized via its hydrodynamic radius compared to a standard, generally polystyrene. The main parameters reported from a GPC experiment describing the molar mass distribution are number average molecular weight (M_n), weight average molecular weight (M_w), and their ratio, dispersity ($Đ = M_w/M_n$). The weight average molecular weight is a higher value than the number average molecular weight due to an increased weighting factor in its calculation. Thus, dispersity will always be 1 or greater. A dispersity of 1 indicates that all polymer chains in the sample are the same length, with increasing values indicating a broader distribution of chain lengths. For the polymers featured in this dissertation, GPC was typically performed

in 1,2,4 trichlorobenzene at temperatures between 140 °C and 160 °C on a Tosoh EcoSEC HT GPC instrument with a refractive index detector.

2.2 Polymer solution characterization

Since solution processing is a central technique to this thesis, characterization of materials in solution is critical for complete understanding of each system.

2.2.1 UV/visible absorption spectroscopy

UV/vis absorption spectroscopy was performed both on solutions and films, using either a Varian Cary 5000 Scan UV-Vis-NIR double-beam spectrophotometer, or an Ocean Optics Flame VIS-NIR diode spectrometer. The Cary 5000 has an incredibly broad spectral range and high sensitivity, along with a thermoelectric heater for variable temperature solution measurements. This high sensitivity is achieved through a long optical path length requiring the use of a mechanically controlled diffraction grating and slits, which means that spectra are built up one wavelength at a time. Additionally, this instrument has a double beam configuration, where a blank (pure solvent) is measured simultaneously as the sample to correct for subtle changes in light intensity inherent to the instrument. Conversely, the Ocean Optics Flame has compact charge coupled device (CCD) array, whereby the entire spectrum is measured at once. This allows for rapid spectra acquisition required for the real time UV/vis absorption and reflection spectroscopy techniques presented in this work. Whereas a typical spectral acquisition on the Cary 5000 takes about 1 minute, the Ocean Optics Flame can operate with a scan rate as fast as approximately 30 ms.

Solution UV/vis was exclusively conducted on the Cary 5000. A typical concentration of 0.02 mg mL^{-1} was used in order to achieve an absorbance of approximately 1.0 with a 1.0 cm path length quartz cuvette. It should be noted that the absorbance unit is a logarithm of a ratio of light intensity out vs. light intensity in and is therefore dimensionless. Given the challenges of measuring tens of micrograms for the few mLs required for this experiment, a stock solution of ca. 0.2 mg mL^{-1} was generally made and then diluted 10x to a concentration suitable for UV/vis. Sample holders on the Cary 5000 may be swapped out to accommodate thin film UV/vis on glass slides.

2.2.2 Thermochromism and temperature dependent aggregation

In order to control solution temperature during the UV/vis experiment, a thermoelectric system coupled with a water bath was used to regulate the temperature from ~10 °C to ~100 °C. If the temperature is dropped below ambient, care should be taken to ensure that moisture does not condense on the cuvette. This can be achieved with an inert gas blanket, like argon or nitrogen, but this was not used for any of the work presented here. We are instead interested in exploring the effect of increasing temperature on polymer UV/vis absorption spectra, which can coil the polymer backbone which relates to de-aggregation of polymer and cause the spectra to blueshift. For the work in this dissertation, the heater is generally scanned from 25 °C to 95 °C in 10 °C increments for each scan, waiting for 5 minutes after the target temperature has been reached in order to allow the solution to equilibrate. Teflon capped cuvettes are used to prevent solvent evaporation, which would otherwise concentrate the solution and increase the absorption intensity.

2.2.3 Solubility characterization

Solution UV/vis spectroscopy can be used to quantify solubility. A calibration curve is created from a few known solutions, generally beginning with a solution with absorbance around 1.0 and diluting serially to span a range from 1.0 down to approximately 0.1. A saturated polymer solution is then centrifuged to separate the undissolved material from the solution. This supernatant is then diluted to an absorbance value within a range of the initial calibration, at which point the resulting absorbance can be compared to the calibration curve and related back to the dilution used.

2.3 Thin film characterization

2.3.1 UV/vis absorption spectroscopy

As mentioned in the previous section, high resolution UV/vis absorption measurements were collected with the Cary 5000 with a slide holder. Films were processed via spin coating or blade coating onto cleaned glass slides, since there are minimal to no changes in absorption spectra when coating on ZnO/ITO/glass slides as used for a device configuration. The solid-state absorption spectra were used to estimate the optical band gap. As will be discussed in section 2.4, in situ absorption spectroscopy was collected with an ocean optics CCD spectrometer to allow for rapid data acquisition.

2.3.2 Profilometry

Film thickness was measured via profilometry using a Bruker DektakXT stylus profiler. This profilometer is equipped with a diamond-tipped stylus with a radius of 12.5 μm, and 3 mg of contact force is typically used on the sample. In general, the profilometer was used to measure active layer films on glass/ITO/ZnO substrates. The active layer film

was scratched in a zig-zag manner with a razor blade in order to generate parallel scratches on the order of 300 µm – 600 µm apart. Care was taken to ensure that all the active layer was removed while not disturbing the layers below, which was achieved due to the higher integrity of the ZnO nanoparticle surface; much higher force with the razor blade is required to remove the ZnO film relative to the active layer film. For the measurement, the stylus is dragged linearly across the film over a distance that spans at least two scratches at a speed of approximately 10 mm s^{-1}. The line profile was zeroed to the two scratches and the thickness was computed as the average difference in height between one of the scratches and the adjacent film in between the two scratches. In general, three separate measurements for a film were taken and averaged; the location of these three measurements were dependent on the coating technique. For spin coated films, there is generally a radial thickness gradient, with increasing film thickness from the edges of the film to the center. For blade coated films, there is generally a linear thickness gradient in the coating direction, with decreasing film thickness as the coating progresses. Film thicknesses were measured on almost all devices after fabrication and electrical testing.

2.3.3 Atomic force microscopy

Atomic force microscopy (AFM) is a surface mapping technique that uses a similar technique to profilometry to measure topology. A sharp stylus is moved across the surface in order to map both height and mechanical properties as a function of position. For the measurement, a laser is aligned onto the back of the stylus and the subsequent reflection is directed into a split photodetector (i.e. a pixel array). Changes in the surface properties will move the tip and therefore adjust the position that the laser reflection hits the detector. Early forms of AFM used a contact mode, similar to profilometry, where the stylus is kept

in constant contact with the surface. Because the tip is being physically dragged across the surface, strong lateral forces can cause rapid sample and tip degradation, and extended contact with the surface can cause electrostatic charging which can affect accurate surface measurement.

To date, tapping mode is the most widely used AFM method for organic film measurement. Instead of having the stylus in constant contact with the surface, a piezoelectric crystal vibrates the tip at frequencies in the range of 50 kHz to 300 kHz. This minimizes the forces incident on the sample and improves both the life of the tip and the sample. In addition to the change in amplitude of the reflected laser oscillation that is the basis for the height measurement, the phase change between the driving piezo oscillation frequency and the measured laser oscillation frequency is recorded. This forms a phase image in addition to a height image and represents contrast of different material properties within the surface such as elasticity, adhesion, and friction. The effect of sample approach on the signal amplitude and oscillating frequency is shown in Figure 2-1. In tapping mode, height and phase images are collected simultaneously. AFM images featured in this dissertation were conducted on a Bruker Dimension Icon, using probes with resonance frequencies in the range of 100 kHz to 160 kHz, with a spring constant of 5 N m^{-1}.

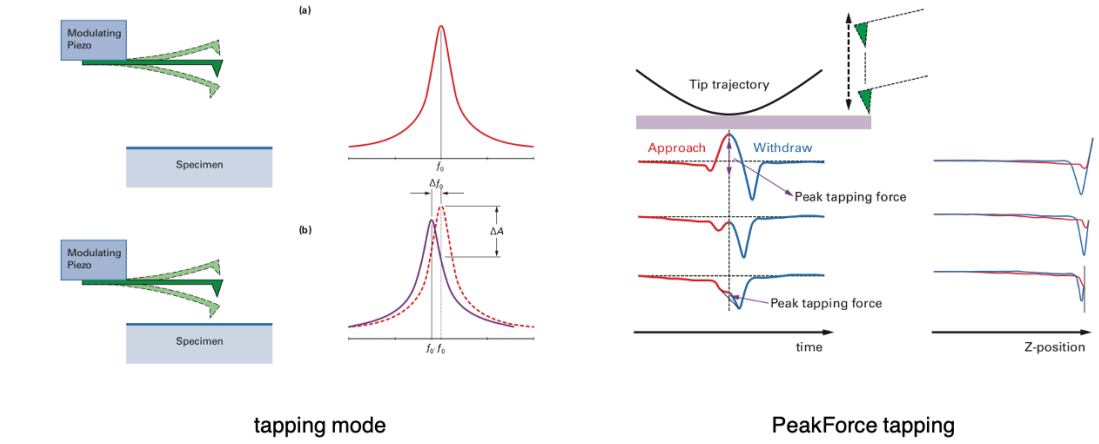

Figure 2-1 – Schematic of AFM methods: tapping mode and PeakForce tapping. The tapping mode diagram shows the change in resonance frequency and oscillator amplitude from the driving signal as the probe contacts the surface. The PeakForce tapping mode shows the force curve as a function of time and Z-position for a single probe approach. Reproduced from bruker.com.

There is a constant feedback loop during the tapping process that reflects the fundamental interactions during the tapping process. As the tip approaches the surface, van der Waals forces attract the tip to the surface and decrease the force incident on the tip. As the tip becomes closer, Coulomb forces which act more strongly, but at a shorter distance, act to increase the force on the tip. As the top comes back up, van der Waals forces take over again and provide another attractive force. The probe backs up even further at which point the tip does not sense the presence of the surface, and then the cycle repeats. PeakForce Tapping is a Bruker proprietary technology that performs dynamic analysis of this force curve in order to drastically improve imaging resolution, especially on soft samples. This force curve is shown in Figure 2-1, both as a function of time and Z-position, A probe with a spring constant of 0.4 N m^{-1} is used, which is over one order of magnitude lower than the spring constant of tapping mode probes described above. Three different

sample types are shown, indicating the flexibility that this measurement has among samples with different hardness. Soft samples like those shown in the bottom most curve would not be able to be imaged with tapping mode. PeakForce tapping offers increased sensitivity which was crucial in imaging the polymer nanofibers shown in Chapter 3.

2.3.4 Optical microscopy

Optical microscopy is used to gain insight into structural features in thin films on the micron scale, generally from tens of microns to millimeters. Optical microscopy was performed with an Olympus BX51 upright microscope, though its use was limited to other projects in my graduate career that will not be presented in this dissertation. This microscope has a set of polarizers that can be used to measure structural order in birefringent materials, which are materials whose refractive index is dependent on the polarization and propagation direction of light. This microscope can also be equipped with a stage that can be heated or cooled to observe optical changes associated with thermal transitions.

When performing optical microscopy, users are often tempted to place their sample on the microscope, focus the image, and quickly collect a micrograph. However, care should be taken to ensure optimal illumination in order to achieve the highest quality imaging. This generally involves the establishment of Köhler illumination, which is an illumination technique established in the nineteenth century by August Köhler.[127] The need for this technique arises in part because the origin of the light is some sort of filament in a lightbulb, and this filament should not be directly focused on the sample. Achieving Köhler illumination involves perfectly defocusing the microscope light source at the focal level of

the sample, so that the sample is uniformly illuminated and any dust or imperfections on the condenser lens are not visible in the image.

In order to measure quantitative optical information from an optical microscope, the image output can be sent into a monochromator or spectrophotometer to get an absorbance or fluorescence spectrum from a point or a line. To build up a complete image at a size common to an optical micrograph, e.g. 100 μm by 100 μm up to 1 mm by 1 mm, the entire field of view needs to be scanned point by point or line by line, collecting one spectrum at a time.

2.3.5 Hyperspectral microscopy

Hyperspectral microscopy is a technique that can capture spatially and spectrally resolved optical data via the use of volume Bragg gratings (VBG). For this dissertation, hyperspectral microscopy was conducted on an IMA-VIS from Photon etc. With this instrument, the entire field of view is directed into the VBG and images that are approximately monochromatic are isolated and sent into a camera. Shown in Figure 2-2 is a labeled photograph of the Georgia Tech hyperspectral fluorescence microscope. This microscope has two different excitation sources: a 3-watt 532 nm continuous wave laser and a broadband mercury lamp. The fluorescence excitation source is reflected into the sample via a long-pass dichroic mirror in one of the filter cube turrets on the microscope. The light is focused into the microscope objective to excite the sample, and subsequent emission is collected by the same objective and transmitted through the long-pass dichroic mirror. The light is then sent into the hyperspectral VBGs, of which there are two; one is designed for wavelengths from 400 nm – 650 nm, and the other is designed for wavelengths

from 550 nm – 1000 nm. Spectra can be stitched together across these two VBGs but intensity needs to be properly normalized. Data from this instrument is used exclusively in Chapter 3, where films were excited with the 532 nm laser and emission was collected from 550 nm – 1000 nm with a single VBG.

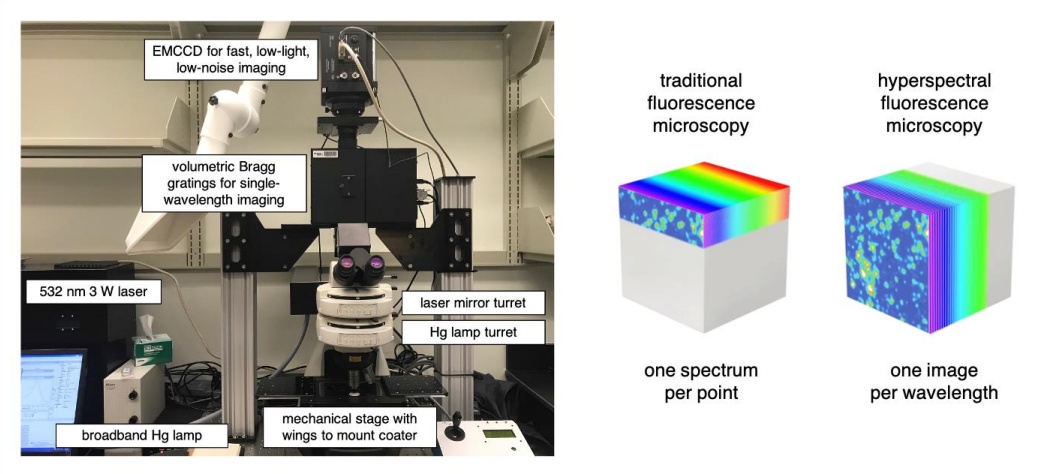

Figure 2-2 – Hyperspectral microscope photograph, with vital components labeled (left). Fundamental differences in spectral acquisition from traditional fluorescence microscopy and hyperspectral fluorescence microscopy (right). Image reproduced from photonetc.com/ima/.

Due to slight divergence in the optical path, the entire light incident on the VBG does not all come in at the same angle in the horizontal direction. As a result, the output from broad spectrum emission incident on the VBR is a gradient of wavelengths, where the center of the image is tuned to the desired wavelength and the edges of the image are +50 nm on one side and -50 nm on the other side. As the VBR is mechanically scanned to build a series of images, each instance of a single wavelength is progressively collected across the field of view. These images are stitched together with the included proprietary software (PhySpec) in order to generate true monochromatic images. A comparison of the

process in which traditional and hyperspectral fluorescence microscopy images are generated is shown on the right side of Figure 2-2.

Images are collected with an electron-multiplying charge-coupled-device (EMCCD) camera, which is a special camera designed to eliminate the intrinsic noise generated during the readout process of a CCD camera. This EMCCD was chosen for this microscope due to its high signal to noise ratio, which is beneficial for low light applications and rapid image acquisition. Coupled with a blade coater or wire-bar coater onto the stage of the microscope, this camera can be used to capture the dynamics of the film formation as a solution is coated and the film dries. Using a fixed wavelength, images can be collected in intervals as fast as 30 ms. This is an effective technique for rapid film monitoring on micron length scales.

The previous chapter discussed the importance of real time monitoring of thin film development via X-ray scattering and absorption measurements, which can characterize molecular conformations and nanoscale morphology. Real time characterization with this instrument is used to develop understanding on a longer length scale, encompassing 10s of μm to 100s of μm. However, real time data collection has limitations. Most notably is the effect of the excitation source on the drying process; the high energy from a focused laser with sufficient flux to get a reasonable signal provides enough energy to heat and to boil the solvent and drastically alter typical drying characteristics.

2.3.6 Grazing incidence wide angle X-ray scattering (GIWAXS)

Grazing incidence wide angle X-ray scattering (GIWAXS) is a technique used to determine structural order and orientation of thin films on length scales from approximately

0.2 nm to 2.0 nm. GIWAXS uses hard X-rays, which for this work consisted of X-rays with energies of either 12.7 keV or 13.5 keV. Scattering of hard X-rays is observed due to periodic regularities in electron density within a film. Due to low scattering length density of the organic materials used in this dissertation arising from their low degree of crystallinity, a high-flux synchrotron light source is used (10^{12} photons s^{-1} or greater). The relative differences in intensity between the incident X-ray light and the scattered X-ray light require that the reflected beam be physically blocked from the detector; otherwise, detector damage would occur from X-ray exposure. The X-ray beam is directed at a shallow angle that is large enough to penetrate the film depth, but not so large that the high dielectric constant substrate is measured; this defines the grazing incidence geometry. A 2D area detector is placed approximately 150 mm – 300 mm from the sample, which is used to measure the position and relative intensity of scattered light. A schematic of this setup is shown in Figure 2-3.

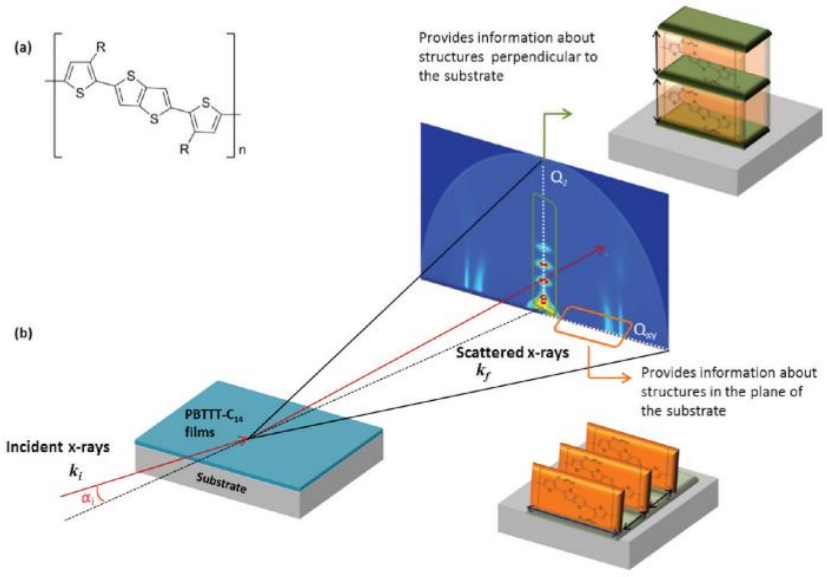

Figure 2-3 – Schematic of the GIWAXS experiment and resulting 2D scattering pattern for PBTTT-C_{14} (R = n-tetradecyl). Schematic diagrams of polymer lamellar

stacking in the out-of-plane direction (Q_z, green planes) and π-π stacking in the in-plane direction (Q_{xy}, orange planes) are shown. Reproduced from Cho et al.[128]

The patterns recorded on the 2D area detector are a function of the constructive interference of scattered light, which is observed due to periodic structures found within the film, i.e. crystals. A representative scattering pattern of the biaxially aligned and highly ordered polymer, poly(2,5-bis(3-alkylthiophene-2-yl)thieno[3,2-b]thiophene) (PBTTT) with n-tetradecyl side chains, after annealing, is shown in Figure 2-3. Scattering techniques are a reciprocal space technique, so patterns that are further from the origin correspond to smaller distances in real space. Visible on the scattering pattern are four peaks in the vertical Q_z direction, which correspond to four orders of lamellar stacking (*h*00) in the out-of-plane direction. The first peak at the smallest q (at approximately 0.30 $Å^{-1}$) corresponds to a lamellar spacing distance of nominally 21 Å. This length scale for first order (100) lamellar stacking corresponds to two backbones that are aligned and somewhat interdigitated. Increasing orders of reflection that are visible correspond to constructive interference between the backbones, indicating that not only are the backbones aligned, but there is a high amount order among the side chains between them. In the Q_{xy} direction, two distinct peaks are seen at a higher q value compared to any of the out-of-plane side chain reflections. The sharp reflection at the edge of the image is at q = 1.71 $Å^{-1}$, which corresponds to a π-π stacking distance of 3.67 Å, and the slightly broader reflection at smaller q is from in-plane order of the backbones, due to their strong interdigitation and ordering. This final feature is not typically seen for semi-crystalline polymers and is not observed for the polymers studied in this dissertation. All together, these observations show that PBTTT in this film is in a strong edge-on orientation, with lamellar stacking in the vertical direction and π-π stacking in the horizontal direction.

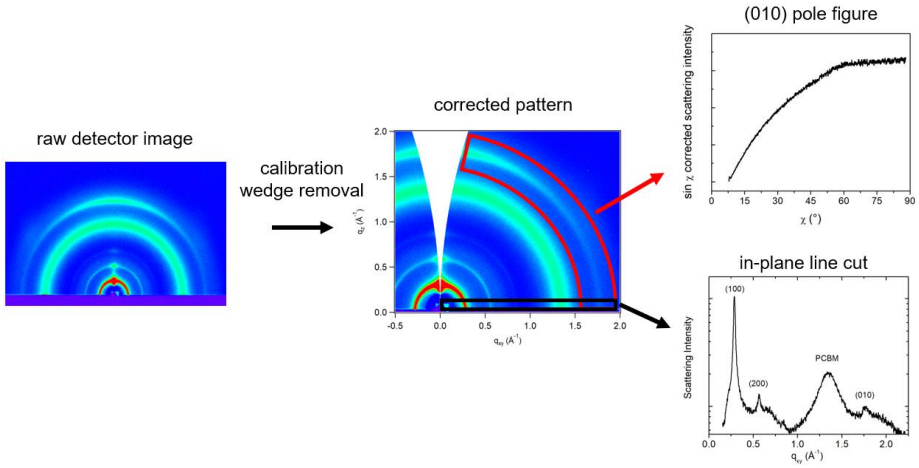

Figure 2-4 – Typical GIWAXS data processing workflow for a blend film of PffBT4T$_{80}$-co-3T$_{20}$-2OD:PC$_{71}$BM. The raw detector image is calibrated with a known standard, and the missing wedge is removed. Two common data reduction methods are shown: (1, red) taking a specific peak and measuring the angle dependence to generate a pole figure, or (2, black) monitoring the scattering intensity in a single direction as a function of q to generate a line cut.

Once scattering reflection patterns are collected, a series of data workup steps are typically done in order to process the data and ease interpretation. A representation of this process is shown in Figure 2-4, for a blend film used in chapter 4, of PffBT4T$_{80}$-co-3T$_{20}$-2OD:PC$_{71}$BM. The position of scattering peaks on the detector is dependent on the sample to detector distance and the beam energy, which are both adjustable. Therefore, once these two variables are fixed for a particular run, GIWAXS scattering experiments begin with the measurement of a known calibrant, typically lanthanum hexaboride (LaB_6) or silver behenate. Both materials are highly crystalline with known diffraction peaks, and the resulting scattering pattern can used to map detector pixels to q values. This process, which is called calibration, also typically removes a wedge in the region around q_z (i.e. $q_{xy} \approx 0$ $Å^{-1}$) and slightly adjusts peak positions as a function of χ, the polar angle. This latter correction takes into account the curvature of the Ewald sphere, which is a geometric

correction that links together the wavevector of the incident and diffracted rays, the diffraction angle for a given reflection (q) and the reciprocal lattice of the crystal (peaks measured on the detector).[129] Essentially, the constructive interference from a particular elastic scattering feature occurs around the surface of a sphere, and since we are mapping the constructive interference with a planar detector, a correction needs to be made. For the organic films we are working with the X-ray scattering pattern is generally symmetric across the q_z axis due to a lack of in-plane alignment. For this reason, processed data generally only features approximately one quadrant, as shown in the corrected pattern and the data selected for reduction. The intensity is scaled to film thickness to make general comparisons across data sets, but quantitative data comparisons are done with reduced data sets.

The two most common ways to reduce GIWAXS patterns into 1-dimensional graphs are shown on the right side of Figure 2-4, with a pole figure (top) and a line cut (bottom). For a line cut, a linear sector is generally taken in either the in-plane or out-of-plane direction. The data used to create an in-plane line cut is shown in the black box. It is important to note the non-zero width of the box in the vertical direction: this box should be large enough to average out any background noise, but not so high that the peak begins to curve away from the initial peak position at $q_z = 0$ Å^{-1}, and not so low that the extra intensity from the Yoneda peak is included in the average. The same box dimensions should be used for all data that is to be directly compared, data should be normalized to film thickness, and the data is generally plotted on a logarithmic scale to ease comparison of the strongly scattering (100) lamellar stacking compared to other weaker scattering features. For the in-plane line cut shown here, the (100), (200), and (010) scattering features are clearly seen

for the polymer, along with a broad peak at $q \approx 1.3$ $Å^{-1}$ which corresponds to isotropic PCBM aggregation.

In order to quantitatively understand the crystalline film texture, a pole figure is generated. A pole figure describes the orientation distribution of the diffracted intensity of a chosen diffraction peak as a function of angle. This is shown in the red box in Figure 2-4, where a q-range is chosen to capture a specific diffraction peak, and the intensity within that q-range is recorded as a function of χ , the polar angle. Due to distortion of the Ewald sphere, crystals oriented perfectly normal to the substrate ($\chi = 0°$) are not observed for this experiment (i.e. the missing wedge), and due to the scattering enhancement from the Yoneda peak, crystals oriented perfectly in-plane (χ = +/- 90°) are also not recorded.[130] Therefore, pole figures are presented as a subset of the full quadrant, here shown from ~ 7° to ~ 88°. An additional correction to compensate for the instrumentation geometry is the inclusion of the sin χ term, where the pole figure is plotted as the product of intensity and sin χ vs. χ .[131] This data can be used to understand the relative orientation of the crystallites as well as the relative degree of crystallinity for the film.

The relative degree of crystallinity (rDoC) describes the degree of crystallinity of one film compared to another film of the same material. Comparing different materials' crystallinity with this technique is non-trivial and would involve reference samples of completely amorphous and completely crystalline material, and it is essentially impossible to achieve the latter with semi-crystalline semiconducting polymers. Different processing conditions can greatly affect the film crystallinity of the same material, so being able to quantitatively classify the rDoC is crucial in understanding solid state performance. As with line-cuts, data should be normalized to the volume of material illuminated by the

incident X-ray, which is proportional to film thickness for samples that have the same in-plane area. The degree of crystallinity is calculated via the following linear integral:

$$DoC \propto \int_0^{\pi/2} \sin(\chi)\, \mathrm{I}(\chi)\, \mathrm{d}\chi \tag{2-1}$$

As we have plotted the pole figure above as I • sin χ vs. χ, the relative degree of crystallinity is simply the normalized area under the curve.

The average orientation of a lattice plane is represented by a molecular orientation parameter, $f_\perp$, which is the orientation of the lattice plane relative to the substrate normal. The Herman orientation parameter, S, is a convenient formalism for representing orientation with a single number. S is a number from -0.5 to 1.0, where -0.5 represents the case of all lattice planes being oriented perpendicular to the substrate normal and 1.0 represents the case of all lattice planes being oriented parallel to the substrate. For (010) lamellar stacking, which we are measuring here, S = -0.5 is completely edge-on and S = 1.0 is completely face-on with respect to the substrate.[132]

$$f_\perp = \frac{\int_0^{\pi/2} \cos^2(\chi) \sin(\chi)\, \mathrm{I}(\chi)\, \mathrm{d}\chi}{\int_0^{\pi/2} \sin(\chi)\, \mathrm{I}(\chi)\, \mathrm{d}\chi} \tag{2-2}$$

$$\mathrm{S} = \frac{1}{2}\,(3\, f_\perp - 1) \tag{2-3}$$

Static GIWAXS measurements featured in this dissertation were conducted at Stanford Synchrotron Radiation Laboratory (SSRL) and Brookhaven National Laboratory (BNL). GIWAXS at SSRL was measured at beamline 11-3 in a helium-filled chamber with

an X-ray wavelength of 0.976 Å and sample to detector distance of 250 mm at an incident angle of 0.13°. Spectra were recorded on a Rayonix MARCCD area detector. GIWAXS at BNL was collected at NSLS-II, 11-BM Complex Materials Scatting beamline, in a sample chamber under vacuum, with scattering from a 13.5 keV beam collected on an area detector. In both cases, data were processed using the Nika software package for Wavemetrics Igor, in combination with WAXStools.[66,133]

2.3.7 Grazing incidence small angle X-ray scattering (GISAXS)

While GIWAXS is used to measure molecular packing on length scales from 0.2 nm – 2.0 nm, grazing incidence small angle X-ray scattering (GISAXS) is used to measure domain and phase behavior on length scales from nominally 10 nm – 100 nm. With a similar X-ray energy used compared to GIWAXS, the detector is moved further away from the sample and thus smaller scattering angles are recorded. Because scattering is a reciprocal space technique, moving to smaller angles in real space correlates to measurement of larger features in reciprocal space. In contrast to GIWAXS, this technique does not require materials to be crystalline; signal is derived from differences in electron density between phases of two different materials. Therefore, it is very useful for measuring polymer:fullerene blends, but not typically used for pristine polymer films. The GISAXS intensity as a function of q contains information about the size, distance, and nature of the interfaces of two phases in a BHJ blend film.

Compared to GIWAXS, which uses a sample-to-detector distance of around 250 mm to measure a q-range between 0.2 $Å^{-1}$ and 3.0 $Å^{-1}$, GISAXS measurements for this

dissertation were generally done at a sample-to-detector distance of around 3.0 m, which provides a q-range between 0.004 $Å^{-1}$ and 0.2 $Å^{-1}$. Those q-values correspond to real space distances of 157 nm and 3.1 nm respectively. Therefore, due to typical experimental limitations, domain sizes of larger that 157 nm cannot be accurately measured. Additionally, the SAXS signal typically drops off before the high q cut-off, thus giving a minimum measurable domain size of around 10 nm.

For this work, GISAXS data is again collected with a 2D detector, with a representative sample shown below in Figure 2-5. This data is reproduced from chapter 3, and demonstrates the effect of cosolvent addition on the resultant domain size of a polymer:fullerene blend film. Again, as with GIWAXS, we operate above the critical angle of the blend materials in order to probe the entire depth of the film. The Yoneda peak is the enhanced signal at $q_z \sim 0$ $Å^{-1}$, and we assume that it is a good proxy for q_{xy}.[134] As a result, the GISAXS experiment for our purposes exclusively measures in-plane phase behavior, since the thin film and overall weak SLD of organics gives very weak scattering signal in the vertical direction.

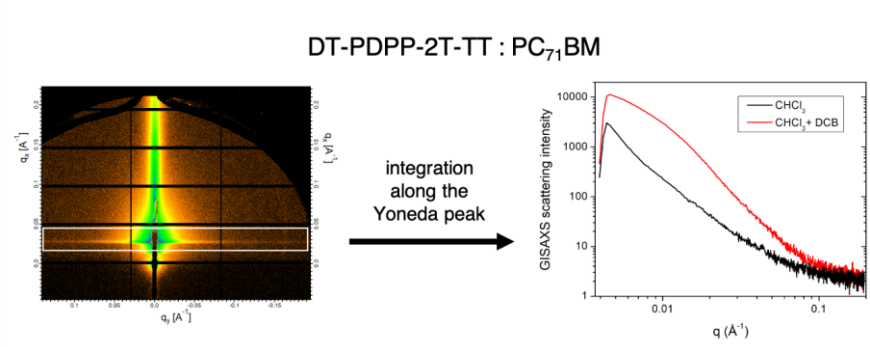

Figure 2-5 – GISAXS data reduction of a blend of DT-PDPP2T-TT:$PC_{71}BM$, taken from chapter 3. Integration along the Yoneda peak (white box) gives an intensity vs. q plot. Use of DCB as a cosolvent drastically increases small length-scale

populations compared to the $CHCl_3$ only cast film, indicating a reduction in domain size for the blend film.

Due to the complex nature of the BHJ and the variety of domain sizes, length scales, and interfaces that are present in the blend film, interpretation and analysis of GISAXS data is nontrivial. Because the single curve is representative of an average of all the features in the film, the complexities of the BHJ are lost. However, relative comparisons among materials can often be made. For example, the GISAXS plot on the right side of Figure 2-5 shows a comparison of scattering profiles between at blend of DT-PDPP2T-TT:$PC_{71}BM$ cast from a single solvent or a cosolvent system. One notable feature to look out for is the "knee" that defines the characteristic length scale of the system. For the red curve representative of the cosolvent cast film, this occurs around q = 0.01 $Å^{-1}$, corresponding to a length scale of around 60 nm. On the other hand, for the black curve from the single solvent system, only the beginning of the slight onset of this knee is apparent at the lowest q and we have actually missed much of the scattering from the domains due to the beam-stop at very low q. Therefore, the characteristic length scale is larger than the limit of this experiment, which is at q = 0.004 $Å^{-1}$ equivalent to the real space length scale of 157 nm. This increase in domain size to a length well past the exciton diffusion length explains the drastic drop in photovoltaic power conversion efficiency when cosolvent is not used.

2.4 In situ thin film monitoring techniques

As mentioned in the Introduction, the final morphology of the active layer is strongly dependent on the drying process. Therefore, following the film solidification process in real time is crucial in understanding what processing variables contribute to morphology changes, and the mechanism by which the morphology changes occur. The real time

measurements used in this dissertation are UV/visible absorption spectroscopy, white light interferometry, GIWAXS, and GISAXS. These techniques are made available by way of a custom-built blade coater initially designed by Stafford et al.[135] at the National Institute of Standards and Technology. The blade coater is modular, features a heated stage, can accommodate spectroscopic analysis, and can be moved to a beamline for in situ X-ray scattering measurements. A simplified schematic of this blade coater is shown in Figure 2-6, where real-time reflectometry and GIWAXS data are simultaneously being collected on a drying film that was just coated.

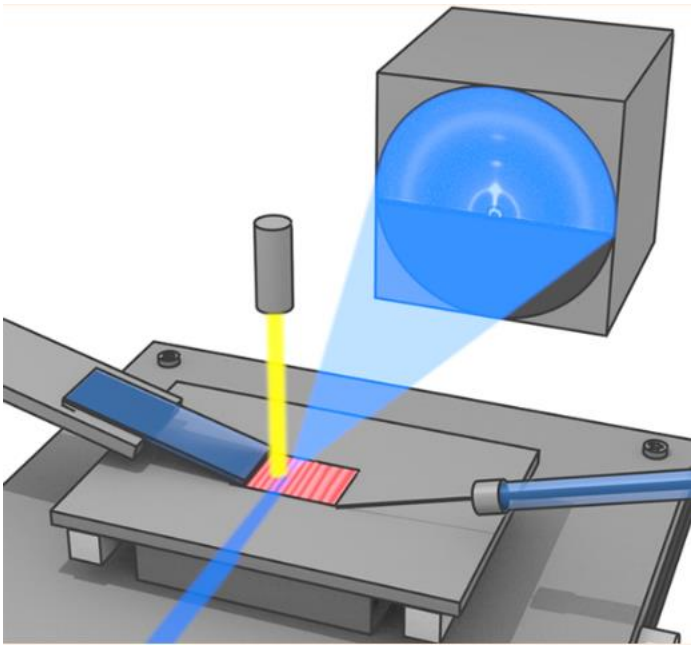

Figure 2-6 – Schematic of the blade coating process with in situ measurement of optical reflectometry (yellow beam) for film thickness and GIWAXS (blue beam) for crystallinity. Reproduced from Richter et al.[101]

2.4.1 UV/vis absorption spectroscopy

For real time UV/vis absorption spectroscopy during blade coating, an Ocean Optics fiber spectrometer using an HL-2000 series tungsten halogen light source was used. This

technique is used to monitor drastic polymer conformational changes during the drying process that result in significant changes in the UV/vis absorption spectra of the wet film. This light source was directed to the blade coater substrate with a fiber optic cable and a collimating lens, and the light transmitted through the film passed through a hole machined through the center of the blade coating stage. This transmitted light was then collected by another fiber optic cable and collimating lens and was then directed into the spectrometer. Spectra were generally collected at the fastest scan rate available, which was ~ 30 ms. The optics through the film were aligned at a nominally 45° angle relative to the substrate normal in order to reduce any reflection.

2.4.2 White light interference

In order to measure film thickness as a function of time during coating, white light interference, aka optical reflectometry, was used. A coaxial fiber optic reflection probe (Ocean Optics R200-7-UV-VIS) was used to simultaneously illuminate the sample with the same light source as above and collect the resulting reflection spectra. In general, reflected light from a thinning solution will constructively and destructively interfere at a single wavelength when the wet film thickness is a multiple of that wavelength. Therefore, with a known final film thickness measured via profilometry, the resultant film thickness over time can be back calculated and estimated via a peak counting method.

However, in reality, the reflected light spectrum is a convolution of the absorption of the film and the broadband interference between the incident and reflected beams as a function of layer thickness and the refractive index of the materials. Therefore, ellipsometry of the dry films must be performed and the subsequent time dependent

reflection data modeled. For the work presented in this dissertation, the real time data was processed with custom code written by Sebastian Engmann and further analyzed with commercial ellipsometry code.[76,101]

2.4.3 X-ray scattering techniques

Both in situ GIWAXS and GISAXS were collected in order to understand how crystallization and domain formation occurs during the coating process. The custom NIST designed blade coater was brought to either ALS or BNL for the measurement. Since the X-ray hutch needs to be void of people during the measurement for safety, the entire coating process must be automated. A glass syringe is loaded with solution and mounted above the blade coater, with a thermocouple jacket that can be used to heat the solution. The syringe plunger is attached to a motor that is controlled remotely. When the X-ray hutch is cleared and ready, data collection for reflectometry and X-ray scattering were started simultaneously. The solution is dispensed in the gap to form a meniscus, and the blade is translated across the substrate to coat the film.

Multiple 2D X-ray patterns were taken during the coating process and worked up into forms that are more easily interpretable. Code written by Sebastian Engmann was used to take a series of 2D patterns and reduce them into a variety of forms. For GIWAXS: A 2D plot of a pole figure over time, which can be reduced into a 1D plot of the rDoC over time; or a 2D plot of a particular line cut over time, which can be reduced into a single peak position's evolution in intensity over time.[76,134] For GISAXS the intensity of the Yoneda peak over the measured q-range can be integrated to calculate a relative domain purity over time.

2.5 Device fabrication and measurement

Complete device fabrication and measurement is a multi-step process; each step must be performed consistently well in order to isolate the effect of whatever variable is to be modified in a series. This chapter describes in detail the typical series of steps for photovoltaic device fabrication, and briefly discusses the construction and measurement of single carrier devices to estimate charge mobilities.

2.5.1 Inverted device fabrication

As mentioned in the introduction, the conventional device architecture typically featuring PEDOT:PSS as the bottom hole-transporting layer and calcium metal or LiF as the top electron-transporting layer has a few drawbacks. As a result, this architecture was not used in the work featured in this dissertation, and instead, inverted devices were built exclusively. Patterned indium tin oxide (tin-doped indium oxide, ITO) on 25 mm square glass slides were purchased from Latech Scientific Supply. Before use, the edges of the ITO/glass substrates were sanded with fine grit sandpaper to smooth them. The ITO/glass substrates were scrubbed with a solution of sodium dodecyl sulfate in distilled water using a Kimwipe. The ITO/glass substrates were placed in a custom Teflon slide holder and sonicated (Branson 2510 Ultrasonic Cleaner) in the same solution for 10 minutes. The solution was dumped out and the slides were rinsed with several washes of fresh distilled water. The slides were then sonicated in distilled water for 10 minutes, the water was

dumped out, and the beaker was filled with isopropyl alcohol (IPA) for 10 minutes. At this point, slides could be held overnight in IPA, but were typically used immediately. The ITO slides were blown dry with argon gas and placed into a UV-ozone cleaner (Novascan PSD Pro Series Digital UV-ozone cleaner) for 10 minutes.

Zinc oxide (ZnO) films were spun coat onto the cleaned substrates from a pre-prepared precursor solution. The ZnO solution was made with 0.11 mol L^{-1} Zn acetate dihydrate and 0.11 mol L^{-1} ethanolamine combined in 2-methoxyethanol (all materials purchased from Sigma Aldrich). This solution was stirred overnight at room temperature, then filtered with a 0.45 μm PTFE syringe filter before use. The ZnO solution was deposited on the cleaned ITO substrates by spin-coating (Laurell WS-650MZ-23NPP) for 30 seconds at 4000 rpm in ambient atmosphere to get a layer thickness of ~30 nm. After spin-coating, the ZnO layer was annealed in air at 150 ˚C for 10 min followed by slow cooling to room temperature for another 10 minutes.

The active layer was deposited within 1 hour of ZnO substrate fabrication, either via spin coating (in an argon glovebox, MBRAUN) or blade coating (ambient air, custom design). For spin coating, the spin acceleration and speed can be varied to tune film properties like thickness. For blade coating, the blade speed, blade-substrate gap, and substrate temperature can be varied. The coated active layers were brought into the evaporator chamber side of the MBRAUN argon glovebox. If the films were made with a high-boiling point solvent additive, the films were brought into the vacuum chamber of a thermal evaporator and left undisturbed (i.e. the films were not placed on top of an evaporation shadow mask). The chamber was evacuated for ~ 45 minutes and reached a vacuum level of ~ 10^{-5} mbar. This served to remove the high boiling point solvent without

disturbing the still-wet film. After refilling the chamber, the substrates were then placed upside down in a slide holder on top of a shadow mask, and the vacuum chamber was again evacuated. The top electrodes MoO_3 and Ag were deposited by vacuum deposition with layer thicknesses of 15 nm and 160 nm, respectively, to obtain complete solar cell devices with an electrode overlap area of 0.07 cm^2. Fast drying Ag paint (Ted Pella, 16040-30) was applied to the ITO electrodes to improve contact with the device switchbox.

2.5.2 Photovoltaic characterization via solar simulator

An aperture with area 0.049 cm^2 was aligned with the electrode overlap area to ensure accurate measurement of the active area. The *J-V* (current density vs. voltage) characteristics of all photovoltaic devices were evaluated under simulated AM 1.5G solar illumination (100 mW cm^{-2}) using a Keithley SMU 2410 with a Newport Oriel 94021A solar simulator calibrated with a reference silicon solar cell (Newport 91150V). The output light spectrum was evaluated with an Ocean Optics fiber spectrophotometer in order to confirm an appropriate spectral match.

2.5.3 Incident photon to charge carrier efficiency (IPCE)

In order to measure photocurrent as a function of wavelength, incident photon to charge carrier efficiency (IPCE), also known as external quantum efficiency (EQE), was used. The EQE is the ratio of the number of charge carriers collected by the solar cell to the number of incident photons. This can be broken down further into internal quantum efficiency (IQE), which is the ratio of the number of charge carriers collected by the solar cell to the number of incident photons *that are absorbed* by the solar cell. Therefore, IQE is a measurement of both electrical efficiency as well as light that is absorbed rather than

reflected or scattered. In general, EQE is more often reported in the literature and is a greater measure of overall performance, since it can be used to directly calculate J_{SC} an important device metric. As a result, IQE will not be discussed further here.

Optical alignment and calibration are essential for the generation of accurate and reproducible data. A schematic of the Newport QE-PV-SI, used for the EQE measurements presented in this dissertation, is shown below in Figure 2-7. In brief, a broadband xenon arc lamp is directed in a monochromator, the output power is measured with a calibrated reference photodiode as the monochromator is scanned, and this result is then compared to the solar cell to be tested, outputting EQE as a function of wavelength. Because this system is modular and tunable, it is important to know the alignment and calibration procedure. To align, first, the monochromator cover should be removed, and the condenser lens defocused, to create an image of the lamp on the second mirror in the monochromator. The arc lamp housing has two sets of screws: one set to adjust the position of the lamp (shown in the diagram), and another set to adjust the lamp reflector (not shown in the diagram). Since the bulb emits relatively isotropically, the reflector is used to drastically increase the signal in a single direction for the measurement. These screws are used to center the image of the arc and its reflection on that second monochromator mirror. Once the images are aligned, the condenser lens is adjusted until a uniform beam spot, encompassing most of the mirror, is formed. Before the light enters the monochromator, it passes through a filter wheel which is used to block out second-harmonic generated light, a chopper connected to the lock-in-amplifier to reduce measurement noise, and an input slit which is used to decrease the bandwidth and improve resolution. Broadband white light enters the monochromator, and monochromatic light exits through a slit that should be set to the same

width as the input slit (generally 50 µm, but this can be increased if additional signal is needed, at the expense of reduced optical resolution).

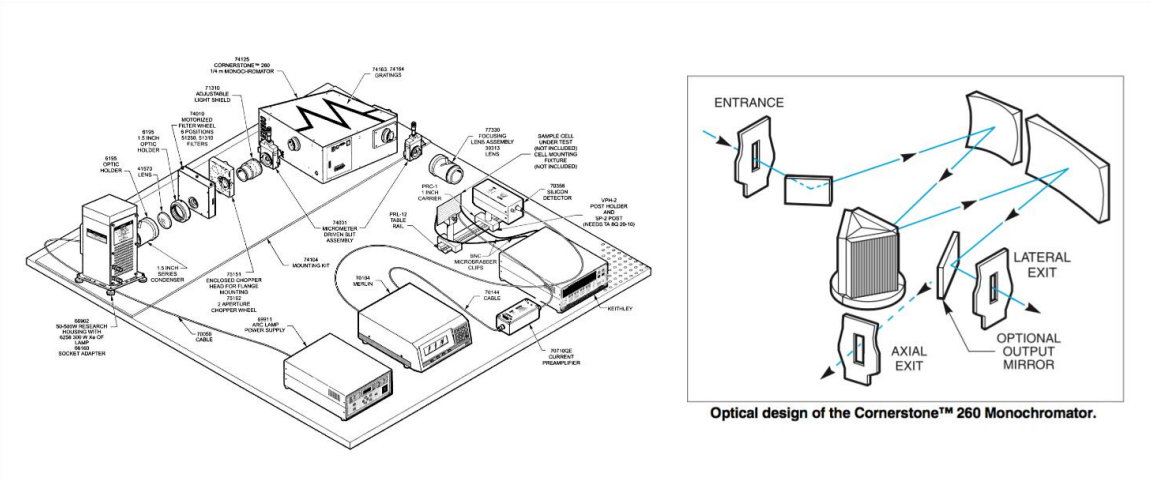

Figure 2-7 – Exploded schematic of external quantum efficiency setup (Newport QE-PV-SI) along with an internal diagram of the monochromator. Taken from newport.com.

This output light is first measured with a calibrated reference silicon photodetector of known responsivity, connected to the same lock-in-amplifier. This process corrects for variance in alignment and changes in lamp output intensity and should be done before every series of measurements (i.e. each time the equipment is turned on). Ideally, the spot coming out of the monochromator will underfill the device as well as the reference detector, but in our case one dimension of the spot is a bit longer than the device. Therefore, for both the reference measurement and the device measurement, the same aperture for solar simulated performance is used. The device is measured in short circuit condition, where V = 0 and maximum current is measured. Finally, the EQE of another known solar cell should be tested. In our case, we use the same model of silicon solar cell as used for solar simulator calibration (Newport 91150V), with a known, calibrated EQE dataset from the company.

This can help isolate changes in various system components over time. For example, the recommended recalibration service for the reference detector is expensive and often; internal calibration using tools available within the lab can extend the window in which reliable data can be collected. Finally, the resultant EQE spectra should be integrated across the AM1.5G solar spectrum to give the short circuit current density, which should be no more than 10% different than the J_{SC} measured from the solar simulator experiment.[136]

2.5.4 Space-charge-limited current (SCLC) device fabrication and measurement

In order to understand how individual charge mobilities are affected by various processing conditions, space-charge limited current (SCLC) devices were fabricated and measured. Changes in material properties as well as morphology will often change the efficiency at which free charges may be transported through the bulk of a film. Charge mobilities can be isolated for a specific charge carrier (electron vs. hole) via selection of appropriate work functions. In comparison to an organic solar cell, which features an active layer stacked between an electron transport layer and a hole transporting layer, an SCLC device will feature the same layers on top and bottom of the stack. For hole-only devices, feature in this dissertation, the active layer was sandwiched with molybdenum oxide layers on either side. To prove the interaction of the polymer with the acceptor, SCLC devices were typically made with blend films.

Hole-only devices were built with ITO substrates cleaned as described above in the inverted device fabrication section. After UV/ozone treatment, the ITO slides were brought into the thermal evaporator, where 15 nm of MoO_x was deposited without a shadow mask. Active layer films were deposited via spin coating or blade coating, and once dried were

brought into the evaporator again for sequential deposition of 15 nm MoO_x and 160 nm silver with a shadow mask. Fast drying Ag paint (Ted Pella, 16040-30) was applied to the ITO electrodes to improve contact with the device switchbox. Devices were broken in via sequential scans of 0.01 V to 3.00 V, 0.01 V to 5.00 V, and finally 0.01 V to 7.00 V with a Keithley 2410 SMU. This procedure helped to prevent device breakdown at higher voltages. The use of thicker films, those greater than 200 nm, also support higher currents. The resulting J-V curves were modeled with a modified Child's law, shown below, via the fitting function in OriginPro from OriginLab.

At low voltages, the number of charge carriers in the device does not change in the internal electric field, and current linearly follows Ohm's law. As voltage increases, so does charge carrier concentration, which forms a space-charge region that limits the output current with the applied voltage and current scales with the voltage squared.[137–139] The current density, J, in the space-charge-limited current regime can be described by Child's law:

$$J = \frac{9}{8}\,\varepsilon_r\,\varepsilon_0\,\mu\,\frac{V^2}{L^3} \tag{2-4}$$

In this equation, ε_r is the dielectric constant of the material and assumed to be 4,[140] ε_0 is the vacuum permittivity ($8.854 \bullet 10^{-12}$ F m^{-1}), μ is the charge carrier mobility, V is the effective voltage, and L is the active layer film thickness. Because transport in disordered organic materials is generally limited by energetic traps that are field dependent, the measured mobility needs to take into account the applied electric field via the following equation:

$$\mu = \mu_0 \, e^{(0.891 \, \gamma \sqrt{E})} \tag{2-5}$$

Where μ_0 is the zero-field mobility, γ is the field dependence parameter, and E is the electric field.

These equations are combined and fit to the experimentally measured J-V curves, generally in the range of 2 V – 7 V. The SCLC regime will generally be seen in this region, where J is proportional to V^2, as per equation 2-4. The electric field is assumed to be the applied voltage. The field dependence parameter, γ, is allowed to vary to improve the fit, and is around 10^{-4} for blends with a strong field dependence and closes to 0 for systems with minimal traps that are field independent ($e^0 = 1$, so $\mu = \mu_0$).

CHAPTER 3. CO-SOLVENT EFFECTS WHEN BLADE COATING A LOW-SOLUBILITY CONJUGATED POLYMER

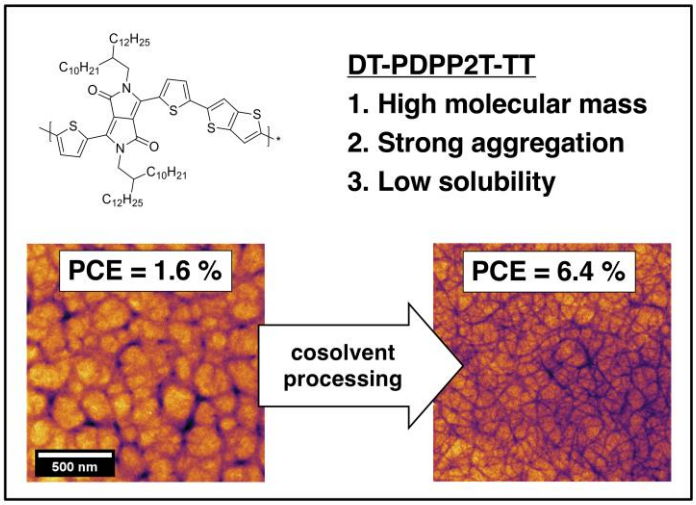

The work presented in this chapter was a combined effort with great help from my coauthors: Dr. Jeff L. Hernandez, Dr. Sebastian Engmann, Dr. Andrew A. Herzing, and Dr. Lee J. Richter. Jeff began this project by traveling to the National Institute of Standards and Technology (NIST) to collaborate with Sebastian, Andrew, and Lee. Through this collaboration, Jeff brought the technology of the NIST custom built blade coater to the Reynolds Group, as well as the use of real time characterization methods for in situ film monitoring. This blade coater was used for this project and the two others in this dissertation, and the NIST networking connection allowed for my participation in similar in situ film monitoring studies presented in Chapter 4. Sebastian wrote and provided assistance with the computer code used to process the real time data, Andrew collected the STEM images (shown above), and Lee was the primary investigator on the NIST side of

the project. My contribution to this project was to expand the scope of the device and solid-state morphology sections, as well as generate the manuscript.

This project explores the characterization and application of a low solubility polymer, DT-PDPP2T-TT, which was chosen for study due to its ability to work well in thick film solar cells. When processing a blend of this polymer and $PC_{71}BM$, device performance was strongly dependent on the introduction of either *o*-dichlorobenzene (DCB), 1,8-diiodooctane (DIO), or diphenyl ether (DPE) co-solvent into the chloroform ($CHCl_3$) solution, which were all shown to drastically improve the morphology. To understand the origin of these morphological changes as a result of the addition of the co-solvent, in-situ studies with grazing incidence X-ray scattering and optical reflection interferometry were performed. Use of any of the co-solvents decreases domain size relative to the single solvent system and moved the drying mechanism away from what is likely liquid-liquid phase separation toward a nucleation and growth process. Comparing the $CHCl_3$ + DCB cast films to the $CHCl_3$ only cast films, we observed both the formation of small domains and an increase in crystallinity during the evaporation of DCB, due to a high nucleation rate from super-saturation. This resulted in percolated bulk-heterojunction networks that performed similarly well with a wide range of film thicknesses from 180 nm to 440 nm, making this system amenable to continuous roll-to-roll processing methods.

This chapter has been adapted from a manuscript entitled “Co-solvent effects when blade coating a low-solubility conjugated polymer for bulk-heterojunction organic photovoltaics”, which was submitted to ACS Applied Materials & Interfaces on March 3, 2020.

3.1 Background and motivation

3.1.1 Thick film solar cells and diketopyrrolopyrrole

There is great fundamental and practical research interest in generating thick film solar cells for compatibility with roll-to-roll processing techniques. While optimized active layer thicknesses for fullerene-based OPV devices are often around 100 nm to 150 nm, there are several advantages to developing devices that function with thicker active layers. Thick film solar cells benefit from enhanced light absorption, likely increasing short circuit current densities, and ease of processing via roll-to-roll coating methods, due to the minimization of pinhole defects that arise from thickness inhomogeneities.[141] The diketopyrrolopyrrole-thiophene based polymer DT-PDPP2T-TT (2-decyltetradecyl diketopyrrolopyrrole 2,5-di-2-thienylthieno[3,2-b]thiophene, see Fig. 1a) has been shown to perform well as the donor phase material in solar cells with active layers deposited via spin coating to thicknesses over 200 nm, which we will refer to here as 'thick films',[142–144] when paired with [6,6]-phenyl-C_{71}-butyric acid methyl ester, $PC_{71}BM$. The ability to maintain a high fill factor in thick films reflects the interplay of bimolecular recombination and carrier extraction that arise from the phase separation morphology and carrier mobility.[145] The DPP acceptor moiety is the basis for many polymers with high hole mobilities.[146] DT-PDPP2T-TT in particular, along with many similar DPP-thiophene based polymers, has been shown to form an interconnected fibrillar network when cast into a thin film. That property, coupled with its high charge carrier mobility, leads to reduced bimolecular recombination allowing for high-performing thick-film solar cells.[147] This is also a result of the strong electron withdrawing nature of the DPP moiety and its high polarity, which enhances the tendency of this polymer to aggregate and crystallize.[148]

There exists already a body of work that describes the co-solvent dependent behavior of DT-PDPP2T-TT and similar DPP-thiophene based polymers.[142,144] Multiple solvents (chloroform, $CHCl_3$, and chlorobenzene, CB) and additives (dichlorobenzene, DCB, diphenylether, DPE, 1,8-diiodooctane, DIO, etc.) have been studied. In all cases, when additives are used, current and fill factors increase drastically due to improved active layer morphology. The use of co-solvents or solvent additives to modulate blend morphology is ubiquitous in the field of OPV.[149,150] Using a co-solvent mixture for morphology enhancement was reported by Zhang et al., where coarse phase separation of MDMO-PPV:$PC_{61}BM$ was refined when a small amount of CB was added to the chloroform host solvent.[151] The use of CB to improve morphology originated from single solvent processing of the same blend of MDMO-PPV:$PC_{61}BM$ blend, where performance was enhanced when switching the casting solvent from toluene to CB.[152] The development of the final morphology in solution processed OPV arises from the specific nature of the phase separation: liquid-liquid vs. liquid-solid, the kinetics of that phase separation: nucleation and growth vs. spinodal decomposition, and the external time scales determined by solvent evaporation rate and possible vitrification of the film.

3.1.2 Blade coating and scalable processing

The previously reported cases of DT-PDPP2T-TT based solar cells were deposited via spin coating and were built into a conventional device architecture.[142,144] While highly reproducible, spin coating is a poor model for scalable, large area deposition schemes such as spray- or slot-die coating. We seek to explore scalable processes, where the dynamics associated with coating a small laboratory-scale film and a large industrial scale-film do not significantly change.[153] For this study, we employ blade coating, an established model

for slot-die coating.[105] Additionally, with blade coating, thick films may easily be generated with negligible material waste and, unlike spin coating, the stationary nature of the substrate facilitates the in situ spectroscopic analysis carried out in this work and allows for better control of heat and airflow during the coating process. To further expand this study's applicability toward scalable processability, we have built inverted devices with the active layer deposited in ambient conditions. Inverted devices are typically more stable due to the omission of two problematic materials generally found in conventional devices: PEDOT:PSS as a hole transport layer, which is acidic and can degrade the indium-tin-oxide transparent conductor, and low work function electron transport layers, such as calcium metal, which are unstable to ambient air.[154] Here, we report average power conversion efficiencies of ≈ 6.5 % with three different solvent additives, which is comparable to results from previously reported conventional devices built via spin coating,[144] demonstrating this system's flexibility among a variety of device processing methods. Monitoring the drying dynamics of these OPV systems is of great interest due to the extent that the final film morphology is established during the coating process and is directed by the properties of the coating solution.[101,155,156] In this study, we address the dynamics of the solidification and drying process for this blend system for a processing method with tightly controlled experimental parameters that is comparable to other continuous coating methods.

3.2 Results and discussion

3.2.1 Photovoltaic performance

In order to confirm the efficacy of this polymer:fullerene blend system for photovoltaic applications, inverted solar cells were fabricated and characterized. Films

were blade coated in ambient air onto room temperature substrates and were immediately moved into a thermal evaporator vacuum chamber in an argon filled glove box. This ensured that all co-solvent cast films were dried at a high rate, set by evaporation kinetics. Solutions were stirred for 12 hours at 50 °C and then allowed to cool to room temperature. Device parameters are shown in Table 3-1 along with active layer film thicknesses, and boiling point and vapor pressures of the solvents used in this study. Overall, a significant enhancement of power conversion efficiency from 1.6 % to over 6.0 % was seen with the use of all three co-solvents, namely from the increase in short circuit current density (J_{SC}) and fill factor (FF). Champion current-density-voltage (J-V) curves and external quantum efficiency (EQE) data are shown in Supporting Figure 3-1. The increase in J_{SC} is associated with a dramatic change in the EQE response in the region of polymer absoption. These results suggest a drastic change in active layer morphology, to one in which excitons are more likely to reach a donor-acceptor phase interface and contribute to device photocurrent, rather than recombine in a large polymer domain. In general, the performance of the blade-coated, inverted devices is similar to that reported for spun-coated, conventional devices[143,144] suggesting that DT-PDPP2T-TT devices should scale well. In order to determine the origin of the co-solvent induced improvements in performance, we have performed detailed morphological characterization of the active layer and real-time studies of its development during deposition. Due to the comparable performance of this system with three different additives, we focus only on *o*-dichlorobenzene for more detailed processing and morphological characterization. Due to the comparable performance and similar final film morphologies of this system with three different additives as shown with grazing incidence wide-angle X-ray scattering (GIWAXS), atomic

force microscopy (AFM) and hyperspectral microscopy (vide infra), we focus only on *o*-dichlorobenzene for more detailed processing and morphological characterization.

Table 3-1 – Photovoltaic results from inverted devices with active layers cast from the various solvent systems. [a]Values were averaged over 8 devices and error bars indicate one standard deviation of the mean. Active layer thicknesses are reported. Device architecture: Glass/ITO/ZnO/active layer/MoO_x/Ag. Active area = 0.049 cm^2 defined with an aperture. [b]Solvent properties are included for reference, for $CHCl_3$ and each co-solvent (data taken from Sigma Aldrich).

Solvent system	J_{SC} (mA cm^{-2})	V_{OC} (V)	FF (%)	PCE (%)[a]	Film thickness (nm)	Boiling point of solvent (°C)[b]	Vapor pressure of solvent (kPa)[b]
$CHCl_3$	4.3 ± 0.4	0.69 ± 0.01	55 ± 3	1.6 ± 0.1	150 ± 5	61	21.2
+ DCB	13.4 ± 1.3	0.67 ± 0.01	70 ± 1	6.4 ± 0.6	210 ± 4	180	0.181
+ DIO	13.8 ± 1.0	0.67 ± 0.01	67 ± 3	6.1 ± 0.4	202 ± 8	258	2.67×10^{-3}
+ DPE	16.0 ± 0.5	0.66 ± 0.01	64 ± 4	6.7 ± 0.2	180 ± 4	168	3.07×10^{-5}

3.2.2 Thick film photovoltaic performance

To further explore the efficacy of this blend system for potential application, thick film active layers were used in device construction. Due to the gel-like nature of the blend solution attributed to the polymer's low solubility, thicker films are easily made with this material simply by coating the same solution formulation at a higher blade speed, since we are operating in the Landau-Levich drying regime as discussed in Chapter 2.[135] By increasing the blade coating speed from 20 mm s^{-1} to 40 mm s^{-1}, the active layer thickness of the + DPE film, which was the highest performing in our initial testing, was varied from 180 nm to 440 nm. Even at this remarkably high film thickness, overall power conversion efficiencies were maintained, as shown in Supporting Figure 3-2 and Supporting Table 3-1.

As film thickness increases, the average J_{SC} increases from 16.0 mA cm^{-2} to 17.7 mA cm^{-2} at the expense of the fill factor, which decreases from 64 % to 53 %. This increase in current and decrease in fill factor as a result of increasing film thickness is ubiquitous in the OPV field. Even with the 440 nm thick film, there is still some transparency in the visible region between 550 nm and 700 nm owing to the large disparity in optical band gaps between the polymer and $PC_{71}BM$, as seen in Supporting Figure 3-2b. This provides some motivation for application of this system for thick-film OPV devices that are semi-transparent.

3.2.3 Polymer properties

The repeat unit structure of DT-PDPP2T-TT is shown in Figure 3-1, along with its temperature- and solvent-dependent ultraviolet-visible (UV/vis) spectroscopic properties. The polymer was shown to be analytically pure (see elemental analysis in Supporting Table 3-2), and was characterized with gel permeation chromatography in 1,2,4-trichlorobenzene at 160 °C (Supporting Figure 3-3 and Supporting Table 3-3), yielding a distinct bimodal molar mass distribution with number average molar masses of 49 kg/mol and 348 kg/mol, with dispersities for each component of 1.6 to 1.7, suggesting possible aggregation. The high molar mass distribution measured here is comparable to the previously reported molar mass distribution of the same polymer, especially considering the higher mass reported in that study (447 kg/mol) was measured in *o*-dichlorobenzene (DCB) at only 80 °C.[144] The bimodality and high mass is not necessarily a problem as there is precedent for high molar mass polymers to yield high viscosity solutions, which are amenable to thick-film fabrication via blade coating, coupled with improved morphological stability and device performance.[157] With this in mind, studying the properties of high-mass, low-solublility

conjugated polymers is relevant to thick-film, roll-to-roll compatible active layer processing.

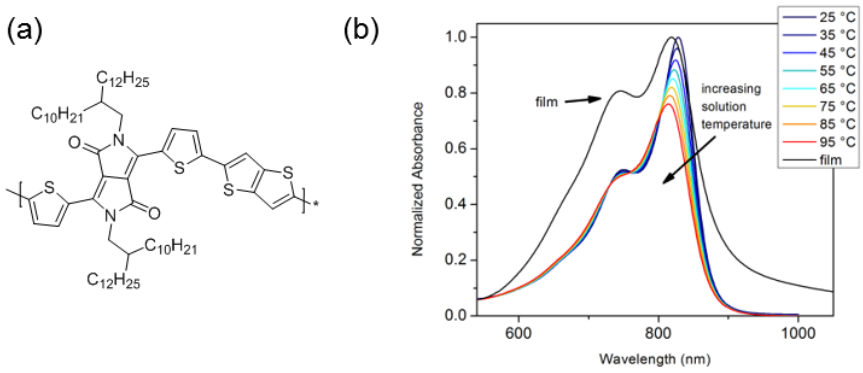

Figure 3-1 – (a) Chemical repeat unit structure of DT-PDPP2T-TT. (b) Temperature dependent UV/vis spectra of 0.02 mg mL^{-1} DT-PDPP2T-TT in DCB solution, along with the spectrum of a film cast from $CHCl_3$.

Temperature dependent UV/vis spectroscopy from 25 °C to 95 °C was performed in DCB and is shown in Figure 3-1b, with results that show a decrease in intensity of the lowest energy peak and blueshift of the peak maximum with increasing temperature as well as a slight decrease in intensity of the higher energy shoulder. These small changes seen over a wide range of temperatures demonstrate the strong rigidity of the polymer backbone, which can indicate aggregation.[114] This contrasts to the properties of other highly aggregated, low-solubility polymers, such as PffBT4T-2OD (aka PCE11), where in dilute solution UV/vis spectroscopy temperatures of around 60 °C are sufficient to molecularly dissolve the polymer and remove all evidence of aggregated species.[11,134] This polymer and its aggregation will be discussed in greater detail in Chapter 4. The solvent-dependent UV/vis spectra in Supporting Figure 3-4 show the room temperature absorbance of the polymer:fullerene blend in $CHCl_3$ alone and in a 92.5 %:7.5 % $CHCl_3$:DCB (by volume)

mixture. Aside from minor differences in absorbance across the entire spectrum attributed to slightly different solution concentrations, there are no additional features observed in the co-solvent solution spectra, such as a low energy shoulder, which has been seen in aggregated P3HT.[76,117,158,159] These identical spectra suggest that any effect imparted by the co-solvent will be during the film drying and solidification process, rather than in the processing solution itself. With this in mind, studying the dynamics of the solidification process immediately after coating is crucial to understanding the effect of the additive on film morphology and photovoltaic performance.[74] Lastly, our photovoltaic devices were made with a notably low total solution concentration of 13 mg mL^{-1}, with a 1:3 ratio of polymer to fullerene. This high ratio of fullerene is required for reasonable current from shorter wavelengths where this low band gap polymer does not absorb. It is important to note that a solution concentration of 13 mg mL^{-1} is quite low relative to typical concentrations used for blade coating or even spin coating (≈40 mg mL^{-1} and ≈20 mg mL^{-1}, respectively). Even at a polymer concentration of 3.25 mg mL^{-1}, the solution achieves a high viscosity that is amenable to blade coating.[160] Comparable wet film thicknesses are reported with P3HT:$PC_{61}BM$ (≈6 μm vs. our ≈8 μm, vide infra), where the total solids content is 40 mg mL^{-1}, with a P3HT concentration six times higher than the concentration of DT-PDPP2T-TT used here, indicating a higher viscosity for the latter.[76,106]

3.2.4 Blend film morphological characterization

Atomic force microscopy (AFM) tapping mode height images of the blend films (Supporting Figure 3-5) show a change in surface texture with the addition of co-solvent. The $CHCl_3$ only film features two distinct morphologies: a rough, textured domain roughly

3 μm long and 1.5 μm wide, seen in the center depressed below the surface, surrounded all around by a smoother textured surface with 100 nm scale domains. This morphology is representative of the $CHCl_3$ cast film, which appears to be relatively uniform with these rough embedded structures breaking through the matted surface across the whole film when measured in multiple spots. For all three additive-cast films, the texture is more uniform, with roughness values generally smaller than the $CHCl_3$ cast film. There are a variety of smaller scale defects in the additive cast films, especially with the +DIO film that features numerous, small, uniformly-distributed indentations.

Using low-force AFM, we can occasionally observe a nanofibrillar texture on the surface of these blend films cast with co-solvent. An example of this phenomenon is shown in Figure 3-2. While the $CHCl_3$ only film looks similar to that shown in Supporting Figure 3-5, all three of the co-solvent cast films have visible nanofibers on the surface of the film. Methods of controlling nanofibril morphology of DPP-based polymers through solvent selection and repeat unit structure have been well studied by others.[120,161–163]

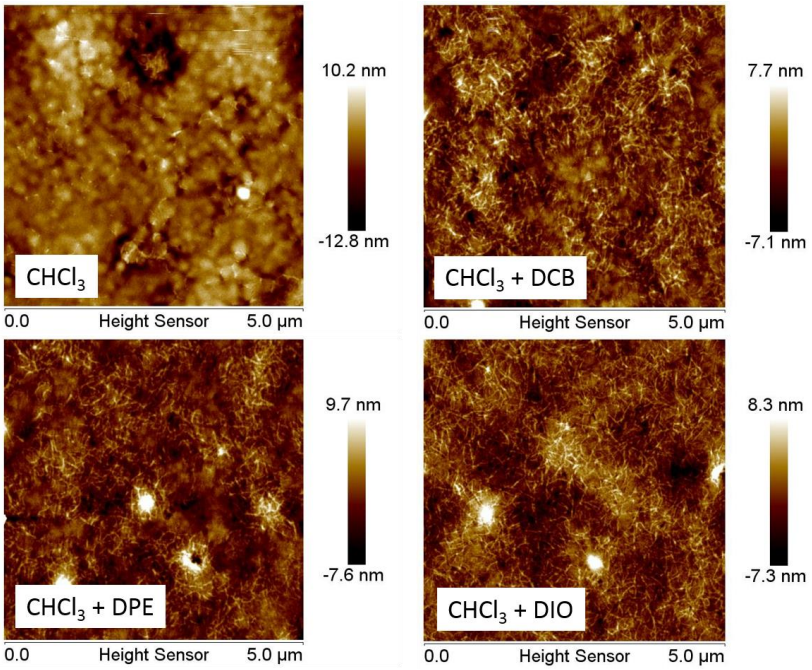

Figure 3-2 – Low-force atomic force microscopy height images of blend films, with a scan area of 5 µm square.

Scanning transmission electron microscopy (STEM) results for the $CHCl_3$ and $CHCl_3$ + DCB cast films, shown in Figure 3-3, supports the idea that the co-solvent encourages the formation of a dispersed network of percolating high-mobility polymer domains which are able to effectively transport charge through relatively thick films. While high aspect ratio polymer features are present in both the chloroform only as well as the chloroform:*o*-dichlorobenzene cast film, narrower nanofiber structure is much apparent in the latter. This is consistent with the EQE results that show that the dichlorobenzene co-solvent-cast film is more efficient at dissociating polymer excitons when built into a device, since the smaller domain size will have more polymer-fullerene interfacial surface area that improves charge separation and ultimately gives high fill factors even in thick films.

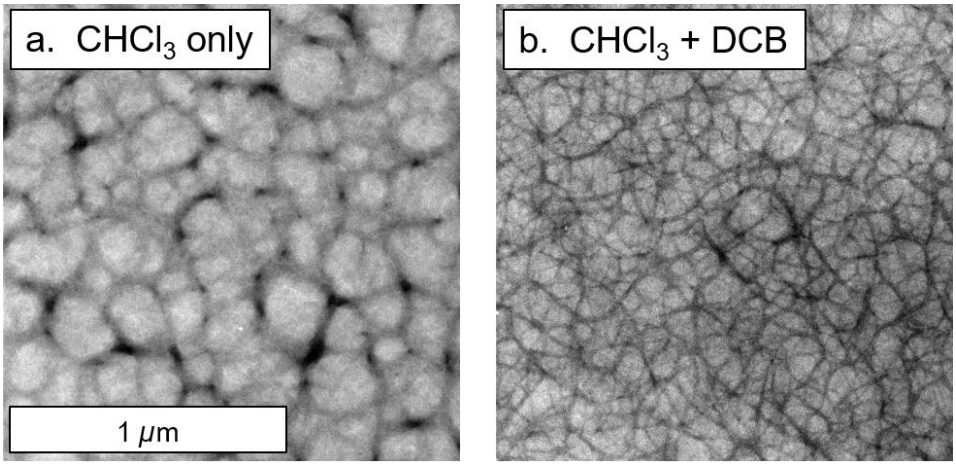

Figure 3-3 – STEM images of blend films cast from (a) chloroform and (b) $CHCl_3$ + DCB. The intensity in the low-angle annular dark-field images scales with density. In this case, brighter regions indicate PCBM-rich domains while polymer-rich regions appear dark.

To extract quantitative information on the domain structure, we compared the domain size results from STEM image processing to grazing-incidence small-angle X-ray scattering (GISAXS) profiles. GISAXS profiles of the BHJ films are shown in Supporting Figure 3-6a. Complete domain information of the film cast from $CHCl_3$ alone could not be acquired in full due to the large-scale phase separation present in the film and the detector limit of 0.004 $Å^{-1}$ (157 nm). Supporting Figure 3-6b shows the Kratky plot (Iq^2 vs. q) of the STEM Fourier transform along with the GISAXS of BHJ films processed using $CHCl_3$ and $CHCl_3$ + DCB. Mean domain sizes for the two blend systems as measured via STEM are 111 nm and 27 nm, respectively, confirming a drastic decrease in domain size with the use of DCB as a co-solvent. The integrated scattering intensity (ISI) represents a relative average domain purity and is determined using $ISI \equiv \int_{q_{min}}^{q_{max}} dq\, I\, q^2$, where I is the GISAXS scattered intensity (STEM power spectrum), and q is the momentum transfer. The ISI was normalized to 1.0 for the BHJ processed from $CHCl_3$+DCB and is 0.79 for the

$CHCl_3$-processed BHJ. An increase in average domain purity, typically due to co-solvent or additive, has been shown to be an important morphological factor seen in high performance OPVs as it is thought to reduce bimolecular recombination.[29,164,165] The results from AFM, STEM, and GISAXS confirm that the addition of DCB significantly reduces domain size, increases phase purity, and increases the polymer:fullerene surface area relative to single-solvent processing, consistent with the improved J_{SC} and FF.

To further characterize the inhomogeneities and defects seen in all the blend films, hyperspectral fluorescence microscopy was employed to characterize the μm-scale morphology. While the primary length scales relevant to bulk heterojunction morphology are generally on the order of 100 nm or less, given that large μm-scale features were seen on the AFM images, we sought to characterize them in an attempt to elucidate their composition. With this optical microscopy technique, a continuous wave 532 nm laser with an incident power of 4.5 mW was focused onto the blend film with a 100x objective, and emission was collected from 550 nm to 1000 nm.[166] This is a global imaging technique whereby the entire field of view of the microscope image is excited by the laser and the emission of the same field of view is collected one wavelength at a time via a volume Bragg grating that can diffract a single wavelength of an entire image uniformly. Hyperspectral microscopy has been used for characterization of inhomogeneities of perovskite films, in order to understand the properties of film defects and subsequent decreases in device performance.[167–169]

The hyperspectral fluorescence microscopy characterization is shown in Figure 3-4, with Figure 3-4a and Figure 3-4b showing monochromatic images at 770 nm of the $CHCl_3$

and + DCB blend films, respectively. The $CHCl_3$ only film is heterogeneous, as first seen in the AFM image in Figure 3-2**,** with similarly sized μm-scale inhomogeneities. To identify the composition of the μm-sized defects in the film, the fluorescence spectrum of a single region on the dark spots highlighted in each of the red boxes in Figure 3-4a was measured. The spectra shown are representative of the spectra on any part of the aggregate. The large aggregate in the bottom right has a peak fluorescence at 860 nm, which is the characteristic fluorescence of the polymer. On the other hand, the aggregate on the bottom left of the image has a strong peak fluorescence at 710 nm, which is characteristic of $PC_{71}BM$ (reference film shown in Supporting Figure 3-7). For all co-solvent cast films, such as + DCB as shown in Figure 3-4b, due to the smaller domain size characteristics of high performing bulk heterojunction films cast with co-solvent, there are no μm-scale aggregates visible. With this smaller domain size and increased mixing of the two materials, fluorescence is more efficiently quenched, especially from the polymer, so the overall emission from the film is lower (note the difference in intensity gray level). Since there is 3 times as much PCBM relative to the amount of polymer in these films, it is reasonable that essentially all polymer fluorescence is quenched while some PCBM signal remains.

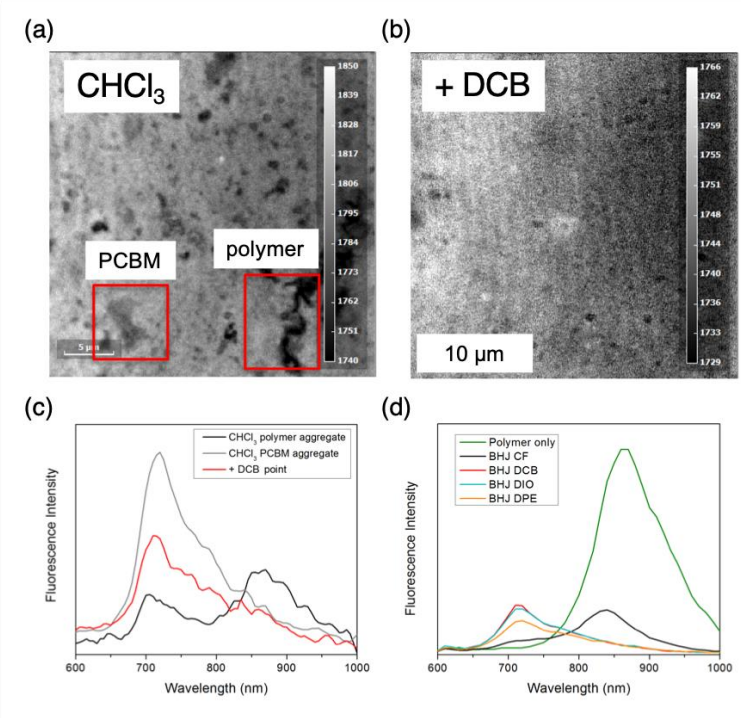

Figure 3-4 – Monochromatic fluorescence microscopy images of blend films cast from (a) $CHCl_3$ only and (b) $CHCl_3$ + DCB measured at 770 nm. (c) Fluorescence spectra of blend films cast from $CHCl_3$ only or $CHCl_3$ + DCB. Polymer and $PC_{71}BM$ aggregate spectra from the $CHCl_3$ only film are taken from a single region (≈ 1 μm^2) on the aggregates shown in the red boxes in (a). (d) Fluorescence spectra averaged across the microscope field of view of all four blend films as well as the pristine polymer film. Characteristic polymer fluorescence at 860 nm is seen for the pristine film as well as the chloroform only film. Characteristic $PC_{71}BM$ fluorescence at 710 nm is seen in the co-solvent cast blend films.

For a global picture, the fluorescence intensity of a featureless 10 μm by 10 μm scan area was averaged for all four blend films, as well as a film of only the polymer in Figure 3-4d, with the microscopy images shown in Supporting Figure 3-8. This experiment is analogous to traditional thin film fluorescence spectroscopy. As alluded to in the previous section, the polymer only film is strongly fluorescent with a peak emission wavelength of 860 nm. Once $PC_{71}BM$ is added, polymer fluorescence is strongly quenched, and only for the $CHCl_3$ cast film is there still a significant polymer signal. This reflects the presence of polymer domains in the film larger than exciton diffusion lengths which are on

the order of 10 nm to 20 nm.[81] This large-scale phase separation is consistent with low J_{SC} values, suppressed polymer EQE, and poor OPV performance seen with the device data for the $CHCl_3$ cast film. The +DPE film, with the highest photocurrent, has the greatest amount of $PC_{71}BM$ fluorescence quenching as well as the highest EQE in the short wavelength region where $PC_{71}BM$ absorbs (Supporting Figure 3-1b).

Grazing-incidence wide-angle X-ray scattering (GIWAXS) was used to probe the molecular packing of the blend films, as shown in Figure 3-5. In general, the blade-coated films are similar to previously reported spin coated films.[142,143] In the film cast from chloroform alone, a slight preference for face-on orientation is observed, as seen in Figure 3-5a. This is evident from the intense π-π stacking peak seen only in the out-of-plane direction, at $q_z \approx 1.7$ Å^{-1}, and the break in orientations of the (100) lamellar stacking peak in both the in-plane and out-of-plane directions. Conversely, with any of the films cast with co-solvent, the out-of-plane π-π stacking peak decreases in intensity, the (100) lamellar stacking becomes more isotropic, and second-degree lamellar ordering becomes more pronounced. Here, in Figure 3-5b, the $CHCl_3$ + DCB cast film is shown as a representative sample, but the + DIO and + DPE cast films have a similar appearance (Supporting Figure 3-9).

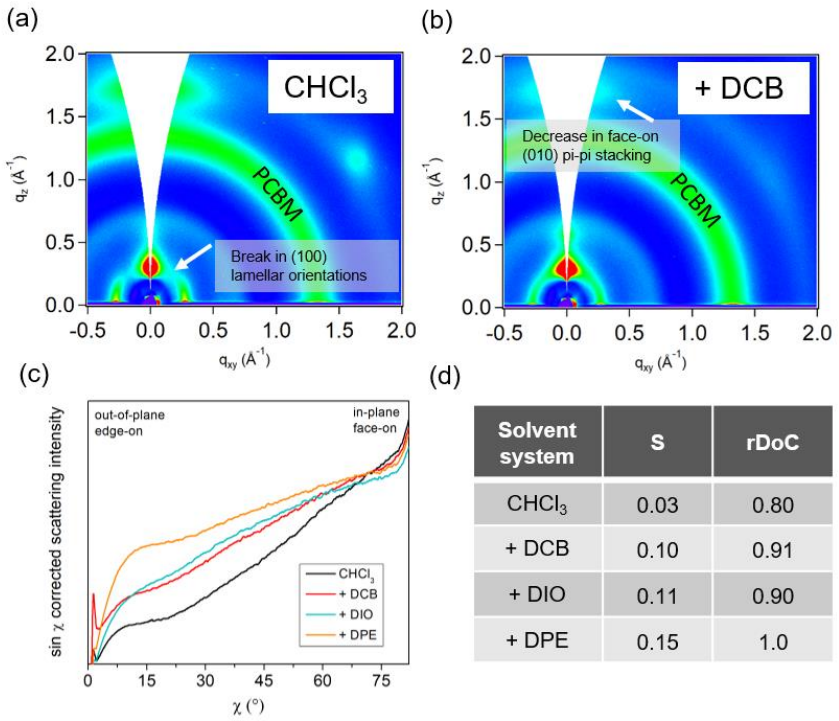

Solvent system	S	rDoC
$CHCl_3$	0.03	0.80
+ DCB	0.10	0.91
+ DIO	0.11	0.90
+ DPE	0.15	1.0

Figure 3-5 – GIWAXS images of blend films cast from (a) $CHCl_3$ and (b) $CHCl_3$ + DCB, with the significant differences between the two films labeled. (c) Thickness normalized and sin χ corrected pole figure of the (100) lamellar stacking peak for the blend films. (d) Hermans orientation parameter, S, and relative degree of crystallinity, rDoC, for the blend films as calculated from the pole figure in (c).

To characterize the degree of crystallinity and orientation in the blend films, a thickness normalized and sin χ corrected pole figure of the (100) lamellar stacking peak was generated from the scattering patterns and is shown in Figure 3-5c.[121] This figure is a representation of the angular distribution of (100) lamellar crystallites in the film. As we move from the $CHCl_3$ only blend film, to + DCB and + DIO, and finally + DPE, there is an increase in the crystalline populations near $\chi = 0°$, which is indicative of increased edge-on polymer orientation. In addition, as the intensity of edge-on polymer scattering increases, there is little change in the face-on polymer scattering intensity, indicating that the overall crystallinity of the film is increasing. In order to quantify these observations,

the Hermans orientation parameter and the relative degree of crystallinity were calculated and are shown in Figure 3-5d. The Hermans orientation parameter, S, represents the average orientation of the lattice plane, and is a number from -0.5 to 1.0, where -0.5 represents the case of all lattice planes being oriented perpendicular to the substrate normal and 1.0 represents the case of all lattice planes being oriented parallel to the substrate. For (100) lamellar stacking, which we are measuring here, S = -0.5 is completely face-on and S = 1.0 is completely edge-on with respect to the substrate. The increase in S from 0.03 to 0.15 as we move from $CHCl_3$ to + DPE is indicative of a small yet measurable move toward a more edge-on orientation. The relative degree of crystallinity (rDoC) is used to compare two films of the same material and is calculated via integrating the sin χ corrected pole figure from $\sim 0° < \chi < 80°$. The rDoC for each blend film follows a similar trend to the crystalline orientation, in that the + DPE cast film has the highest crystallinity, followed by + DIO and + DCB which are similar, and finally $CHCl_3$ only which has the lowest crystallinity. The increase in crystallinity for all three co-solvent solutions relative to $CHCl_3$ is consistent with expectation of improved mobility and the consistent increase in FF, which explains why decent fill factors are observed even in thick film devices.[170,171] In order to test the reproducibility of this experiment, this pole figure analysis was repeated on a different set of films, cast from separately prepared solutions (Supporting Figure 3-10). Despite slight differences in the absolute values of S and rDoC, the overall trend of increasing edge-on orientation and crystallinity when adding co-solvent is consistent with the data presented in Figure 3-5.

To summarize the results so far, we have shown from static morphology characterization that the drastic enhancement of fill factor and current for the co-solvent

cast films is a direct result of domain size reduction. The $CHCl_3$ system is coarsely separated and is drastically more refined with co-solvent as seen with the STEM domain sizes and fluorescence quenching. In addition, the co-solvent films appear to have more ordered polymer-rich regions as seen from the rDoC calculations. This reduction in domain size and slight increase in crystallinity with the use of co-solvent has been seen for other similarly low-crystalline polymers such as PBDTTT-C-T.[172] This is in contrast to more highly crystalline systems like P3HT:$PC_{61}BM$ that is too finely mixed when cast without additives and requires either co-solvent or annealing to increase crystallinity and the degree of phase separation.[76,173]

3.2.5 In situ coating and drying measurements

To attempt to assess the mechanism by which the co-solvents produce such dramatic changes in morphology, we performed in-situ GIWAXS and GISAXS measurements, concurrent with reflection optical interferometry. The $CHCl_3$ + DCB co-solvent system was chosen to compare to the $CHCl_3$ only system, since DCB has the highest vapor pressure among all co-solvents used in this study and, thus, does not require post-processing vacuum removal. As a result, the solid-state morphology obtained at the completion of the real time experiments is directly representative of the active layer fabrication processed used in the DCB device measurements above. These time-resolved techniques probe various length scales relevant to the device operation: GIWAXS measures crystallinity on the 1 Å to 1 nm scale, GISAXS measures domain size on the 10 nm to 100 nm scale, and optical reflection measures wet film thickness on the 100 nm to 10 μm scale. By combining these three methods, we can obtain a complete picture of the film formation process in real time. Representative raw data for the in situ GIWAXS,

GISAXS, and optical reflection can be found in the supporting information (Supporting Figure 3-11, Supporting Figure 3-12, and Supporting Figure 3-13). Due to the rapid drying of the $CHCl_3$ only cast film, we were unable to obtain reliable real time scattering measurements. However, because the film dries within 2 seconds after coating, we can assume that all features seen in the dried film are established in the same window of time. Figure 3-6 shows the film thickness from reflectivity measurements, volume normalized integrated (100) lamellar stacking scattering intensity from GIWAXS, and integrated scattering invariant (ISI) from GISAXS, as a function of time, during solidification of the BHJ cast from $CHCl_3$ + DCB. While the integrated (100) scattering intensity is generated from the pole figure, representative line cuts in the in-plane and out-of-plane direction can be found in the supporting information (Supporting Figure 3-9).

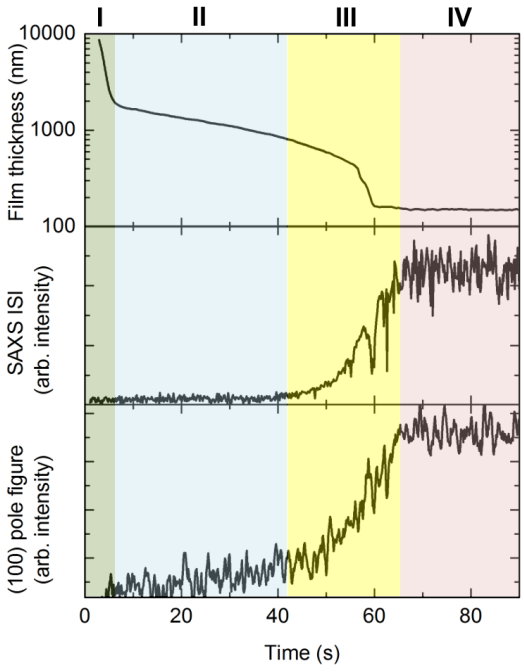

Figure 3-6 – In situ film thickness, integrated scattering intensity (ISI), and (100) peak scattering intensity as a function of time after coating, measured via optical reflection interferometry, GISAXS, and GIWAXS respectively for the $CHCl_3$ +

DCB cast blend film. Note the simultaneous evolution of domain formation and crystallization during the final stages of drying that begins around 40 sec, at stage III.

There were four stages identified during solidification of the BHJ film when cast from co-solvent. In stage I, $CHCl_3$ rapidly evaporates, leading to a significant thinning of the wet film thickness, and a sharp increase in concentration from the initial 13 mg mL^{-1} solution to 74 mg mL^{-1} in an assumed nominally single DCB solvent film ≈ 4 s after blade passage. Stage II is dominated by initial evaporation of the DCB, where solvent evaporates without any corresponding morphological developments. Stage III signifies the evaporation of the last of the DCB, wherein a large crystallization event occurs toward final DCB removal at a concentration of approximately 246 mg mL^{-1}, which corresponds to a solvent volume fraction of 81 %. Stage IV signifies the final dry thin film morphology, where crystalline and domain evolution has stopped. Here, we find there is a two-step solidification occurring where $CHCl_3$ evaporates first, followed by delayed evaporation of DCB leading to a significant crystallization event. The ISI as determined from the GISAXS data shows a similarly sharp increase, also starting around 40 s after coating in stage III, indicating that through a single transition, crystallization and domain evolution occur simultaneously. Furthermore, the GISAXS line profile does not evolve in shape over the course of drying indicating that the measured ≈27 nm domain sizes develop in this single transition (Supporting Figure 3-13). This demonstrates that the evolution of both distinct phases as well as their purity occurs during the final removal of DCB. The GIWAXS and GISAXS data fit a two-phase model system (Supporting Figure 3-14), in which one phase is composed of crystalline polymer, and the other is a mixed amorphous phase of polymer and fullerene, similar to behavior described in previous reports.[76,174] The nominally

simultaneous evolution of the scattering and polymer crystallinity is consistent with the film morphology being driven by a single, solid-liquid phase transition associated with the crystallization of the polymer, as is the case in processing P3HT from chlorobenzene with 1-chloronaphthalene as the co-solvent.[158]

Given the large length scale and rapid solvent evaporation shown by the single-solvent system, the fast quench generates large domains that behave like a similar polymer, PDPP5T, which was reported by van Franeker et al. to solidify via liquid-liquid phase separation.[74] Similarly, for PBDTTT-C-T reported by Bokel et al., casting from a single solvent (chlorobenzene) yields coarse grained films, with modeled phase behavior supported by real time GISAXS indicating liquid-liquid phase separation.[172] For both our DT-PDPP2T-TT and the reported PDPP5T, the EQE response from co-solvent cast films are slightly redshifted, indicating increased polymer backbone planarization. Since the PDPP5T co-solvent cast system was shown to proceed via solid-liquid phase separation to a more finely phase separated morphology, it is likely that the mechanism for DT-PDPP2T-TT is similar. Since the chloroform is a better solvent for the polymer than the co-solvents, its removal induces additional aggregation leading to solidification.[175] For our system, the addition of co-solvent likely pushes this system from a liquid-liquid dominated phase separation to solid-liquid phase separation, driven by polymer aggregation. As with the case of PDPP5T, at around 80 % volume fraction total solids content, crystallization and phase separation occurs in a super-saturated solution, leading to a dried film and the final morphology. Under these poor solvent conditions, we observe a densification of the fibrillar network that agrees with previous reports.

3.3 Conclusion

The high molcular mass and strongly aggregating characteristics of DT-PDPP2T-TT limit the solvent selection for production of thick films. However, when processed from good solvents such as $CHCl_3$, apparent liquid-liquid phase separation occurs with resultantly coarse film morphology and poor device performance. All high boiling point co-solvents used to process this DT-PDPP2T-TT:$PC_{71}BM$ blend induce the system into behavior that tends toward solid-liquid phase separation, which initializes crystallization and domain formation before liquid-liquid phase separation can proceed. With any of the co-solvents used in this study, domain size decreases with co-solvent and nanofibers emerge both on the surface (AFM) and within the bulk (STEM) of the film. This is consistent with a decrease in solvent quality for the polymer as the host solvent chloroform evaporates, leading to eventual polymer aggregation and crystallization. $PC_{71}BM$ tends to aggregate during this drying phenomenon for many polymer:$PC_{71}BM$ blends, but because this particular polymer also tends to aggregate due to low solubility, a variety of additives are capable of achieving optimal morphologies and improved photovoltaic performance over the $CHCl_3$ only cast film. When the polymer:fullerene blend is processed from a mixture of $CHCl_3$ and DCB, polymer crystallization and phase separation is delayed until the end of the drying process. As the last *o*-dichlorobenzene evaporates, polymer crystallization, domain formation, and domain purity evolve simultaneously. The resulting improved morphology has increased interfacial area between polymer and fullerene while maintaining an interconnected high mobility network for charges to be extracted. As a result, average PCEs of 6.5 % are maintained with a remarkable range of active layer film thicknesses from 180 nm to 440 nm.

3.4 Supporting information

3.4.1 Materials

Solvents for all studies and reagents for ZnO synthesis were purchased from Sigma Aldrich. DT-PDPP2T-TT (OS0300) was purchased from 1-Material and used as received. Origins of other materials used in this study are described below.

3.4.2 Polymer characterization

Number average molecular mass (M_n) and dispersity ($Đ$) were determined by Gel Permeation Chromatography (GPC) using a Tosoh EcoSEC HT GPC instrument with a RI detector. Experiments were run with TCB as eluent at 160 °C at a flow rate of 1 mL/min on two sequentially connected 30 mm by 7.8 mm GMHhr-H(S) HT2 columns (Tosoh Bioscience). The instrument was calibrated vs. polystyrene standards (1,390 to 1,214,000 g/mol), and data were analyzed using EcoSEC High Temperature GPC Workstation Software. To prepare polymer samples for GPC measurements, the polymer was dissolved in HPLC grade TCB at a concentration of 1.0 mg/mL and then stirred for at least 3 h at 120 °C prior to filtering through a 0.45 mm PTFE filter.

UV/vis spectroscopy was measured with a Cary 5000 double-beam UV/VIS/NIR spectrophotometer.

3.4.3 Device fabrication and measurements

An inverted bulk heterojunction solar cell architecture comprising of glass/ITO/ZnO/polymer:$PC_{71}BM$/MoO_3/Ag was used to fabricate the solar cell devices in this work. Before the device processing, the patterned ITO-coated glass substrates (Latech Scientific Supply Pte. Ltd., sheet resistance 10 Ω/sq) were cleaned by sonicating

sequentially with sodium dodecyl sulfate in Millipore water, pure Millipore water, and finally isopropanol for 10 minutes each. The cleaned substrates were blown dry with Argon and placed in a UV/O_3 chamber for 10 minutes. For the electron transport layer, a ZnO solution was made with 0.11 mol/L Zn acetate dihydrate and 0.11 mol/L ethanolamine combined in 2-methoxyethanol. This solution was stirred overnight at room temperature, then filtered with a 0.45 µm PTFE syringe filter before use.

The ZnO solution was deposited on the cleaned ITO substrates by spin-coating for 30 seconds at 419 rad/s (4000 rpm) in ambient atmosphere to get a layer thickness of ~30 nm. After spin-coating, the ZnO layer was annealed in air at 150 ˚C for 10 min followed by slow cooling to room temperature. The photoactive layer solution was prepared by dissolving polymer and $PC_{71}BM$ (ADS71BFA, American Dye Source) in either chloroform only or a solvent mixture of chloroform:cosolvent (92.5:7.5 v/v ratio). The ratio of polymer:fullerene used was 1:3 (wt/wt) with a polymer concentration of 3.25 mg/mL. The solution was stirred at 50 ˚C for 12 hours to ensure complete dissolution. The active layer solution was allowed to cool to ≈25 °C before coating and was blade coated on top of the ZnO layer in ambient air with a custom blade coater, with a blade gap of 400 µm and blade speed of 20 mm/s. To remove the additive from the photoactive layer without disturbing the wet film, the samples were placed in a vacuum chamber with a pressure of 1×10^{-3} Pa (1×10^{-5} mbar) for 45 min. The top electrodes MoO_3 and Ag were deposited by vacuum deposition with layer thicknesses of 20 and 160 nm, respectively, to obtain complete solar cell devices with an electrode overlap area of 0.07 cm². Fast drying Ag paint (Ted Pella, 16040-30) was applied to the ITO electrodes to improve contact with the device switch-box. An aperture with area 0.049 cm^2 was aligned with the electrode overlap area

for solar and external quantum efficiency (EQE) measurements. The *J-V* characteristics of all photovoltaic devices were evaluated under AM 1.5G solar illumination (100 mW cm^{-2}) using a Keithley SMU 2410 with a Newport Thermal Oriel 94021A solar simulator calibrated with a reference silicon solar cell.

External quantum efficiency was measured with a Newport QE-PV-SI Oriel Quantum Efficiency Measurement Kit, calibrated with a reference silicon solar cell as with the above solar measurements.

3.4.4 Thin film characterization

Grazing-incidence wide-angle X-ray scattering (GIWAXS) samples of polymer:$PC_{71}BM$ blends were prepared on silicon wafer substrates using the optimized conditions for device preparation. GIWAXS was measured at the Stanford Synchrotron Radiation Lightsource (SSRL) beamline 11-3 in a helium-filled chamber with an X-ray wavelength of 0.976 Å and sample to detector distance of 250 mm at an incident angle of 0.13°. Spectra were recorded on a Rayonix MARCCD area detector and processed using the Nika software package for Wavemetrics Igor, in combination with WAXStools.[66,133]

Atomic Force Microscopy of the blend films used for devices was measured with a Bruker Dimension Icon Atomic Force Microscope. For traditional tapping mode, the instrument was operated in tapping mode with a tapping frequency around 150 kHz. For low-force atomic force microscopy, low spring constant Bruker SCANASYST-AIR probes were used.

Hyperspectral microscopy was performed with an IMA PL VIS from Photon, etc. A 3 W continuous wave 532 nm laser was focused onto the blend film with a 100x objective and tuned to an incident power of 4.5 mW, and emission was collected from 550 nm –

1000 nm. This is a global imaging technique, whereby the entire field of view of the microscope image is excited by the laser, and the emission of the same field of view is collected one wavelength at a time via a volume Bragg grating that can diffract a single wavelength of an entire image uniformly.

Scanning transmission electron microscopy (STEM) was carried out using a FEI Titan 80-300 STEM (FEI Company, Hillsboro, Oregon) equipped with a double-hexapole spherical aberration corrector (CEOS GmbH, Heidelberg, Germany). Low-angle annular dark-field (LAADF) images of each specimen were collected using a post-specimen detector (Model 3000, E. A. Fischione Instruments, Export, Pennsylvania). A small (3 mrad) probe-forming aperture was used and the post-specimen optics were configured such that the ADF detector inner and outer angles were 17 mrad and 95 mrad, respectively. A low spot number was used to produce an electron probe containing a current of approximately 45 pA when using this small probe-forming aperture.

3.4.5 In situ GIWAXS and optical reflection

In-situ hard X-ray scattering measurements were performed at the Advanced Light Source beam line 7-3-3, with a beam energy of 10 keV.[76,122] For the GIWAXS measurements a 2D image detector (Dectris Pilatus 2M) was located at a distance of ≈260 mm from the sample center. Slits were adjusted to produce a nominally 0.3 mm high beam which overfilled the nominally 2 cm wide substrate. In situ grazing-incidence small-angle X-ray scattering, GISAXS, was performed at the same beam line with the 2D image detector-to-sample distance 3850 mm. An evacuated flight tube was used to minimize air scatter. The X-ray beam was attenuated to eliminate sample damage. The detector was

calibrated with a silver behenate standard. Both GIWAXS and GISAXS data were reduced with the Nika software package.[133] Simultaneous with both GIWAXS and GISAXS measurements, normal incidence spectral reflectometry was performed with a home-made, fiber spectrometer based system. Care was taken to overlap the reflectometry probe beam (≈0.3 mm diameter) with the stripe illuminated by X-rays. The reflectometry was analyzed using a commercial ellipsometry code (JA Woollam WVASE32). X-ray data were recorded with a variable integration time and period. The initial 120 s were recorded at ≈0.1 s integration and period, while the next minute was recorded with 9 s integration and 1.5 s period. The reflectometry was recorded at a constant ≈0.1 s integration and period for films cast from chloroform. For films cast from $CHCl_3$ + DCB the initial 120 s were recorded at ≈0.1 s integration and period while the 3.5 minutes was recorded with 1 s integration and 1 s period. Ex situ (static) scattering measurements were performed with 9 s integration.

For quantitation of GISAXS, we make the approximation that the enhanced signal at exit angles near the critical angle (the Yoneda peak) is a good proxy for q_x and assume a 3D isotropic scattering pattern such that the scattering invariant becomes: $\int dqIq^2$. We note that the ≈4 m flight path of the GISAXS measurement limits the low q range and, a significant amount of low q scattering is missed in the in situ experiment. This can lead to a bias in relative phase purity when interpreting the evolution of the ISI.

3.4.6 Supporting figures and tables

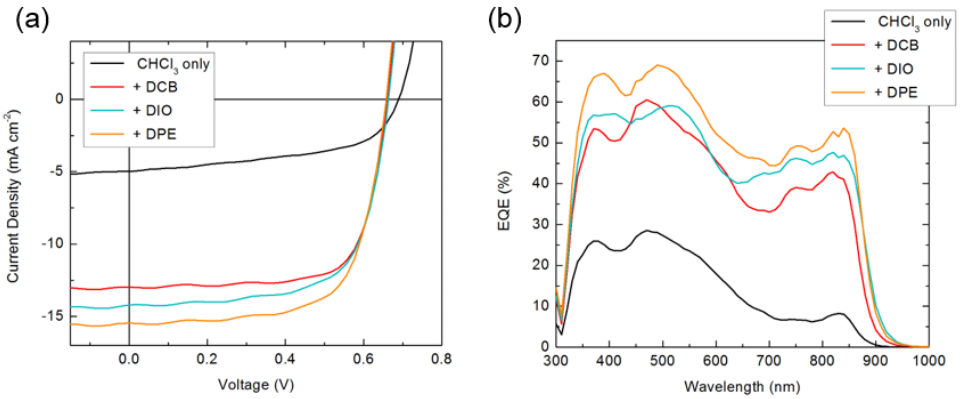

Supporting Figure 3-1 – Current density-Voltage, J-V, curves and external quantum efficiency, EQE, of champion solar cells.

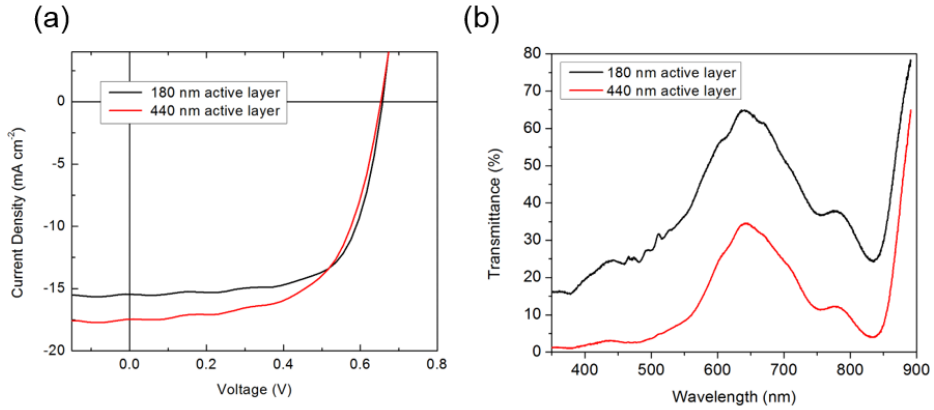

Supporting Figure 3-2 – (a) J-V curves and (b) transmittance of thin and thick film + DPE devices (180 nm and 440 nm active layers, respectively). Average photovoltaic parameters are shown in Supporting Table 3-1 below. J-V curves in (a) both represent individual champion pixels, each with 7.0 % PCE.

Supporting Table 3-1 – Photovoltaic results from thin and thick active layer inverted devices made with the + DPE solution. 180 nm data is taken from Table 3-1 in the main text. Values were averaged over 8 pixels and error bars indicate one standard deviation from the mean.

Active layer thickness	J_{SC} (mA cm^{-2})	V_{OC} (V)	FF (%)	PCE (%)
180 nm	16.0 ± 0.5	0.66 ± 0.01	64 ± 4	6.7 ± 0.2
440 nm	17.7 ± 0.3	0.65 ± 0.01	53 ± 5	6.1 ± 0.6

Supporting Table 3-2 – Elemental analysis confirms the polymer purity, with measured values less than 0.4% different compared to the theoretically calculated composition.

Element	Theory	Found
C	73.59	73.30
H	9.45	9.45
N	2.52	2.55
S	11.55	11.60

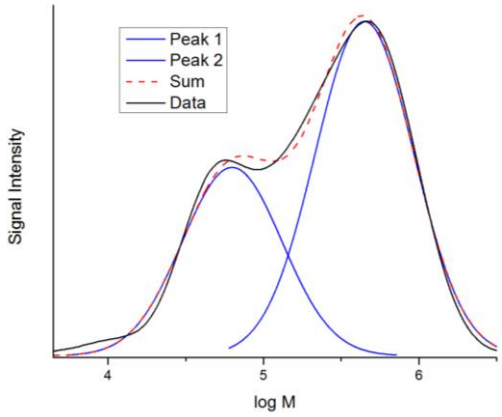

Supporting Figure 3-3 – GPC chromatogram of DT-PDPP-2T-TT, using 1,2,4-trichlorobenzene at 160 °C, with polystyrene as a standard. The bimodal trace (black) was deconvoluted into two gaussian distributions (blue). The sum of those two fits (dashed red) is combined to compare to the raw data and confirm the validity of the fit.

Supporting Table 3-3 – Number average molecular mass and dispersity for the raw GPC trace in Supporting Figure 3-3 above, as well as the two deconvoluted peaks.

Peak	**M_n (kg/mol)**	***Đ***
Raw data	98.9	3.86
Peak 1	48.6	1.68
Peak 2	348	1.64

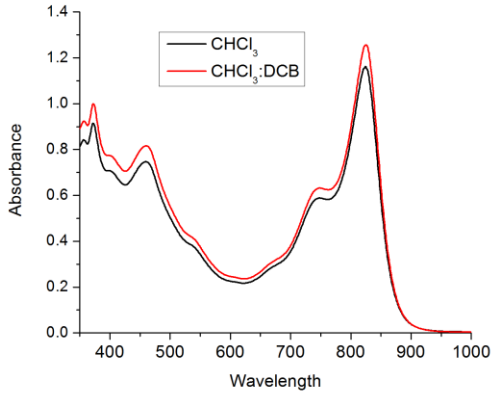

Supporting Figure 3-4 – Solution UV/vis spectra of the polymer:fullerene blend (1:3 weight ratio) in either $CHCl_3$ or 92.5:7.5 $CHCl_3$: DCB solution at a concentration of 0.02 mg mL^{-1}, at 25 °C. Subtle differences in overall absorption intensity are due to small differences in concentration between the two solutions.

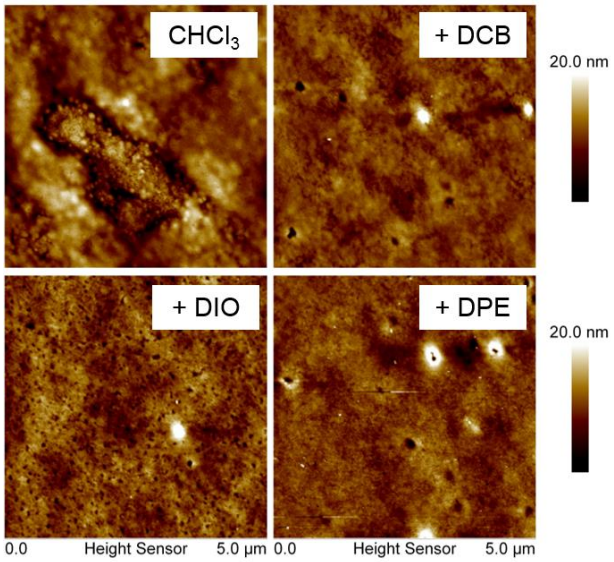

Supporting Figure 3-5 – Atomic Force Microscopy (AFM) images of blend films. Scan area is 5 µm square, and all height scale bars are 20 nm. Root mean square

roughness values are as follows: $CHCl_3$ = 2.8 nm, + DCB = 1.8 nm, + DIO = 2.3 nm, + DPE = 3.2 nm.

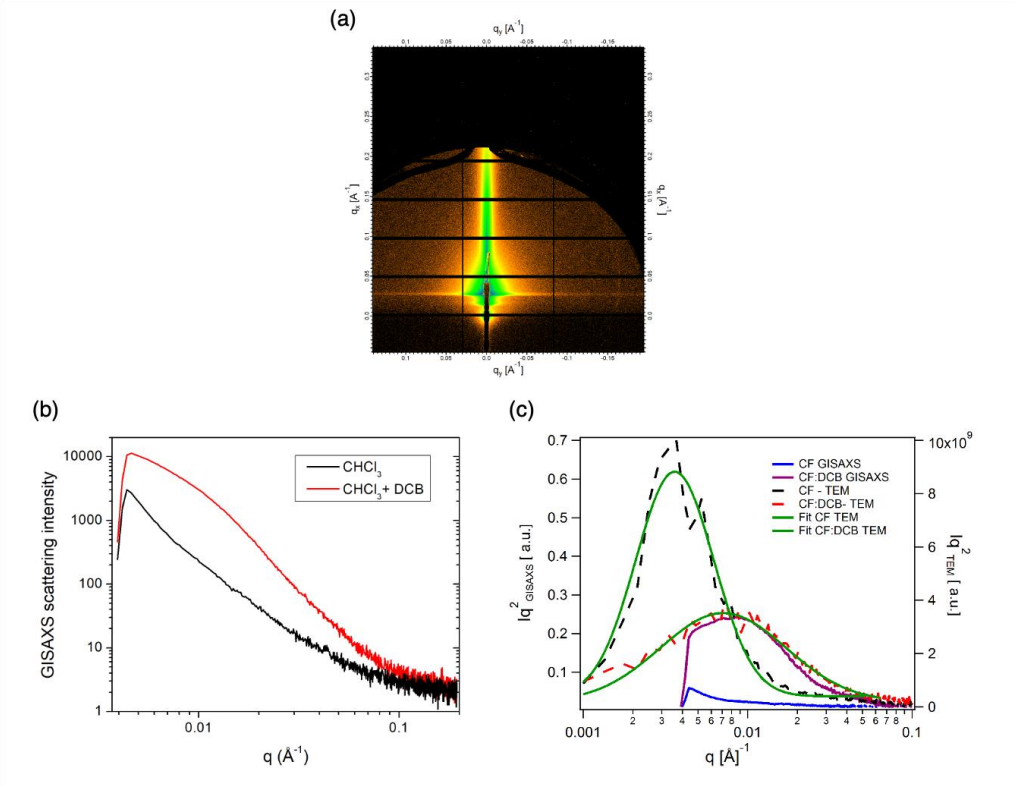

Supporting Figure 3-6 – (a) GISAXS image of a BHJ processed from $CHCl_3$ + DCB. (b) GISAXS curve (I vs. q) of BHJ films processed using $CHCl_3$ or $CHCl_3$+DCB. The q_{xy} data was extracted from a horizontal cut through the Yoneda scattering enhanced intensity. The characteristic length scale from the $CHCl_3$ cast film is out of range, due to the detector limit of q = 0.004 $Å^{-1}$. (b) Kratky plot (Iq^2 vs. q) of the STEM and GISAXS of BHJ films processed using $CHCl_3$ or $CHCl_3$+DCB. Mean domain sizes for the two blend systems are 111 nm and 27 nm, respectively, as

calculated from the TEM fits (green curve). Film thicknesses for the $CHCl_3$ and $CHCl_3$+DCB films are 64 nm and 151 nm, respectively.

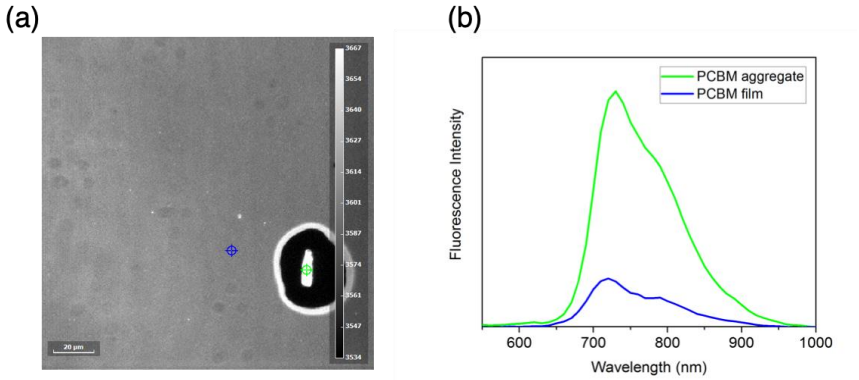

Supporting Figure 3-7 – (a) Monochromatic fluorescence microscopy image of a pristine $PC_{71}BM$ film at 770 nm. (b) Local fluorescence spectra of a point on the smooth film (blue) and an aggregate (green), showing characteristic $PC_{71}BM$ fluorescence with a peak at ~710 nm.

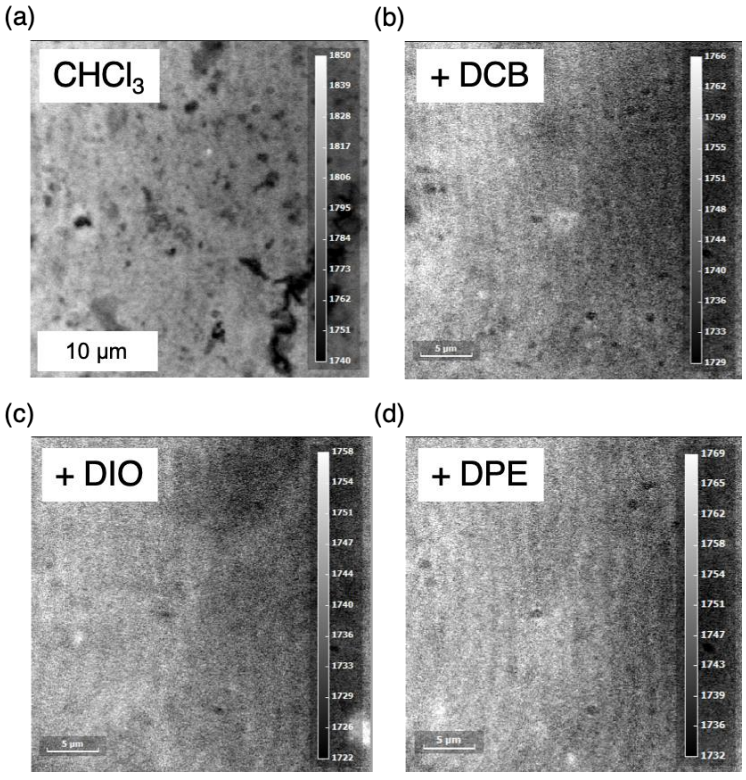

Supporting Figure 3-8 – Monochromatic fluorescence microscopy images of blend films cast from (a) $CHCl_3$ only, (b) $CHCl_3$ + DCB, (c) $CHCl_3$ + DIO, and (d) $CHCl_3$

+ DPE, measured at 770 nm. (a) and (b) are reproduced from Figure 3-4. Note the significantly lower gray level for all three cosolvent cast films, indicating much lower fluorescence due to finer phase separation.

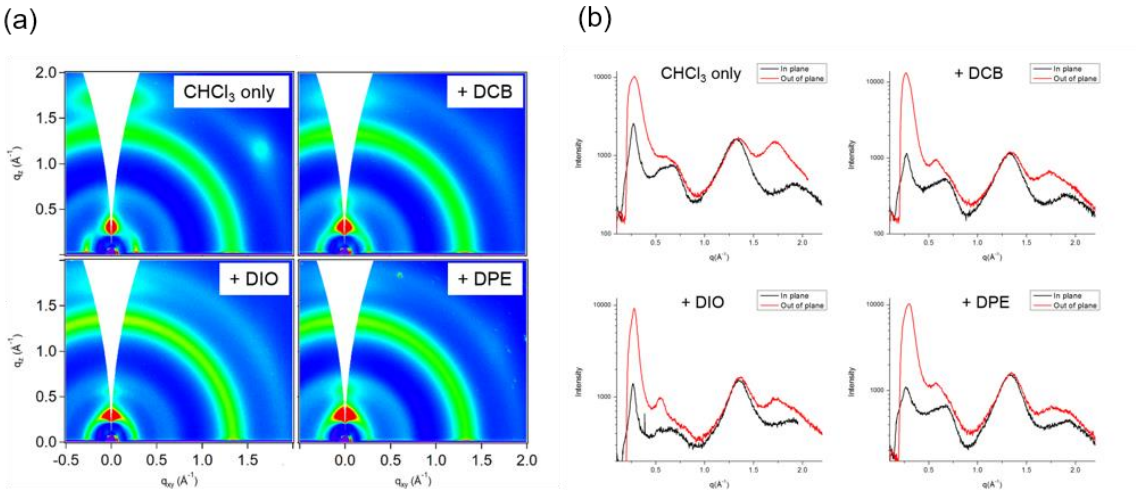

Supporting Figure 3-9 – (a) GIWAXS 2D scattering patterns for blend films. $CHCl_3$ and +DCB are reproduced from the main text. (b) In plane (black) and out of plane (red) line cuts for all four blend films.

(a)

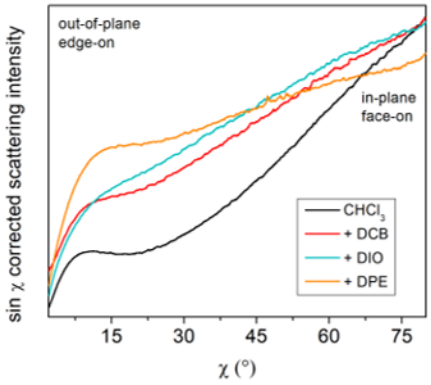

(b)

Solvent system	S	rDoC
$CHCl_3$	0.12	0.76
+ DCB	0.19	0.95
+ DIO	0.19	0.98
+ DPE	0.25	1.0

Supporting Figure 3-10 – (a) Thickness normalized and sin χ corrected pole figure of the (100) lamellar stacking peak for the blend films. (b) Hermans orientation parameter, S, and relative degree of crystallinity, rDoC, for the blend films as calculated from the pole figure in (a). This data was performed on separate films, cast from different solutions compared to the pole figure and subsequent workup

shown in Figure 5 in the main text, in order to confirm the reproducibility of the measurement.

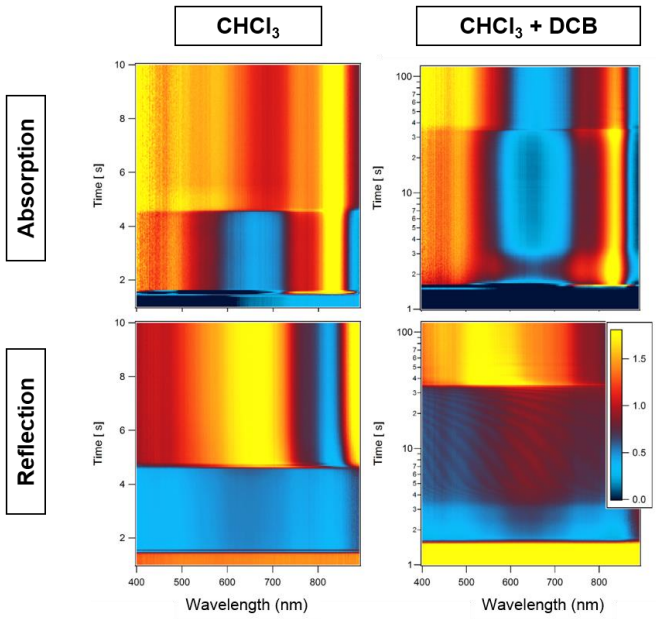

Supporting Figure 3-11 – In situ UV/vis absorption and reflection spectroscopy for blend films cast from either $CHCl_3$ only or $CHCl_3$ + DCB. Note the linear time scale for $CHCl_3$ and the log scale for $CHCl_3$ + DCB.

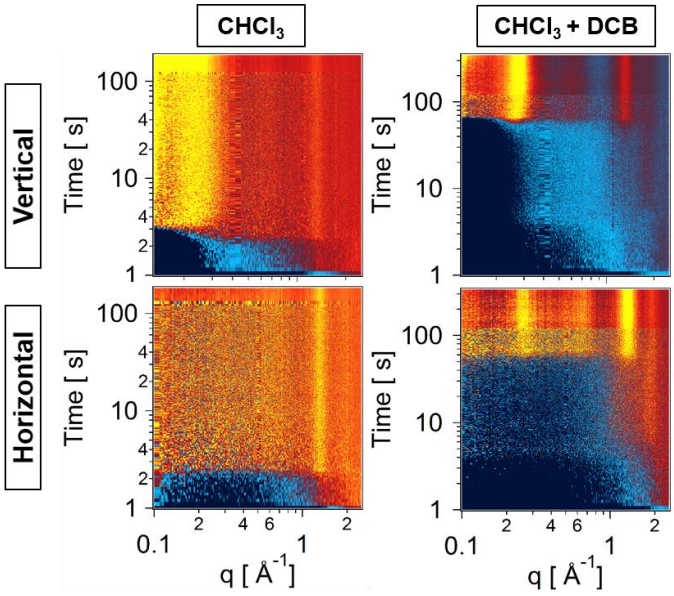

Supporting Figure 3-12 – In situ GIWAXS line cuts in the vertical and horizontal direction (i.e. out of plane and in plane, respectively), for blend films cast from

either $CHCl_3$ only or $CHCl_3$ + DCB. This data is related to the in situ (100) peak scattering intensity shown in Figure 6 in the main text. The (100) lamellar stacking peak for the $CHCl_3$ only cast film is obfuscated by reflectivity and low signal, thus this in situ data could not be used for further analysis.

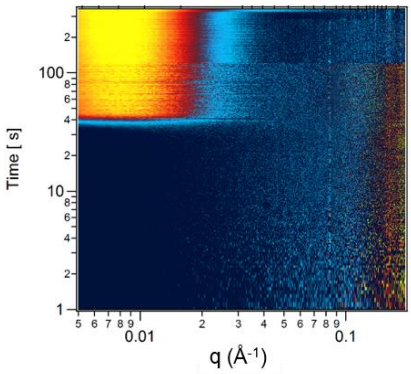

Supporting Figure 3-13 – In situ GISAXS line profile measured for the blend film cast from $CHCl_3$ + DCB. This data is used to calculate in situ GISAXS integrated scattering intensity (ISI) data shown in Figure 3-6 in the main text and Supporting Figure 3-14 below.

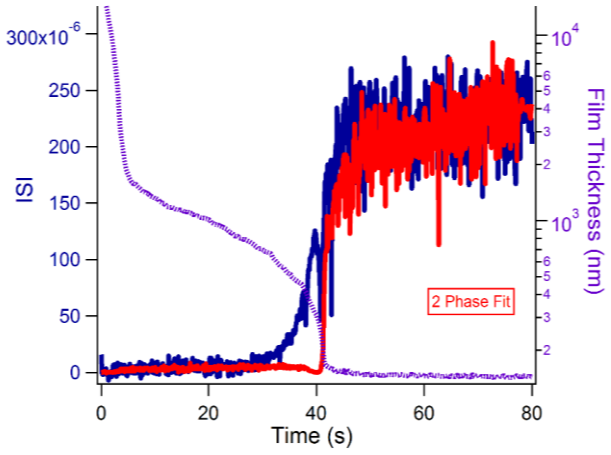

Supporting Figure 3-14 – Fit of the GISAXS Integrated Scattering Intensity (ISI) (blue) for the blend film cast from $CHCl_3$ + DCB to a two-phase model (red) as described in Ref 4. The ISI and film thickness are reproduced here from Figure 3-6.

CHAPTER 4. PROBING CRYSTALLIZATION EFFECTS WHEN PROCESSING BULK-HETEROJUNCTION ACTIVE LAYERS: COMPARING FULLERENE AND NON-FULLERENE ACCEPTORS

The work presented in this chapter would not exist without the synthetic expertise of Dr. Bing Xu and Dr. Austin L. Jones. Bing designed and synthesized the initial family of random terpolymers, and Austin synthesized two batches of the new composition that is the focus of the work presented in this chapter. The in situ GIWAXS and WLI data collection and interpretation were done with the mentorship of Dr. Lee J. Richter, who worked up the WLI data to generate the thickness vs. time curves.

As a follow up to our initial PffBT4T-2OD based random copolymer study, where we synthesized random terpolymers of the structure PffBT4T$_m$-co-3T$_n$-2OD to improve processability while maintaining solid state properties and device performance with $PC_{71}BM$, we sought to explore non-fullerene acceptors (NFAs) and processing via blade coating. We have determined that a new copolymer composition, PffBT4T$_{80}$-co-3T$_{80}$-2OD (80-20), is on par with our best previously reported copolymers and is the best candidate for processing IDTBR blend films without heating the substrate prior to coating, achieving power conversion efficiencies (PCEs) approaching 9%. However, there is still a decrease in PCE going from $PC_{71}BM$ to IDTBR due to the fill factor, which we attribute to IDTBR's tendency to disrupt polymer crystallization during processing. Both acceptors affect the kinetics and degree of polymer crystallization, but while the presence of $PC_{71}BM$ increases the polymer crystallinity, IDTBR slows polymer solidification, leading to lower

crystallinity in the blend. Ultimately this work sheds light upon the current state of the non-fullerene acceptor photovoltaic materials field and helps explain why successful polymer:NFA blends typically do not start with highly ordered polymers.

4.1 Introduction

4.1.1 Polymer aggregation and crystallinity with non-fullerene acceptors

Compared to fullerene acceptors, NFAs have vast potential for synthetic tunability which allows for the facile modification of light absorption, energetics, solubility, and solid-state microstructure. However, as high performance NFA OPVs have only been developed over the last few years with a focus on new materials design, there is a lack of work done on in-depth morphology characterization and exploring the transition from spin coating to blade coating. Especially for these new NFA systems, and even for the much more extensively studied fullerene systems, the exact nature of the drying process is not well understood due to a variety of changes happening on multiple different length scales. Optimized processing conditions are system dependent, and minimal changes such as adding a small amount of solvent additive or slightly altering the solution temperature can drastically change morphology and device performance.[134] Solvent additives, for example, have been shown via real-time morphology measurements to affect aggregation in solution[176] as well as the mechanism of drying with respect to aggregation vs. phase separation phenomena.[74]

Aside from aggregation in solution, polymer crystallinity in the solid state is often a significant contributor to device performance. Looking back at poly(3-hexylthiophene) (P3HT), it was seen that regioregular P3HT is significantly more ordered than regiorandom

P3HT on multiple length scales.[177] This increase in ordering when comparing regiorandom to regioregular P3HT drastically increases the device efficiency and thermal stability.[178] Moving beyond P3HT, there have been high-performing PCBM-based systems of both relatively amorphous polymers such as PBDTTT-EFT (PTB7-Th)[179] and more crystalline polymers such as PffBT4T-2OD.[29] However, in the rapidly expanding field of NFA-based OPVs, many of the well studied donor polymers used to blend with these new molecular acceptors have relatively few degrees of order. A few examples of minimally ordered polymer donors blended with NFAs to achieve PCEs over 12% include PBDB-T, its halogenated derivatives PBDB-T-2F and PBDB-T-2Cl (PM6 and PM7, respectively),[52,115] the regiorandom PTQ10,[95] and P2F-EHp.[180] Thus, there seems to be some correlation with polymer ordering in the solid state and compatibility with NFAs, the latter of which are typically more ordered than $PC_{71}BM$. Therefore, we sought to explore the interaction between a highly ordered donor polymer and an ordered NFA.

4.1.2 Random terpolymers for improved processability

PffBT4T-2OD (aka PCE11) is well known to have low solubility, as evident by its strong temperature dependent aggregation (TDA) and high crystallinity, and as a result requires both the coating solution and device substrate to be kept at elevated temperatures of ~100 °C during processing.[134] The low solubility is a result of a combination of fluorine atoms on the benzothiadiazole and the quarterthiophene (4T) unit, which both serve to increase polymer ordering and crystallinity in the solid state that ensures reasonably high charge mobilities that contributes to its high performance.[29] We previously reported on the random incorporation of increasing amounts of a shorter terthiophene (3T) unit into the backbone in order to improve processability.[11] With this method, we were able to reduce

the extent of TDA and process blend solutions onto room temperature substrates while maintaining solid state texture and device performance using $PC_{71}BM$ as the acceptor molecule. The general structure of these random copolymers is shown in Figure 4-1, the random terpolymers have a naming scheme of PffBT4T$_m$-co-3T$_n$-2OD, and PffBT4T-2OD has m = 1 and n = 0. Incorporating 10%, 30%, and 50% of 3T into the backbone (where m-n is 90-10, 70-30, and 50-50 respectively) gave devices with average PCEs of 9.5% compared to the 8.7% that was achieved with PffBT4T-2OD coated on a hot substrate (data reproduced in Supporting Table 4-1). When coating on a room temperature substrate, PffBT4T-2OD immediately gels up, giving a 5 µm thick film with negligible photocurrent, while the above-mentioned random copolymers (90-10, 70-30, and 50-50) achieved the same high efficiencies as the hot substrate devices. We attributed the enhanced processability to the increased entropy afforded by the randomly structured backbone as well as an increase in side-chain density on the 3T unit compared to 4T.

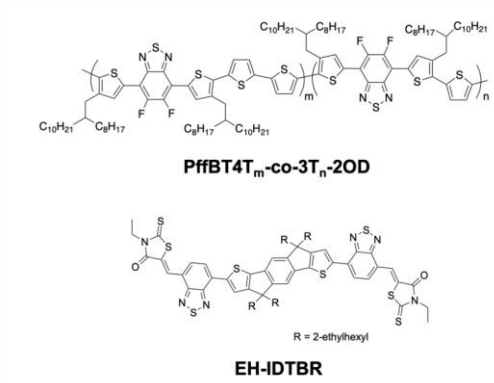

Figure 4-1 – Structures of the materials used in this study: PffBT4T$_m$-co-3T$_n$-2OD and EH-IDTBR.

Inspired by success of the random copolymer approach toward improving polymer processability while maintaining performance, we explored NFAs to blend with this family

of polymers. PffBT4T-2OD and its derivatives, when blended with IDTBR (Supporting Table 4-1), have achieved high performing solar cells with greater open circuit voltages (V_{OC}) and lower current densities relative to their PCBM counterparts.[50,181] A higher voltage is derived from more favorable energy levels, with IDTBR having a higher electron affinity (EA) than PCBM, thus increasing the difference between the acceptor EA and donor ionization potential (IP), which determines the maximum possible V_{OC}. Furthermore, by extending the side-chain length of PffBT4T-2OD from 2-octyldodecyl (2OD) to 2-decyltetradecyl (2DT), an even greater enhancement in photovoltaic performance was demonstrated from a wide variety of single solvent solutions deposited via spin coating.[51] Notably, while this study from Wadsworth et al. used heated solutions (T_{sol} = 100°C) and substrates (T_{sub} = 100 °C) for chlorobenzene coating, non-halogenated solutions were processed from room temperature solutions onto room temperature substrates. Side chain extension effectively breaks-up the polymer aggregation relative to PffBT4T-2OD, as evident by a reduced temperature required to blue shift the UV/vis absorption spectra (45 °C vs. 75 °C). Similar random terpolymer techniques coupled with increasing the side-chain density on the overall repeat unit have been shown to improve polymer compatibility with NFAs.[182] Furthermore, the enhanced solubility and processability will be more important for blade coating studies, where the active layer solution concentration is increased twofold when moving from spin coating to blade coating, so using polymers that are already close to their solubility limit can introduce challenges in film deposition.[106] Given that our random terpolymers are similarly easier to de-aggregate relative to PffBT4T-2OD, we hypothesized that they would behave similarly well with IDTBR and for blade coating studies.

Our group's recent work explored the effect of terpolymer composition, i.e. aggregation, on device performance and morphology of IDTBR blends processed via spin coating.[183] Using a heated solution (T_{sol} = 100 °C) and a heated substrate ($T_{sub} \approx$ 100 °C), the blends were analyzed with morphological and electrical characterization techniques. In contrast to the fullerene active layers, which were cast from a 1:1 chlorobenzene:o-dichlorobenzene solvent mixture with 3% 1,8-diiodooctane solvent additive, the IDTBR active layers were cast from pure chlorobenzene. Unlike the fullerene devices, which featured comparably high performance among the three random terpolymers (90-10, 70-30, and 50-50), the IDTBR devices showed higher sensitivity to polymer structure (Supporting Table 4-1). Notably, 90-10 was the champion polymer with solutions processed onto hot substrates, with an average PCE of 8.7%. Moving to 70-30, the average PCE drops to 6.8% due to slightly lower current and fill factor, and 50-50 performance drops even further to 2.2%. This study highlights the importance of strong TDA in solution on the resultant solid state blend microstructure when using IDTBR. From resonant soft X-ray scattering (RSoXS) data, large scale domains of ~100 nm were present in all blend films. However, compared to blends with 70-30 and 50-50, the blend with 90-10 has a broad distribution of smaller domains, suggesting a multiscale morphology with intermixed domain interfaces, which should be good for exciton dissociation.

To that end, we trialed a series of IDTBR devices processed via spin coating with two thermal conditions just as our previous studies on fullerene and IDTBR blend devices: with a heated substrate ($T_{sub} \approx$ 100 °C) and with a room temperature substrate, both with heated solutions (T_{sol} = 110 °C). Power conversion efficiencies are provided in the supporting information. Unlike the PCBM devices, which featured comparably high

performance among the three polymers (90-10, 70-30, and 50-50) and two thermal conditions, the IDTBR devices showed higher sensitivity to both polymer structure and thermal condition. Notably, 90-10 was the champion polymer with solutions processed onto hot substrates, with an average PCE of 8.7%. Moving to 70-30, the average PCE drops to 6.8% due to slightly lower current and fill factor, and 50-50 performance drops even further to 2.2%. Using room temperature substrates, 90-10 performance drops to 5.4% due to low current and fill factor and 70-30 and 50-50 performance remains low, which we attribute to coarser phase separation. These results suggest that polymer aggregation is helpful in improving the morphology of IDTBR blend devices, but a fast quench associated with dropping a hot solution at the threshold for aggregation on a cool substrate can disrupt solid state microstructure, as evident with the 25 °C solution UV/vis spectra of 90-10 which is identical to that of PCE11, shown in Figure 2a. Others have shown that increased crystallinity of PCE11, which is often related to aggregation, leads to increased device performance due to reduced recombination losses.[184]

In attempt to elucidate the optimal levels of aggregation as a function of solution and substrate temperatures, we expanded our original random terpolymer family with the synthesis of PffBT4T$_{80}$-co-3T$_{20}$-2OD (80-20). In this study, we have examined in depth the spin and blade coating of 80-20 with both PC$_{71}$BM and EH-IDTBR to understand the effect of processing temperature on solution and solid state properties. We sought to highlight the relationship between solution state polymer aggregation, solid state microstructure, and device performance. We highlight the changes when comparing an amorphous acceptor like PC$_{71}$BM to an acceptor like IDTBR which is shown to order more strongly. Through spin coating and blade coating device characterization, and a

combination of solid state and real-time processing characterization, we attempt to clarify the relationship between 80-20, $PC_{71}BM$, and IDTBR.

4.2 Results and discussion

4.2.1 Polymer properties

Polymer synthetic details and standard characterization (^{1}H-nuclear magnetic resonance spectroscopy, elemental analysis, differential pulsed voltammetry, and gel permeation chromatography) can be found in the supporting information (Supporting Figure 4-1, Supporting Figure 4-2, Supporting Figure 4-3, and Supporting Figure 4-4). The 25 °C solution UV/vis spectra of two different batches of 80-20 are shown in Figure 4-2(a), along with the original family of random copolymers reproduced from our previous work.[11] The UV/vis absorption profiles of both polymers lie between the original 90-10 and 70-30 polymers, with the higher weight M_n = 62 kDa showing a distinct long wavelength shoulder, indicating slight deaggregation at 25 °C. The slightly lower weight batch, at M_n = 51 kDa, only has a small hint of the long wavelength shoulder with an absorption profile that looks like 70-30. As a result, with the 80-20 composition, we have hit the very edge of room temperature aggregation, which may have an effect on room temperature processing relative to the adjacent compositions of 90-10 and 70-30. Complete temperature dependent UV/vis solution spectroscopy for both polymers is shown in Supporting Figure 4-5, and for both polymers, 45 °C is enough to remove all aggregate character. The thermal properties of the two polymers are also quite similar, with the second heating and cooling scans as measured by differential scanning calorimetry (DSC) shown in Figure 4-2(b). The curves have the same general shape, with peak melt transition temperatures (T_m) of 257 °C

and 259 °C for the 51 kDa and 62 kDa polymers, respectively, and peak crystallization temperatures of 239 °C and 240 °C. The average of the melt and crystallization temperatures are shown as a function of 3T composition, in Figure 4-2(c), again indicating that this new batch of polymer has expected properties lying between 90-10 and 70-30. 2D grazing incidence wide angle x-ray scattering (GIWAXS) patterns also show that the two molecular weight batches of 80-20 have similar microstructures (Supporting Figure 4-6).

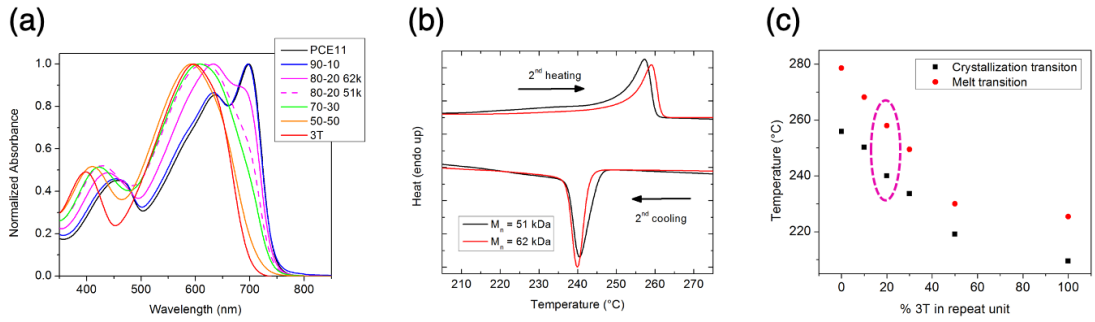

Figure 4-2 – (a) Solution UV/vis spectra of the original family of PCE11 random terpolymers as well as two different samples of 80-20 composition designed for this study. Solutions are made at 0.02 mg mL^{-1} in o-DCB and are at 25 °C. (b) Second differential scanning calorimetry (DSC) scans of two different batches of pristine 80-20 polymer. (c) DSC melt and crystallization temperatures from the peak of the transition for the 2nd scan. Note that both molecular weight samples have the same transition temperatures within 2 °C. Data for the original family is taken from our previous work.[11]

4.2.2 Spin coating morphology and performance

In order to demonstrate the ability to process this new polymer over a range of temperatures and understand morphological changes as a function of temperature, we began with spin coated devices at the two previously mentioned thermal conditions, followed by a third where we attempted to further lower the thermal budget required for processing. Again using a room temperature substrate ($T_{sub} \approx 22$ °C), we allowed the

solution to cool to ≈ 50 °C before coating. The GIWAXS pattern for the 80-20:$PC_{71}BM$ blend film cast from a 110 °C solution onto a 100 °C substrate is shown below in Figure 4-3(a), while the other two thermal conditions are shown in Supporting Figure 4-7. There are no significant changes in the scattering features across the three different films as the total heat used for processing (T_{sol} + T_{sub}) is reduced. The polymer is in an overall face-on orientation, with strong out-of-plane π-π stacking at $q_z \approx 1.7$ $Å^{-1}$ (d ≈ 3.7 Å) and up to three orders of lamellar stacking, predominantly in the in-plane direction. The isotropic halo at $q \approx 1.4$ $Å^{-1}$ (d ≈ 4.5 Å) corresponds to $PC_{71}BM$ aggregation. The GIWAXS pattern for the 80-20:IDTBR film coated from the same 110 °C solution / 100 °C substrate condition is shown in Figure 4-3(b). IDTBR lamellar stacking is visible exclusively in the in-plane direction, at $q_{xy} \approx 0.4$ $Å^{-1}$ (d ≈ 15.7 Å), indicating that this molecule is predominantly ordered in a face-on orientation, with expectedly shorter lamellar stacking distances than 80-20 due to its shorter side chains. The subtly visible out-of-plane π-π stacking peak again corresponds to the polymer as it resides at the same q value (1.7 $Å^{-1}$) as for the $PC_{71}BM$ film. For the other two thermal conditions shown in the supporting information (Supporting Figure 4-7), the π-π stacking peak for IDTBR is visible; it resides at a slightly smaller q value of ≈ 1.6 $Å^{-1}$, which corresponds to a slightly larger stacking distance (d ≈ 3.9 Å) relative to the polymer's π-π stacking. What is most striking about the IDTBR blend films is the apparent suppression of polymer ordering compared to the $PC_{71}BM$ blend films. The (300) lamellar stacking peak visible at $q_{xy} \approx 0.8$ $Å^{-1}$ in the PCBM film is not visible for the IDTBR blend film, and the (200) peak at $q \approx 0.5$ $Å^{-1}$ is weaker, localized to the out-of-plane direction, and is broader, the latter of which indicates a reduction in order within the

lamellar stack. These observations could explain the overall drop in performance when moving from PCBM to IDTBR solar cells for this family of polymers.

In order to quantify this suppression of order, we conducted pole figure analysis of the polymer's (100) lamellar stacking peak to determine the relative degree of crystallinity (rDoC) and the Hermans orientation parameter (S) of the blend films. The pole figure, shown in Supporting Figure 4-8, is a representation of the angular distribution and total scattering volume of (100) lamellar crystallites in the film. The area under the curve represents the relative volume of scattering entities, which is a function of the crystallinity. There is a drastic increase in intensity at large angles for the $PC_{71}BM$ BHJ, resulting in a film that has over twice as much (100) lamellar polymer crystallinity compared to the IDTBR BHJ (rDoC of 1.00 vs. 0.43). The higher intensity of lamellar stacking is at large polar angles, indicating that the lamellar stacks are primarily oriented in the in-plane direction, and the polymer is subsequently in a face-on orientation. The Hermans orientation parameter, S, represents the average orientation of the lattice plane, and is a number from -0.5 to 1.0, where -0.5 represents the case of all lattice planes being oriented perpendicular to the substrate normal and 1.0 represents the case of all lattice planes being oriented parallel to the substrate. For (100) lamellar stacking, which we are measuring here, S = -0.5 is completely face-on and S = 1.0 is completely edge-on with respect to the substrate. Comparing the polymer properties in the $PC_{71}BM$ BHJ to the IDTBR BHJ, the polymer is in a more face on orientation with PCBM, while it is relatively isotropic when blended with IDTBR.

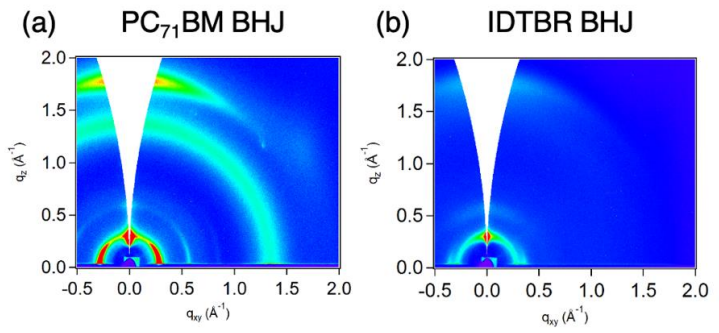

Figure 4-3 – GIWAXS patterns of blend films of 80-20 and (a) $PC_{71}BM$ or (b) EH-IDTBR. Films were processed via spin coating 110 °C solutions onto 100 °C substrates. (c) Relative degree of crystallinity (rDoC) and Hermans orientation parameter (S) of the blend films, calculated from the sin χ corrected pole figures of the (100) lamellar stacking peak. The pole figure is shown in Supporting Figure 4-8.

The corresponding statistics for devices made from these conditions above are shown in Table 1. While keeping the fullerene blend solution hot yields comparable device results, there is a statistically significant drop in performance when cooling the solution down to 50 °C just before coating. These fullerene device results are identical to the previously reported results from 90-10 and 70-30, showing high performance across all thermal conditions. The results with this polymer and IDTBR indicated that we effectively bridged the gap between 90-10 and 70-30, with comparable performance on hot substrates (8.5% PCE) and a much smaller drop in efficiency when coating onto room temperature substrates (6.9% PCE). Therefore, with 80-20 as our champion polymer across all spin coating thermal conditions, we scaled it up for in depth morphological characterization and blade coating studies. To the best of our knowledge, there are limited in depth morphological studies on thermal and temporal effects when comparing the processing of fullerene vs. non-fullerene acceptors, as with spin coating vs. blade coating.

Table 4-1 – Spin coated device statistics for both acceptors each processed at three different thermal conditions. Values were averaged over 8 pixels and error bars indicate one standard deviation from the mean. Device architecture: Glass/ITO/ZnO/active layer/MoO_x/Ag. Active area = 4.9 mm^2 as defined with an aperture.

Acceptor	Solution temp. (°C)	Substrate temp. (°C)	J_{SC} (mA cm^{-2})	V_{OC} (V)	FF (%)	PCE (%)
$PC_{71}BM$	110	100	18.1 ± 0.5	0.72 ± 0.01	73 ± 1	9.5 ± 0.4
	110	25	17.6 ± 0.4	0.74 ± 0.01	72 ± 1	9.4 ± 0.3
	50	25	17.6 ± 0.6	0.72 ± 0.01	71 ± 2	9.0 ± 0.4
IDTBR	110	100	14.4 ± 0.7	1.01 ± 0.03	58 ± 2	8.4 ± 0.7
	110	25	15.0 ± 1.5	1.00 ± 0.03	50 ± 4	6.9 ± 0.7
	50	25	15.5 ± 1.0	1.01 ± 0.02	45 ± 4	6.1 ± 0.5

4.2.3 Blade coating morphology and performance

In order to understand how thermal changes in the processing conditions would translate to blade coating, we explored polymer behavior as it is coated from a pristine solution. With our custom blade coater, we are able to independently heat the stage and solution, as well as monitor the UV/vis absorption spectra of the deposited wet film as it dries. As mentioned before with the temperature dependent UV/vis spectra (Supporting Figure 4-5), this polymer is slightly aggregated at 25 °C, but is in a more molecularly dissolved state at just 45 °C. To establish behavior at the thermal extremes with respect to the stage temperature, the polymer was coated from a 100 °C solution in chlorobenzene onto either a 25 °C or a 90 °C stage. The UV/visible absorption spectra were acquired in real time during the coating and drying process, and selected spectra during the drying transition are shown in Figure 4-4 (a) and (b), for the 25 °C and 90 °C stage respectively. The high temperature of the coating solution ensures that as the solution is deposited, the polymer is in the blueshifted, deaggregated state with peak absorption around 580 nm.

However, once the solution hits a cool substrate, the polymer is immediately aggregated with its peak absorption redshifted to around 625 nm. As the film dries over the course of ~ 150 seconds, the spectrum evolves with a distinct long wavelength shoulder. Conversely, with the stage heated up to 90 °C, the polymer is coated in its dissolved state, and we can observe the aggregation transition concurrently with solvent evaporation that starts just 3.1 seconds after coating.

These drastically different aggregation dynamics result in different solid state morphologies measured via GIWAXS, as shown in Figure 4-4 (c) and (d). The 25 °C stage cast film shows the polymer in an edge-on orientation, with high order lamellar stacking up to (400) in the out of plane direction and a strong π-π stacking peak (010) in the in-plane direction. Conversely, the 90 °C stage cast film has a slight face-on preference, with relatively isotropic lamellar stacking and a π-π stacking peak that favors the out-of-plane direction. Thus, we can conclude that aggregate morphology in the solution state directs the nanoscale polymer microstructure. This slight face-on preference is correlated with improved device performance when blade coating $PC_{71}BM$ blend films, as seen with the spin-coated $PC_{71}BM$ devices (Figure 4-3 and Supporting Figure 4-6). However, these results differ from the spin coating results, where drastically changing the substrate temperature while maintaining a heated solution did not affect solid state morphology. This is likely due to two factors: an almost twofold increase in polymer concentration, and large heat sink of the metal blade coater stage compared to the spin coater chuck.

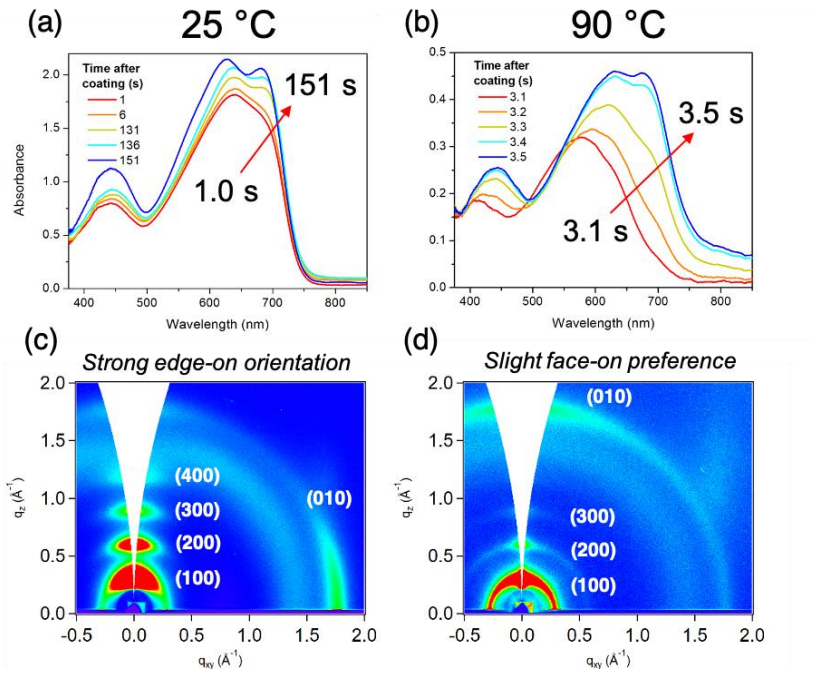

Figure 4-4 – (a,b) In situ UV/vis spectroscopy of blade-coated films of pristine 80-20 cast from a 100 °C solution onto either a (a) 25 °C or (b) 90 °C substrate. (c,d) resulting GIWAXS patterns from the films cast at the two substrate temperatures above.

Since increasing the total solution concentration, relative to spin coating, is required for blade coating in order to generate films of the same thickness, we sought to combat the issue of a having a large heatsink for the substrate by moderately heating the stage to only 50 °C. This keeps the polymer in a de-aggregated state as evident by the temperature dependent UV/vis solution spectroscopy described above (Supporting Figure 4-5). As seen in Supporting Figure 4-9 and Supporting Figure 4-10, both for pristine polymer and polymer:$PC_{71}BM$ blend films, increasing the substrate temperature from 25 °C to 50 °C is enough to completely alter the polymer crystallite orientation toward more isotropic, which should be good for transporting charges through the relatively thick active layers employed in devices here (200 nm – 400 nm). Less drastic changes were seen from increasing the stage temperature further, to 90 °C, at all three solution temperatures studied.

In general, pristine polymers cast at room temperature adopt an edge-on orientation, while polymer:PCBM blends adopt a more face-on orientation; therefore it is likely that solidification is directed by not only the solution-air and solution-substrate, but also the presence of acceptor. This provides further evidence that IDTBR is the source of polymer crystallization suppression as seen for the blade coated blends (Supporting Figure 4-11) as well as the spin coated blends as discussed above. This crystallization suppression can be seen in the pole figure of the blade coated blends cast from 50 °C solutions onto a 50°C stage, where the IDTBR BHJ has significantly lower polymer crystallinity than the $PC_{71}BM$ BHJ (Supporting Figure 4-12). Interestingly, polymer crystallinity is higher in the $PC_{71}BM$ blend compared to the pristine polymer, suggesting that $PC_{71}BM$ is influencing polymer behavior during solidification.

Using the 50 °C stage as our starting point for blade coated devices, as it is sufficient to move into the more isotropic crystalline polymer region, we fabricated PCBM devices varying the solution temperature from 50 °C to 100 °C. Lowering the solution temperature below 50 °C causes gelation that makes blade coating difficult, and temperatures above 100 °C are challenging to maintain reliably during deposition with a handheld syringe or micropipette. Device results are shown below in Table 4-2. An increase in film thickness as a result of increased viscosity with decreasing temperature explains the increase in short circuit current density from 11.5 mA cm^{-2} to 17.4 mA cm^{-2}. However, this does not also explain the increase in V_{OC} or fill factor. It is possible that the drastic difference in solution and substrate temperature causes the polymer to solidify aggressively on the substrate, and since we are building inverted devices with the electron transport layer on the substrate, excessive polymer solidification at this interface compared to fullerene will lower the

voltage.[62] At these same conditions, IDTBR also reaches a maximum power conversion efficiency of 7.5 %, which is about one percent lower than the spin coated case, comparable to the trend in the $PC_{71}BM$ devices. A summary of the optimized results is presented in Table 4-3.

Table 4-2 – Statistics of blade coated 80-20:$PC_{71}BM$ devices deposited on a 50 °C stage while varying the solution temperature. The solution was initially stirred at 100 °C and was allowed to cool gradually between coatings.

Solution temp. (°C)	J_{SC} (mA cm^{-2})	V_{OC} (V)	FF (%)	PCE (%)
100	11.5 ± 0.7	0.65 ± 0.01	59 ± 1	4.4 ± 0.3
85	14.4 ± 0.4	0.66 ± 0.01	63 ± 1	6.0 ± 0.3
75	14.7 ± 0.8	0.68 ± 0.01	67 ± 1	6.6 ± 0.4
50	17.4 ± 0.5	0.70 ± 0.01	68 ± 1	8.2 ± 0.4

Table 4-3 – Optimized device data for spin coating and blade coating with $PC_{71}BM$ and IDTBR. Spin coated data are optimized at a solution temperature of 110 °C and substrate temperature of ≈ 100 °C. Blade coated device data are optimized at a solution temperature of 50 °C and a stage temperature of 50 °C.

Acceptor	Method	J_{SC} (mA cm^{-2})	V_{OC} (V)	FF (%)	PCE (%)
$PC_{71}BM$	Spin	18.1 ± 0.5	0.72 ± 0.01	73 ± 1	9.5 ± 0.4
	Blade	17.4 ± 0.5	0.70 ± 0.01	68 ± 2	8.2 ± 0.4
IDTBR	Spin	14.4 ± 0.7	1.01 ± 0.03	58 ± 2	8.4 ± 0.7
	Blade	12.5 ± 0.6	1.02 ± 0.06	60 ± 1	7.5 ± 0.3

4.2.4 In situ GIWAXS and WLI

In order to understand how the resultant morphology is established during the coating process, we conducted real-time GIWAXS measurements on this system during the blade coating process. We also simultaneously measured white light interferometry (WLI) in order to monitor film thickness over time. Together, these two measurement techniques are used to correlate crystallization with the concentration of the wet film in

order to characterize blend component solubility and solidification. Using the optimized blade coating conditions with both a solution and substrate at 50 °C, we coated solutions of pristine polymer, pristine IDTBR, the polymer:$PC_{71}BM$ blend, and the polymer:IDTBR blend. However, in order to begin with a direct comparison, all three systems were coated from chlorobenzene. This solvent system accurately represents the pristine polymer and IDTBR cast films in the previously discussed experiments but does not represent the optimum conditions for the $PC_{71}BM$ blend.

Shown in Figure 4-5 is a compilation of the data used to understand the in situ experiment: the top panels are of the dried films, and the bottom panels are of the real time experiment. The in-plane line cuts were chosen for comparison because, while the polymer (100) lamellar ordering is relatively isotropic, the IDTBR lamellar ordering is predominantly in-plane. Figure 4-5(a) shows the in-plane line cuts from the three dry films in order to identify the region of interest to explore with the in situ measurement. Since the strongest scattering features are from the lamellar stacking peaks, those were chosen for real-time analysis. The 2D GIWAXS image of the polymer:IDTBR dry film is shown in Figure 4-5(b). The in-plane region from 0.1 $Å^{-1} < q_{xy} < 0.6$ $Å^{-1}$, which is chosen to capture the various first-degree lamellar features of these blend systems, is highlighted with a black box. While the out-of-plane π-π stacking peaks for the polymer and IDTBR also lie at different q values, the signal is much weaker, and that q-range is obfuscated by the broad isotropic scattering due to solvent. This low q region is expanded and monitored as a function of time after coating as shown in Figure 4-5(d) below. The q-range shown in Figure 4-5 is negative because we are using the left side of the area detector in order to avoid a gap in the right side of the detector that lies at positive q (visible at the right edge

of the 2D pattern in Figure 4-5(b)). Scattering features reflected across q_{xy} = 0 Å^{-1} are symmetric, therefore subsequent references in the text will use positive numbers for simplicity.

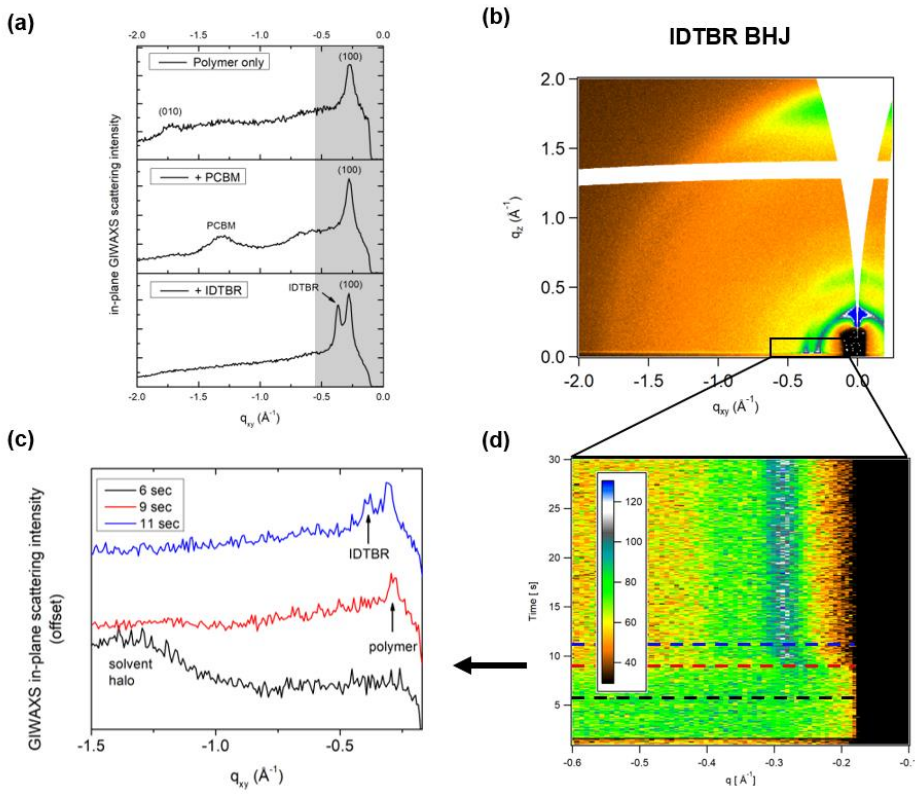

Figure 4-5 – (a) GIWAXS in-plane line cuts of dry films after the in situ experiment, featuring pristine 80-20, the $PC_{71}BM$ blend, and the IDTBR blend. Peaks that will be tracked are highlighted in grey: first order scattering for both the polymer and IDTBR. (b-d) In situ workflow and data analysis: (b) 2D GIWAXS scattering pattern of the 80-20:IDTBR blend with the in-plane region from -0.6 Å^{-1} < q < -0.1 Å^{-1} highlighted and expanded into (d) the false color contour plots of the in plane line cuts over time, highlighting the solvent halo at short times, the polymer (100) peak at low q (q = 0.28 Å^{-1}), and the IDTBR peak at higher q (q = 0.37 Å^{-1}). (c) Select line cuts from the false color contour plots highlighting three aspects of the coating process: black at 6 seconds, early coating dominated by the solvent halo; red at 9 seconds, emergence of the polymer peak; and blue at 11 seconds, IDTBR peak

and dried film. These in situ runs are analyzed in depth in the supporting information.

The line cuts presented in Figure 4-5(c) were chosen to highlight specific stages in the coating process, and their origins are labeled with dotted colored lines in the false color contour plot in Figure 4-5(d). In early times after coating, indicated by the black curve taken at 6 seconds, the signal is dominated by broad isotropic scattering due to the solvent halo, the broad peak around q = 1.3 $Å^{-1}$. No significant features appear in the low q region where we expect to see 80-20 and IDTBR lamellar stacking. At 9 seconds, the red curve shows the emergence of a polymer peak as well as a strong decrease in the amount of solvent in the film. Two seconds later, the blue curve shows the emergence of the IDTBR peak at q = 0.37 $Å^{-1}$ next to the polymer peak at q = 0.28 $Å^{-1}$, at which point the film is dry and the final morphology is established.

In order to quantify the wet film concentration at each of these steps of the drying process, WLI was used to monitor film thickness over time. A coaxial fiber-optic reflection probe sends white light into the film and collects the light reflected through the film and back into the fiber-optic probe. The reflected light spectrum is a convolution of the absorption of the film and the broadband interference between the incident and reflected beams as a function of layer thickness and the refractive index of the materials. Therefore, ellipsometry of the dry films was performed and the subsequent time dependent reflection data fit to an optical model. The ellipsometry results of pristine polymer and IDTBR are presented in Supporting Figure 4-13, and the modeled wet and dry films are presented in Supporting Figure 4-14. This modeled data is then used to calculate wet film thickness as a function of time, which is shown for the four coating conditions in Supporting Figure

4-15. Combined with the GIWAXS peak evolution data, this data can be used to calculate the solids volume fraction of individual materials during the coating process, in order to measure how long each material stays in solution before solidifying.

In order to rigorously quantify the crystallinity during coating, the evolution of the peaks in the line cuts shown above in Figure 4-5 (c) and (d), the lamellar stacking peaks were fit to a constrained Gaussian. The fitting process and results are shown in Supporting Figure 4-16, Supporting Figure 4-17, Supporting Figure 4-18, Supporting Figure 4-19, and Supporting Figure 4-20; the IDTBR BHJ was fit twice, separately for the polymer peak and the IDTBR peak. We examined each lamellar peak in 0.2 s intervals and fit the peaks to a Gaussian function with a constrained width and positive area. Peaks were manually evaluated in order to determine goodness of fit and remove curves with a high degree of noise, as well as curves that represent a film that has already dried. The peak heights as a function of time were analyzed with a linear regression and extrapolated to a peak height of zero in order to estimate the onset of crystallization. This assumes that volume of growing crystals expands linearly. The wet film thickness at this time was used to measure the solids volume fraction within the film. Those results are summarized in Supporting Table 4-3, with the solids volume fraction alone presented in Table 4-4.

Table 4-4 – Volume fraction of solids at the onset of diffraction, calculated from in situ GIWAXS and WLI, measured for 80-20 diffraction (at q = 0.28 $Å^{-1}$) and IDTBR diffraction (q = 0.37 $Å^{-1}$).

	Volume fraction of solids at diffraction onset (%)	
	80-20 diffraction	**IDTBR diffraction**
80-20 only	11.5 polymer	-

IDTBR only	-	15 IDTBR
80-20:$PC_{71}BM$ BHJ	7.6 total / 3.5 polymer	-
80-20:IDTBR BHJ	9.7 total / 4.5 polymer	13 total / 7.1 IDTBR

For the 80-20 only film, polymer diffraction onset is at 12.2 seconds, which corresponds to a solids volume fraction of 11.5 %. For comparison, the IDTBR diffraction onset for the pristine IDTBR film is at a solids volume fraction of 15 %, suggesting that IDTBR is slightly more soluble than the polymer in chlorobenzene. For the $PC_{71}BM$ BHJ, the total solids volume faction at the onset of diffraction is 7.6 %, which corresponds to a polymer volume fraction of 4%. Therefore, with $PC_{71}BM$, the polymer crashes out of solution earlier than the pristine case, indicating that $PC_{71}BM$ acts as a mild anti-solvent for the polymer. We showed earlier with the pole figure of the blade coated blends that polymer crystallinity is enhanced when $PC_{71}BM$ is added to the coating solution; this supports the ant-solvent hypothesis: the fact that $PC_{71}BM$ forces the polymer out of solution leading to higher crystallinity. In the IDTBR BHJ, the total solids content at the onset of polymer diffraction is comparable to the polymer only case (9.7 % vs. 11.5 %); therefore, IDTBR helps solubilize the polymer and extends the drying window to the pristine case. This could delay the onset of crystallization and limit the final polymer crystallinity in the dried film. The rate of crystallization for polymer in IDTBR is the fastest of all the crystallization transitions that were measured (Supporting Figure 4-20), so rapid crystal formation is not likely to establish an optimum BHJ that supports high J_{SC} and FF like we observe for the $PC_{71}BM$ devices.

4.3 Conclusions and perspective

In agreement with our previous work, the work presented here supports the idea that developing polymer crystallinity via aggregation is important for BHJ morphology in IDTBR based NFAs.[183] Similarly, Hamid et al. have recently shown that with blends of PffBT4T-2DT and either O-IDTBR or O-IDFBR, solid-liquid de-mixing via aggregation dictates phase separation behavior and prevents over coarsening of the system.[185] Park et al. have used random terpolymers based on the PffBT4T-2OD repeat unit and have found gradual crystallization to be helpful in forming a distribution of domain sizes, which often improves photovoltaic efficiency with small domains that are beneficial for exciton diffusion and large domains that are beneficial for charge transport.[64,186] Baran et al. have shown that for a blend of P3HT with IDTBR, using a small addition of the less ordered acceptor molecule IDFBR to the blend changes phase behavior and ultimately drives up the photovoltaic performance.[187] Too much IDFBR was shown to vitrify the IDTBR domains while maintaining order within pure domains of P3HT, highlighting the complexity of ternary systems. Our system here is different, in that despite the strong aggregation of PffBT4T$_{80}$-co-3T$_{20}$-2OD, its crystallinity was affected by the presence of acceptor. In general, it is important to investigate how polymer molecule blends changes the solidification dynamics and resultant microstructure relative to the pristine behavior, as we have done here.

The development of polymer order, essential for optimum photovoltaic performance, is dependent on the identity of the acceptor blended with this particular aggregated polymer, PffBT4T$_{80}$-co-3T$_{20}$-2OD. Through thermal analysis we discovered the minimum temperature required to process in a slightly de-aggregated state, which was sufficient to develop isotropic semi-crystalline polymer structure. However, the nature of

the blend films at a fixed temperature is dependent on the acceptor molecule, whereby increasing the crystallinity of the acceptor further disrupts the crystallinity of the polymer. We observe through in situ GIWAXS and WLI that $PC_{71}BM$ acts as an anti-solvent and pushes the polymer to solidify and crystallize. The presence of IDTBR in the blend film slows the polymer crystallization relative to the pristine and $PC_{71}BM$ blend, and the abrupt crystallization of IDTBR locks the polymer into a lower crystallinity state. Due to a lack of IDTBR crystallization until the end of the drying process, it appears both crystallizable materials affect each other, which explains why both the current and fill factor drop when comparing PCBM to IDTBR. Ultimately this work emphasizes the importance of choosing polymer:molecule pairs with complementary degrees of crystallinity in order to develop an optimum morphology, as well as the importance of monitoring the processing temperature of TDA polymers to tune aggregation and crystallinity.

4.4 Supporting information

4.4.1 Materials

All solvents and regents were purchased and used without further purification unless otherwise noted below. The zinc acetate dihydrate, ethanolamine and 2-methoxyethanol used for the ZnO synthesis were purchased from Sigma Aldrich. EH-IDTBR was purchased from Sigma Aldrich and compound 1 was purchased from SunaTech and used as received. The monomers 2 and 3 used for the synthesis of PffBT4T_{80}-co-3T_{80}-2OD were synthesized according to a literature procedure.[188,189] Chlorobenzene used for the polymerizations was dried over activated 4 Å molecular sieves for 48 hours before used and argon purged for at least 4 hours.

4.4.2 Characterization methods

^{1}H NMR and ^{13}C NMR spectra for all monomers and molecular precursors were acquired on a Varian Mercury Vx 300 MHz instrument using $CDCl_3$ as solvent; the residual $CHCl_3$ peak was used as a reference for all reported chemical shifts (^{1}H: $\delta = 7.26$ ppm, ^{13}C: $\delta = 77.16$ ppm).

^{1}H NMR for all polymers were acquired on a Bruker 400 MHz instrument using 1,1,2,2-tetrachloroethane ($C_2D_2Cl_4$) at 110 °C; the residual $C_2H_2Cl_4$ peak was used as a reference for all reported polymer chemical shifts (^{1}H: $\delta = 6.0$ ppm).

Gel permeation chromatography (GPC) was performed using a Tosoh EcoSEC high temperature GPC instrument with RI detector to determine the number average molecular weight (M_n), weight average molecular weight (M_w) and dispersity ($Đ$) for all polymers. Experiments were run using 1,2,4-trichlorobenzene (TCB) as eluent at 140 °C at a flow rate of 1 mL/min on two 7.8 mm x 30 cm, 13 μm TSK-Gel GMH_{HR}-H(S) HT2 columns in series. The instrument was calibrated using polystyrene standards (1,390-1,214,000 g/mol) and the data were analyzed using 8321GPC-WS analysis software. The GPC samples were prepared by dissolving the polymers in TCB at a 1 mg/mL concentration and stirred at 110 °C for at least 3 hours before filtering through a 0.45 μm PTFE filter.

Elemental analyses were conducted by Atlantic Microlab Inc. UV-vis absorption spectra were obtained on a Cary 5000 spectrometer. Film thicknesses were measured using a Bruker DektakXT profilometer. Electrochemical analysis was performed using an EG&G

Princeton Applied Research model 273A potentiostat-galvanostat. Cyclic voltammetry (CV) was performed at a 20 mV scan rate and differential pulse voltammetry (DPV) were performed using a 2 mV step size, 80 ms step time and 50 mV pulse amplitude. Voltammetry experiments were performed in a glove box using a standard three-electrode cell including a 0.07 cm^2 glassy carbon button working electrode, an Ag/Ag^+ (0.01 M $AgNO_3$) reference electrode and a platinum flag counter electrode. Polymer and NFA films were drop casted onto the working electrode from a 1 mg/mL chloroform solution and allowed to air dry. Electrochemical experiments were performed using dry acetonitrile with a $TBAPF_6$ supporting electrolyte at a concentration of 0.5 M in an argon filled glovebox. Ferrocene/ferrocenium (-5.12 V vs vacuum) was used as an internal standard calibrated against the Ag/Ag^+ reference electrode ($E_{1/2}$ = 85 mV).

Differential scanning calorimetry was performed from -50 °C to 300 °C at a scan rate of 20 °C/min, using a TA Instruments Q200 DSC.

Static GIWAXS samples of pristine polymer or polymer:acceptor blends were prepared on silicon wafer substrates. Static GIWAXS films were measured at two different places. Some data were collected at Stanford Synchrotron Radiation Lightsource (SSRL) beamline 11-3 in a helium-filled chamber with an X-ray wavelength of 0.976 Å and sample to detector distance of 250 mm at an incident angle of 0.13°. Spectra were recorded on a Rayonix MARCCD area detector. The remainder of the GIWAXS data was collected at Brookhaven National Lab, NSLS-II, 11-BM Complex Materials Scatting beamline, in a sample chamber under vacuum, with scattering from a 13.5 keV beam collected on an area detector. Static GIWAXS data was processed using the Nika software package for Wavemetrics Igor, in combination with WAXStools.[66,133]

In situ GIWAXS data were collected at Brookhaven National Lab, NSLS-II, 11-BM Complex Materials Scatting beamline. Solutions were prepared and loaded into a glass syringe, which itself was loaded into a temperature-controlled syringe jacket prior to deposition. During the coating process, simultaneous white light interference and GIWAXS data were collected over time on a area detector.

Solar cells were constructed in an inverted architecture comprising of glass/ITO/ZnO/polymer:acceptor/MoO_3/Ag. Before device processing, the patterned ITO-coated glass substrates (Latech Scientific Supply Pte. Ltd., sheet resistance 10 Ω/sq) were cleaned by scrubbing with sodium dodecyl sulfate in Millipore water, followed by sonicating sequentially with sodium dodecyl sulfate in Millipore water, pure Millipore water, and finally isopropanol for 10 minutes each. The cleaned substrates were blown dry with argon and placed in a UV/O_3 chamber for 10 minutes.

For the electron transport layer, a ZnO solution was made with 0.11 M Zn acetate dihydrate and 0.11 M ethanolamine combined in 2-methoxyethanol (Sigma Aldrich). This solution was stirred overnight at room temperature, then filtered with a 0.45 μm PTFE syringe filter before use. The ZnO solution was deposited on the cleaned ITO substrates by spin-coating for 30 seconds at 4000 rpm in ambient atmosphere to get a layer thickness of ~30 nm. After spin-coating, the ZnO layer was annealed in air at 150 ˚C for 10 min followed by slow cooling to room temperature and brought into an Ar filled glovebox for active layer spin coating or left in air for immediate active layer blade coating.

Active layer solutions were prepared in an Ar filled glovebox. For spin coating, PCBM blend solutions were made with a polymer concentration of 11 mg/mL, with a

polymer:PCBM weight ratio of 1:1.2 in a mixed solvent of 1:1 chlorobenzene:o-dichlorobenzene with 3%$_v$ of 1,8-diiodooctane as a solvent additive. IDTBR blend solutions were made with a polymer concentration of 6 mg/mL, with a polymer:IDTBR weight ratio of 1:1.2 in pure chlorobenzene solvent. For blade coating, PCBM blend solutions were made with a polymer concentration of 20 mg/mL, with a polymer:PCBM weight ratio of 1:1.2 in a mixed solvent of 1:1 chlorobenzene:o-dichlorobenzene with 3%$_v$ of 1,8-diiodooctane as a solvent additive. IDTBR blend solutions were made with a polymer concentration of 20 mg/mL, with a polymer:IDTBR weight ratio of 1:1.2 in pure chlorobenzene solvent. Solutions were stirred at 110 °C for 2 hours before use.

For spin coating, the active layer solution was coated on top of the ZnO layer in an Argon-filled glove box at 600 rpm for 30 sec. Prior to spin coating, both the polymer solution and ITO substrate were preheated on a hot plate at 110 ˚C for 5 minutes. For films deposited on a heated substrate, a custom fabricated chuck for the spin coater with elevated edges was used to prevent heat dissipation from the hot substrate to the spin coater. After coating, PCBM films were immediately brought into the vacuum chamber of a thermal evaporator to remove residual DIO additive without disturbing the film. IDTBR films dried within minutes, and some were thermally annealed inside an argon filled glovebox at 120 °C for 5 minutes.

For ambient air blade coating, a custom-built blade coater with a glass blade and a stage with heaters was used. Solutions were stirred on a hot plate at various temperatures before use, and the stage was heated to various temperatures before coating. Solutions were used within 1 hour of being brought outside the glovebox and were not reused once opened to air for a set of coatings. For blade coating of PCBM blend films, a blade gap of 300 μm

was used with a speed of 38 mm/s. For blade coating of IDTBR blend films, a blade gap of 150 µm was used with a speed of 26 mm/s.

After coating, PCBM films were immediately brought into the vacuum chamber of a thermal evaporator to remove residual DIO additive without disturbing the film. IDTBR films dried within minutes and did not require immediate vacuum treatment. Some were thermally annealed inside an argon filled glovebox at 120 °C for 5 minutes.

To apply top contacts, the samples were placed in a vacuum chamber for 1 – 2 hours to reach a target pressure of 1×10^{-3} Pa (1×10^{-5} mbar). The top electrodes MoO_3 and Ag were deposited by vacuum deposition to layer thicknesses of 15 nm and 160 nm, respectively, to obtain complete solar cell devices with an electrode overlap area of 7 mm². Fast drying Ag paint (Ted Pella, 16040-30) was applied to the ITO electrodes to improve contact with the device switch-box. An aperture with area 4.9 mm^2 was aligned with the electrode overlap area for solar and EQE measurements. The *J-V* characteristics of all photovoltaic devices were evaluated under AM 1.5G solar illumination (100 mW/cm²) using a Keithley SMU 2410 with a Newport Thermal Oriel 94021 solar simulator calibrated with a reference silicon solar cell.

4.4.3 Polymerization of PffBT4T$_{80}$-co-3T$_{20}$-2OD

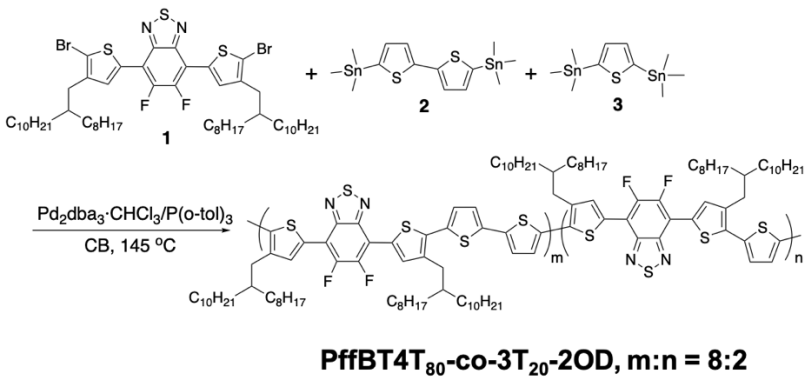

PffBT4T$_{80}$-co-3T$_{20}$-2OD, m:n = 8:2

Supporting Scheme 1 – Polymerization scheme of PffBT4T$_{80}$-co-3T$_{20}$-2OD

A dry 50 mL round bottom flask was equipped with a stir bar, compound 1 (1 g, 0.948 mmol), compound 2 (373 mg, 0.758) and compound 3 (77.66 mg, 0.19 mmol) and transferred into a glove box with a condenser. Inside the glove box, $Pd_2dba_3{\bullet}CHCl_3$ (20 mg, 0.19 mmol) and P(*o*-tol)$_3$ (23 mg, 0.076 mmol) were added to the reaction flask. The flask was sealed and brought out of the glovebox and immediately placed under a blanket of argon through the top of the condenser. Then 15 mL of argon purged chlorobenzene was added to the reaction flask and followed by 10 minutes of stirring to dissolve all the contents. The flask was then lowered into an oil bath that was preheated to 145 °C and was stirred for 24 hours. The polymerization was then cooled to 90 °C and exposed to air to add an excess amount of Pd scavenger diethylammonium diethyldithiocarbamate and 10 mL of additional chlorobenzene. The mixture was stirred for 1 hour before it was precipitated into 400 mL of methanol. The impure polymer was filtered through a nylon extraction thimble and subjected to successive soxhlet extractions with methanol, acetone, hexanes, dichloromethane and finally collected in chloroform. The polymer chloroform solution was concentrated under reduced pressure and precipitated into methanol. Finally,

the pure polymer was collected *via* vacuum filtration and dried under vacuum for 24 hours to produce a dark purple solid (906 mg, 92%). M_n: 51.0 kDa, M_w: 94.0 kDa, *Đ*: 1.84 (GPC in 1, 2, 4-trichlorobenzene vs. polystyrene). ^{1}H NMR (400 MHz, $C_2D_2Cl_4$, 100 °C): δ (ppm) 8.22 (s, 2H), 7.35 (s, 0.43 H), 7.28 (s, 3.28 H), 2.94 (m, 4H), 1.94 (m, 2H), 1.46-1.33 (m, 64 H), 0.98-0.92 (m, 14.84 H). Anal. calcd. for $C_{61.2}H_{87.6}N_2F_2S_{4.8}$: C (70.47%), H (8.47%), N (2.68%), S (14.73%); Found: C (70.70%), H (8.35%), N (2.55%), S (14.62%).

Polymerization of the second batch of **PffBT4T$_{80}$-co-3T$_{20}$-2OD** was performed in the same manner as described above. Monomer 1 (200 mg, 0.189 mmol), monomer 2 (74.5 mg, 0.151 mmol), monomer 3 (15.5 mg, 0.038 mmol), $Pd_2(dba)_3$•$CHCl_3$ (4 mg, 0.0038 mmol), P(*o*-tol)$_3$ (5 mg, 0.016 mmol) and 3 mL of chlorobenzene were used. The polymer was collected as a dark purple solid (175 mg, 88%). M_n: 62.0 kDa, M_w: 120.0 kDa, *Đ*: 1.93 (GPC in 1, 2, 4-trichlorobenzene vs. polystyrene). Anal. calcd. for $C_{61.2}H_{87.6}N_2F_2S_{4.8}$: C (70.47%), H (8.47%), N (2.68%), S (14.73%); Found: C (70.87%), H (8.45%), N (2.77%), S (14.70%).

4.4.4 Supporting figures and tables

Supporting Table 4-1 – Power conversion efficiencies of the family of PffBT-4T-co-3T polymers for spin coated devices with both PC$_{71}$BM and IDTBR, with hot solutions and either hot or RT substrates. PCBM data taken from our previous work.[11] IDTBR data processed with a 100 °C substrate is also taken from our previous work.[183]

Polymer	Average PCE (%)			
	PCBM 100 °C substrate	PCBM RT substrate	IDTBR 100 °C substrate	IDTBR RT substrate
PffBT4T-2OD	8.7 ± 0.6	< 0.5	8.0 ± 0.3	< 0.5
PffBT4T$_{90}$-co-3T$_{10}$	9.6 ± 0.6	9.6 ± 0.5	8.7 ± 0.2	5.4 ± 0.3
PffBT4T$_{80}$-co-3T$_{20}$	9.5 ± 0.4	9.4 ± 0.3	8.5 ± 0.5	6.9 ± 0.4

PffBT4T$_{70}$-co-3T$_{30}$	9.6 ± 0.6	9.5 ± 0.3	6.8 ± 0.7	6.5 ± 0.3
PffBT4T$_{50}$-co-3T$_{50}$	9.1 ± 0.6	9.1 ± 0.6	2.2 ± 0.4	2.1 ± 0.4
PffBT3T-2OD	5.1 ± 0.7	6.0 ± 0.9	1.8 ± 0.2	1.5 ± 0.4

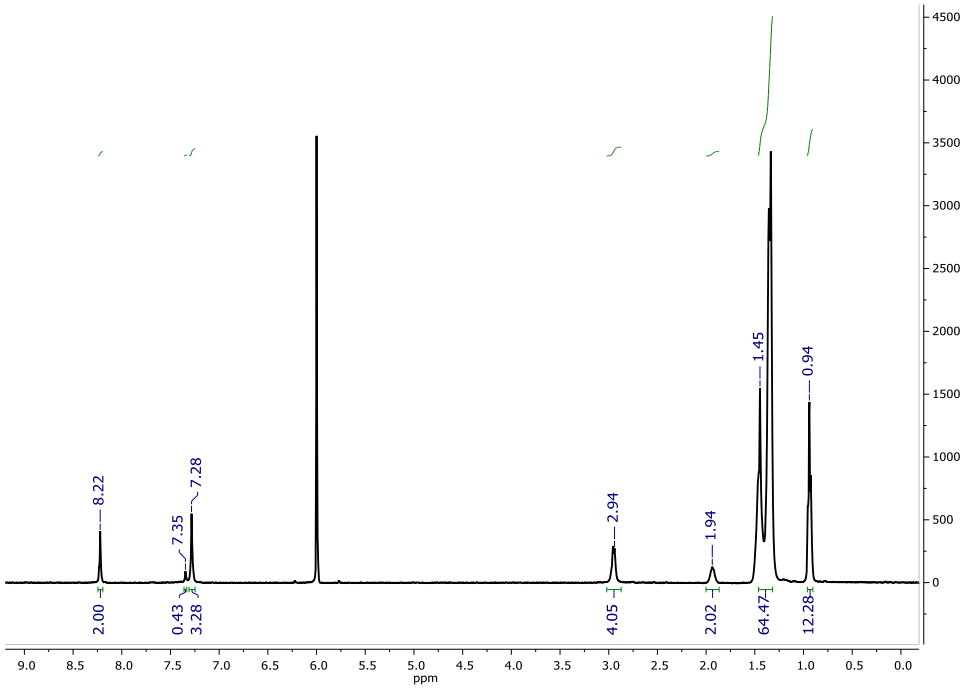

Supporting Figure 4-1 – ^{1}H NMR of the 51 kDa polymer sample (TCE-d2, 10 mg/mL, 110 °C, d1 = 8s)

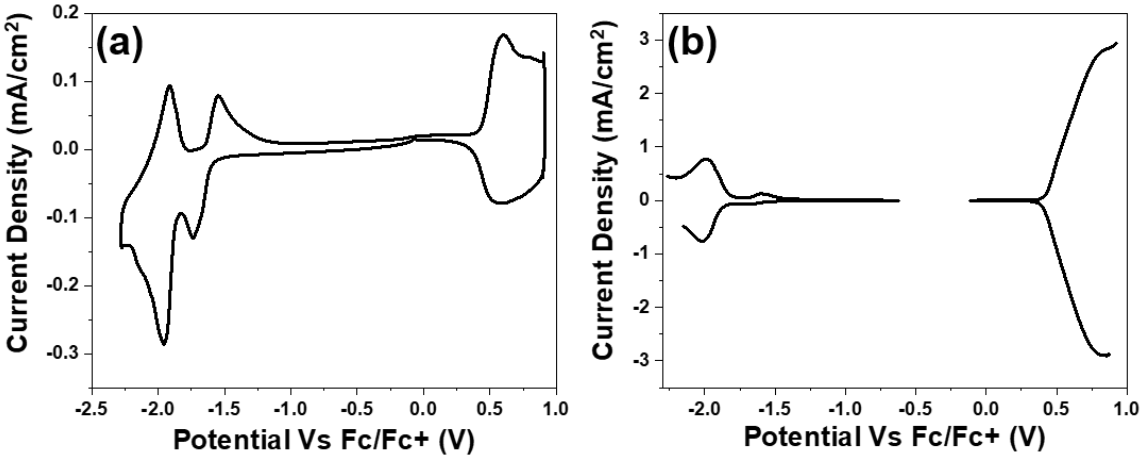

Supporting Figure 4-2 – The (a) CV trace and (b) DPV trace of the 51 kDa polymer.

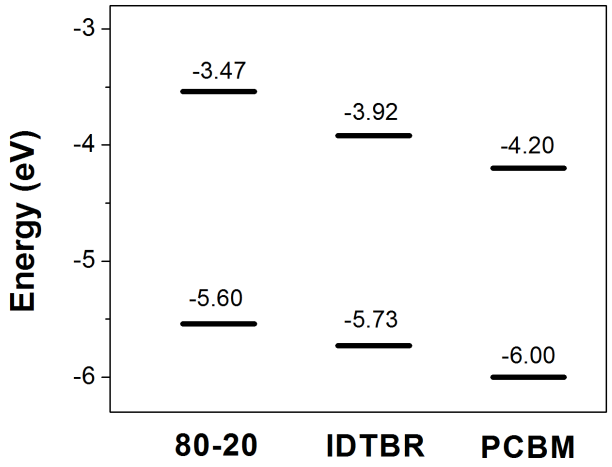

Supporting Figure 4-3 – Energy level diagram of 80-20, IDTBR, and $PC_{71}BM$. 80-20 energy levels were taken from the DPV above vs. 5.12 eV. IDTBR energy levels were taken from our previous work.[190] PCBM values were taken from Thompson et al.[191]

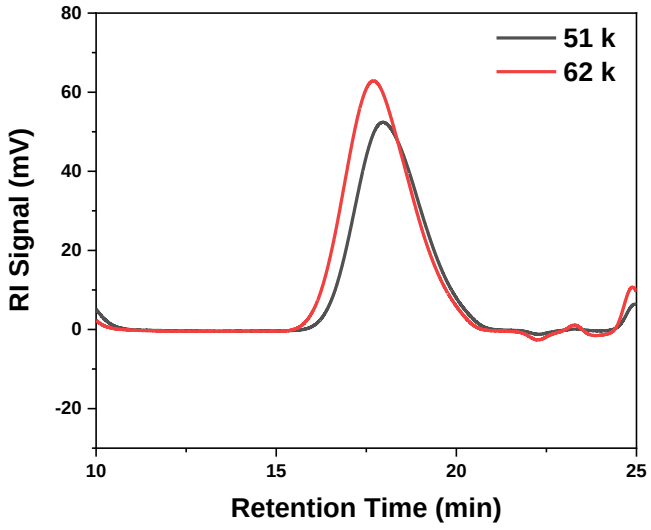

Supporting Figure 4-4 – High temperature (140 °C) GPC traces in 1,2,4-trichlorobenzene.

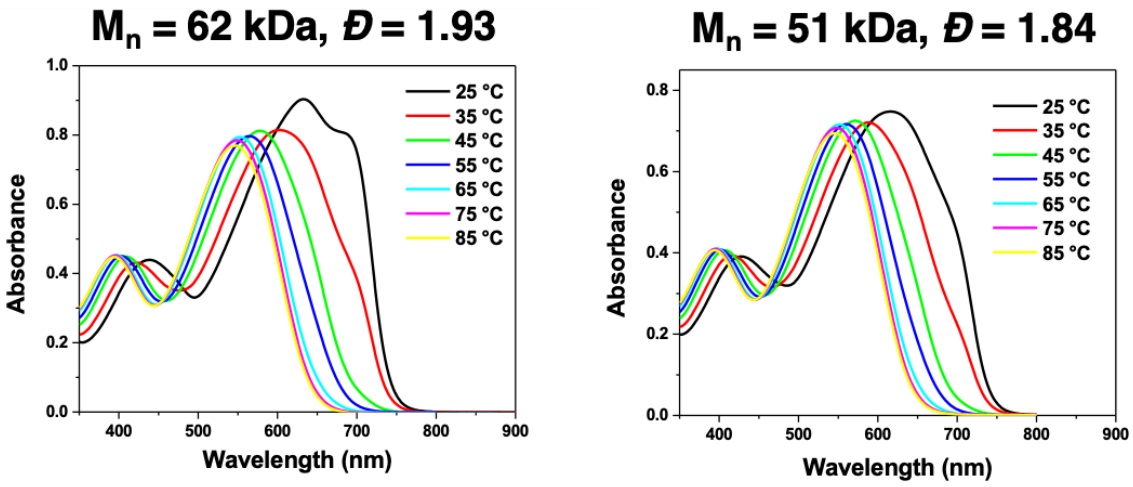

Supporting Figure 4-5 – Solution UV/vis spectra of the two PffBT4T$_{80}$-co3-T$_{20}$-2OD polymers used in this study, in 0.02 mg/mL o-DCB, from 25°C to 85°C. Solutions were allowed to equilibrate at each temperature for 5 minutes before each spectrum was recorded.

Supporting Table 4-2 – Summarized optoelectronic data for 80-20 51 kDa as measured via cyclic voltammetry and differential pulsed voltammetry: oxidation and reduction potentials, HOMO/IP and LUMO/EA values, the electrochemical band gap calculated from CV and DPV, and the optical band gap calculated from the solution UV/vis.

$E_{ox,\ onset}$ (V)		$E_{red,\ onset}$ (V)		E_{HOMO} (eV)		E_{LUMO} (eV)		E_g^{Echem} (eV)		E_g^{Opt} (eV)
CV	DPV	CV	DPV	CV	DPV	CV	DPV	CV	DPV	UV-VIS
0.43	0.42	-1.58	-1.58	5.55	5.54	3.54	3.54	2.01	2.00	1.65

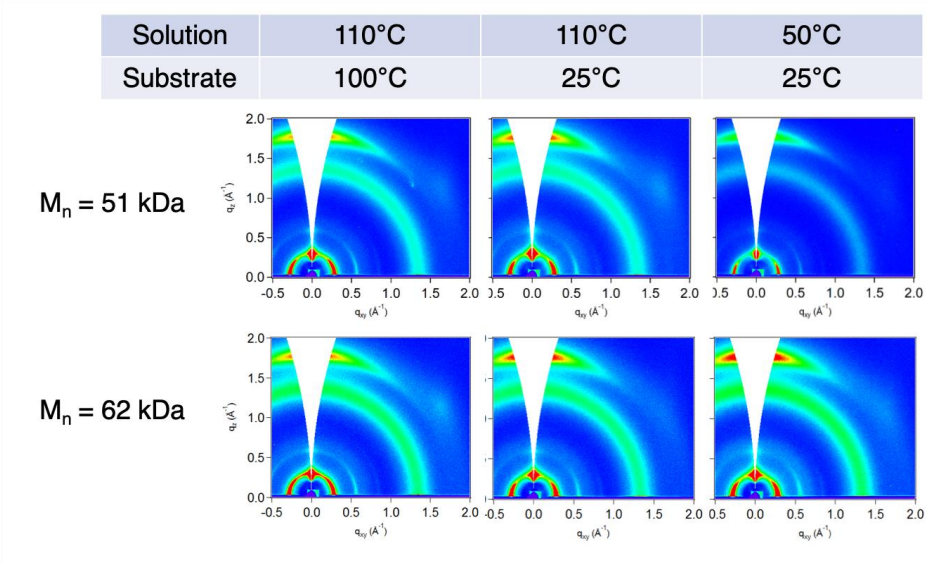

Supporting Figure 4-6 – GIWAXS patterns of spin-coated blend films of the two different batches of 80-20 with the $PC_{71}BM$. The solution and substrate temperatures were varied as indicated above. Image intensities were approximately normalized to film thickness. We do not observe any significant changes between the two molecular weights.

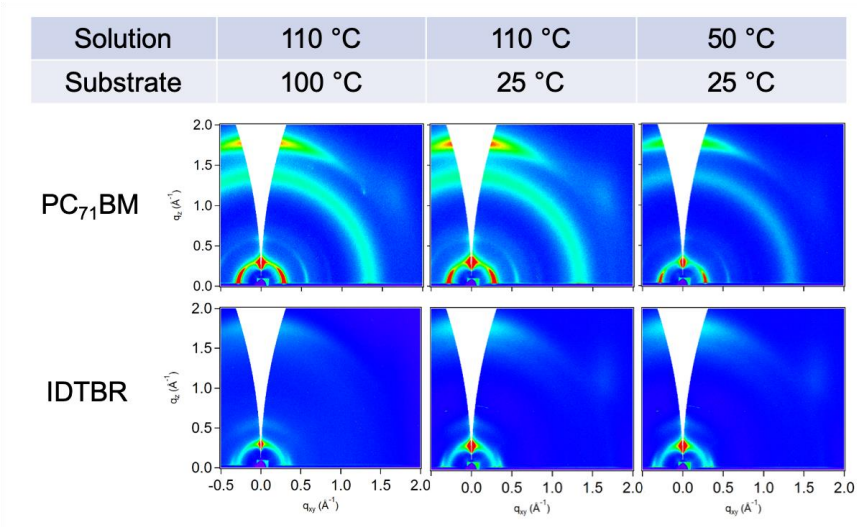

Supporting Figure 4-7 – GIWAXS patterns of spin-coated blend films of M_n = 51 kDa 80-20 with the two acceptor molecules use in this study. PCBM data is reproduced from Figure S6 above. The solution and substrate temperatures were varied as indicated above. Image intensities were approximately normalized to film thickness.

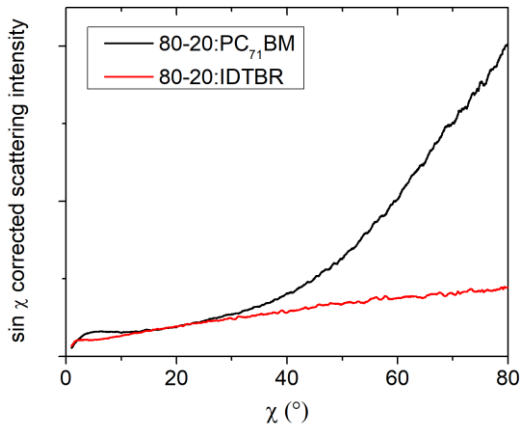

Supporting Figure 4-8 – Sin χ corrected pole figures of the (100) lamellar stacking peak for the spin coated blend films processed from 110 °C solutions onto 100 °C substrates.

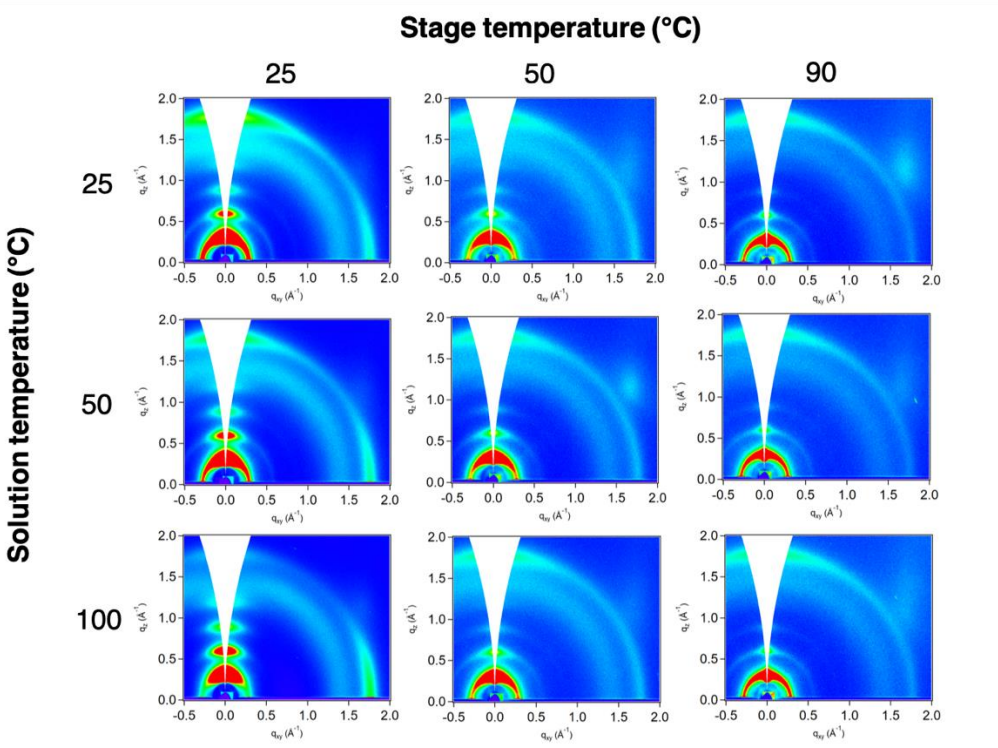

Supporting Figure 4-9 – GIWAXS patterns of pristine Mn = 51 kDa 80-20 blade coated at a variety of different solution and stage temperatures cast from chlorobenzene only.

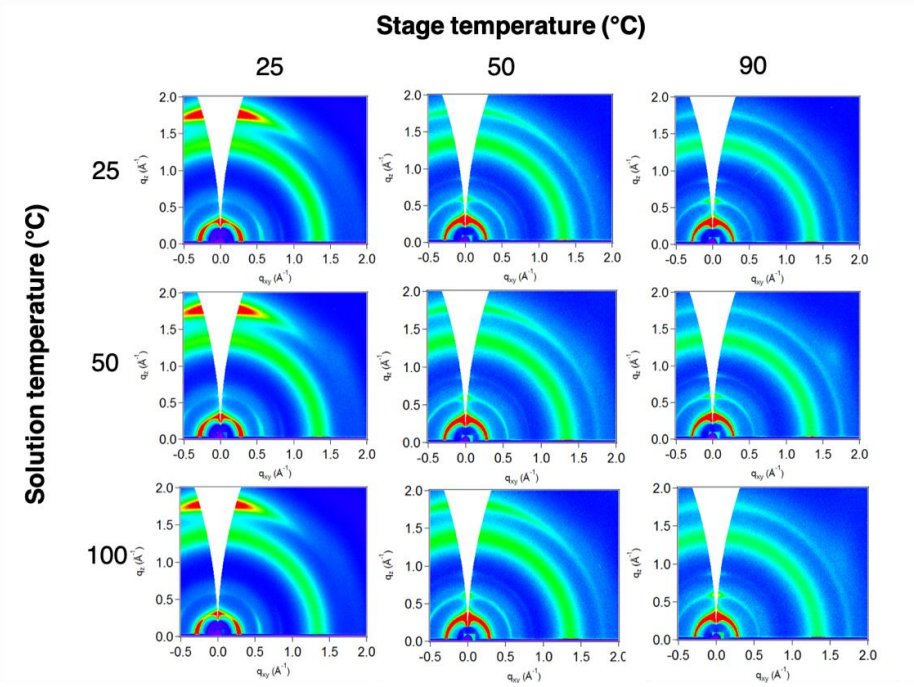

Supporting Figure 4-10 – GIWAXS patterns of Mn = 51 kDa 80-20 : PCBM blend films blade coated at a variety of different solution and stage temperatures.

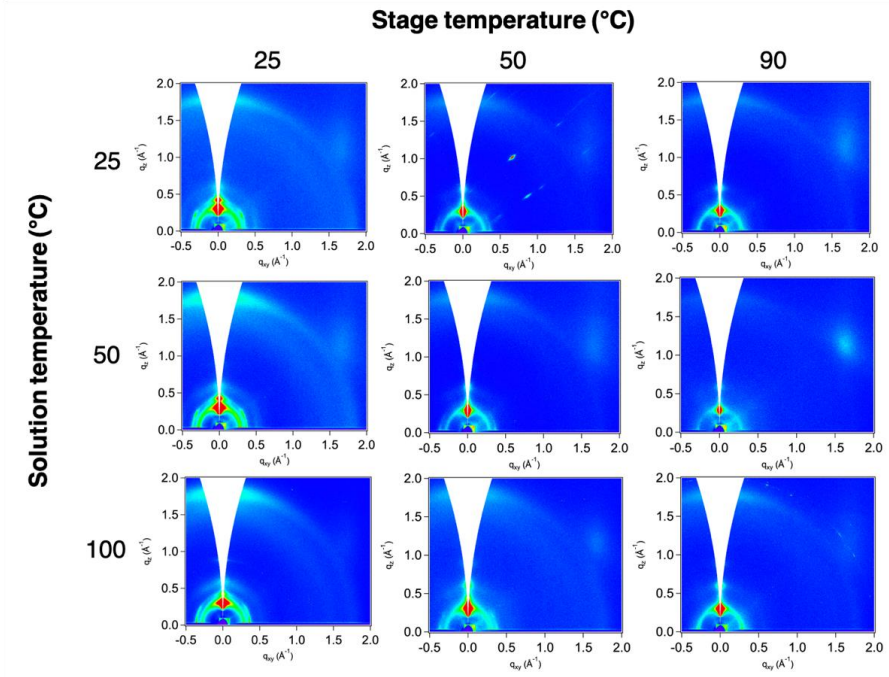

Supporting Figure 4-11 – GIWAXS patterns of Mn = 51 kDa 80-20 : IDTBR blend films blade coated at a variety of different solution and stage temperatures.

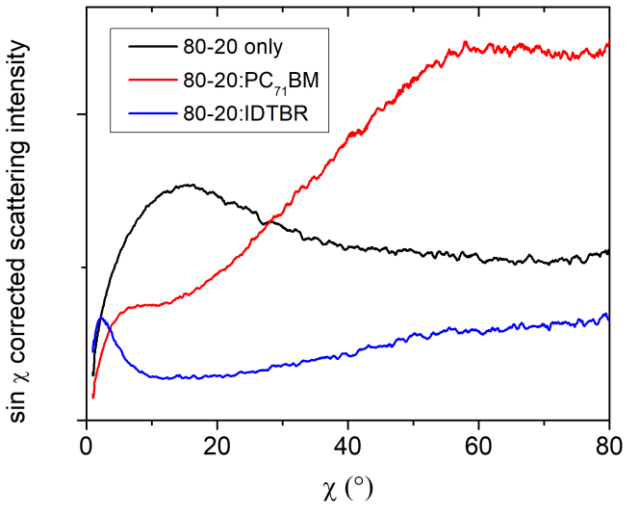

Supporting Figure 4-12 – Sin χ corrected pole figures of the (100) lamellar stacking peak for the blade coated pristine and blend films processed from 50 °C solutions with a 50 °C stage.

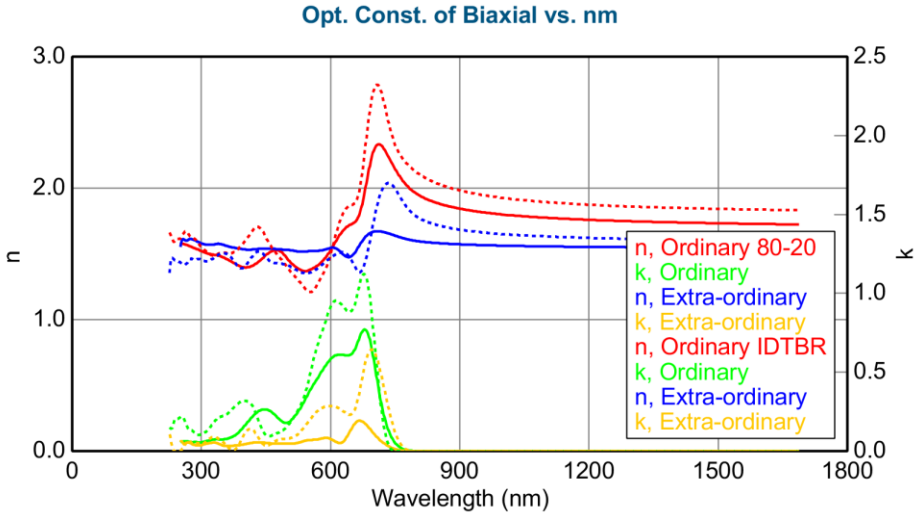

Supporting Figure 4-13 – Complex refractive indices of 80-20 and IDTBR measured via ellipsometry.

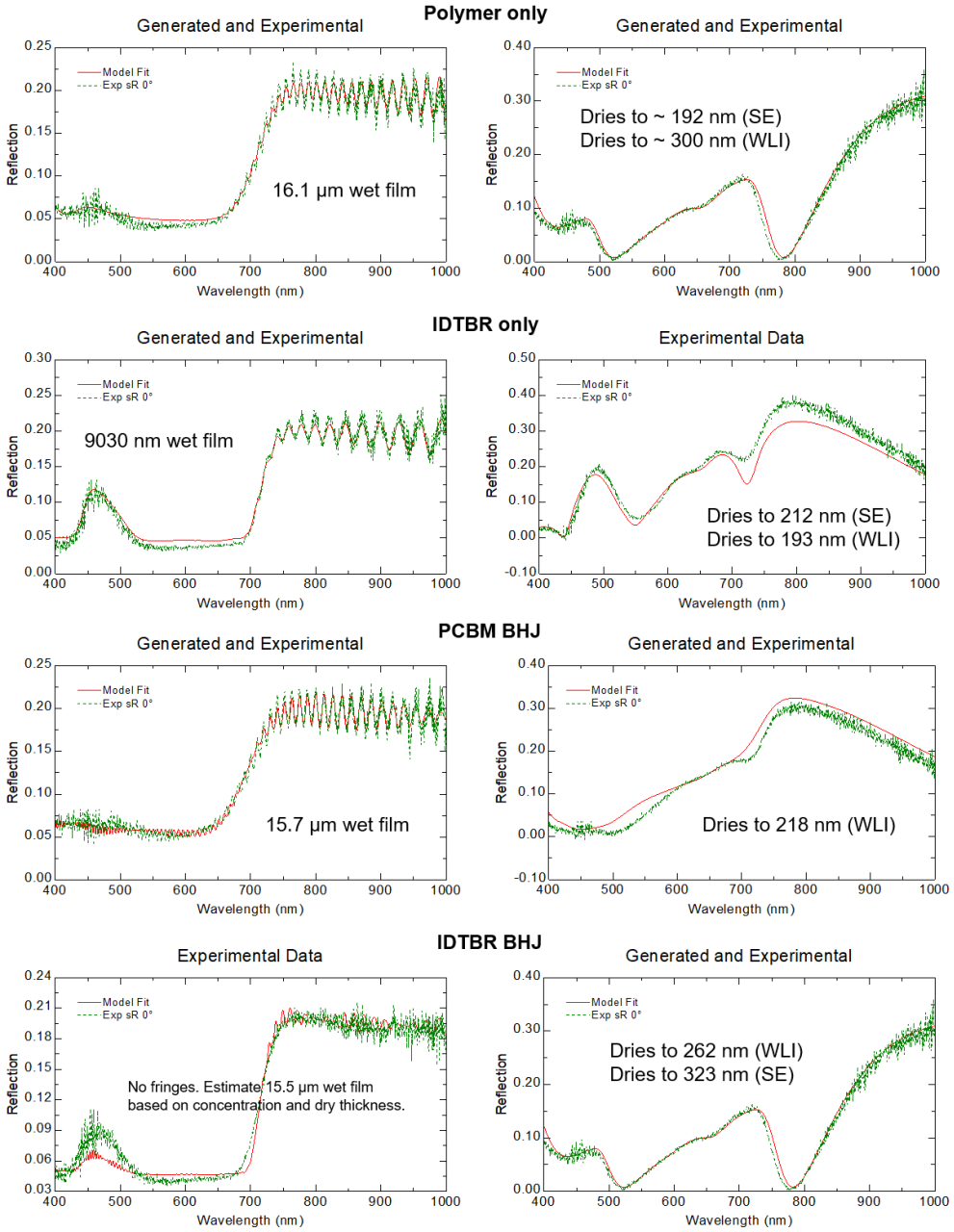

Supporting Figure 4-14 – White light interferometry results of the four in situ cases (polymer only, IDTBR only, PCBM BHJ, and IDTBR BHJ) from initially cast wet films (left) and dried films (right). Film thicknesses were modeled via the complex refractive indices.

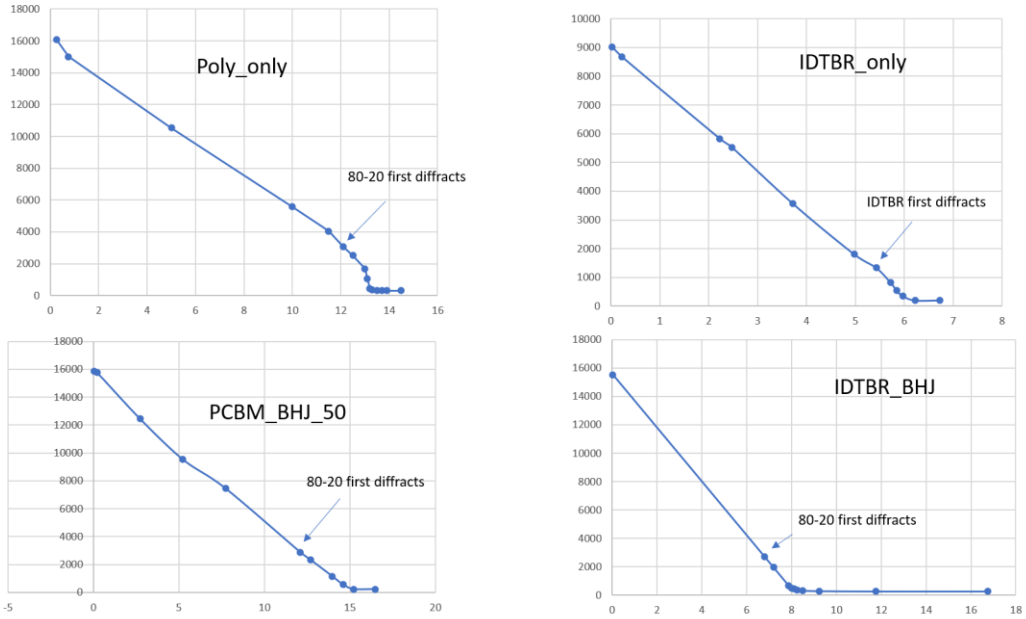

Supporting Figure 4-15 – Film thickness (nm) vs. time (s) for the four in situ cases, calculated from the WLI modeling data in Supporting Figure 4-14.

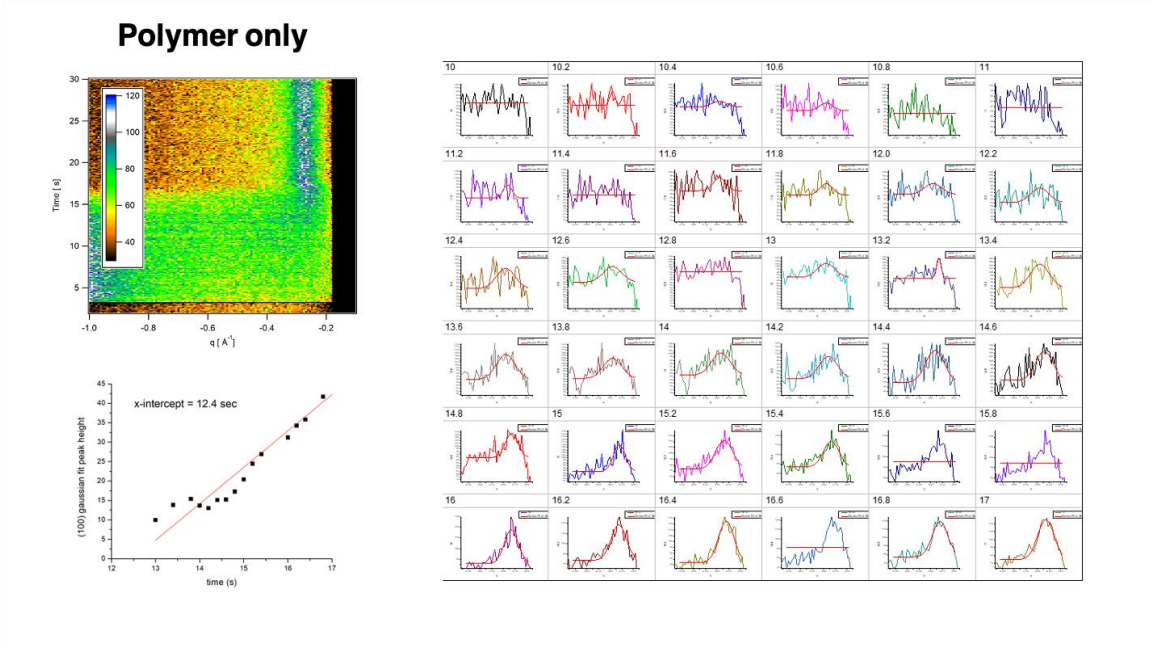

Supporting Figure 4-16 – In situ GIWAXS workup of the polymer only film. (top left) 2D false color plot of the out-of-plane line cut over time. (right) constrained Gaussian fits to the evolving lamellar stacking peak at q = 0.28 Å^{-1}, at 0.2 second intervals. (bottom left) compiled peak heights from the Gaussian fits vs. time. The x-intercept is used to estimate the onset of crystallization.

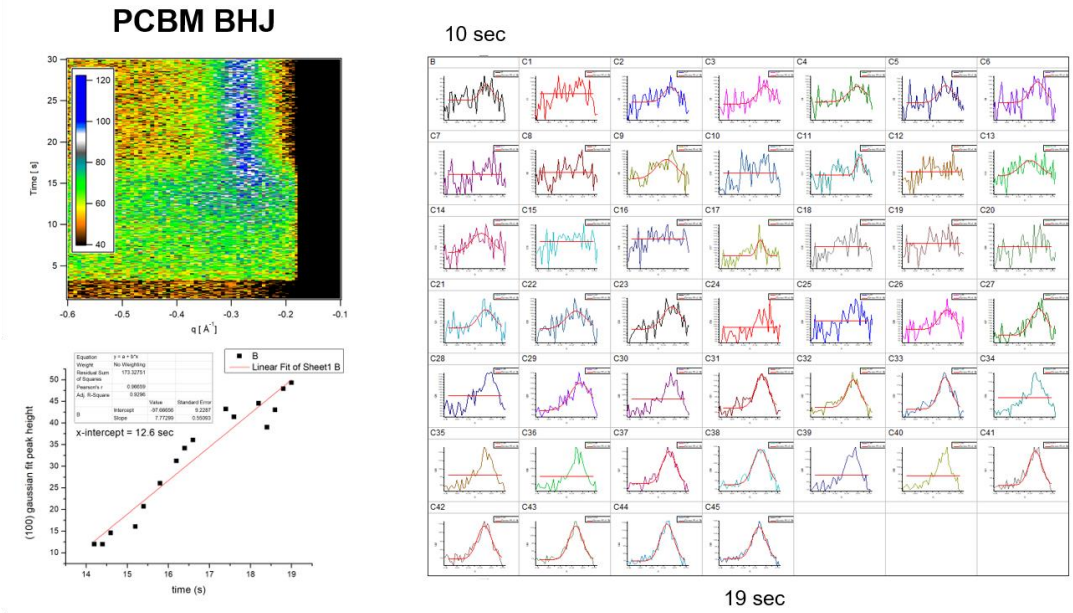

Supporting Figure 4-17 – In situ GIWAXS workup of the polymer:PCBM BHJ. (top left) 2D false color plot of the out-of-plane line cut over time. (right) constrained Gaussian fits to the evolving lamellar stacking peak at q = 0.28 Å^{-1}, at 0.2 second intervals. (bottom left) compiled peak heights from the Gaussian fits vs. time. The x-intercept is used to estimate the onset of crystallization.

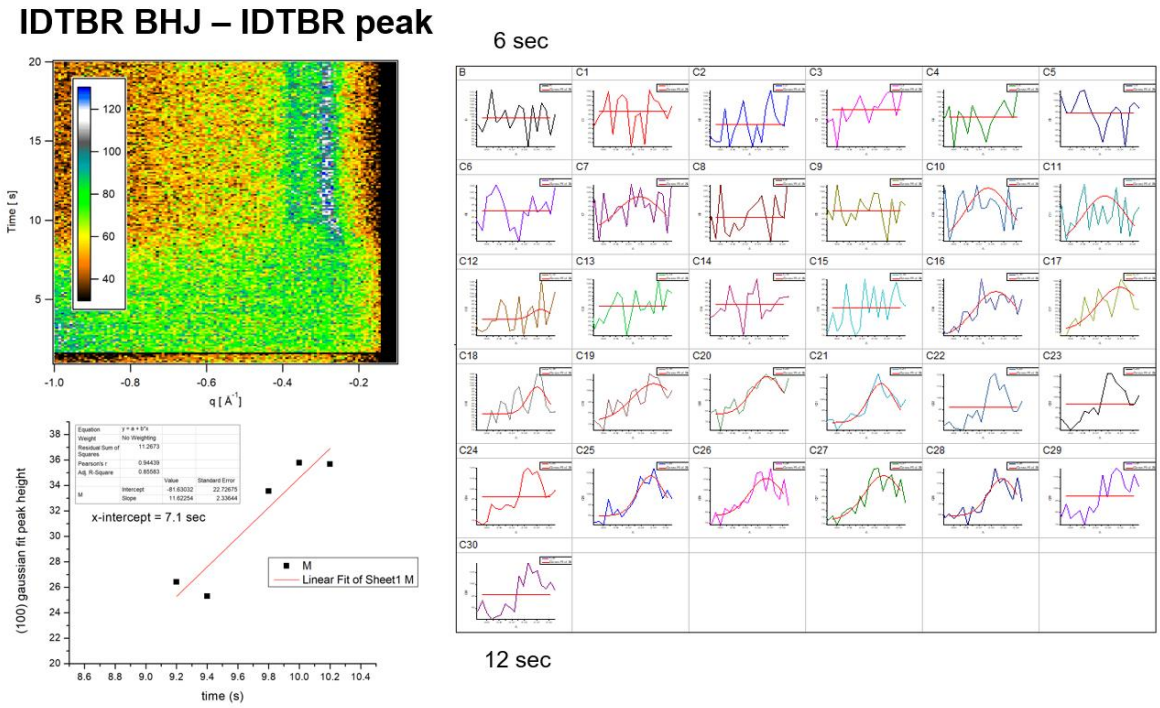

Supporting Figure 4-18 – In situ GIWAXS workup of the IDTBR lamellar peak of the polymer:IDTBR BHJ. (top left) 2D false color plot of the out-of-plane line cut over time. (right) constrained Gaussian fits to the evolving lamellar stacking peak at q = 0.37 Å^{-1}, at 0.2 second intervals. (bottom left) compiled peak heights from the Gaussian fits vs. time. The x-intercept is used to estimate the onset of crystallization.

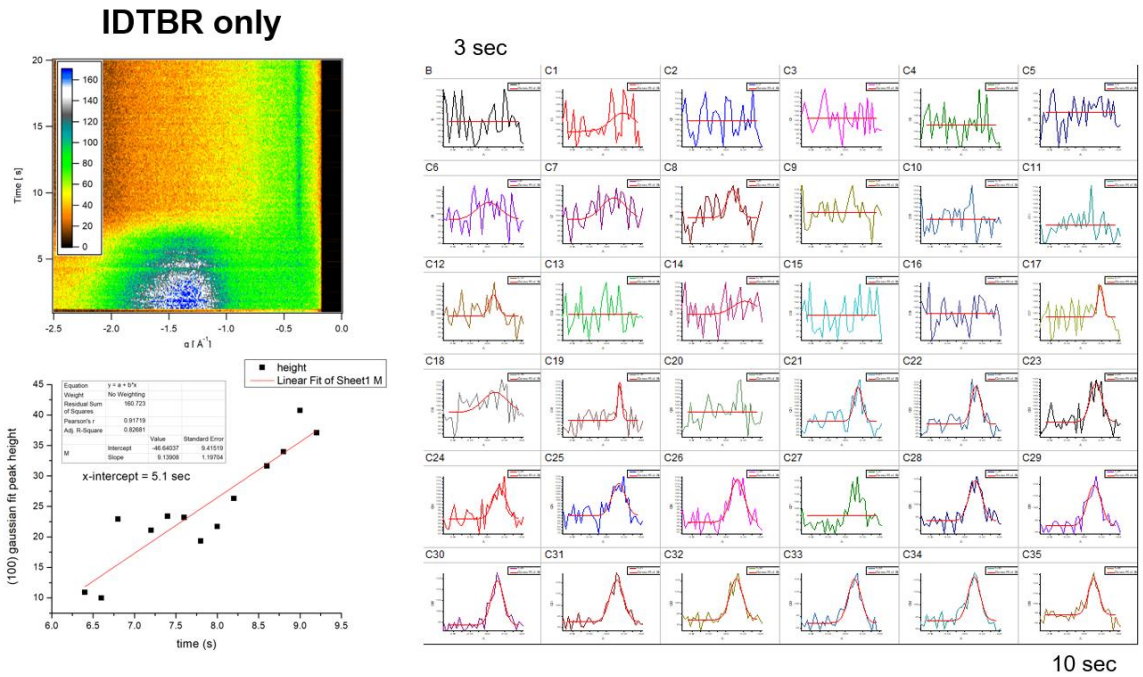

Supporting Figure 4-19 – In situ GIWAXS workup of the IDTBR only film. (top left) 2D false color plot of the out-of-plane line cut over time. (right) constrained Gaussian fits to the evolving lamellar stacking peak at q = 0.37 Å^{-1}, at 0.2 second intervals. (bottom left) compiled peak heights from the Gaussian fits vs. time. The x-intercept is used to estimate the onset of crystallization.

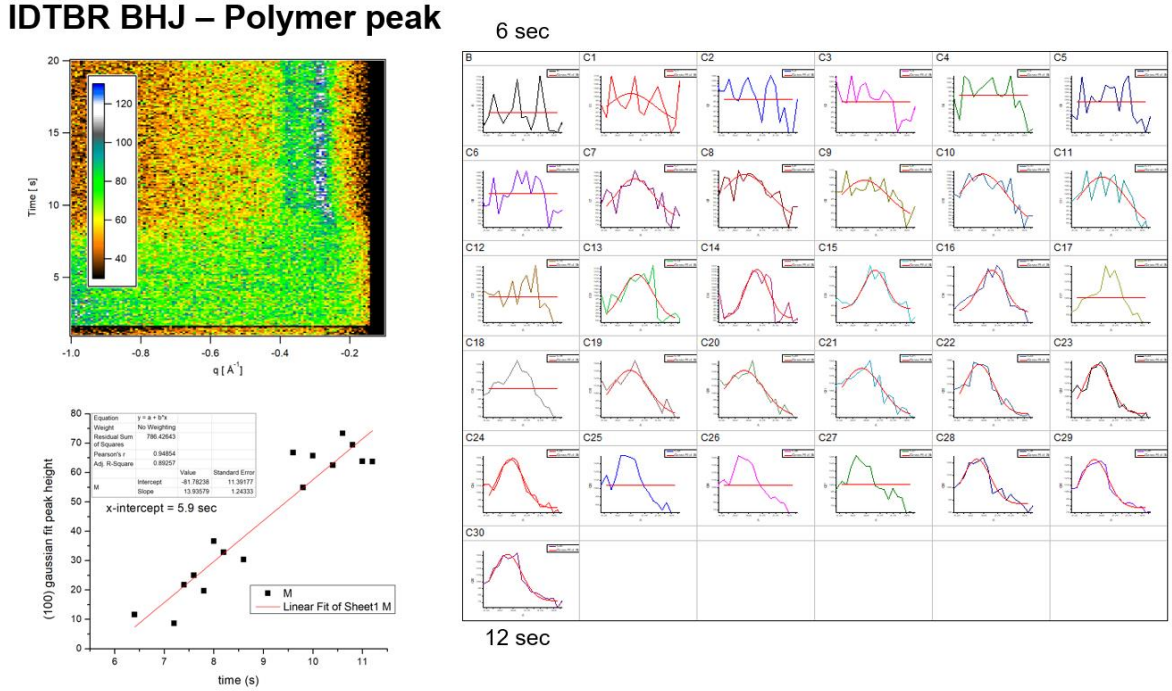

Supporting Figure 4-20 – In situ GIWAXS workup of the polymer lamellar peak of the polymer:IDTBR BHJ. (top left) 2D false color plot of the out-of-plane line cut over time. (right) constrained Gaussian fits to the evolving lamellar stacking peak at q = 0.28 Å^{-1}, at 0.2 second intervals. (bottom left) compiled peak heights from the Gaussian fits vs. time. The x-intercept is used to estimate the onset of crystallization.

Supporting Table 4-3 – Compiled information from the in situ GIWAXS and WLI experiment. The onset of 80-20 and IDTBR diffraction is shown as a function of time, wet film thickness, and solids volume fraction for the four in situ runs.

	80-20 diffraction onset			IDTBR diffraction onset		
	Time (s)	Wet film thickness (um)	Solids volume fraction (%)	Time (s)	Wet film thickness (um)	Solids volume fraction (%)
Polymer only	12.4	2.6	11.5 polymer	-	-	-
IDTBR only	-	-	-	5.1	1.3	15 IDTBR
Polymer:PCBM BHJ	12.6	2.9	7.6 total / 3.5 polymer	-	-	-
Polymer:IDTBR BHJ	5.9	2.7	9.7 total / 4.5 polymer	7.1	1.9	13 total / 7.1 IDTBR

CHAPTER 5. NON-HALOGENATED SOLVENT PROCESSING OF P(DTG-TPD)

The work presented in this chapter would not exist without the synthetic expertise of Dr. Rylan M. W. Wolfe, who synthesized and characterized P(DTG-TPD).

5.1 Introduction

5.1.1 Non-halogenated solvent processing for OPV

With halogenated solvents unlikely to be permitted for industrial use in solution processing of organic solar cells, there is great practical interest in developing systems that may be processed from non-halogenated solvents. The prevalent use of chlorinated solvents to process active layers has limited the commercialization potential of OPVs and their environmental sustainability. To date, most high-performance OPV active layer films are processed from the following chlorinated solvents: chloroform ($CHCl_3$), chlorobenzene (CB), or o-dichlorobenzene (DCB). These solvents are particularly good at dissolving conjugated polymers that are often highly planar and can tend to aggregate, as was demonstrated in the two previous chapters of this dissertation. As was discussed in the introduction, some champion solvent additives are the halogenated 1,8-diiodooctane (DIO) and 1-chloronaphthalene (CN), which both have high-boiling points and low vapor pressures. During blade coating of the active layer, $CHCl_3$ evaporates rapidly in ambient room temperatures. Mild heating at 50 °C is sufficient to drive off CB in 30 seconds or less, shown for the 80-20 blends in Chapter 4, and even at room temperature, the 7.5 % loading of DCB used for the DT-DPP-2T-TT blend in Chapter 3 evaporated in just over 60

seconds (Figure 3-6). Conversely, DIO at the same loading of 7.5 % takes hours to dry at ambient temperatures, so additional care needs to be taken to ensure safe removal. For this reason, when exploring non-halogenated systems for blends that require additives, careful attention needs to be paid to both the host solvent and additive to assess their functionality as well as their toxicity. While the previous two projects in this dissertation focus solely on the mechanism of solvent evaporation and film solidification, this section will look at the practical use of non-halogenated solvents for OPV.

Halogenated solvents are typically preferred for processing OPV materials due to their ability to solubilize conjugated materials and their ability to form a nanostructured BHJ with a reasonable morphology during the drying process. Photovoltaic performance of materials processed with non-halogenated solvents generally lags behind the performance of those processed with typical halogenated solvents. There appears to be a trade-off between solvent greenness and performance; the less harmful the solvent, the more poorly performing the device. The Innovative Medicines Initiative (IMI)-CHEM21 is a public-private partnership which promotes sustainable biological and chemical methodologies. They have developed a classification guide of common solvents to assess their greenness with respect to industrial implementation, ranging from hazardous solvents like chloroform and benzene, to recommended solvents that imbue no significant industrial problems to the handling of solvent.[192]

Recommended solvents include water and ethanol, which have been explored for OPV active layer processing, but use of those solvents typically requires modifications to the active materials to improve solubility. For example, Kim et al. functionalized both a methoxyphenylene-benzothiadiazole based polymer and a $PC_{61}BM$ derivative with

glycolated side chains, which were processed from a mixture of water and ethanol and gave power conversion efficiencies of up to 1.4 %.[193] The devices have fill factors less than 50 %, indicating that substantial morphological challenges need to be overcome before fully glycolated materials can approach state-of-the-art power conversion efficiencies. Other techniques for aqueous processing include nanoparticle processing; a recent high efficiency report from Xie et al. featured nanoparticles of P3HT and IDTBR stabilized by a surfactant to give power conversion efficiencies of over 5 %.[194] However, creation of the nanoparticles requires a multistep process via in situ thermal modulation of the surfactant, which complicates processing.

Instead, we are interested in exploring solvent systems that do not require changes in the functionality of the semiconductor materials, which generally limits the processing solvents to organics. With the use of Hansen Solubility Parameters (HSPs), discussed in Chapter 1, several groups have proposed solvent systems with similar solubility parameters to common combinations such as CB, DCB, and DCB/DIO. For example, Park et al. showed that a combination of mesitylene and acetophenone had very similar HSPs to DCB, and the resulting P3HT:PCBM devices had PCE values close to the DCB-processed devices (3.4 % vs. 3.9 % PCE).[195] Other active layers have been processed from solvents such as tetrahydrofuran (THF) and 2-methyltetrahydrofuran (2-MeTHF) and have achieved power conversion efficiencies closer to devices processed from halogenated solvents. Fan et al. built an all polymer solar cell with PTzBI and N2200 cast from 2-MeTHF, with average power conversion efficiencies of 9.0 %.[196]

The state of the art for green solvent processing is a device with PCE of 12.5% using a sequentially processed bilayer device. This work, by Ye et al., used PBnDT-FTAZ

as the polymer donor and IT-M, an ITIC derivative, as the molecular acceptor.[197] Both materials have typical alkyl chains as solubilizing groups, but PBnDT-FTAZ was dissolved in (R)-(+)-limonene and IT-M was dissolved in 2MeTHF. Limonene can be derived from renewable biosources such as lemons and oranges. Compared to PBnDT-FTAZ processed from chlorobenzene, o-xylene, or 1,2,4-trimethylbenzene, the polymer had the strongest lamellar ordering when processed from limonene. However, despite the fact that PBnDT-FTAZ is soluble in limonene, IT-M is not, and therefore BHJ devices processed in a single step were not functional. On the other hand, device performance of BHJs processed via toluene was comparable to the sequentially deposited cells.

For this study we have used 1,2,4-trimethylbenzene (TMB) as the host solvent, after trialing toluene and o-xylene and finding poorer film forming properties from those two solvents. TMB has been reported in the literature as a non-halogenated host solvent for highly performing OPVs, both with fullerene and non-fullerene acceptors. An early report of this solvent's application in OPV is from Chueh et al., where they achieved solar cells with three different active layers and found comparable performance when using either TMB or DCB.[198] For example, PffBT4T-2DT achieved power conversion efficiencies with O-IDTBR of over 10 % cast from TMB.[51] A PffBT4T-2DT derivative with a slightly shorter side chain, PffBT4T-C_9C_{13}, achieved PCEs up to 11.7 % with $PC_{71}BM$ when using 2-phenylnaphthalene as an additive.[30] Work by Cai et al. showed comparable performance with P(DTS-TPD):$PC_{71}BM$ processing from a blend of TMB and 1,5-dimethylnaphthalene (DMN) compared to the traditional casting solvent of CB + DIO for the family of P(DTX-TPD) polymers, which will be introduced in the next section.[199]

5.1.2 One atom change

The synthesis of poly-(dithienogermole-alt-thienopyrrolodione) (P(DTG-TPD)) was first reported in 2011 by Chad M. Amb et al. from the Reynolds group.[200] P(DTG-TPD) is a copolymer of dithienogermole (DTG) and thienopyrroledione (TPD), with attached bis 2-ethylhexyl groups and n-octyl groups, respectively, with DTG as the electron rich unit and TPD as the electron deficient unit. The repeat unit structure of P(DTG-TPD) is shown below in Figure 5-1. The synthesis of this material followed work from analogues that, instead of germanium as the heteroatom, used carbon (DTC, aka cyclopentadithophene, CPD) or silicon (DTS), which are in the same family on the periodic table. Early work from Yang Yang and coworkers showed that additive-free device performance was drastically improved when changing the DTC/CPD unit in PCPDTBT to DTS, with average power conversion efficiencies increasing from 3.2 % to 4.7 % when using $PC_{71}BM$.[201] A follow up study showed that PDTSTBT had improved π-π stacking and higher hole mobilities compared to PCPDTPD, which was attributed to the long C-Si bond length compared to the bond length of C-C shown via density functional theory (DFT) calculations.[202] Moving the side chains just a little bit further from the backbone enhanced interchain interactions without limiting solubility.

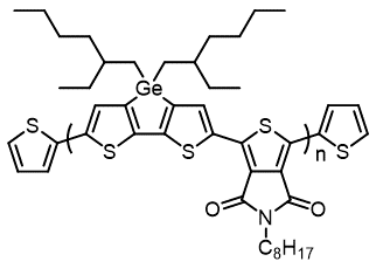

P(DTG-TPD)

Figure 5-1 – Repeat unit structure of P(DTG-TPD)

In order to continue to probe the beneficial nature of the C-Si bond length toward improved molecular packing for OPV applications, an even larger atom, germanium, was used to make P(DTG-TPD). With Chem3D MM2 optimized calculations, it was shown that the C-Ge bond is longer than the C-Si bond, and thus the side chain is further removed from the backbone.[200] With drastically improved photovoltaic performance in PC71BM based devices using DIO as an additive, average PCEs with P(DTG-TPD) were 7.3 % compared to 6.6 % for P(DTS-TPD). In the additive free cases, cross-sectional TEM images showed fullerene droplets in a polymer matrix, with lateral dimensions of up to 350 nm; this explains poor performance in the additive-free cases, where the current and fill factors drop substantially and lead to efficiencies of less than half of the DIO optimized devices (device statistics were not reported in that study). Using DIO creates a finely intermixed BHJ with appropriate length scaled domains for efficient photovoltaic operation.

Work done in our group by Kin Lo et al. took a careful approach to the effect of heteroatom substitution on this system and involved three parallel polymerizations of

P(DTX-TPD), where X is either C, Si, or Ge.[10] This work was motivated by a desire to develop strong structure property relationships within a polymer family by isolating any changes among the polymers exclusively to substitution of the heteroatom. Once the three polymers were synthesized via the same technique, confirmed to be analytically pure and have approximately the same molecular mass distributions, their solution and solid state behavior was studied in depth. Number average molecular weights (M_n) in kg mol^{-1} and dispersities ($Đ$) were as follows: P(DTC-TPD) – 25.4/1.4; P(DTS-TPD) – 24.5/1.7; P(DTG-TPD) – 20.8/1.7. This work concluded that P(DTC-TPD) has different aggregation behavior in both the solution and the solid state when compared to both P(DTS-TPD) and P(DTG-TPD). From time dependent density functional theory (TD-DFT) calculations, UV/vis absorption spectroscopy, solution and solid state NMR spectroscopy, it was shown that the torsional angle between the DTC and TPD units are different compared to the polymers with DTS and DTG, which were relatively similar to each other. The latter two polymers have stronger intramolecular interactions involving the aromatic protons on the DTS/DTG unit and the carbonyl oxygen on the TPD unit, which creates a curved moiety in the backbone. As a result, P(DTC-TPD) had a more linear backbone, leading to distinct melt and crystallization peaks in the DSC thermograms and tighter lamellar spacing as seen with the GIWAXS both pristine and in a blend with $PC_{71}BM$. Furthermore, upon annealing P(DTC-TPD) formed oriented crystallites, while the polymers with DTS and DTG were relatively unchanged with relatively isotropic order.

Non-halogenated solvent processing of P(DTS-TPD):$PC_{71}BM$ has been demonstrated by Cai et al., whereby the CB only and CB + DIO processed active layers were compared to those processed via 1,2,4-trimethylbenzene (TMB) and TMB + 1,5-

dimethylnaphthalene (1,5-DMN).[199] Like DIO, methylated naphthalene's are relatively good solvents for fullerenes, so these additives should similarly prevent large fullerene droplets from forming during the drying process.[203] The study from Cai et al. acknowledged that 1,2-DMN is worse performing that 1,5-DMN, but did not provide specifics. We sought to explore any subtle differences in morphology that may arise from slight modifications to the methylation position on the additive. Therefore, we compared both 1,2-DMN and 1,5-DMN to the pristine TMB only case and compared those non-halogenated solvent systems to the CB and CB + DIO systems. This project makes use of P(DTG-TPD) in order to understand the effect of processing conditions on polymer morphology, with a polymer that is relatively disordered and minimally crystalline.

5.2 Results and discussion

5.2.1 Polymer properties

The polymer was synthesized as previously reported in a scaled-up batch of almost 1 gram, and was chosen for scale-up due to its champion performance.[10] The polymer repeat unit structure shown in Figure 5-2(a), and the GPC trace, thin film UV/vis spectra, and electrochemical results are presented in the supporting information (Supporting Figure 5-1, Supporting Figure 5-2, Supporting Figure 5-3, and Supporting Table 5-1). Figure 5-2(a) shows the temperature dependent solution UV/vis absorption spectroscopy of P(DTG-TPD) dissolved in DCB. There are no significant changes in the solution UV/vis spectra with increasing temperature other than a slight decrease in overall absorption intensity. This is in contrast to the changes seen for DT-PDPP2T-TT and PffBT4T$_{80}$-co-3T$_{20}$-2OD, shown in Chapters 3 and 4 respectively, and indicates that there are no

accessible aggregation transitions in the range of typical processing temperatures. Similarly, the DSC thermogram of the pristine polymer, shown below in Figure 5-2(b), is featureless aside from a small processing induced endotherm on the first cooling that is erased once the material is cycled. The 2nd cycle thermogram shown here agrees with the thermogram from the previous report which is also featureless in the same range of -50 °C to 350 °C.[10]

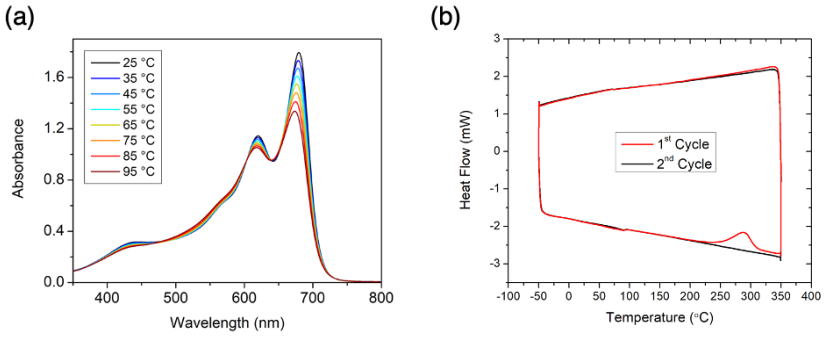

Figure 5-2 – (a) Temperature dependent solution UV/vis spectroscopy of P(DTG-TPD) at a concentration of 0.02 mg mL^{-1} in DCB. (b) DSC thermograms of the first and second temperature cycles of the P(DTG-TPD).

5.2.2 Photovoltaic results

Previous reports of devices made of P(DTX-TPD):$PC_{71}BM$ blends have all featured active layers processed via spin coating. Therefore, we trialed this new batch of P(DTG-TPD) by comparing spin coating to blade coating with the CB + DIO system to ensure the efficacy of blade coating for this particular blend. The J-V curves of champion devices and statistics from a series of devices are shown in Supporting Figure 5-4 and Supporting Table 5-2 respectively. Average PCEs are almost 6.5%, with champion efficiencies of 7.0%. The similarity between the two processing techniques indicates that we can go forward with

blade coating for the remainder of the study. Indeed, device performance appears to be slightly more reproducible with active layers deposited via blade coating rather than spin coating, likely due to a more uniform coating process.

We note that the maximum PCEs achieved here are lower than the highest reported PCEs for P(DTG-TPD):$PC_{71}BM$ solar cells processed via spin coating, which reach averages of 8.5 % PCE processed in a glovebox and 7.7 % PCE when processed in air.[204] We suspect the molecular weight of the polymer sample used plays a role in the maximum performance achievable, however, the use of different elution solvents and temperatures can prevent direct comparison or reported molecular weights. For solar cells made from PCPDTBT derivatives, a strong increase in power conversion efficiency was shown with increasing molecular weight.[23] The previously reported sample of P(DTG-TPD) was reported as having M_n = 48 kg mol^{-1} with $Đ$ = 1.7, using $CHCl_3$ as the eluent.[200] P(DTG-TPD) from the Lo et al. study has M_n = 20.8 kg mol^{-1} and $Đ$ = 1.7, and achieved an average PCE of 7.7 %. The molecular weight for the scaled-up P(DTG-TPD) used here has a similar mass distribution, with M_n = 23 and $Đ$ = 1.6, as shown in Supporting Figure 5-1. This suggests that the PCEs achieved in this study may be improved with further optimization.

Turning to the non-halogenated devices, solutions were made of either the host solvent alone or host solvent plus some additive. For the CB + DIO processed film, the DIO concentration of 5 % by volume was found to be optimum, as per previous reports.[10,200] Similarly, loading of TMB with either of the DMN additives was at 3 % by volume, which also agrees with reports of P(DTS-TPD):$PC_{71}BM$ processed with TMB + 1,5-DMN.[199] Interestingly, 1,5-DMN has a melting point of ~ 80 °C, while 1,2-DMN has a melting point of ~ 0 °C; therefore, 1,5-DMN is weighed out on a balance rather than

measured by volume. Device statistics for these series of devices are shown below in Table 5-1. The drastic increase in current and fill factor when adding DIO to the CB only case agrees with previous reports and suggests that strong fullerene aggregation has been suppressed forming an optimally phase separated bulk heterojunction morphology.

Table 5-1 – Device statistics for P(DTG-TPD):$PC_{71}BM$ devices processed via blade coating, with a variety of different solvent systems. Values were averaged over 8 devices and error bars represent one standard deviation of the mean.

solvent system	J_{SC} (mA cm^{-2})	V_{OC} (V)	FF (%)	PCE (%)
CB	3.5 ± 0.8	0.82 ± 0.01	45 ± 4	1.1 ± 0.3
CB + DIO	12.5 ± 1.0	0.81 ± 0.01	63 ± 2	6.3 ± 0.5
TMB	3.1 ± 0.7	0.79 ± 0.01	42 ± 2	1.0 ± 0.3
TMB + 1,5-DMN	12.1 ± 1.3	0.78 ± 0.01	59 ± 3	5.8 ± 0.5
TMB + 1,2-DMN	11.3 ± 1.3	0.78 ± 0.01	59 ± 4	5.8 ± 0.6

The trend in performance enhancement via the use of additive holds for the non-halogenated solvent processed devices. Similar to the CB only cast film, the TMB only device exhibits low current and fill factor, leading to an average PCE of 1.0 %, indicating a poor morphology. The addition of either 1,2-DMN or 1,5-DMN is effective in improving the morphology with an expected increase in current and fill factor akin to the additive processed halogenated solvent films. However, we note a subtle decrease in efficiency for the non-halogenated additive cast films compared to the CB + DIO case, resulting again from slight degreases in current and fill factor.

5.2.3 Morphological characterization

In order to understand the origin of these subtle changes in performance with casting solvent, GIWAXS and GISAXS were used to characterize the morphology of the dried films. GIWAXS was used to measure molecular packing and orientation on length scales

from 0.2 nm to 2.0 nm, and GISAXS was used to measure domain sizes on the order of 10 nm to 100 nm. Films were processed identically to those made for devices, via blade coating in air followed by vacuum drying to remove any residual additive, and the same films were used for GIWAXS and GISAXS. In-plane line cuts for the blend films processed from the five different solvent conditions are shown below in Figure 5-3, and are normalized for film thickness and offset vertically for clarity. Visible in all line cuts are a (100) lamellar stacking peak, a broad and weak (200) lamellar stacking peak, a broad $PC_{71}BM$ halo at q ~ 1.3 $Å^{-1}$. The non-halogenated solvent processed films have a weak (010) π-π stacking signal at q ~ 1.7 $Å^{-1}$. Looking at the changes between CB and CB + DIO, we see a sharp increase in the intensity of the (100) peak along with a shift to a slightly higher q, indicating a compression of the lamellar stack.

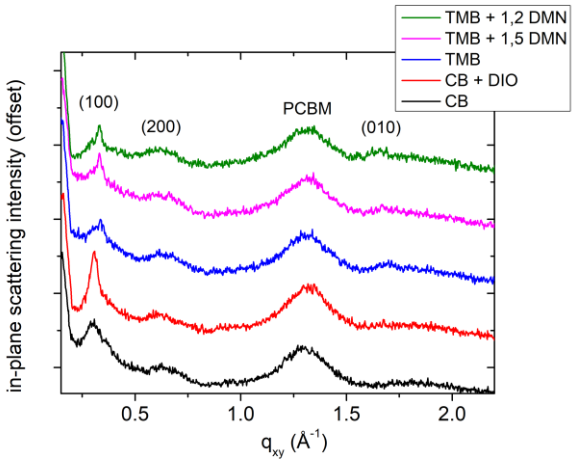

Figure 5-3 – GIWAXS in-plane line cuts for P(DTG-TPD):$PC_{71}BM$ blend films processed from a variety of solvent systems. Line cuts are normalized to film thickness and vertically offset for clarity.

In order to extract quantitative information from the GIWAXS line cuts, the (100) lamellar stacking peaks were fit to a gaussian function in order extract average lamellar spacing and average crystallite grain size.[121] For this analysis, it is important to note the

low intensity of the three TMB cast films which will add to the error in the measurement. In addition, Scherrer analysis, which is used to extract information about the size of the crystallite grains from the peak with, should not be used on the (100) to extract absolute grain size. This is due to the effect of cumulative disorder on the system, and is present in all semi-crystalline polymer films with solubilizing alkyl side chains.[205,206] However, this technique can be used to make relative comparisons between films of the same material, which is how it will be used here. The $d_{(100)}$ spacing is calculated via Braggs law, $q = 2\pi/d$, and the coherence length is calculated from the Scherrer equation: $L_c = 2\pi k/\Delta q$, where k is a shape factor and assumed to be 1, and Δq is the full with at half max (FWHM). These data are tabulated in Table 5-2.

Table 5-2 – Extracted lamellar spacing distances (d) and relative crystal correlation length (L_c) for P(DTG-TPD):$PC_{71}BM$ films cast from different solvent systems. Data are extracted from the in-plane line cuts shown in Figure 5-3, from a gaussian fit to the (100) peak in the range 0.248 $Å^{-1}$ < q < 0.390 $Å^{-1}$.

solvent system	$d_{(100)}$ (Å)	relative L_c (Å)
CB	21.0	83
CB + DIO	20.5	159
TMB	19.9	63
TMB + 1,5-DMN	19.2	161
TMB + 1,2-DMN	19.1	166

Results from quantitation of the GIWAXS line cuts reveal a slight compression in lamellar spacing when additive is used, which suggests improved polymer order. The addition of DIO decreases the lamellar spacing by 0.5 $Å^{-1}$, while the use of DMN decreases spacing even further by 0.7 $Å^{-1}$ to 0.8 $Å^{-1}$. These results correlate with the results from the Scherrer analysis, which quantitatively represents the sharpness of the peak and uniformity of lamellar spacing distances. The relative grain size from L_c increases twofold with the

use of additive and suggests the presence of polymer domains with improved order that should be good for charge transport.

To further analyze the effect of additive on morphological properties, GISAXS was conducted to investigate the phase behavior on the length scales that correspond to polymer and fullerene domains. A representative line cut along the Yoneda peak, comparing the CB only cast blend to the CB + DIO blend, is shown in Figure 5-4. The line cut from the additive-free case dominates at low q and indicates domain sizes well above q ~ 0.02 $Å^{-1}$, corresponding to domain sizes above 31 nm, longer than the exciton diffusion length.[81] Conversely, the line cut from the CB + DIO film extends to higher q, to q ~ 0.04 $Å^{-1}$, which corresponds to a length scale of 15 nm that is appropriate for efficient exciton dissociation.

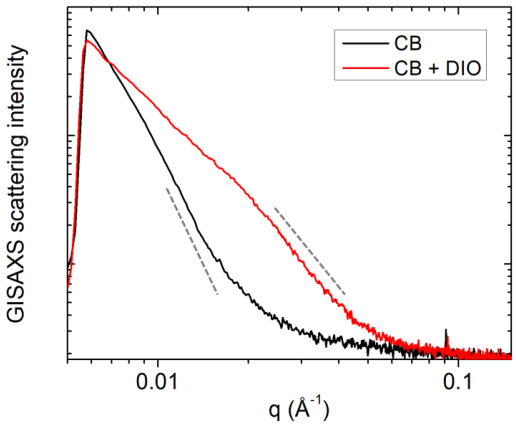

Figure 5-4 – GISAXS line cuts of P(DTG-TPD):$PC_{71}BM$ blends processed via either CB or CB + DIO. The grey dotted lines are used to visualize the angle of the system's smallest features, where a sharper boundary will have a steeper drop off, as is seen for the CB cast film.

In order to extract additional information about the phase behavior from the GISAXS data, the line cuts were analyzed with a unified fitting model,[207] which combines Guiner's law and Porod's law in order to describe the scattering of a hierarchical

nanostructure.[208,209] Guiner's law is an exponential function that describes scattering of features at small q, which correspond to the size of domains. Porod's law is a power law used to analyze large q features and describes the interfacial roughness between domains, i.e. mixing. This technique has been successfully use to describe phase behavior in block copolymer systems[210] as well as polymer:fullerene bulk heterojunctions.[211,212] At low q ranges, the decay of scattering intensity with increasing q is used to obtain a radius of gyration (R_g) of the scattering features. For this analysis, we have assumed spherical domains and converted R_g into the radius of a sphere (R_{sphere}), where $R_{sphere}^2 = (5/3) \bullet R_g^2$. This approximation is used to aid comparison and is not indicative of the true BHJ morphological landscape, which is complex and certainly not composed of perfect and uniform spherical domains. At high q, near the edge of the scattering signal, the slope of the scattering curve is used to calculate the boundary diffusivity parameter, P, and is a measure of the average degree of mixing between domains. For BHJs, P generally ranges from 3.5 to 2.0, where a value of 3.5 corresponds to a sharp slope and well-defined domain boundaries, while a value of 2.0 corresponds to a shallow slope and diffuse boundaries with mixing. The representative slopes are shown as dotted grey lines parallel to the GISAXS curves in Figure 5-4, in the regions used for fitting. Data for the five systems is combined and presented in Table 5-3, along with a qualitative assessment of domain mixing taken from the value of P.

Table 5-3 – Summary of domain information from GISAXS data processed with the Unified fit. Qualitative assessment of domain mixing is interpreted from P, the boundary diffusivity parameter, which decreases with increasing mixing.

solvent system	R_g (nm)	R_{sphere} (nm)	P	domain mixing
CB	33	42	3.4	weak

CB + DIO	12	15	2.4	strong
TMB	32	41	3.6	weak
TMB + 1,5-DMN	20	26	2.9	moderate
TMB + 1,2-DMN	21	27	2.8	moderate

The results from the two halogenated solvent blend films reflect the improvement in device performance, with domain size decreasing by almost a factor of three to length scales more appropriate for exciton diffusion. Domain mixing also becomes drastically stronger, moving from sharp interfaces at high P to diffuse interfaces at low P. Data from TMB is very comparable to the CB case, but the improvements in morphology seen with the two DMN additive films are not as strong as the CB to CB + DIO improvement. Domains do become smaller, and interfaces mix better, but not to the extent of the CB + DIO case for either variable. This morphological data explains the improvements in device data for all additive cases, as well as why the non-halogenated additive devices are not quite as high performing as the DIO counterpart, and is likely a result of DIO being a slightly better solvent for $PC_{71}BM$ relative to the dimethylnaphthalenes.[203]

5.3 Conclusion

In this work, we have compared halogenated and non-halogenated solvent processing of P(DTG-TPD):$PC_{71}BM$ blends for photovoltaic applications. The relatively low degree of order and crystallinity of P(DTG-TPD) likely allows for facile transfer among different processing conditions. Spin coated and blade coated devices, cast from the traditional halogenated solvent system of CB + DIO have virtually identical photovoltaic properties. When blade coating from non-halogenated solvent systems of 1,2,4-trimethylbenzene with two different dimethylnaphthalene additives, we observe a slight drop in performance

compared to the CB + DIO device. These slight changes were probed with detailed morphological studies via GIWAXS and GISAXS. Compared to the CB + DIO cast film, the TMB + DMN cast films were less crystalline, featured larger domains, and less domain mixing, all of which can explain the small drop in photovoltaic performance. This work highlights the use of low crystalline systems to adjust processing techniques and take advantage of non-halogenated solvent processing for printing of organic semiconductors.

5.4 Supporting information

5.4.1 Materials

Solvents for all studies and reagents for ZnO synthesis were purchased from Sigma Aldrich. Origins of other materials used in this study are described below.

5.4.2 Polymer synthesis and characterization

The polymer P(DTG-TPD) was synthesized as previously reported, and its purity was confirmed with elemental analysis.[10,213]

Number average molecular mass (M_n) and dispersity ($Đ$) were determined by Gel Permeation Chromatography (GPC) using a Tosoh EcoSEC HT GPC instrument with a RI detector. Experiments were run with TCB as eluent at 140 °C at a flow rate of 1 mL/min on two sequentially connected 30 mm by 7.8 mm GMHhr-H(S) HT2 columns (Tosoh Bioscience). The instrument was calibrated vs. polystyrene standards (1,390 to 1,214,000 g/mol), and data were analyzed using EcoSEC High Temperature GPC Workstation Software. To prepare polymer samples for GPC measurements, the polymer was dissolved

in HPLC grade TCB at a concentration of 1.0 mg/mL and then stirred for at least 3 h at 120 °C prior to filtering through a 0.45 mm PTFE filter.

Differential scanning calorimetry was performed from -50 °C to 350 °C at a scan rate of 20 °C/min, using a TA Instruments Q200 DSC.

UV/vis spectroscopy was measured with a Cary 5000 double-beam UV/VIS/NIR spectrophotometer.

5.4.3 Device fabrication and measurements

An inverted bulk heterojunction solar cell architecture comprising of glass/ITO/ZnO/polymer:$PC_{71}BM$/MoO_3/Ag was used to fabricate the solar cell devices in this work. Before the device processing, the patterned ITO-coated glass substrates (Latech Scientific Supply Pte. Ltd., sheet resistance 10 Ω/sq) were cleaned by sonicating sequentially with sodium dodecyl sulfate in Millipore water, pure Millipore water, and finally isopropanol for 10 minutes each. The cleaned substrates were blown dry with Argon and placed in a UV/O_3 chamber for 10 minutes. For the electron transport layer, a ZnO solution was made with 0.11 mol/L Zn acetate dihydrate and 0.11 mol/L ethanolamine combined in 2-methoxyethanol. This solution was stirred overnight at room temperature, then filtered with a 0.45 μm PTFE syringe filter before use.

The ZnO solution was deposited on the cleaned ITO substrates by spin-coating for 30 seconds at 419 rad/s (4000 rpm) in ambient atmosphere to get a layer thickness of ~30 nm. After spin-coating, the ZnO layer was annealed in air at 150 ˚C for 10 min followed by slow cooling to room temperature. The photoactive layer solution was prepared by

dissolving polymer and $PC_{71}BM$ (ADS71BFA, American Dye Source) in a ratio of 1:1.5. For halogenated solvent processing, either CB only or a solvent mixture of CB:DIO (95:5 v/v ratio). For non-halogenated solvent processing, either TMB only, a solvent mixture of TMB:1,2 DMB (97:3 v/v ratio), or a solution of 30 mg mL^{-1} 1,5 DMN in TMB was used (melting point of TMB is ~ 80 °C) which corresponds to the same volume ratio of 97:3. The solution was stirred at 80 °C for 2 hours to ensure complete dissolution. The active layer solution was allowed to cool to ≈25 °C before coating and was blade coated on top of the ZnO layer in ambient air with a custom blade coater, with a blade gap of 150 µm and blade speed of 12 mm/s. To remove the additive from the photoactive layer without disturbing the wet film, the samples were placed in a vacuum chamber with a pressure of 1×10^{-3} Pa (1×10^{-5} mbar) for 45 min. The top electrodes MoO_3 and Ag were deposited by vacuum deposition with layer thicknesses of 20 and 160 nm, respectively, to obtain complete solar cell devices with an electrode overlap area of 0.07 cm^2. Fast drying Ag paint (Ted Pella, 16040-30) was applied to the ITO electrodes to improve contact with the device switch-box. An aperture was not used for solar measurements (but it should have been). The *J-V* characteristics of all photovoltaic devices were evaluated under AM 1.5G solar illumination (100 mW cm^{-2}) using a Keithley SMU 2410 with a Newport Thermal Oriel 94021A solar simulator calibrated with a reference silicon solar cell.

5.4.4 Thin film characterization

Grazing-incidence wide-angle X-ray scattering (GIWAXS) samples of polymer:$PC_{71}BM$ blends were prepared on silicon wafer substrates using the optimized conditions for device preparation. GIWAXS was measured at the Stanford Synchrotron Radiation Lightsource (SSRL) beamline 11-3 in a helium-filled chamber with an X-ray

wavelength of 0.976 Å and sample to detector distance of 250 mm at an incident angle of 0.13°. Spectra were recorded on a Rayonix MARCCD area detector and processed using the Nika software package for Wavemetrics Igor, in combination with WAXStools.[66,133]

Grazing-incidence small-angle X-ray scattering (GISAXS) measurements were made on the same samples used for GIWAXS. GISAXS was measured at the Stanford Synchrotron Radiation Lightsource (SSRL) beamline 1-5 with a helium-filled scattering flight tube, with an X-ray wavelength of 0.976 Å and sample to detector distance of 3.0 m at an incident angle of 0.13°. Data were processed with Nika[133] and Irena[207] software packages for Wavemetrics Igor.

Atomic Force Microscopy of the blend films used for devices was measured with a Bruker Dimension Icon Atomic Force Microscope. For traditional tapping mode, the instrument was operated in tapping mode with a tapping frequency around 150 kHz.

5.4.5 Supporting figures and tables

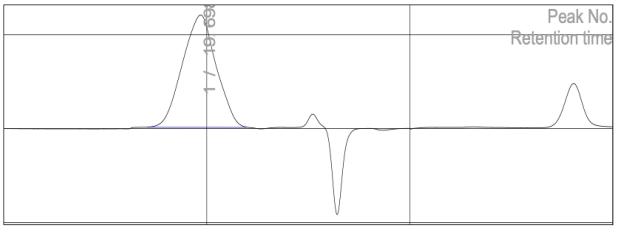

GEL PERMEATION CHROMATOGRAPHY

M_n	M_w	$Đ$	SOLVENT	TEMPERATURE	STANDARD
23.1 kDa	37.8 kDa	1.6	TCB	140 °C	polystyrene

Supporting Figure 5-1 – GPC trace of P(DTG-TPD).

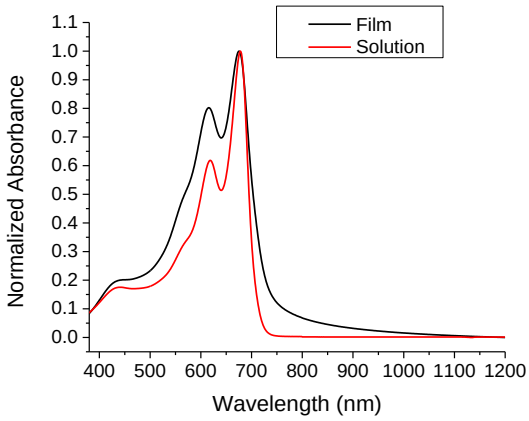

Supporting Figure 5-2 – Solution and thin film UV/vis of P(DTG-TPD). Solution UV/vis was conducted in chlorobenzene, and the thin film was spin coated from a chlorobenzene solution.

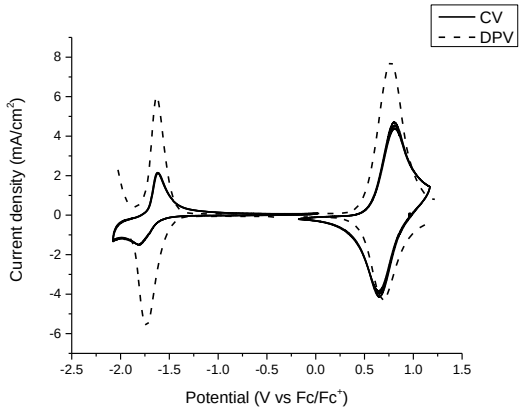

Supporting Figure 5-3 – CV and DPV traces of P(DTG-TPD).

Supporting Table 5-1 – Tabulated electrochemical and optical properties taken from the CV, DPV, and UV/vis data.

ELECTROCHEMICAL ANALYSIS (Reference: Fc/Fc^+, -5.1 eV vs Vacuum)									
CV $E_{1/2}$ (V)		DPV Peak (V)		DPV Onset (V)		Energy level by DPV onset (eV)		E_g^{Echem} (eV)	E_g^{Opt} (eV)
Ox	Red	Ox	Red	Ox	Red	HOMO	LUMO	2.02	1.70
0.73	-1.72	0.77	-1.73	0.49	-1.53	-5.59	-3.57		

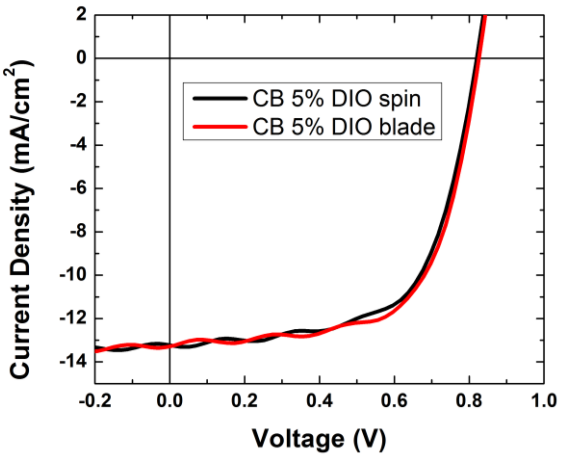

Supporting Figure 5-4 – Champion J-V curves from P(DTG-TPD):$PC_{71}BM$ blends processed from CB with 5% DIO via either spin coating or blade coating. Both pixels have PCEs of 7.0%.

Supporting Table 5-2 – Average photovoltaic parameters of devices processed from CB with 5% DIO via either spin coating or blade coating. Error bars represent one standard deviation, averaged from 8 devices.

	J_{sc} (mA cm^{-2})	V_{oc} (V)	FF (%)	PCE avg (best)
CB – DIO spin	12.5 ± 1.3	0.82 ± 0.01	58 ± 5	6.20 ± 0.75 (6.98)
CB – DIO blade	12.5 ± 1.0	0.81 ± 0.01	63 ± 2	6.38 ± 0.45 (7.03)

CHAPTER 6. OUTLOOK AND PERSPECTIVE ON BLADE COATING IN OPV

The three projects presented in this dissertation each covered a specific aspect of active layer processing via blade coating for OPV. Each chapter uses a different polymer system to explore a different problem in the field of solution processing. Chapter 3 discussed a highly aggregated and low solubility polymer, DT-PDPP2T-TT, and the effect of different high boiling point solvent additives on solidification and thin film morphology. Chapter 4 explored the new polymer, PffBT4T$_{80}$-co-3T$_{20}$-2OD, and the effect of its readily accessible thermal aggregation transition on its crystallinity and solidification alongside a crystalline molecular acceptor, IDTBR. Chapter 5 investigated non-halogenated solvent processing of P(DTG-TPD), and subtle morphological changes that result from transferring solvent systems. By isolating specific variables and taking care to keep all others constant, the subtle differences between processing with different solvent additives, molecular acceptors, solvent systems, or coating methods could be identified.

Chapter 2 of this dissertation explored in detail the nuances of many experimental techniques that are easy to take for granted, until they begin to malfunction. Over the years that the projects above were completed, various pieces of equipment required maintenance, reconstruction, or recalibration. This has highlighted aspects of the field of OPV that require some scrutiny, since failure to make proper measurements is a detriment to reproducibility and the foundation of a reliable knowledge base. To this day, papers are published that do not completely explain the steps need to reproduce the presented work. For example, some papers will report active layer thicknesses but do not share what

processing conditions generated that thickness. As explained in the Introduction, in the section about blade coating comparing the evaporative vs. Landau-Levich coating regimes, two different solution concentrations can be blade coated at vastly different speeds to achieve the same film thickness, but the resultant coating and drying dynamics can lead to drastically different morphologies. Spin coating acceleration rates and speeds should be reported, as should blade coating speeds and blade gaps. Solar cell devices should be tested with an aperture to ensure an accurate measure of the illuminated area and subsequent accurate measure of current density.[136] Power conversion efficiencies should be reported and compared on the basis of average performance, not champion performance; this distinction has been addressed whenever values are cited in this dissertation.

With subtle changes in experimental design and rigorous experimental protocol in mind, the remainder of this final chapter will summarize some of the work presented and address some challenges and ideas with which to explore the future of OPV.

6.1 The future of fullerenes

Fullerene-based molecular acceptors have dominated the field of OPV for most of its existence. All three projects in this dissertation are based on fullerene acceptor solar cells; only Chapter 4 features a comparison of $PC_{71}BM$ to the FREA IDTBR. As was discussed in the introduction, after the success of the PBDB-T:ITIC blend solar cell surpassing $PC_{71}BM$ performance, the field of NFA based solar cells began to dominate state-of-the-art photovoltaic devices. State-of-the-art for $PC_{71}BM$ solar cells remains at 11.7 % PCE,[30] while NFA based solar cells are regularly reported with PCEs exceeding 16 %. Aside from the improved photovoltaic performance, NFAs are more synthetically tunable and

accessible, and NFA-based devices are often more stable than their fullerene counterparts.[47] Downsides to the continued pursuit of NFAs over fullerenes are minimal. In general, starting new research efforts into fullerene acceptor based binary organic photovoltaic devices is not recommended.

However, fullerene acceptors have found present use as the minor third component to ternary solar cells, featuring a polymer donor and NFA as the major components of the active layer.[214] Fullerenes possess excellent charge carrier mobilities and can aggregate in various length scales in order to accommodate a variety of blends with different morphological properties, as was the case with original polymer:fullerene binary systems. Most polymer:NFA blend systems are designed to absorb light in the visible and NIR. Therefore, the addition of a UV light absorber further expands the breadth of light absorption of the active layer. A recent paper demonstrated that devices with the well-studied and highly performing PM6:Y6 blend, discussed in the introduction, have improved J_{SC}, V_{OC}, and FF with 10 % loading of $PC_{71}BM$ compared to the binary system, giving average PCEs of 16.4 % compared to 15.2 %.[215] A more robust morphology in the ternary blend likely would likely improve the likelihood of facile transition to blade coating.

6.2 Polymer aggregation: from spin coating to blade coating

Of the three polymers used in this dissertation, the two with a simple transition from spin coating to blade coating were DT-PDPP2T-TT and P(DTG-TPD). These polymers were both processed from relatively low temperature solutions (22 °C and 45 °C, respectively), avoiding any possible aggregation transition that we could visualize with

UV/vis absorption spectroscopy. These polymers had relatively low degrees of lamellar order when processed into a pristine film or a BHJ with PCBM. With minimal optimization, both of these polymers were built into devices with similar performance whether via spin coating inside a glovebox or blade coating in ambient air. Like the work from Jeff Hernandez et al. in our group with P(T3-TPD), processing from aggregated polymer solutions at low temperatures can simplify the transition from spin coating to blade coating.[216]

Conversely, PffBT4T$_{80}$-co-3T$_{20}$-2OD is overall more challenging to work with. Optimal performance was found when the polymer was cast from a solution heated to at least 50 °C, which is a temperature sufficient to break up the aggregates. Substrate heating of 50 °C was also generally used, especially for blade coating. Lower solution and stage temperatures increase the viscosity and changes handling protocols for both process methods. This polymer forms highly ordered films from a variety of coating temperatures via either spin coating or blade coating; only the use of IDTBR as the molecular acceptor was effective at supressing the crystallinity to an appreciable extent. In contrast to the polymers above, spin coating and blade coating device data did not achieve parity, with blade coating devices performing approximately 10 % worse with either acceptor. This goes back to the observation in the introduction to Chapter 4 that most high performing OPV devices with NFAs do not typically feature highly ordered polymers.

6.3 Designing new polymers for performance and facile solution processing

Several key factors have been established that control polymer solubility and processability: repeat unit structure, side chain volume and arrangement and molecular

weight. In chapter 3 we attributed strong aggregation to the combination of the planar backbone containing DPP and TT. In chapter 4 we showed the effectiveness of random terpolymer on de-aggregation for improved processability. However, in addition to randomness in the backbone conferred by the design of the random polymerization, we also essentially increased the side chain density, since while the side chains did not change between the ffBTD-T4 and ffBTD-3T repeat units, the one less thiophene makes the side-chain contribute more to the mass of the repeat unit. Our polymer, PffBT4T$_{80}$-co3T$_{20}$-2OD (80-20) is not as highly performing with PC$_{71}$BM or IDTBR compared to reported PffBT4T-2OD (C$_8$C$_{12}$) derivatives with longer side chains published from different groups: PffBT4T-C$_9$C$_{13}$ with PC$_{71}$BM has reported average/maximum efficiencies of 11.3 % / 11.7 %.[30] and PffBT4T-2DT (C$_{10}$C$_{14}$) with IDTBR has a reported average/maximum efficiencies of 10.7 % / 11.1 % PCE.[51] It is challenging to compare these polymers directly to ours given the various experimental data reported. Our 80-20 polymer has reported M_n and $Đ$ of 51 kg mol^{-1} and 1.84, respectively, with GPC performed in 1,2,4-trichlorobenzene at 140 °C. PffBT4T-C$_9$C$_{13}$ has a reported M_n of 68 kg mol^{-1} and $Đ$ of 1.62, and the molecular mass distribution of PffBT4T-2DT was not reported. These data are summarized in Table 6-1 in comparison to our data from (80-20) reported in chapter 4.

Table 6-1 – Polymer properties and spin coated power conversion efficiencies of PffBT4T-2OD derivatives processed via spin coating.

Polymer	M_n (kg mol^{-1})	$Đ$	GPC info	Avg (max) PCE with PC$_{71}$BM	Avg (max) PCE with IDTBR	Ref
PffBT4T$_{80}$-co3T$_{20}$-2OD (C$_8$C$_{12}$)	51	1.84	140 °C in 1,2,4-TCB	9.5 (9.9)	8.4 (8.9)	This work
PffBT4T-C$_9$C$_{13}$	68	1.62	170 °C in TCB	11.3 (11.7)	-	Zhao et al.[51]

PffBT4T-2DT ($C_{10}C_{14}$)	-	-	-	-	10.7 (11.1)	Wadsworth et al.[51]

Compared to 80-20, which has its aggregation broken up at 50 °C as per temperature dependent UV/vis spectroscopy, PffBT4T-C_9C_{13} has a small aggregate shoulder and long wavelengths until 70 °C, and PffBT4T-2DT has some evidence of aggregate character until 90 °C. From these results we can conclude that the random terpolymer technique is more effective than small side chain extension of PffBT4T-C_9C_{13} at more easily breaking up polymer aggregation. We can also conclude from the very high temperature to completely de-aggregate PffBT4T-2DT that the molecular mass is likely very high, at least 80 kg mol^{-1}. These results demonstrate the importance of aggregation in obtaining high performance, some of which we have lost with the de-aggregation shown by 80-20.

In order to regain some degree of aggregation, while still maintaining the ability to process at a variety of temperatures, I propose that a new family of polymers be made as similarly as possible to isolate the variables of structure and control for molecular mass distribution, as per the one atom change project by Kin Lo discussed in Chapter 5. In order to maintain the processing benefits of the random terpolymers while adding aggregate character to the system, I propose that to the random terpolymer synthesis be added a small amount of terthiophene monomer, in addition to the mono- and bithiophene monomers. I suggest a starting ratio of 75-20-5 (T4-T3-T5), to start with a minimal change to the structure of 80-20. The hope is that this large and complicated polymer structure is still slightly less aggregated than PffBT4T-2OD. The proposed synthetic scheme and resultant polymer repeat unit structure of PffBT4T$_m$-co-3T$_m$-co-5T$_x$-2OD is shown in Figure 6-1.

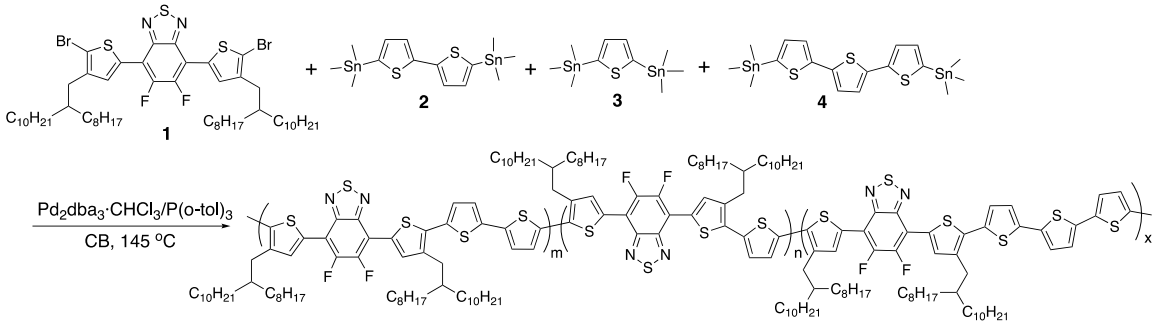

Figure 6-1 – Proposed synthetic scheme and repeat unit structure of the random polymer PffBT4T$_m$-co-3T$_m$-co-5T$_x$-2OD.

As I am not a synthetic chemist, I cannot speak to the viability of this synthetic scheme. Reproducibility of synthesis could be hampered by use of four monomer units and the extent of complexity of the backbone; perhaps this complexity could limit the polymer molecular mass. However, once in hand, this polymer would have some interesting aggregation properties. I would expect TDA transitions of the 75-20-5 composition to occur within the typical window that we see transitions for PffBT4T-2OD based polymers, that is, between 50 °C and 90 °C. In the solid state I would expect strong interchain interactions between the 5T repeat units which could be beneficial for charge transport and reduce bimolecular recombination in devices. Compared to PffBT4T-2OD, this polymer has increase aggregation due to the 5T unit and decreased aggregation due to the random component and the inclusion of 3T. This balance of aggregation and de-aggregation properties would make for an interesting morphological study, especially when comparing it to 80-20, PffBT4T-C_9C_{13}, and PffBT4T-2DT.

6.4 Thermal considerations for practical processing

Due to the ease with which processing temperatures can be controlled, and the potentially drastic changes to solution properties and to film properties, these variables

were commonly explored in the work presented in this dissertation. It was shown that PffBT4T-2OD, even coming from a 110 °C solution, instantly gels on a room temperature substrate. Through synthetic modification we improved processability and allowed for the use of a room temperature substrate. Even by reducing the spin coating solution temperature to 50 °C and keeping the substrate at room temperature (which was measured to be approximately 22 °C), device performance was similar to those made at higher temperatures. Specifically, PCEs of 80-20 with $PC_{71}BM$ drop from an average of 9.5 % to 9.0 %, while PCEs with IDTBR drop from 8.4 % to 6.1 %. As was explained in Chapter 4, this greater change with IDTBR was attributed to the polymer crystallization suppression we identified in those blend films with in situ GIWAXS measurements, compared to the $PC_{71}BM$ blend films. Presumably, for both acceptors, cooling the solution further would continue to decrease the overall power conversion efficiency, mainly through a reduction in fill factor. Despite the enhancements in processability with the random terpolymer approach, a typical coating solution of 80-20 still gels to some degree at room temperature.

In that work, we targeted a reduction in the temperature required for processing, with the assumption that lowering the thermal budget for processing is favorable for industrial processing. However, that work has not addressed the following question: what is the optimum processing temperature for OPV active layers? More specifically, do we target a processing temperature of ambient room temperature? By the fact that I have not supplied a specific temperature, the answer must be no; room temperature is relative and variable. Room temperature is not a specific temperature that is designed for an industrial setting; it is a range of temperatures around 22 °C that is comfortable for most people. The means by which substrates and solutions of 22 °C are achieved for processing in an enclosed

industrial setting can depend on the location and time of year. In Atlanta, GA, this would require heating in the winter and cooling in the summer. Other places may require only heating or cooling to maintain 22 °C over the course of one year.

Active heating of both the solution and substrate for the devices built in chapter 4 was achieved through readily available equipment: a standard laboratory hot plate and resistive heaters integrated into an aluminum stage. Even for the in situ GIWAXS coatings, where the solution needed to be autonomously dispensed, resistive heaters were similarly used around an aluminum jacket for the syringe. Processing of heated solutions onto heated substrates is similarly achieved in an industrial setting and is commonly used. Active cooling, on the other hand, poses a greater challenge. Cooling can induce ambient condensation in humid environments and maintaining active cooling like a compressor or chemical coolants like liquid N_2 or dry ice requires more attention and is more expensive than the aforementioned resistive heaters. Maintaining an ambient temperature of 22 °C in Atlanta would require both heating and cooling systems. Therefore, I will suggest here that an ideal processing temperature for solution processing, of both the stage and substrate, is approximately 40 °C. This temperature is sufficiently above ambient conditions in most of the world, during most of the year, while still being easily accessible via heaters. Ideal processing conditions for 80-20 blends in chapter 4 were demonstrated to be 50 °C, which is near this suggested temperature.

6.5 Moving towards more environmentally benign solvents for processing

Chapter 5 makes use of 1,2,4-trimethylbenzene and dimethylnaphthalenes for the processing of P(DTG-TPD):$PC_{71}BM$ blends, and while one might expect non-halogenated

aromatics to be safer than their counterparts, the differences between the two are not so clear. While the IMI-CHEM21 solvent selection guidelines advise that chlorinated solvents are in general better for lab use and safety compared to non-chlorinated counterparts, both xylenes (similar to TMB, which is not mentioned) and chlorobenzene are in the 'problematic' category.[192] Looking deeper, these two are problematic for different reasons. While xylenes have a moderately good safety score (based primarily on flash point) and environmental score, chlorobenzene has a better safety score and poor environmental score, due to its higher boiling point and deleterious environmental impact. Surprisingly, both xylenes and chlorobenzene have a similarly safe health score of 2 out of 10. Biodegradation of aromatic hydrocarbons such as xylene and TMB has been observed, which contributes to the environmental score,[217] and the low score of chlorobenzene also considers the environmental impact of producing halogenating aromatics. Therefore, one should not confuse the environmental and industrial benefits of non-halogenated aromatic solvent processing for improved health of those handling those materials.

Promising results for healthier solution processing of conjugated polymers was also discussed in Chapter 5, where (R)-(+)-limonene, a terpene, was recently used to deposit PBnDT-FTAZ, the donor polymer of a bilayer device.[197] Limonene is found in orange peels and appears to be safe for human use, so it would likely be overall safe scoring as per the IMI CHEM21 guidelines and a true eco-friendly solvent. However, for that blend, the acceptor ITIC-M was not soluble in limonene and was instead deposited by chlorobenzene. Terpenes have been shown before to be used to deposit the active layer of organic solar cells, albeit with DIO for reasonable performance; both PTB7 and $PC_{71}BM$ are soluble in terpinolene and were processed with 5% DIO to make solar cells with comparable

efficiencies to the CB + DIO processed active layers (6.2 % vs. 7.2 %).[218] Together these results show the promising use of eco-friendly terpenes but highlight their limitations in building a complete active layer for a device.

REFERENCES

(1) Ponder, J. F.; Reynolds, J. R. Conducting Polymers: Redox States in Conjugated Systems. *WSPC Ref. Org. Electron. Org. Semicond.* **2016**, *2*, 1–18.

(2) Salzner, U.; Lagowski, J.; Pickup, P.; Poirier, R. Comparison of Geometries and Electronic Structures of Polyacetylene, Polyborole, Polycyclopentadiene, Polypyrrole, Polyfuran, Polysilole, Polyphosphole, Polythiophene, Polyselenophene and Polytellurophene. *Synth. Met.* **1998**, *96* (1998), 177–189.

(3) Chamberlain, G. A. Organic Solar Cells: A Review. *Sol. Cells* **1983**, *8* (1), 47–83.

(4) Tang, C. W. Two-Layer Organic Photovoltaic Cell. *Appl. Phys. Lett.* **1986**, *48* (2), 183–185.

(5) Sariciftci, N. S.; Smilowitz, L.; Heeger, A. J.; Wudl, F. Photoinduced Electron Transfer from a Conducting Polymer to Buckminsterfullerene. *Science (80-.).* **1992**, *258* (5087), 1474–1476.

(6) Kraabel, B.; Lee, C. H.; McBranch, D.; Moses, D.; Sariciftci, N. S.; Heeger, A. J. Ultrafast Photoinduced Electron Transfer in Conducting Polymer-Buckminsterfullerene Composites. *Chem. Phys. Lett.* **1993**, *213* (3–4), 389–394.

(7) Yu, G.; Heeger, A. J. Charge Separation and Photovoltaic Conversion in Polymer Composites with Internal Donor/Acceptor Heterojunctions. *J. Appl. Phys.* **1995**, *78* (7), 4510–4515.

(8) Hummelen, J. C.; Knight, B. W.; Lepeq, F.; Wudl, F.; Yao, J.; Wilkins, C. L. Preparation and Characterization of Fulleroid and Methanofullerene Derivatives. *J. Org. Chem.* **1995**, *60* (3), 532–538.

(9) Havinga, E. E.; ten Hoeve, W.; Wynberg, H. Alternate Donor-Acceptor Small-Band-Gap Semiconducting Polymers; Polysquaraines and Polycroconaines. *Synth. Met.* **1993**, *55* (1), 299–306.

(10) Lo, C. K.; Gautam, B. R.; Selter, P.; Zheng, Z.; Oosterhout, S. D.; Constantinou, I.; Knitsch, R.; Wolfe, R. M. W.; Yi, X.; Brédas, J. L.; et al. Every Atom Counts: Elucidating the Fundamental Impact of Structural Change in Conjugated Polymers for Organic Photovoltaics. *Chem. Mater.* **2018**, *30* (9), 2995–3009.

(11) Xu, B.; Pelse, I.; Agarkar, S.; Ito, S.; Zhang, J.; Yi, X.; Chujo, Y.; Marder, S.; So, F.; Reynolds, J. R. Randomly Distributed Conjugated Polymer Repeat Units for High-Efficiency Photovoltaic Materials with Enhanced Solubility and Processability. *ACS Appl. Mater. Interfaces* **2018**, *10* (51), 44583–44588.

(12) Beaupré, S.; Shaker-Sepasgozar, S.; Najari, A.; Leclerc, M. Random D-A1-D-A2

Terpolymers Based on Benzodithiophene, Thiadiazole[3,4-e]Isoindole-5,7-Dione and Thieno[3,4-c]Pyrrole-4,6-Dione for Efficient Polymer Solar Cells. *J. Mater. Chem. A* **2017**, *5* (14), 6638–6647.

(13) Jung, J. W.; Liu, F.; Russell, T. P.; Jo, W. H. Semi-Crystalline Random Conjugated Copolymers with Panchromatic Absorption for Highly Efficient Polymer Solar Cells. *Energy Environ. Sci.* **2013**, *6* (11), 3301–3307.

(14) Kang, T. E.; Cho, H. H.; Kim, H. J.; Lee, W.; Kang, H.; Kim, B. J. Importance of Optimal Composition in Random Terpolymer-Based Polymer Solar Cells. *Macromolecules* **2013**, *46* (17), 6806–6813.

(15) Kang, T. E.; Choi, J.; Cho, H. H.; Yoon, S. C.; Kim, B. J. Donor-Acceptor Random versus Alternating Copolymers for Efficient Polymer Solar Cells: Importance of Optimal Composition in Random Copolymers. *Macromolecules* **2016**, *49* (6), 2096–2105.

(16) Lee, J. W.; Ahn, H.; Jo, W. H. Conjugated Random Copolymers Consisting of Pyridine- and Thiophene-Capped Diketopyrrolopyrrole as Co-Electron Accepting Units to Enhance Both JSC and VOC of Polymer Solar Cells. *Macromolecules* **2015**, *48* (21), 7836–7842.

(17) Zhu, X.; Lu, K.; Xia, B.; Fang, J.; Zhao, Y.; Zhao, T.; Wei, Z.; Jiang, L. Improving the Performances of Random Copolymer Based Organic Solar Cells by Adjusting the Film Features of Active Layers Using Mixed Solvents. *Polymers (Basel).* **2016**, *8* (4), 8010004.

(18) Gao, X.; Wu, Y.; Tao, Y.; Huang, W. Conjugated Random Terpolymer Donors towards High-Efficiency Polymer. *Chinese J. Chem.* **2020**, *38*, 10.1002/cjoc.201900503.

(19) Kline, R. J.; McGehee, M. D.; Kadnikova, E. N.; Liu, J.; Fréchet, J. M. J. Controlling the Field-Effect Mobility of Regioregular Polythiophene by Changing the Molecular Weight. *Adv. Mater.* **2003**, *15* (18), 1519–1522.

(20) Goh, C.; Kline, R. J.; McGehee, M. D.; Kadnikova, E. N.; Fŕchet, J. M. J. Molecular-Weight-Dependent Mobilities in Regioregular Poly(3-Hexyl-Thiophene) Diodes. *Appl. Phys. Lett.* **2005**, *86* (12), 122110.

(21) Zen, A.; Saphiannikova, M.; Neher, D.; Grenzer, J.; Grigorian, S.; Pietsch, U.; Asawapirom, U.; Janietz, S.; Scherf, U.; Lieberwirth, I.; et al. Effect of Molecular Weight on the Structure and Crystallinity of Poly(3-Hexylthiophene). *Macromolecules* **2006**, *39* (6), 2162–2171.

(22) Schilinsky, P.; Asawapirom, U.; Scherf, U.; Biele, M.; Brabec, C. J. Influence of the Molecular Weight of Poly(3-Hexylthiophene) on the Performance of Bulk Heterojunction Solar Cells. *Chem. Mater.* **2005**, *17* (8), 2175–2180.

(23) Coffin, R. C.; Peet, J.; Rogers, J.; Bazan, G. C. Streamlined Microwave-Assisted Preparation of Narrow-Bandgap Conjugated Polymers for High-Performance Bulk Heterojunction Solar Cells. *Nat. Chem.* **2009**, *1* (8), 657–661.

(24) Choi, J.; Kim, W.; Kim, D.; Kim, S.; Chae, J.; Choi, S. Q.; Kim, F. S.; Kim, T. S.; Kim, B. J. Importance of Critical Molecular Weight of Semicrystalline N-Type Polymers for Mechanically Robust, Efficient Electroactive Thin Films. *Chem. Mater.* **2019**, *31* (9), 3163–3173.

(25) Deshmukh, K. D.; Matsidik, R.; Prasad, S. K. K.; Connal, L. A.; Liu, A. C. Y.; Gann, E.; Thomsen, L.; Hodgkiss, J. M.; Sommer, M.; McNeill, C. R. Tuning the Molecular Weight of the Electron Accepting Polymer in All-Polymer Solar Cells: Impact on Morphology and Charge Generation. *Adv. Funct. Mater.* **2018**, *28* (18), 1707185.

(26) He, Y.; Li, Y. Fullerene Derivative Acceptors for High Performance Polymer Solar Cells. *Phys. Chem. Chem. Phys.* **2011**, *13* (6), 1970–1983.

(27) Wadsworth, A.; Moser, M.; Marks, A.; Little, M. S.; Gasparini, N.; Brabec, C. J.; Baran, D.; McCulloch, I. Critical Review of the Molecular Design Progress in Non-Fullerene Electron Acceptors towards Commercially Viable Organic Solar Cells. *Chem. Soc. Rev.* **2019**, *48* (6), 1596–1625.

(28) Wienk, M. M.; Kroon, J. M.; Verhees, W. J. H.; Knol, J.; Hummelen, J. C.; Van Hal, P. A.; Janssen, R. A. J. Efficient Methano[70]Fullerene/MDMO-PPV Bulk Heterojunction Photovoltaic Cells. *Angew. Chemie - Int. Ed.* **2003**, *42* (29), 3371–3375.

(29) Liu, Y.; Zhao, J.; Li, Z.; Mu, C.; Ma, W.; Hu, H.; Jiang, K.; Lin, H.; Ade, H.; Yan, H. Aggregation and Morphology Control Enables Multiple Cases of High-Efficiency Polymer Solar Cells. *Nat. Commun.* **2014**, *5* (9), 5293.

(30) Zhao, J.; Li, Y.; Yang, G.; Jiang, K.; Lin, H.; Ade, H.; Ma, W.; Yan, H. Efficient Organic Solar Cells Processed from Hydrocarbon Solvents. *Nat. Energy* **2016**, *1* (2), 15027.

(31) He, Y.; Chen, H. Y.; Hou, J.; Li, Y. Indene - C60 Bisadduct: A New Acceptor for High-Performance Polymer Solar Cells. *J. Am. Chem. Soc.* **2010**, *132* (4), 1377–1382.

(32) Kolesov, V. A.; Fuentes-Hernandez, C.; Chou, W. F.; Aizawa, N.; Larrain, F. A.; Wang, M.; Perrotta, A.; Choi, S.; Graham, S.; Bazan, G. C.; et al. Solution-Based Electrical Doping of Semiconducting Polymer Films over a Limited Depth. *Nat. Mater.* **2017**, *16* (4), 474–481.

(33) Larrain, F. A.; Fuentes-Hernandez, C.; Chou, W. F.; Rodriguez-Toro, V. A.; Huang, T. Y.; Toney, M. F.; Kippelen, B. Stable Solvent for Solution-Based Electrical Doping of Semiconducting Polymer Films and Its Application to Organic Solar

Cells. *Energy Environ. Sci.* **2018**, *11* (8), 2216–2224.

(34) Huang, T. Y.; Larrain, F. A.; Borca, C. H.; Fuentes-Hernandez, C.; Yan, H.; Schneider, S. A.; Chou, W. F.; Rodriguez-Toro, V. A.; Steinrück, H. G.; Cao, C.; et al. Morphology of Organic Semiconductors Electrically Doped from Solution Using Phosphomolybdic Acid. *Chem. Mater.* **2019**, *31* (17), 6677–6683.

(35) Campoy-Quiles, M.; Ferenczi, T.; Agostinelli, T.; Etchegoin, P. G.; Kim, Y.; Anthopoulos, T. D.; Stavrinou, P. N.; Bradley, D. D. C.; Nelson, J. Morphology Evolution via Self-Organization and Lateral and Vertical Diffusion in Polymer:Fullerene Solar Cell Blends. *Nat. Mater.* **2008**, *7* (2), 158–164.

(36) Tremolet De Villers, B. J.; O'Hara, K. A.; Ostrowski, D. P.; Biddle, P. H.; Shaheen, S. E.; Chabinyc, M. L.; Olson, D. C.; Kopidakis, N. Removal of Residual Diiodooctane Improves Photostability of High-Performance Organic Solar Cell Polymers. *Chem. Mater.* **2016**, *28* (3), 876–884.

(37) Zhan, X.; Facchetti, A.; Barlow, S.; Marks, T. J.; Ratner, M. A.; Wasielewski, M. R.; Marder, S. R. Rylene and Related Diimides for Organic Electronics. *Adv. Mater.* **2011**, *23* (2), 268–284.

(38) Sharenko, A.; Proctor, C. M.; Van Der Poll, T. S.; Henson, Z. B.; Nguyen, T. Q.; Bazan, G. C. A High-Performing Solution-Processed Small Molecule: Perylene Diimide Bulk Heterojunction Solar Cell. *Adv. Mater.* **2013**, *25* (32), 4403–4406.

(39) Wu, Q.; Zhao, D.; Schneider, A. M.; Chen, W.; Yu, L. Covalently Bound Clusters of Alpha-Substituted PDI-Rival Electron Acceptors to Fullerene for Organic Solar Cells. *J. Am. Chem. Soc.* **2016**, *138* (23), 7248–7251.

(40) Liu, J.; Chen, S.; Qian, D.; Gautam, B.; Yang, G.; Zhao, J.; Bergqvist, J.; Zhang, F.; Ma, W.; Ade, H.; et al. Fast Charge Separation in a Non-Fullerene Organic Solar Cell with a Small Driving Force. *Nat. Energy* **2016**, *1* (7), 16089.

(41) Yan, H.; Chen, Z.; Zheng, Y.; Newman, C.; Quinn, J. R.; Dötz, F.; Kastler, M.; Facchetti, A. A High-Mobility Electron-Transporting Polymer for Printed Transistors. *Nature* **2009**, *457* (7230), 679–686.

(42) Moore, J. R.; Albert-Seifried, S.; Rao, A.; Massip, S.; Watts, B.; Morgan, D. J.; Friend, R. H.; McNeill, C. R.; Sirringhaus, H. Polymer Blend Solar Cells Based on a High-Mobility Naphthalenediimide-Based Polymer Acceptor: Device Physics, Photophysics and Morphology. *Adv. Energy Mater.* **2011**, *1* (2), 230–240.

(43) Holcombe, T. W.; Norton, J. E.; Rivnay, J.; Woo, C. H.; Goris, L.; Piliego, C.; Griffini, G.; Sellinger, A.; Brédas, J. L.; Salleo, A.; et al. Steric Control of the Donor/Acceptor Interface: Implications in Organic Photovoltaic Charge Generation. *J. Am. Chem. Soc.* **2011**, *133* (31), 12106–12114.

(44) Fan, B.; Ying, L.; Zhu, P.; Pan, F.; Liu, F.; Chen, J.; Huang, F.; Cao, Y. All-Polymer

Solar Cells Based on a Conjugated Polymer Containing Siloxane-Functionalized Side Chains with Efficiency over 10%. *Adv. Mater.* **2017**, *29* (47), 1703906.

(45) Kim, Y.; Song, C. E.; Moon, S. J.; Lim, E. Rhodanine Dye-Based Small Molecule Acceptors for Organic Photovoltaic Cells. *Chem. Commun.* **2014**, *50* (60), 8235–8238.

(46) Qiu, N.; Zhang, H.; Wan, X.; Li, C.; Ke, X.; Feng, H.; Kan, B.; Zhang, H.; Zhang, Q.; Lu, Y.; et al. A New Nonfullerene Electron Acceptor with a Ladder Type Backbone for High-Performance Organic Solar Cells. *Adv. Mater.* **2017**, *29* (6), 1–5.

(47) Zhao, W.; Qian, D.; Zhang, S.; Li, S.; Inganäs, O.; Gao, F.; Hou, J. Fullerene-Free Polymer Solar Cells with over 11% Efficiency and Excellent Thermal Stability. *Adv. Mater.* **2016**, *28* (23), 4734–4739.

(48) Zhang, Y.; Yao, H.; Zhang, S.; Qin, Y.; Zhang, J.; Yang, L.; Li, W.; Wei, Z.; Gao, F.; Hou, J. Fluorination vs. Chlorination: A Case Study on High Performance Organic Photovoltaic Materials. *Sci. China Chem.* **2018**, *61* (10), 1328–1337.

(49) Zhao, W.; Li, S.; Yao, H.; Zhang, S.; Zhang, Y.; Yang, B.; Hou, J. Molecular Optimization Enables over 13% Efficiency in Organic Solar Cells. *J. Am. Chem. Soc.* **2017**, *139* (21), 7148–7151.

(50) Holliday, S.; Ashraf, R. S.; Wadsworth, A.; Baran, D.; Yousaf, S. A.; Nielsen, C. B.; Tan, C. H.; Dimitrov, S. D.; Shang, Z.; Gasparini, N.; et al. High-Efficiency and Air-Stable P3HT-Based Polymer Solar Cells with a New Non-Fullerene Acceptor. *Nat. Commun.* **2016**, *7*, 1–11.

(51) Wadsworth, A.; Ashraf, R. S.; Abdelsamie, M.; Pont, S.; Little, M.; Moser, M.; Hamid, Z.; Neophytou, M.; Zhang, W.; Amassian, A.; et al. Highly Efficient and Reproducible Nonfullerene Solar Cells from Hydrocarbon Solvents. *ACS Energy Lett.* **2017**, *2* (7), 1494–1500.

(52) Yuan, J.; Zhang, Y.; Zhou, L.; Zhang, G.; Yip, H. L.; Lau, T. K.; Lu, X.; Zhu, C.; Peng, H.; Johnson, P. A.; et al. Single-Junction Organic Solar Cell with over 15% Efficiency Using Fused-Ring Acceptor with Electron-Deficient Core. *Joule* **2019**, *3* (4), 1140–1151.

(53) Yan, T.; Song, W.; Huang, J.; Peng, R.; Huang, L.; Ge, Z. 16.67% Rigid and 14.06% Flexible Organic Solar Cells Enabled by Ternary Heterojunction Strategy. *Adv. Mater.* **2019**, *31* (39), 1–8.

(54) Liu, L.; Kan, Y.; Gao, K.; Wang, J.; Zhao, M.; Chen, H.; Zhao, C.; Jiu, T.; Jen, A. -Y.; Li, Y. Graphdiyne Derivative as Multifunctional Solid Additive in Binary Organic Solar Cells with 17.3% Efficiency and High Reproductivity. *Adv. Mater.* **2020**, *1907604*, 1907604.

(55) Wang, C.; Zhang, Z.; Pejić, S.; Li, R.; Fukuto, M.; Zhu, L.; Sauvé, G. High Dielectric Constant Semiconducting Poly(3-Alkylthiophene)s from Side Chain Modification with Polar Sulfinyl and Sulfonyl Groups. *Macromolecules* **2018**, *51* (22), 9368–9381.

(56) Kippelen, B.; Brédas, J. L. Organic Photovoltaics. *Energy Environ. Sci.* **2009**, *2* (3), 251–261.

(57) Pelzer, K. M.; Darling, S. B. Charge Generation in Organic Photovoltaics: A Review of Theory and Computation. *Mol. Syst. Des. Eng.* **2016**, *1* (1), 10–24.

(58) Chen, S.; Small, C. E.; Amb, C. M.; Subbiah, J.; Lai, T. H.; Tsang, S. W.; Manders, J. R.; Reynolds, J. R.; So, F. Inverted Polymer Solar Cells with Reduced Interface Recombination. *Adv. Energy Mater.* **2012**, *2* (11), 1333–1337.

(59) Constantinou, I.; Shewmon, N. T.; Lo, C. K.; Deininger, J. J.; Reynolds, J. R.; So, F. Photodegradation of Metal Oxide Interlayers in Polymer Solar Cells. *Adv. Mater. Interfaces* **2016**, *3* (23).

(60) Shaw, P. E.; Ruseckas, A.; Samuel, I. D. W. Exciton Diffusion Measurements in Poly(3-Hexylthiophene). *Adv. Mater.* **2008**, *20* (18), 3516–3520.

(61) Mikhnenko, O. V.; Azimi, H.; Scharber, M.; Morana, M.; Blom, P. W. M.; Loi, M. A. Exciton Diffusion Length in Narrow Bandgap Polymers. *Energy Environ. Sci.* **2012**, *5* (5), 6960–6965.

(62) Brabec, C. J.; Heeney, M.; McCulloch, I.; Nelson, J. Influence of Blend Microstructure on Bulk Heterojunction Organic Photovoltaic Performance. *Chem. Soc. Rev.* **2011**, *40* (3), 1185–1199.

(63) Westacott, P.; Tumbleston, J. R.; Shoaee, S.; Fearn, S.; Bannock, J. H.; Gilchrist, J. B.; Heutz, S.; Demello, J.; Heeney, M.; Ade, H.; et al. On the Role of Intermixed Phases in Organic Photovoltaic Blends. *Energy Environ. Sci.* **2013**, *6* (9), 2756–2764.

(64) Chen, W.; Xu, T.; He, F.; Wang, W.; Wang, C.; Strzalka, J.; Liu, Y.; Wen, J.; Miller, D. J.; Chen, J.; et al. Hierarchical Nanomorphologies Promote Exciton Dissociation in Polymer/Fullerene Bulk Heterojunction Solar Cells. *Nano Lett.* **2011**, *11* (9), 3707–3713.

(65) Bartelt, J. A.; Beiley, Z. M.; Hoke, E. T.; Mateker, W. R.; Douglas, J. D.; Collins, B. A.; Tumbleston, J. R.; Graham, K. R.; Amassian, A.; Ade, H.; et al. The Importance of Fullerene Percolation in the Mixed Regions of Polymer-Fullerene Bulk Heterojunction Solar Cells. *Adv. Energy Mater.* **2013**, *3* (3), 364–374.

(66) Oosterhout, S. D.; Savikhin, V.; Zhang, J.; Zhang, Y.; Burgers, M. A.; Marder, S. R.; Bazan, G. C.; Toney, M. F. Mixing Behavior in Small Molecule:Fullerene Organic Photovoltaics. *Chem. Mater.* **2017**, *29* (7), 3062–3069.

(67) Hildebrand, J. H. A Critique of the Theory of Solubility of Non-Electrolytes. *Chem. Rev.* **1949**, *44* (1), 37–45.

(68) Flory, P. J. Thermodynamics of High Polymer Solutions. *J. Chem. Phys.* **1942**, *10*, 51–61.

(69) Huggins, M. L. Solutions of Long Chain Compounds. *J. Chem. Phys.* **1941**, *9*, 440.

(70) Hansen, C. M. The Three Dimensional Solubility Parameter and Solvent Diffusion Coefficient. Their Importance in Surface Coating Formulation. *J. Paint Technol.* **1967**, 104.

(71) Patterson, D. Role Of Free Volume In Polymer Solution Thermodynamics. *Pure Appl. Chem.* **1972**, *31* (1–2), 133–150.

(72) Chang, M.; Choi, D.; Fu, B.; Reichmanis, E. Solvent Based Hydrogen Bonding: Impact on Poly(3-Hexylthiophene) Nanoscale Morphology and Charge Transport Characteristics. *ACS Nano* **2013**, *7* (6), 5402–5413.

(73) Kouijzer, S.; Michels, J. J.; Van Den Berg, M.; Gevaerts, V. S.; Turbiez, M.; Wienk, M. M.; Janssen, R. A. J. Predicting Morphologies of Solution Processed Polymer:Fullerene Blends. *J. Am. Chem. Soc.* **2013**, *135* (32), 12057–12067.

(74) Van Franeker, J. J.; Turbiez, M.; Li, W.; Wienk, M. M.; Janssen, R. A. J. A Real-Time Study of the Benefits of Co-Solvents in Polymer Solar Cell Processing. *Nat. Commun.* **2015**, *6*, 6229.

(75) Schmidt-Hansberg, B.; Sanyal, M.; Klein, M. F. G.; Pfaff, M.; Schnabel, N.; Jaiser, S.; Vorobiev, A.; Müller, E.; Colsmann, A.; Scharfer, P.; et al. Moving through the Phase Diagram: Morphology Formation in Solution Cast Polymer-Fullerene Blend Films for Organic Solar Cells. *ACS Nano* **2011**, *5* (11), 8579–8590.

(76) Richter, L. J.; Delongchamp, D. M.; Bokel, F. A.; Engmann, S.; Chou, K. W.; Amassian, A.; Schaible, E.; Hexemer, A. In Situ Morphology Studies of the Mechanism for Solution Additive Effects on the Formation of Bulk Heterojunction Films. *Adv. Energy Mater.* **2015**, *5* (3), 1400975.

(77) McDowell, C.; Abdelsamie, M.; Toney, M. F.; Bazan, G. C. Solvent Additives: Key Morphology-Directing Agents for Solution-Processed Organic Solar Cells. *Adv. Mater.* **2018**, *30* (33), 1–30.

(78) Ho, V.; Boudouris, B. W.; Segalman, R. A. Tuning Polythiophene Crystallization through Systematic Side Chain Functionalization. *Macromolecules* **2010**, *43* (19), 7895–7899.

(79) Mei, J.; Bao, Z. Side Chain Engineering in Solution-Processable Conjugated Polymers. *Chem. Mater.* **2014**, *26* (1), 604–615.

(80) Zhang, M.; Guo, X.; Ma, W.; Ade, H.; Hou, J. A Polythiophene Derivative with Superior Properties for Practical Application in Polymer Solar Cells. *Adv. Mater.* **2014**, *26* (33), 5880–5885.

(81) Hoppe, H.; Niggemann, M.; Winder, C.; Kraut, J.; Hiesgen, R.; Hinsch, A.; Meissner, D.; Sariciftci, N. S. Nanoscale Morphology of Conjugated Polymer/Fullerene-Based Bulk-Heterojunction Solar Cells. *Adv. Funct. Mater.* **2004**, *14* (10), 1005–1011.

(82) Peet, J.; Soci, C.; Coffin, R. C.; Nguyen, T. Q.; Mikhailovsky, A.; Moses, D.; Bazan, G. C. Method for Increasing the Photoconductive Response in Conjugated Polymer/Fullerene Composites. *Appl. Phys. Lett.* **2006**, *89* (25), 7–9.

(83) Mühlbacher, D.; Scharber, M.; Morana, M.; Zhu, Z.; Waller, D.; Gaudiana, R.; Brabec, C. J. High Photovoltaic Performance of a Low-Bandgap Polymer. *Adv. Mater.* **2006**, *18* (21), 2884–2889.

(84) Soci, C.; Hwang, I. W.; Moses, D.; Zhu, Z.; Waller, D.; Gaudiana, R.; Brabec, C. J.; Heeger, A. J. Photoconductivity of a Low-Bandgap Conjugated Polymer. *Adv. Funct. Mater.* **2007**, *17* (4), 632–636.

(85) Peet, J.; Brocker, E.; Xu, Y.; Bazan, G. C. Controlled β-Phase Formation in Poly(9,9-Di-n-Octylfluorene) by Processing with Alkyl Additives. *Adv. Mater.* **2008**, *20* (10), 1882–1885.

(86) Jae, K. L.; Wan, L. M.; Brabec, C. J.; Yuen, J.; Ji, S. M.; Jin, Y. K.; Lee, K.; Bazan, G. C.; Heeger, A. J. Processing Additives for Improved Efficiency from Bulk Heterojunction Solar Cells. *J. Am. Chem. Soc.* **2008**, *130* (11), 3619–3623.

(87) Tan, Z. K.; Vaynzof, Y.; Credgington, D.; Li, C.; Casford, M. T. L.; Sepe, A.; Huettner, S.; Nikolka, M.; Paulus, F.; Yang, L.; et al. In-Situ Switching from Barrier-Limited to Ohmic Anodes for Efficient Organic Optoelectronics. *Adv. Funct. Mater.* **2014**, *24* (20), 3051–3058.

(88) Huang, W.; Gann, E.; Xu, Z. Q.; Thomsen, L.; Cheng, Y. B.; McNeill, C. R. A Facile Approach to Alleviate Photochemical Degradation in High Efficiency Polymer Solar Cells. *J. Mater. Chem. A* **2015**, *3* (31), 16313–16319.

(89) Chen, H.; Hsiao, Y. C.; Hu, B.; Dadmun, M. Tuning the Morphology and Performance of Low Bandgap Polymer:Fullerene Heterojunctions via Solvent Annealing in Selective Solvents. *Adv. Funct. Mater.* **2014**, *24* (32), 5129–5136.

(90) McDowell, C.; Abdelsamie, M.; Zhao, K.; Smilgies, D. M.; Bazan, G. C.; Amassian, A. Synergistic Impact of Solvent and Polymer Additives on the Film Formation of Small Molecule Blend Films for Bulk Heterojunction Solar Cells. *Adv. Energy Mater.* **2015**, *5* (18), 1–9.

(91) Yu, R.; Yao, H.; Hong, L.; Qin, Y.; Zhu, J.; Cui, Y.; Li, S.; Hou, J. Design and

Application of Volatilizable Solid Additives in Non-Fullerene Organic Solar Cells. *Nat. Commun.* **2018**, *9* (1), 1–9.

(92) Cai, J.; Wang, H.; Zhang, X.; Li, W.; Li, D.; Mao, Y.; Du, B.; Chen, M.; Zhuang, Y.; Liu, D.; et al. Fluorinated Solid Additives Enable High Efficiency Non-Fullerene Organic Solar Cells. *J. Mater. Chem. A* **2020**, *8* (8), 4230–4238.

(93) Padinger, F.; Rittberger, R. S.; Sariciftci, N. S. Effects of Postproduction Treatment on Plastic Solar Cells. *Adv. Funct. Mater.* **2003**, *13* (1), 85–88.

(94) Ma, W.; Yang, C.; Gong, X.; Lee, K.; Heeger, A. J. Thermally Stable, Efficient Polymer Solar Cells with Nanoscale Control of the Interpenetrating Network Morphology. *Adv. Funct. Mater.* **2005**, *15* (10), 1617–1622.

(95) Sun, C.; Pan, F.; Bin, H.; Zhang, J.; Xue, L.; Qiu, B.; Wei, Z.; Zhang, Z. G.; Li, Y. A Low Cost and High Performance Polymer Donor Material for Polymer Solar Cells. *Nat. Commun.* **2018**, *9* (1), 1–10.

(96) Li, G.; Shrotriya, V.; Huang, J.; Yao, Y.; Moriarty, T.; Emery, K.; Yang, Y. High-Efficiency Solution Processable Polymer Photovoltaic Cells by Self-Organization of Polymer Blends. *Nat. Mater.* **2005**, *4* (11), 864–868.

(97) Tang, H.; Lu, G.; Li, L.; Li, J.; Wang, Y.; Yang, X. Precise Construction of PCBM Aggregates for Polymer Solar Cells via Multi-Step Controlled Solvent Vapor Annealing. *J. Mater. Chem.* **2010**, *20* (4), 683–688.

(98) Zhao, F.; Wang, C.; Zhan, X. Morphology Control in Organic Solar Cells. *Adv. Energy Mater.* **2018**, *8* (28), 1–34.

(99) McDowell, C.; Bazan, G. C. Organic Solar Cells Processed from Green Solvents. *Curr. Opin. Green Sustain. Chem.* **2017**, *5*, 49–54.

(100) Chen, X.; Liu, X.; Burgers, M. A.; Huang, Y.; Bazan, G. C. Green-Solvent-Processed Molecular Solar Cells. *Angew. Chemie - Int. Ed.* **2014**, *53* (52), 14378–14381.

(101) Richter, L. J.; Delongchamp, D. M.; Amassian, A. Morphology Development in Solution-Processed Functional Organic Blend Films: An in Situ Viewpoint. *Chem. Rev.* **2017**, *117* (9), 6332–6366.

(102) Khim, D.; Han, H.; Baeg, K. J.; Kim, J.; Kwak, S. W.; Kim, D. Y.; Noh, Y. Y. Simple Bar-Coating Process for Large-Area, High-Performance Organic Field-Effect Transistors and Ambipolar Complementary Integrated Circuits. *Adv. Mater.* **2013**, *25* (31), 4302–4308.

(103) Norrman, K.; Ghanbari-Siahkali, A.; Larsen, N. B. Studies of Spin-Coated Polymer Films. *Annu. Reports Prog. Chem. - Sect. C* **2005**, *101*, 174–201.

(104) Seifrid, M. T.; Oosterhout, S. D.; Toney, M. F.; Bazan, G. C. Kinetic Versus Thermodynamic Orientational Preferences for a Series of Isomorphic Molecular Semiconductors. *ACS Omega* **2018**, *3* (8), 10198–10204.

(105) Søndergaard, R.; Hösel, M.; Angmo, D.; Larsen-Olsen, T. T.; Krebs, F. C. Roll-to-Roll Fabrication of Polymer Solar Cells. *Mater. Today* **2012**, *15* (1–2), 36–49.

(106) Davis, R. L.; Jayaraman, S.; Chaikin, P. M.; Register, R. A. Creating Controlled Thickness Gradients in Polymer Thin Films via Flowcoating. *Langmuir* **2014**, *30* (19), 5637–5644.

(107) Shaw, L.; Hayoz, P.; Diao, Y.; Reinspach, J. A.; To, J. W. F.; Toney, M. F.; Weitz, R. T.; Bao, Z. Direct Uniaxial Alignment of a Donor-Acceptor Semiconducting Polymer Using Single-Step Solution Shearing. *ACS Appl. Mater. Interfaces* **2016**, *8* (14), 9285–9296.

(108) Murphy, C. E.; Yang, L.; Ray, S.; Yu, L.; Knox, S.; Stingelin, N. Wire-Bar Coating of Semiconducting Polythiophene/Insulating Polyethylene Blend Thin Films for Organic Transistors. *J. Appl. Phys.* **2011**, *110* (9), 093523.

(109) Buchaca-Domingo, E.; Ferguson, A. J.; Jamieson, F. C.; McCarthy-Ward, T.; Shoaee, S.; Tumbleston, J. R.; Reid, O. G.; Yu, L.; Madec, M. B.; Pfannmöller, M.; et al. Additive-Assisted Supramolecular Manipulation of Polymer:Fullerene Blend Phase Morphologies and Its Influence on Photophysical Processes. *Mater. Horizons* **2014**, *1* (2), 270–279.

(110) Na, S. I.; Seo, Y. H.; Nah, Y. C.; Kim, S. S.; Heo, H.; Kim, J. E.; Rolston, N.; Dauskardt, R. H.; Gao, M.; Lee, Y.; et al. High Performance Roll-to-Roll Produced Fullerene-Free Organic Photovoltaic Devices via Temperature-Controlled Slot Die Coating. *Adv. Funct. Mater.* **2019**, *29* (6), 1–10.

(111) Xu, C.; Cai, P.; Zhang, X.; Zhang, Z.; Xue, X.; Xiong, J.; Zhang, J. A Wide Temperature Tolerance, Solution-Processed MoOx Interface Layer for Efficient and Stable Organic Solar Cells. *Sol. Energy Mater. Sol. Cells* **2017**, *159*, 136–142.

(112) Zhang, T.; Zhao, X.; Yang, D.; Yang, X. Efficient Polymer Solar Cells Spray-Coated from Non-Halogenated Solvents towards Practical Fabrication. *Energy Technol.* **2018**, *6* (1), 171–177.

(113) Wan, Q.; Guo, X.; Wang, Z.; Li, W.; Guo, B.; Ma, W.; Zhang, M.; Li, Y. 10.8% Efficiency Polymer Solar Cells Based on PTB7-Th and PC71BM via Binary Solvent Additives Treatment. *Adv. Funct. Mater.* **2016**, *26* (36), 6635–6640.

(114) Vezie, M. S.; Few, S.; Meager, I.; Pieridou, G.; Dörling, B.; Ashraf, R. S.; Goñi, A. R.; Bronstein, H.; McCulloch, I.; Hayes, S. C.; et al. Exploring the Origin of High Optical Absorption in Conjugated Polymers. *Nat. Mater.* **2016**, *15* (7), 746–753.

(115) Zhang, Y.; Feng, H.; Meng, L.; Wang, Y.; Chang, M.; Li, S.; Guo, Z.; Li, C.; Zheng,

N.; Xie, Z.; et al. High Performance Thick-Film Nonfullerene Organic Solar Cells with Efficiency over 10% and Active Layer Thickness of 600 Nm. *Adv. Energy Mater.* **2019**, *9* (45), 1902688.

(116) Luo, Z.; Sun, C.; Chen, S.; Zhang, Z. G.; Wu, K.; Qiu, B.; Yang, C.; Li, Y.; Yang, C. Side-Chain Impact on Molecular Orientation of Organic Semiconductor Acceptors: High Performance Nonfullerene Polymer Solar Cells with Thick Active Layer over 400 Nm. *Adv. Energy Mater.* **2018**, *8* (23), 1800856.

(117) Spano, F. C.; Silva, C. H- and J-Aggregate Behavior in Polymeric Semiconductors. *Annu. Rev. Phys. Chem.* **2014**, *65* (1), 477–500.

(118) Dantanarayana, V.; Fuzell, J.; Nai, D.; Jacobs, I. E.; Yan, H.; Faller, R.; Larsen, D.; Moule, A. J. Put Your Backbone into It: Excited-State Structural Relaxation of PffBT4T-2DT Conducting Polymer in Solution. *J. Phys. Chem. C* **2018**, *122* (12), 7020–7026.

(119) Spano, F. C. Modeling Disorder in Polymer Aggregates: The Optical Spectroscopy of Regioregular Poly(3-Hexylthiophene) Thin Films. *J. Chem. Phys.* **2005**, *122* (23).

(120) Li, W.; Hendriks, K. H.; Furlan, A.; Roelofs, W. S. C.; Wienk, M. M.; Janssen, R. A. J. Universal Correlation between Fibril Width and Quantum Efficiency in Diketopyrrolopyrrole-Based Polymer Solar Cells. *J. Am. Chem. Soc.* **2013**, *135* (50), 18942–18948.

(121) Rivnay, J.; Mannsfeld, S. C. B.; Miller, C. E.; Salleo, A.; Toney, M. F. Quantitative Determination of Organic Semiconductor Microstructure from the Molecular to Device Scale. *Chem. Rev.* **2012**, *112* (10), 5488–5519.

(122) Hexemer, A.; Bras, W.; Glossinger, J.; Schaible, E.; Gann, E.; Kirian, R.; MacDowell, A.; Church, M.; Rude, B.; Padmore, H. A SAXS/WAXS/GISAXS Beamline with Multilayer Monochromator. *J. Phys. Conf. Ser.* **2010**, *247*, 012007.

(123) Ade, H.; Hitchcock, A. P. NEXAFS Microscopy and Resonant Scattering: Composition and Orientation Probed in Real and Reciprocal Space. *Polymer (Guildf).* **2008**, *49* (3), 643–675.

(124) Ade, H.; Stoll, H. Near-Edge X-Ray Absorption Fine-Structure Microscopy of Organic and Magnetic Materials. *Nat. Mater.* **2009**, *8* (4), 281–290.

(125) Schmidt-Hansberg, B.; Klein, M. F. G.; Peters, K.; Buss, F.; Pfeifer, J.; Walheim, S.; Colsmann, A.; Lemmer, U.; Scharfer, P.; Schabel, W. In Situ Monitoring the Drying Kinetics of Knife Coated Polymer-Fullerene Films for Organic Solar Cells. *J. Appl. Phys.* **2009**, *106* (12), 124501.

(126) Wang, T.; Dunbar, A. D. F.; Staniec, P. A.; Pearson, A. J.; Hopkinson, P. E.; MacDonald, J. E.; Lilliu, S.; Pizzey, C.; Terrill, N. J.; Donald, A. M.; et al. The Development of Nanoscale Morphology in Polymer:Fullerene Photovoltaic Blends

during Solvent Casting. *Soft Matter* **2010**, *6* (17), 4128–4134.

(127) Köhler, A. Journal of the Royal Microscopical Society. *J. R. Microsc. Soc.* **1894**, *14*, 261–262.

(128) Cho, E.; Risko, C.; Kim, D.; Gysel, R.; Cates Miller, N.; Breiby, D. W.; McGehee, M. D.; Toney, M. F.; Kline, R. J.; Bredas, J. L. Three-Dimensional Packing Structure and Electronic Properties of Biaxially Oriented Poly(2,5-Bis(3-Alkylthiophene-2-Yl)Thieno[3,2- b]Thiophene) Films. *J. Am. Chem. Soc.* **2012**, *134* (14), 6177–6190.

(129) Ewald, P. P. Introduction to the Dynamical Theory of X-ray Diffraction. *Acta Crystallogr. Sect. A* **1969**, *25* (1), 103–108.

(130) Baker, J. L.; Jimison, L. H.; Mannsfeld, S.; Volkman, S.; Yin, S.; Subramanian, V.; Salleo, A.; Alivisatos, A. P.; Toney, M. F. Quantification of Thin Film Cristallographic Orientation Using X-Ray Diffraction with an Area Detector. *Langmuir* **2010**, *26* (11), 9146–9151.

(131) Gomez, E. D.; Barteau, K. P.; Wang, H.; Toney, M. F.; Loo, Y. L. Correlating the Scattered Intensities of P3HT and PCBM to the Current Densities of Polymer Solar Cells. *Chem. Commun.* **2011**, *47* (1), 436–438.

(132) Perez, L. A.; Zalar, P.; Ying, L.; Schmidt, K.; Toney, M. F.; Nguyen, T. Q.; Bazan, G. C.; Kramer, E. J. Effect of Backbone Regioregularity on the Structure and Orientation of a Donor-Acceptor Semiconducting Copolymer. *Macromolecules* **2014**, *47* (4), 1403–1410.

(133) Ilavsky, J. Nika: Software for Two-Dimensional Data Reduction. *J. Appl. Crystallogr.* **2012**, *45* (2), 324–328.

(134) Ro, H. W.; Downing, J. M.; Engmann, S.; Herzing, A. A.; Delongchamp, D. M.; Richter, L. J.; Mukherjee, S.; Ade, H.; Abdelsamie, M.; Jagadamma, L. K.; et al. Morphology Changes upon Scaling a High-Efficiency, Solution-Processed Solar Cell. *Energy Environ. Sci.* **2016**, *9* (9), 2835–2846.

(135) Stafford, C. M.; Roskov, K. E.; Epps, T. H.; Fasolka, M. J. Generating Thickness Gradients of Thin Polymer Films via Flow Coating. *Rev. Sci. Instrum.* **2006**, *77* (2), 023908.

(136) Zimmermann, E.; Ehrenreich, P.; Pfadler, T.; Dorman, J. A.; Weickert, J.; Schmidt-Mende, L. Erroneous Efficiency Reports Harm Organic Solar Cell Research. *Nat. Photonics* **2014**, *8*, 669–672.

(137) Lampert, M. A. Simplified Theory of Space-Charge-Limited Currents in an Insulator with Traps. *Phys. Rev.* **1956**, *103* (6), 1648–1656.

(138) Murgatroyd, P. N. Theory of Space-Charge-Limited Current Enhanced by Frenkel

Effect. *J. Phys. D. Appl. Phys.* **1970**, *3* (2), 151–156.

(139) Dacuña, J.; Salleo, A. Modeling Space-Charge-Limited Currents in Organic Semiconductors: Extracting Trap Density and Mobility. *Phys. Rev. B - Condens. Matter Mater. Phys.* **2011**, *84* (19), 1–35.

(140) Brebels, J.; Manca, J. V.; Lutsen, L.; Vanderzande, D.; Maes, W. High Dielectric Constant Conjugated Materials for Organic Photovoltaics. *J. Mater. Chem. A* **2017**, *5* (46), 24037–24050.

(141) Søndergaard, R. R.; Hösel, M.; Krebs, F. C. Roll-to-Roll Fabrication of Large Area Functional Organic Materials. *J. Polym. Sci. Part B Polym. Phys.* **2013**, *51* (1), 16–34.

(142) Choi, H.; Ko, S. J.; Kim, T.; Morin, P. O.; Walker, B.; Lee, B. H.; Leclerc, M.; Kim, J. Y.; Heeger, A. J. Small-Bandgap Polymer Solar Cells with Unprecedented Short-Circuit Current Density and High Fill Factor. *Adv. Mater.* **2015**, *27* (21), 3318–3324.

(143) Kim, Y. J.; Jang, W.; Ahn, S.; Park, C. E.; Wang, D. H. Dramatically Enhanced Performances and Ideally Controlled Nano-Morphology via Co-Solvent Processing in Low Bandgap Polymer Solar Cells. *Org. Electron.* **2016**, *34*, 42–49.

(144) Li, W.; Hendriks, K. H.; Roelofs, W. S. C.; Kim, Y.; Wienk, M. M.; Janssen, R. A. J. Efficient Small Bandgap Polymer Solar Cells with High Fill Factors for 300 Nm Thick Films. *Adv. Mater.* **2013**, *25*, 3182–3186.

(145) Bartesaghi, D.; Pérez, I. D. C.; Kniepert, J.; Roland, S.; Turbiez, M.; Neher, D.; Koster, L. J. A. Competition between Recombination and Extraction of Free Charges Determines the Fill Factor of Organic Solar Cells. *Nat. Commun.* **2015**, *6*, 7083.

(146) Back, J. Y.; Yu, H.; Song, I.; Kang, I.; Ahn, H.; Shin, T. J.; Kwon, S. K.; Oh, J. H.; Kim, Y. H. Investigation of Structure-Property Relationships in Diketopyrrolopyrrole-Based Polymer Semiconductors via Side-Chain Engineering. *Chem. Mater.* **2015**, *27* (5), 1732–1739.

(147) Zhang, G.; Clarke, T. M.; Mozer, A. J. Bimolecular Recombination in a Low Bandgap Polymer:PCBM Blend Solar Cell with a High Dielectric Constant. *J. Phys. Chem. C* **2016**, *120* (13), 7033–7043.

(148) Li, W.; Hendriks, K. H.; Wienk, M. M.; Janssen, R. A. J. Diketopyrrolopyrrole Polymers for Organic Solar Cells. *Acc. Chem. Res.* **2016**, *49* (1), 78–85.

(149) Pivrikas, A.; Neugebauer, H.; Sariciftci, N. S. Influence of Processing Additives to Nano-Morphology and Efficiency of Bulk-Heterojunction Solar Cells: A Comparative Review. *Sol. Energy* **2011**, *85* (6), 1226–1237.

(150) Liao, H. C.; Ho, C. C.; Chang, C. Y.; Jao, M. H.; Darling, S. B.; Su, W. F. Additives

for Morphology Control in High-Efficiency Organic Solar Cells. *Mater. Today* **2013**, *16* (9), 326–336.

(151) Zhang, F.; Jespersen, K. G.; Björström, C.; Svensson, M.; Andersson, M. R.; Sundström, V.; Magnusson, K.; Moons, E.; Yartsev, A.; Inganäs, O. Influence of Solvent Mixing on the Morphology and Performance of Solar Cells Based on Polyfluorene Copolymer/Fullerene Blends. *Adv. Funct. Mater.* **2006**, *16* (5), 667–674.

(152) Shaheen, S. E.; Brabec, C. J.; Sariciftci, N. S.; Padinger, F.; Fromherz, T.; Hummelen, J. C. 2.5% Efficient Organic Plastic Solar Cells. *Appl. Phys. Lett.* **2001**, *78* (6), 841–843.

(153) Lucera, L.; Kubis, P.; Fecher, F. W.; Bronnbauer, C.; Turbiez, M.; Forberich, K.; Ameri, T.; Egelhaaf, H. J.; Brabec, C. J. Guidelines for Closing the Efficiency Gap between Hero Solar Cells and Roll-To-Roll Printed Modules. *Energy Technol.* **2015**, *3* (4), 373–384.

(154) Sun, Y.; Takacs, C. J.; Cowan, S. R.; Seo, J. H.; Gong, X.; Roy, A.; Heeger, A. J. Efficient, Air-Stable Bulk Heterojunction Polymer Solar Cells Using MoOx as the Anode Interfacial Layer. *Adv. Mater.* **2011**, *23* (19), 2226–2230.

(155) Bourque, A. J.; Engmann, S.; Fuster, A.; Snyder, C. R.; Richter, L. J.; Geraghty, P. B.; Jones, D. J. Morphology of a Thermally Stable Small Molecule OPV Blend Comprising a Liquid Crystalline Donor and Fullerene Acceptor. *J. Mater. Chem. A* **2019**, *7* (27), 16458–16471.

(156) Negi, V.; Wodo, O.; Van Franeker, J. J.; Janssen, R. A. J.; Bobbert, P. A. Simulating Phase Separation during Spin Coating of a Polymer-Fullerene Blend: A Joint Computational and Experimental Investigation. *ACS Appl. Energy Mater.* **2018**, *1* (2), 725–735.

(157) Ding, Z.; Kettle, J.; Horie, M.; Chang, S. W.; Smith, G. C.; Shames, A. I.; Katz, E. A. Efficient Solar Cells Are More Stable: The Impact of Polymer Molecular Weight on Performance of Organic Photovoltaics. *J. Mater. Chem. A* **2016**, *4* (19), 7274–7280.

(158) Shin, N.; Richter, L. J.; Herzing, A. A.; Kline, R. J.; DeLongchamp, D. M. Effect of Processing Additives on the Solidification of Blade-Coated Polymer/Fullerene Blend Films via in-Situ Structure Measurements. *Adv. Energy Mater.* **2013**, *3* (7), 938–948.

(159) Hernandez, J. L.; Reichmanis, E.; Reynolds, J. R. Probing Film Solidification Dynamics in Polymer Photovoltaics. *Org. Electron.* **2015**, *25*, 57–65.

(160) Gu, X.; Shaw, L.; Gu, K.; Toney, M. F.; Bao, Z. The Meniscus-Guided Deposition of Semiconducting Polymers. *Nat. Commun.* **2018**, *9*, 534.

(161) Cao, X.; Li, M.; Liu, J.; Wang, H.; Zhou, K.; Han, Y. Control over Fibril Width via Different Solubility Additives for Diketopyrrolopyrrole-Based Photovoltaic Devices. *Org. Electron.* **2015**, *24*, 280–287.

(162) Li, W.; Hendriks, K. H.; Furlan, A.; Roelofs, W. S. C.; Meskers, S. C. J.; Wienk, M. M.; Janssen, R. A. J. Effect of the Fibrillar Microstructure on the Efficiency of High Molecular Weight Diketopyrrolopyrrole-Based Polymer Solar Cells. *Adv. Mater.* **2014**, *26* (10), 1565–1570.

(163) Choi, Y.; Kim, G.; Kim, H.; Lee, S. H.; Kwon, S.; Kim, J.; Lee, K. Optimized Phase Separation in Low-Bandgap Polymer:Fullerene Bulk Heterojunction Solar Cells with Criteria of Solvent Additives. *Nano Energy* **2016**, *30*, 200–207.

(164) Ma, W.; Tumbleston, J. R.; Wang, M.; Gann, E.; Huang, F.; Ade, H. Domain Purity, Miscibility, and Molecular Orientation at Donor/Acceptor Interfaces in High Performance Organic Solar Cells: Paths to Further Improvement. *Adv. Energy Mater.* **2013**, *3* (7), 864–872.

(165) Mukherjee, S.; Proctor, C. M.; Tumbleston, J. R.; Bazan, G. C.; Nguyen, T. Q.; Ade, H. Importance of Domain Purity and Molecular Packing in Effi Cient Solution-Processed Small-Molecule Solar Cells. *Adv. Mater.* **2015**, *27* (6), 1105–1111.

(166) Delamarre, A. Characterization of Solar Cells Using Electroluminescence and Photoluminescence Hyperspectral Images. *J. Photonics Energy* **2012**, *2* (1), 027004.

(167) El-Hajje, G.; Momblona, C.; Gil-Escrig, L.; Ávila, J.; Guillemot, T.; Guillemoles, J. F.; Sessolo, M.; Bolink, H. J.; Lombez, L. Quantification of Spatial Inhomogeneity in Perovskite Solar Cells by Hyperspectral Luminescence Imaging. *Energy Environ. Sci.* **2016**, *9* (7), 2286–2294.

(168) Hameiri, Z.; Mahboubi Soufiani, A.; Juhl, M. K.; Jiang, L.; Huang, F.; Cheng, Y. B.; Kampwerth, H.; Weber, J. W.; Green, M. A.; Trupke, T. Photoluminescence and Electroluminescence Imaging of Perovskite Solar Cells. *Prog. Photovoltaics Res. Appl.* **2015**, *23* (12), 1697–1705.

(169) Stolterfoht, M.; Wolff, C. M.; Márquez, J. A.; Zhang, S.; Hages, C. J.; Rothhardt, D.; Albrecht, S.; Burn, P. L.; Meredith, P.; Unold, T.; et al. Visualization and Suppression of Interfacial Recombination for High-Efficiency Large-Area Pin Perovskite Solar Cells. *Nat. Energy* **2018**, *3* (10), 847–854.

(170) Yi, Z.; Wang, S.; Liu, Y. Design of High-Mobility Diketopyrrolopyrrole-Based π-Conjugated Copolymers for Organic Thin-Film Transistors. *Adv. Mater.* **2015**, *27* (24), 3589–3606.

(171) Lee, J. S.; Son, S. K.; Song, S.; Kim, H.; Lee, D. R.; Kim, K.; Ko, M. J.; Choi, D. H.; Kim, B. S.; Cho, J. H. Importance of Solubilizing Group and Backbone Planarity in Low Band Gap Polymers for High Performance Ambipolar Field-Effect Transistors. *Chem. Mater.* **2012**, *24* (7), 1316–1323.

(172) Bokel, F. A.; Engmann, S.; Herzing, A. A.; Collins, B. A.; Ro, H. W.; DeLongchamp, D. M.; Richter, L. J.; Schaible, E.; Hexemer, A. In Situ X-Ray Scattering Studies of the Influence of an Additive on the Formation of a Low-Bandgap Bulk Heterojunction. *Chem. Mater.* **2017**, *29* (5), 2283–2293.

(173) Agostinelli, T.; Lilliu, S.; Labram, J. G.; Campoy-Quiles, M.; Hampton, M.; Pires, E.; Rawle, J.; Bikondoa, O.; Bradley, D. D. C.; Anthopoulos, T. D.; et al. Real-Time Investigation of Crystallization and Phase-Segregation Dynamics in P3HT:PCBM Solar Cells during Thermal Annealing. *Adv. Funct. Mater.* **2011**, *21* (9), 1701–1708.

(174) Engmann, S.; Bokel, F. A.; Herzing, A. A.; Ro, H. W.; Girotto, C.; Caputo, B.; Hoven, C. V.; Schaible, E.; Hexemer, A.; DeLongchamp, D. M.; et al. Real-Time X-Ray Scattering Studies of Film Evolution in High Performing Small-Molecule-Fullerene Organic Solar Cells. *J. Mater. Chem. A* **2015**, *3* (16), 8764–8771.

(175) Venkateshvaran, D.; Nikolka, M.; Sadhanala, A.; Lemaur, V.; Zelazny, M.; Kepa, M.; Hurhangee, M.; Kronemeijer, A. J.; Pecunia, V.; Nasrallah, I.; et al. Approaching Disorder-Free Transport in High-Mobility Conjugated Polymers. *Nature* **2014**, *515* (7527), 384–388.

(176) Reichenberger, M.; Baderschneider, S.; Kroh, D.; Grauf, S.; Köhler, J.; Hildner, R.; Köhler, A. Watching Paint Dry: The Impact of Diiodooctane on the Kinetics of Aggregate Formation in Thin Films of Poly(3-Hexylthiophene). *Macromolecules* **2016**, *49* (17), 6420–6430.

(177) Shen, X.; Hu, W.; Russell, T. P. Measuring the Degree of Crystallinity in Semicrystalline Regioregular Poly(3-Hexylthiophene). *Macromolecules* **2016**, *49* (12), 4501–4509.

(178) Heumueller, T.; Mateker, W. R.; Sachs-Quintana, I. T.; Vandewal, K.; Bartelt, J. A.; Burke, T. M.; Ameri, T.; Brabec, C. J.; McGehee, M. D. Reducing Burn-in Voltage Loss in Polymer Solar Cells by Increasing the Polymer Crystallinity. *Energy Environ. Sci.* **2014**, *7* (9), 2974–2980.

(179) Liao, S. H.; Jhuo, H. J.; Cheng, Y. S.; Chen, S. A. Fullerene Derivative-Doped Zinc Oxide Nanofilm as the Cathode of Inverted Polymer Solar Cells with Low-Bandgap Polymer (PTB7-Th) for High Performance. *Adv. Mater.* **2013**, *25* (34), 4766–4771.

(180) Fan, B.; Zhang, D.; Li, M.; Zhong, W.; Zeng, Z.; Ying, L.; Huang, F.; Cao, Y. Achieving over 16% Efficiency for Single-Junction Organic Solar Cells. *Sci. China Chem.* **2019**, *62*, 746–752.

(181) Cha, H.; Wu, J.; Wadsworth, A.; Nagitta, J.; Limbu, S.; Pont, S.; Li, Z.; Searle, J.; Wyatt, M. F.; Baran, D.; et al. An Efficient, "Burn in" Free Organic Solar Cell Employing a Nonfullerene Electron Acceptor. *Adv. Mater.* **2017**, *29* (33), 1701156.

(182) Qing, L.; Zhong, A.; Chen, W.; Cao, Y.; Chen, J. Largely Improved Bulk-Heterojunction Morphology in Organic Solar Cells Based on a Conjugated

Terpolymer Donor via a Ternary Strategy. *Polymer (Guildf).* **2020**, *186*, 122050.

(183) Yi, X.; Peng, Z.; Xu, B.; Seyitliyev, D.; Ho, C. H. Y.; Danilov, E. O.; Kim, T.; Reynolds, J. R.; Amassian, A.; Gundogdu, K.; et al. Critical Role of Polymer Aggregation and Miscibility in Nonfullerene-Based Organic Photovoltaics. *Adv. Energy Mater.* **2020**, *10* (8), 1902430.

(184) Zhang, Y.; Sajjad, M. T.; Blaszczyk, O.; Parnell, A. J.; Ruseckas, A.; Serrano, L. A.; Cooke, G.; Samuel, I. D. W. Large Crystalline Domains and an Enhanced Exciton Diffusion Length Enable Efficient Organic Solar Cells. *Chem. Mater.* **2019**, *31* (17), 6548–6557.

(185) Hamid, Z.; Wadsworth, A.; Rezasoltani, E.; Holliday, S.; Azzouzi, M.; Neophytou, M.; Guilbert, A. A. Y.; Dong, Y.; Little, M. S.; Mukherjee, S.; et al. Influence of Polymer Aggregation and Liquid Immiscibility on Morphology Tuning by Varying Composition in PffBT4T-2DT/Nonfullerene Organic Solar Cells. *Adv. Energy Mater.* **2020**, *10* (8), 1903248.

(186) Park, S. H.; Park, S.; Kurniawan, D.; Son, J. G.; Noh, J. H.; Ahn, H.; Son, H. J. Highly Efficient Large Area Organic Photovoltaic Module with 350 Nm Thick Active Layer Using Random Terpolymer Donor. *Chem. Mater.* **2020**, 10.1021/acs.chemmater.9b05399.

(187) Baran, D.; Ashraf, R. S.; Hanifi, D. A.; Abdelsamie, M.; Gasparini, N.; Röhr, J. A.; Holliday, S.; Wadsworth, A.; Lockett, S.; Neophytou, M.; et al. Reducing the Efficiency-Stability-Cost Gap of Organic Photovoltaics with Highly Efficient and Stable Small Molecule Acceptor Ternary Solar Cells. *Nat. Mater.* **2017**, *16* (3), 363–369.

(188) Pirotte, G.; Agarkar, S.; Xu, B.; Zhang, J.; Lutsen, L.; Vanderzande, D.; Yan, H.; Pollet, P.; Reynolds, J. R.; Maes, W.; et al. Molecular Weight Tuning of Low Bandgap Polymers by Continuous Flow Chemistry: Increasing the Applicability of PffBT4T for Organic Photovoltaics. *J. Mater. Chem. A* **2017**, *5* (34), 18166–18175.

(189) Burkhart, B.; Khlyabich, P. P.; Cakir Canak, T.; Lajoie, T. W.; Thompson, B. C. "Semi-Random" Multichromophoric Rr-P3HT Analogues for Solar Photon Harvesting. *Macromolecules* **2011**, *44* (6), 1242–1246.

(190) Jones, A. L.; Zheng, Z.; Riley, P.; Pelse, I.; Zhang, J.; Abdelsamie, M.; Toney, M. F.; Marder, S. R.; So, F.; Brédas, J. L.; et al. Acceptor Gradient Polymer Donors for Non-Fullerene Organic Solar Cells. *Chem. Mater.* **2019**, *31* (23), 9729–9741.

(191) Thompson, B. C.; Fréchet, J. M. J. Polymer-Fullerene Composite Solar Cells. *Angew. Chemie - Int. Ed.* **2008**, *47* (1), 58–77.

(192) Prat, D.; Wells, A.; Hayler, J.; Sneddon, H.; McElroy, C. R.; Abou-Shehada, S.; Dunn, P. J. CHEM21 Selection Guide of Classical- and Less Classical-Solvents. *Green Chem.* **2015**, *18* (1), 288–296.

(193) Kim, Y.; Choi, J.; Lee, C.; Kim, Y.; Kim, C.; Nguyen, T. L.; Gautam, B.; Gundogdu, K.; Woo, H. Y.; Kim, B. J. Aqueous Soluble Fullerene Acceptors for Efficient Eco-Friendly Polymer Solar Cells Processed from Benign Ethanol/Water Mixtures. *Chem. Mater.* **2018**, *30* (16), 5663–5672.

(194) Xie, C.; Heumüller, T.; Gruber, W.; Tang, X.; Classen, A.; Schuldes, I.; Bidwell, M.; Späth, A.; Fink, R. H.; Unruh, T.; et al. Overcoming Efficiency and Stability Limits in Water-Processing Nanoparticular Organic Photovoltaics by Minimizing Microstructure Defects. *Nat. Commun.* **2018**, *9* (1), 5335.

(195) Park, C. Do; Fleetham, T. A.; Li, J.; Vogt, B. D. High Performance Bulk-Heterojunction Organic Solar Cells Fabricated with Non-Halogenated Solvent Processing. *Org. Electron.* **2011**, *12* (9), 1465–1470.

(196) Fan, B.; Ying, L.; Wang, Z.; He, B.; Jiang, X. F.; Huang, F.; Cao, Y. Optimisation of Processing Solvent and Molecular Weight for the Production of Green-Solvent-Processed All-Polymer Solar Cells with a Power Conversion Efficiency over 9%. *Energy Environ. Sci.* **2017**, *10* (5), 1243–1251.

(197) Ye, L.; Xiong, Y.; Chen, Z.; Zhang, Q.; Fei, Z.; Henry, R.; Heeney, M.; O'Connor, B. T.; You, W.; Ade, H. Sequential Deposition of Organic Films with Eco-Compatible Solvents Improves Performance and Enables Over 12%-Efficiency Nonfullerene Solar Cells. *Adv. Mater.* **2019**, *31* (17), 1808153.

(198) Chueh, C. C.; Yao, K.; Yip, H. L.; Chang, C. Y.; Xu, Y. X.; Chen, K. S.; Li, C. Z.; Liu, P.; Huang, F.; Chen, Y.; et al. Non-Halogenated Solvents for Environmentally Friendly Processing of High-Performance Bulk-Heterojunction Polymer Solar Cells. *Energy Environ. Sci.* **2013**, *6* (11), 3241–3248.

(199) Cai, W.; Liu, P.; Jin, Y.; Xue, Q.; Liu, F.; Russell, T. P.; Huang, F.; Yip, H. L.; Cao, Y. Morphology Evolution in High-Performance Polymer Solar Cells Processed from Nonhalogenated Solvent. *Adv. Sci.* **2015**, *2* (8), 1500095.

(200) Amb, C. M.; Chen, S.; Graham, K. R.; Subbiah, J.; Small, C. E.; So, F.; Reynolds, J. R. Dithienogermole as a Fused Electron Donor in Bulk Heterojunction Solar Cells. *J. Am. Chem. Soc.* **2011**, *133* (26), 10062–10065.

(201) Hou, J.; Chen, H. Y.; Zhang, S.; Li, G.; Yang, Y. Synthesis, Characterization, and Photovoltaic Properties of a Low Band Gap Polymer Based on Silole-Containing Polythiophenes and 2,1,3-Benzothiadiazole. *J. Am. Chem. Soc.* **2008**, *130* (48), 16144–16145.

(202) Chen, H. Y.; Hou, J.; Hayden, A. E.; Yang, H.; Houk, K. N.; Yang, Y. Silicon Atom Substitution Enhances Interchain Packing in a Thiophene-Based Polymer System. *Adv. Mater.* **2010**, *22* (3), 371–375.

(203) Ruoff, R. S.; Tse, D. S.; Malhotra, R.; Lorents, D. C. Solubility of C60 in a Variety of Solvents. *J. Phys. Chem.* **1993**, *97* (13), 3379–3383.

(204) Constantinou, I.; Lai, T. H.; Zhao, D.; Klump, E. D.; Deininger, J. J.; Lo, C. K.; Reynolds, J. R.; So, F. High Efficiency Air-Processed Dithienogermole-Based Polymer Solar Cells. *ACS Appl. Mater. Interfaces* **2015**, *7* (8), 4826–4832.

(205) Guinier, A.; Lorrain, P.; Lorrain, D. S.; Gillis, J. X-Ray Diffraction in Crystals, Imperfect Crystals, and Amorphous Bodies. *Phys. Today* **1964**, *17* (4), 70–72.

(206) Warren, B. E. X-Ray Diffraction Methods. *J. Appl. Phys.* **1941**, *12* (5), 375–383.

(207) Ilavsky, J.; Jemian, P. R. Irena: Tool Suite for Modeling and Analysis of Small-Angle Scattering. *J. Appl. Crystallogr.* **2009**, *42* (2), 347–353.

(208) Beaucage, G.; Schaefer, D. W. Structural Studies of Complex Systems Using Small-Angle Scattering: A Unified Guinier/Power-Law Approach. *J. Non. Cryst. Solids* **1994**, *172–174*, 797–805.

(209) Beaucage, G. Approximations Leading to a Unified Exponential/Power-Law Approach to Small-Angle Scattering. *J. Appl. Crystallogr.* **1995**, *28* (6), 717–728.

(210) Sivanandan, K.; Chatterjee, T.; Treat, N.; Kramer, E. J.; Hawker, C. J. High Surface Area Poly(3-Hexylthiophenes) Thin Films from Cleavable Graft Copolymers. *Macromolecules* **2010**, *43* (1), 233–241.

(211) Verploegen, E.; Miller, C. E.; Schmidt, K.; Bao, Z.; Toney, M. F. Manipulating the Morphology of P3HT-PCBM Bulk Heterojunction Blends with Solvent Vapor Annealing. *Chem. Mater.* **2012**, *24* (20), 3923–3931.

(212) Lou, S. J.; Zhou, N.; Guo, X.; Chang, R. P. H.; Marks, T. J.; Chen, L. X. Effects of 1,8-Diiodooctane on Domain Nanostructure and Charge Separation Dynamics in PC71BM-Based Bulk Heterojunction Solar Cells. *J. Mater. Chem. A* **2018**, *6* (46), 23805–23818.

(213) Wolfe, R. M. W.; Reynolds, J. R. Direct Imide Formation from Thiophene Dicarboxylic Acids Gives Expanded Side-Chain Selection in Thienopyrrolediones. *Org. Lett.* **2017**, *19* (5), 996–999.

(214) Yu, R.; Yao, H.; Hou, J. Recent Progress in Ternary Organic Solar Cells Based on Nonfullerene Acceptors. *Adv. Energy Mater.* **2018**, *8* (28), 1702814.

(215) Pan, M. A.; Lau, T. K.; Tang, Y.; Wu, Y. C.; Liu, T.; Li, K.; Chen, M. C.; Lu, X.; Ma, W.; Zhan, C. 16.7%-Efficiency Ternary Blended Organic Photovoltaic Cells with PCBM as the Acceptor Additive to Increase the Open-Circuit Voltage and Phase Purity. *J. Mater. Chem. A* **2019**, *7* (36), 20713–20722.

(216) Hernandez, J. L.; Deb, N.; Wolfe, R. M. W.; Lo, C. K.; Engmann, S.; Richter, L. J.; Reynolds, J. R. Simple Transfer from Spin Coating to Blade Coating through Processing Aggregated Solutions. *J. Mater. Chem. A* **2017**, *5* (39), 20687–20695.

(217) Acton, D. W.; Barker, J. F. In Situ Biodegradation Potential of Aromatic Hydrocarbons in Anaerobic Groundwaters. *J. Contam. Hydrol.* **1992**, *9* (4), 325–352.

(218) Liu, C.; Zhu, Y.; Chen, J.; Wang, H.; Cao, Y.; Chen, J. Terpinolene Processed PTB7:PC71BM Blend Film for Polymer Solar Cells: A Non-Aromatic and Non-Chlorinated Solvent Predicted by Hansen Solubility Parameters. *Synth. Met.* **2018**, *242*, 17–22.

VITA

Ian Pelse was born and raised in New Jersey. He earned his bachelor's degree in chemistry from Bard College in the spring of 2014, while working under the supervision of Dr. Chris N. LaFratta. His research focused on the construction of a direct laser writing system to fabricate high resolution microfluidic masters. He joined the research group of Dr. John R. Reynolds at the Georgia Institute of Technology in the fall of 2014 and began studying polymer organic photovoltaics. His research was on the processing of organic photovoltaic active layers, and focused on blade coating, polymer aggregation, and morphology characterization. This thesis was compiled during a coronavirus quarantine in the spring of 2020, and Ian expects to graduate in the summer of 2020. Ian will spend his first year out of graduate school as a postdoctoral fellow working with Dr. Meisha Shofner, studying the effects of various sterilization treatments on the chemical structure and mechanical properties of the elastic straps of face masks.